



# **STUDY OF NANOSTRUCTURES USING POSITRON ANNIHILATION SPECTROSCOPY**

*By*

**SANDEEP KUMAR SHARMA**

**CHEM01200804006**

**Bhabha Atomic Research Centre, Mumbai**

*A thesis submitted to the*

*Board of Studies in Chemical Sciences*

*In partial fulfillment of requirements*

*For the Degree of*

**DOCTOR OF PHILOSOPHY**

*of*

**HOMI BHABHA NATIONAL INSTITUTE**



**September, 2012**



# HOMI BHABHA NATIONAL INSTITUTE

## Recommendations of the Viva Voce Board

As members of the Viva Voce Board, we certify that we have read the dissertation prepared by **Sandeep Kumar Sharma** entitled “**Study of Nanostructures Using Positron Annihilation Spectroscopy**” and recommend that it may be accepted as fulfilling the dissertation requirement for the Degree of Doctor of Philosophy.

**Date:**

**Chairman:** Prof. A. Goswami

**Date:**

**Guide:** Prof. P. K. Pujari

**Date:**

**Member 1:** Prof. A. V. R. Reddy

**Date:**

**Member 2:** Prof. B. S. Tomar

**Date:**

**Member 3:** Prof. S. Kapoor

Final approval and acceptance of this dissertation is contingent upon the candidate's submission of the final copies of the dissertation to HBNI. I hereby certify that I have read this dissertation prepared under my direction and recommend that it may be accepted as fulfilling the dissertation requirement.

**Date:**

**Place:**

# **STATEMENT BY AUTHOR**

This dissertation has been submitted in partial fulfillment of requirements for an advanced degree at Homi Bhabha National Institute (HBNI) and is deposited in the Library to be made available to borrowers under rules of the HBNI.

Brief quotations from this dissertation are allowable without special permission, provided that accurate acknowledgement of source is made. Requests for permission for extended quotation from or reproduction of this manuscript in whole or in part may be granted by the Competent Authority of HBNI when in his or her judgment the proposed use of the material is in the interests of scholarship. In all other instances, however, permission must be obtained from the author.

Sandeep Kumar Sharma

# **DECLARATION**

I, hereby declare that the investigation presented in the thesis has been carried out by me. The work is original and has not been submitted earlier as a whole or in part for a degree /diploma at this or any other Institution / University.

Sandeep Kumar Sharma

***Dedicated to.....***

***My Parents***

***Late P. K. Sharma***

***Smt. Sunita Sharma***

# List of Publications

## REFFEREED JOURNALS

1. Positron annihilation studies in ZnO nanoparticles.  
**S. K. Sharma**, P. K. Pujari, K. Sudarshan, D. Dutta, M. Mahapatra, S.V. Godbole, O. D. Jayakumar and A. K. Tyagi  
*Sol. State Commun.* **149** (2009) 550.
2. Characterization of a sucrose/starch matrix through positron annihilation lifetime spectroscopy: unravelling the decomposition and glass transition processes.  
**S. K. Sharma**, G. Roudaut, I. Fabling and G. Duplâtre,  
*Phys. Chem. Chem. Phys.* **12** (2010) 14278.
3. Free volume and microstructural investigation of poly(ethylene terephthalate)-g-acrylic acid(PET-g-AA) copolymer films.  
S. K. Rath, M. Patri, **S. K. Sharma**, K. Sudarshan and P. K. Pujari  
*Rad. Phys. Chem.* **79** (2010) 745.
4. Modification of microstructure of the surface and the bulk in ion-irradiated membrane studied using positron annihilation spectroscopy.  
**S. K. Sharma**, P. Maheshwari, D. Dutta, K. Sudarshan and P. K. Pujari  
*Rad. Phys. Chem.* **79** (2010) 1115
5. Effect of water on glass transition in starch/sucrose matrices investigated through positron annihilation lifetime spectroscopy: a new approach.  
**S. K. Sharma**, A. Zaydouri, G. Roudaut and G. Duplâtre  
*Phys. Chem. Chem. Phys.* **13** (2011) 19338.
6. Direct evidence of Cd vacancies in CdSe nanoparticles: positron annihilation studies.  
**S. K. Sharma**, K. Sudarshan, P. Maheshwari, D. Dutta, P.K. Pujari, C.P. Shah, M. Kumar, and P. Bajaj  
*Eur. Phys. J. B* **82** (2011) 335.

7. Effect of interfacial interaction on free volumes in phenol-formaldehyde resin-carbon nanotube composites: Positron annihilation lifetime and age momentum correlation studies

**S. K. Sharma**, J. Prakash, K. Sudarshan, P. Maheshwari, D. Sathiyamoorthy and P. K. Pujari

*Phys. Chem. Chem. Phys.* **14** (2012) 10972.

8. Investigation of vacancy defects configurations in gold nanoparticles: Density Functional Theory (DFT) calculations and positron annihilation studies.

**S. K. Sharma**, K. Sudarshan and P. K. Pujari

(Manuscript under preparation)

# Acknowledgements

It gives me immense pleasure to acknowledge all the people who have helped me in completing this thesis. First, I express my deep sense of gratitude to my guide Dr. P. K. Pujari. This work could not have been completed without his invaluable guidance and encouragement.

I would also like to thank Dr. G. Duplâtre, IPHC, Strasbourg for his invaluable guidance for the work on natural polymers. I am grateful to Head, Radiochemistry Division, Associate Director and Director, Radiochemistry and Isotope group for permitting me to register for my Ph.D and their support in finishing the work. I would like to thank my thesis committee members for their valuable suggestions and constructive criticism.

I am thankful to Dr. Kathi Sudarshan for teaching me basics of positron annihilation spectroscopy. I would like to thank Dr. Rahul Tripathi for his encouragement and valuable suggestions. Thanks are due to my seniors Dr. R. Acharya, Dr. S. Sodaye and Dr. D. Dutta for their help.

I would like to thank my colleagues P. Maheshwari, A. Kumar, P. N. Patil, S. Mukherjee, C. Aggarwal, S. Chaudhary and others at the Radiochemistry Division, who have helped me on a day to day basis. I am thankful to my friends Brij Kumar, Jyoti Prakash, Amit Verma, Bhaskar Paul, Vijay Kumar and Swayam Mallick for their constant support.

I take this opportunity to thank my uncle Shri Ved Praksh Sharma for supporting me throughout my life. Finally, I would like to thank my wife Reema Sharma and daughter Elakshi Sharma for their support and cooperation.

B.A.R.C., Mumbai

**Sandeep Kumar Sharma**

# **CONTENTS**

	<b>Page No.</b>
<b>SYNOPSIS</b>	<b>1</b>
<b>LIST OF FIGURES</b>	<b>26</b>
<b>LIST OF TABLES</b>	<b>33</b>
<b>CHAPTER-I</b>	
<b>1. INTRODUCTION</b>	<b>35</b>
<b>1.1. Positron and Positronium</b>	<b>36</b>
1.1.1 Discovery	36
1.1.2 Characteristics	38
1.1.3 Annihilation	38
1.1.4 Positronium atom	39
1.1.5 Sources of positron	41
<b>1.2 Positron and positronium as probe of condensed matter</b>	<b>41</b>
<b>1.3. Positron annihilation spectroscopy</b>	<b>42</b>
1.3.1 Positron Annihilation Lifetime Spectroscopy (PALS)	43
1.3.2 Doppler Broadening of Annihilation Radiation (DBAR)	43
1.3.3 Coincidence Doppler Broadening (CDB)	45
<b>1.4 Nanostructures</b>	<b>45</b>
<b>1.5 Positron annihilation spectroscopy in nanostructures and scope of present work</b>	<b>47</b>
<b>CHAPTER-II</b>	
<b>2. EXPERIMENTAL TECHNIQUES AND THEORETICAL CALCULATIONS</b>	<b>54</b>
<b>2.1. Experimental techniques</b>	<b>55</b>
2.1.1. Positron sources	55
2.1.1.1 Conventional measurements	55
2.1.1.2 Depth dependent measurements	58
2.1.2. Positron annihilation lifetime spectroscopy	59



2.1.2.1 Positron lifetime spectrometer	59
2.1.2.2 Lifetime data analysis	61
2.1.2.3 Source correction	64
2.1.2.4 CONTIN analysis	65
2.1.3. Doppler broadening of annihilation radiation	65
2.1.3.1 Doppler broadening spectrometer	65
2.1.3.2 Data analysis	68
2.1.4. Coincidence Doppler broadening measurements	69
2.1.4.1 Data analysis	74
2.1.5. Depth dependent measurements using slow positron beam	74
2.1.5.1 Variable Energy Positron Fit (VEPFIT) analysis	75
<b>2.2. Theoretical calculations</b>	<b>76</b>
2.2.1 Positron lifetime	77
2.2.2 Electron momentum distribution	81
2.2.3 Execution of calculations using MIKA DOPPLER	82
 <b>CHAPTER-III</b>	
<b>3. NANOSTRUCTURE AND GLASS TRANSITION BEHAVIOUR OF STARCH/SUCROSE MATRICES</b>	<b>85</b>
<b>3.1 Sample preparation</b>	<b>88</b>
<b>3.2. Experiments</b>	<b>89</b>
3.2.1 Thermal gravimetric analysis (TGA)	89
3.2.2. Positron annihilation measurements	89
3.2.2.1 Sample holder and PALS devices	89
3.2.2.2 Sample handling, heating and PLAS counting	91
(i) <i>Dry samples</i>	91
(ii) <i>Hydrated samples</i>	91
3.2.2.3 PALS analysis	94
<b>3.3. Effect of sucrose in starch matrix</b>	<b>94</b>
3.3.1 Decomposition study of STS20 using TGA	94
3.3.2 <i>o</i> -Ps lifetime, $\tau_3$ , and intensity, $I_3$	97
<b>3.4. Effect of water on starch/sucrose matrices</b>	<b>107</b>
3.4.1 <i>o</i> -Ps lifetime, $\tau_3$ , and nanoholes average volume, $V$	107

3.4.2 $T_g$ as a function of water content, $c_w$	111
3.4.3 Distribution of $\tau_3$ (and $V$ )	115
3.4.4 Location and role of the water molecules	117
<b>3.5 Conclusion</b>	<b>119</b>

## **CHAPTER-IV**

<b>4. NANOSTRUCTURE OF POLYEHTYLENE TERE PHTHALATE (PET) POLYMER: EFFECT OF GRAFTING AND ION-IRRADIATION</b>	<b>121</b>
<b>4.1. Experiments</b>	<b>123</b>
4.1.1. Sample preparation and characterization	123
4.1.1.1 Grafted samples	123
4.1.1.2 Ion-irradiated and etched samples	125
<b>4.2. Results and Discussion</b>	<b>126</b>
4.2.1. PET-g-AA samples	126
4.2.1.1 Radiation grafting mechanism	126
4.2.1.2 FTIR, XRD and DMA measurements	127
4.2.1.3 Positron annihilation measurements	131
4.2.2. Ion-irradiated and etched samples	137
4.2.2.1 FTIR and XRD measurements	137
4.2.2.2 Positron annihilation measurements	139
4.2.2.3 Depth dependent Doppler broadening measurements	141
<b>4.3 Conclusion</b>	<b>144</b>

## **CHAPTER-V**

<b>5. NANOSTRUCTURE OF POLYMER NANOCOMPOSITE: DEVELOPMENT AND APPLICATION OF AGE MOMENTUM CORRELATION (AMOC)</b>	<b>146</b>
<b>5.1. Development of Age momentum correlation (AMOC) facility</b>	<b>148</b>
5.1.1 Principle	148
5.1.2 Setting up of AMOC system	148

5.1.3 Data analysis	152
<b>5.2. Nanostructure of polymer nanocomposite: Application of AMOC</b>	<b>154</b>
5.2.1. Experiments	156
5.2.1.1 Sample preparation and characterization	156
5.2.1.2 Positron annihilation lifetime measurements	158
5.2.1.3 Age momentum correlation measurements	159
5.2.2. Results and Discussion	159
5.2.2.1 TEM, SEM and XRD	159
5.2.2.2 Positron annihilation lifetime measurements	162
5.2.2.3 Age momentum correlation measurements	169
<b>5.3 Conclusion</b>	<b>171</b>

## **CHAPTER-VI**

<b>6. VACANCY DEFECTS IN SEMICONDUCTOR AND METAL NANOPARTICLES</b>	<b>173</b>
<b>6.1. Experiments</b>	<b>178</b>
6.1.1. Synthesis	178
6.1.1.1 ZnO nanoparticles	178
6.1.1.2 CdSe nanoparticles	178
6.1.1.3 Gold nanoparticles	179
6.1.2 XRD, TEM and photoluminescence characterization	179
6.1.3 Positron annihilation measurements	180
<b>6.2. Theoretical calculations</b>	<b>181</b>
6.2.1 Positron lifetime and electron momentum distribution calculations	181
6.2.2 Calculation of relaxation of lattice and formation energy of defects	182
<b>6.3. Results and Discussion</b>	<b>183</b>
6.3.1. XRD and TEM	183
6.3.1.1 ZnO nanoparticles	183
6.3.1.2 CdSe nanoparticles	184
6.3.1.3 Gold nanoparticles	186
6.3.2. PALS, CDB measurements and theoretical calculations	187
6.3.2.1 ZnO nanoparticles	187
<i>(i) Defects in ZnO nanoparticles</i>	187

<i>(ii) Role of defects in photoluminescence properties</i>	<b>193</b>
6.3.2.2 CdSe nanoparticles	<b>195</b>
6.3.2.3 Gold nanoparticles	<b>201</b>
<b>6.4 Conclusion</b>	<b>207</b>
 <b>SUMMARY</b>	 <b>208</b>
 <b>BIBLIOGRAPHY</b>	 <b>213</b>

## **SYNOPSIS**

Positron, an antiparticle of electron, was first theoretically predicted by P. A. M. Dirac in his theory of holes. It was proposed to explain the negative energy solutions that appeared in describing the electron in the absence of electromagnetic field [Dirac, 1930 and 1935]. Later, positron was experimentally discovered by Anderson in the cloud chamber experiments [Anderson, 1933]. Positrons are generally obtained from radioisotope decay as well as pair-production process. When an energetic positron is injected into a material, it loses most of its energy in a few picoseconds and gets thermalized. The thermalized positron annihilates from delocalized Bloch state (in perfect crystals) with an electron of the medium, and the rate of annihilation depends on the electron density of the material. In the presence of defects (atomic vacancy, vacancy cluster, dislocations, grain boundaries, stacking faults etc.) positrons are trapped in the defects as a result of repulsion from positively charged ion cores. The annihilation rate from the trapped state is lower compared to delocalized state due to reduced electron density at the defect sites. The increase in positron lifetime (inverse of annihilation rate) is correlated to the size of the defects. Positron annihilation lifetime spectroscopy (PALS) is well established technique for study of atomic size defects in crystalline materials. Positron lifetime gives information about the defect size, and the corresponding intensity is correlated to the defects concentration [Brandt et al., 1981]. The experimental positron lifetimes, as deduced from PALS, are often compared with computed theoretical lifetime to elucidate the defect size in a material [Puska et al., 1994].

When a thermalized positron annihilates with an electron, the total energy of positron-electron pair is equal to the energy of annihilating electron as positron is already thermalized. Thus, the two annihilation photons in laboratory frame deviate from anti-collinearity due to finite momentum of annihilating electron. Additionally, the

annihilation photons are Doppler broadened due to finite kinetic energy of electron-positron pair prior to annihilation [Brandt et al., 1981]. The measurement of Doppler broadening of annihilation radiation (DBAR) or coincidence Doppler broadening (CDB) enables one to get the electron momentum distribution in a medium. These techniques have been extensively used for the defect studies in various materials. In addition, CDB measurements can also provide information about the chemical surrounding of the defects [Ashoka-Kumar et al., 1996].

In case of molecular solids like polymers, zeolites and porous materials, thermalized positron can form a quasi bound state, positronium (Ps), with an electron from the material. The properties of Ps atom are quite similar to that of hydrogen atom. Positronium exhibits two spin states, namely, “*ortho*” (triplet) and “*para*” (singlet) Ps depending on the orientation of positron and electron spins. Statistically, the formation probability of *ortho*-positronium (*o*-Ps) to *para*-positronium (*p*-Ps) is 3:1. The *p*-Ps and *o*-Ps intrinsically annihilate into two and three photons with lifetime of 125 ps and 142 ns, respectively [Schrader and Jean, 1988].

In the case of polymers, *o*-Ps is trapped in free volume nanoholes (dynamic or static) of the polymer and collides with the wall of nanoholes. During the collisions, positron from *o*-Ps can annihilate with an electron with opposite spin from the surrounding. This process is called *pick-off* annihilation which reduces the lifetime of *o*-Ps from 142 ns to 1-10 ns depending on the frequency of collision. The *o*-Ps *pick-off* lifetime in a material is correlated to the size of the free volume nanoholes through Tao-Eldrup equation [Tao, 1972 and Eldrup et al., 1981]. Various models have been proposed to correlate *o*-Ps lifetime with the size of the free volumes (pores) of different geometries. The size distribution of free volume nanoholes can be obtained by analyzing lifetime spectrum as a continuous distribution of *o*-Ps lifetimes which can be translated into size

distribution using algorithms based on the Tao-Eldrup equation. The fractional free volume in a polymer is calculated from the *o*-Ps intensity. Free volume nanoholes (size as well as concentration) play an important role in various properties such as thermo-mechanical, as well as transport properties of the polymers. The *o*-Ps lifetime (nanoholes size) in a polymer as a function of temperature increases linearly, and the rate of change in lifetime increases sharply at the glass transition temperature. This method has been extensively used to study the glass transition process of various polymers [Schrader and Jean, 1988].

The current work deals with the positron annihilation studies of nanostructures in both crystalline nanomaterials and amorphous molecular solids. Positron is used as a probe to study the atomic size defects in the crystalline materials, and, positronium is used to probe the molecular level vacant spaces (nanoholes) in molecular solids. The crystalline materials under study are semiconductor as well as metal nanoparticles, and the molecular solids are natural polymers (starch/sucrose matrices), poly (ethylene terephthalate), PET, polymer (grafted and ion-irradiated). A polymer nanocomposite having nanoscale crystalline phase dispersed in polymer matrix has also been studied. The nanostructure of starch has been studied as a function of temperature and additives like sucrose and water. The changes in the nanostructure of starch/sucrose matrices have been investigated from the temperature dependence of *o*-Ps lifetime that has been used to explore the glass transition process in starch/sucrose matrices. The glass transition temperature,  $T_g$ , of starch/sucrose and starch/sucrose/water systems have been evaluated. A simple model has been proposed for the determination of  $T_g$  for starch/sucrose matrix that undergoes decomposition before the onset of glass transition. For the measurement of glass transition temperature of starch/sucrose/water matrix, a new approach has been used

wherein the *o*-Ps lifetime is measured at constant temperature with varying water concentration in the sample.

PALS and DBAR have been used to study the nanostructure of poly (ethylene terephthalate) grafted with acrylic acid (PET-g-AA) as well as ion-irradiated PET polymers. The variation of free positron lifetime and non-additive nature of *o*-Ps lifetime and intensity indicated the phase segregation in PET at higher degree of grafting. Depth dependent Doppler broadening of annihilation radiation using slow positron beam has been used to study the nanostructure in ion-irradiated and etched PET films. These measurements showed the changes in the size as well as density of nanoholes at surface and sub surface region in PET irradiated at low fluence. Age Momentum correlation (AMOC) set up has been developed to investigate the different positron states in polymer nanocomposites.

Various atomic size vacancy defects are produced in nanoparticles depending on their synthesis methods. These defects play key role in determining various properties like thermal, opto-electronic, mechanical and catalytic of nanoparticles, semiconductor or metal. For the studies of defects in semiconductor and metal nanoparticles, PALS and CDB measurements have been carried out in the nanoparticles having size in the range of 4 – 40 nm. To supplement the experimental results, positron lifetimes and electron momentum distribution calculations have been carried out in bulk lattice of the nanoparticles using first principle methods. The calculated lifetimes and electron momentum distribution in the presence of possible vacancy defects have been compared with experimental result to elucidate the size and type of defects present in the nanoparticles. The full details of the work will be described in the thesis. A brief overview of the thesis is as follows.



**CHAPTER-I: Introduction**

In this chapter, the applications of positron annihilation spectroscopy (PAS) to study free volume nanoholes in polymers and atomic defects in nanoparticles are discussed in detail. The scope of the present work is also given in the chapter. Since, positron annihilation spectroscopy is a specialized technique, the preliminary details of positron and positronium formation, and their annihilations characteristics in the materials are also discussed in brief in the chapter.

The triplet state positronium (*o*-Ps) has been extensively used as a probe for the characterization of nanostructure in terms of free volume nanoholes in polymers but its use for natural polymers and polymer nanocomposites are limited. It would be interesting to implement PAS for the characterization of free volume nanoholes in natural polymers and nanocomposites under different conditions to gain insights into polymer nanostructures as well as positron systematics. The understanding of nanostructure as well as its effect on the glass transition behaviour of natural polymers (starch/sucrose) is very important for their use in the industries like food, packaging and pharmaceuticals [Mizuno et al., 1998; Levine and Slade, 1993]. PALS is an established technique to determine the  $T_g$  of polymers by measuring *o*-Ps lifetime or size of nanoholes as a function of temperature [Jean et al., 2003]. In case of pure starch, it has been discovered that decomposition of starch matrices would hamper this quest by inducing a pronounced decrease in both *o*-Ps lifetime and intensity before reaching the  $T_g$ . The *o*-Ps lifetime was found to increase linearly with temperature up to the region of decomposition without any sign of enhancement in the gradient and the data merely indicated that  $T_g$  should lie above about 501 K, in qualitative agreement with previous data on starch of various origins with variable water content [Roudaut et al., 2009]. Sucrose and water act as plasticizers, and  $T_g$  of the starch matrices reduces with sucrose/water concentration [Mizuno et al., 1998 and

Poirier-Brulez et al., 2006]. It would be, therefore, interesting to investigate the changes in nanostructure of starch matrices after adding sucrose and water, and, their effect on glass transition behaviour of the said matrices. It is a challenge to use PALS for determination of  $T_g$  of a polymer which starts undergoing decomposition before reaching its glass transition temperature.

Modifications of polymers by graft copolymerization of functional monomers to impart favorable physico-chemical properties, and, by ion-irradiation to modify their transport properties are well documented. Several techniques have been used to initiate the graft copolymerization including ion-irradiation, ultraviolet light, plasma treatment etc. [He et al., 2003; Song et al., 2006; chu et al., 2006 and Lazea et al., 2005]. Among these techniques radiation induced graft copolymerization is advantageous because of its extensive penetration into the polymer matrix, and its ability to form radicals rapidly and uniformly for initiating the grafting in various kinds of polymers. The irradiation of polymeric materials by energetic heavy ions leads to modification in porosity or transport properties of the polymers, which are further modified by etching the irradiated polymers in acidic or alkaline medium. The resultant polymeric films having controlled and well defined pores are widely used as templates for the synthesis of nanomaterials and in nanofiltration [Apel et al., 2006 and Ferain et al., 1994]. The triplet state of positronium,  $o$ -Ps, being a smallest probe to free volume nanoholes in polymers is used to determine nanoholes size, fractional free volume and nanoholes size distribution. The nanoholes size variation as a function of depth is studied using slow positron beam which provides monoenergetic positrons having a well defined implantation depth [Jean et al., 2003]. Polyethylene terephthalate (PET) films having properties like high crystallinity, thermal stability, hydrophobicity and presence of chemically inert functional groups are used for large number of application in various industries. PET is modified through various

methods like copolymerization, grafting, ion-irradiation etc. to impart favourable properties for specific application. In this work, the nanostructure of PET modified by grafting and heavy ion-irradiation has been studied. These studies are expected to improve the understanding of dependency of macroscopic properties on nanostructure of a polymer.

PALS is a well established technique for the characterization of nanostructure of polymers but in case of polymer nanocomposites, positron systematics change due to the presence of new trapping and annihilation sites (interfaces and nanophase). Age momentum correlation (AMOC) measurements are expected to provide more information on the positron states in polymer nanocomposites. With this objective, AMOC facility has been set up and utilized to identify the positron states in a polymer nanocomposite by measuring the momentum distribution as a function of positron age in the sample [Jean et al., 2003]

In recent years, positron has been identified as a sensitive and self seeking probe for the embedded and colloidal nanoparticles [Xu et al., 1999; Nagai et al., 2000; Xu et al., 2001, Nagai et al., 2001; van Huis et al., 2002; Eijt et al., 2006, and Weber et al., 2002]. Various properties of nanoparticles e.g. electrical, mechanical, optical and catalytic etc. are different from their bulk counterpart mainly because of high surface to volume ratio in nanoparticles [Timp, 1998; Harrison, 1999, and Mattoussi et al., 2000]. Point defects in nanoparticles are thermodynamically stable as they increase the entropy of the system. The local structural properties and electronic structure of the nanoparticles can be revealed via the measurement of electron momentum density using positron annihilation techniques. When positrons are implanted into nanoparticles, a fraction of positrons may diffuse to and annihilates from the surface provided the diffusion length is comparable to the size of nanoparticles. Thus, positron annihilation spectroscopic studies

in nanoparticles give information about the bulk as well as the surface of the nanoparticles. Positron annihilation spectroscopy has been used to study different type of nanoparticles e.g. embedded nanoparticles [Xu et al., 1999; Nagai et al., 2000; Xu et al., 2001, and Nagai et al., 2001] and semiconductor nanoparticles [van Huis et al., 2000; Eijt et al., 2006, and Weber et al., 2000]. These studies demonstrate positron annihilation spectroscopy to be a sensitive technique to correlate the effects of size, quantum confinement, and atomic defects to the electronic and optical properties of the nanoparticles. However, it may be mentioned that the physics of positron systematics in different types of nanoparticles is far from understood and requires extensive studies in different types of nanomaterials. With this objective, positron annihilation spectroscopic studies have been carried out in semiconductor and metal nanoparticles supplemented by density functional theory based calculations.

## **CHAPTER-II: Experimental Techniques and Theoretical Calculations**

PALS, DBAR and CDB measurements have been carried out with the existing facilities using  $^{22}\text{Na}$  source in conventional method. The details of temperature dependent PALS measurements are given in the respective chapters. For AMOC measurements, a set up has been developed. It utilizes two  $\text{BaF}_2$  detectors and one HPGe detector in coincidence for recording the two annihilation photons (511 keV) and the prompt (1275 keV) gamma ray from  $^{22}\text{Na}$ . The details of AMOC are described in chapter V. The conventional fast-fast coincidence circuit was used for the lifetime measurements. The time resolution of the lifetime spectrometer set ups with plastic scintillation detectors and  $\text{BaF}_2$  detectors were in the range of 240 ps to 290 ps. The HPGe detectors with energy resolution of  $\sim 1.1$  keV at 514 keV ( $^{86}\text{Sr}$ ) were used in the DBAR and CDB measurements. Two routines PATFIT [Kirkegaard et al., 1981] and CONTIN

[Provencher et al., 1982] have been used for the analysis of lifetime spectra in terms of discrete lifetime components and continuous lifetime distribution, respectively. The evaluation of parameters ( $S$  and  $W$ ) from DBAR or CDB spectra, and calculation of ratio curves from CDB spectra are also given in the chapter. For depth dependent Doppler broadening of annihilation radiation measurements, a slow positron beam coupled with Doppler broadening set up has been used. This beam provides monoenergetic positrons having energy 200 eV – 50 keV. The program “variable energy positron fit” VEPFIT has been used to fit the (S-E) profiles to evaluate the positron diffusion lengths in the polymer films [van Veen et al., 1990]. The other complimentary techniques like X- ray diffraction, Fourier transform *IR*, Thermal gravimetric analysis, Differential scanning calorimeter, Dynamical mechanical analysis, Transmission electron microscopy and Photoluminescence spectroscopy used in the present studies, are described in the respective chapters.

Calculations of positron lifetime and electron momentum distributions were performed using density functional theory (DFT) method employed in ‘MIKA/DOPPLER package’ [Torsti et al., 2006]. It is used for the calculations of positron lifetime and electron momentum distribution in periodic lattice and can not be used for molecular solids like polymers. The ‘conventional scheme’ was used in the calculations where electron density of a solid is approximated by non-self consistent superposition of free atoms in the absence of positron, and, the potential felt by the positron is also generated in a similar way. The electron positron enhancement factor was parameterized using gradient corrected scheme, and correlation potential developed by Arponen-Pajanne and Boronski-Nieminen were used in the calculations. The positron wave function is obtained by solving the Schrödinger equation using a three-dimensional real space solver. The electron momentum distribution is calculated using the positron wave function as

described in ‘MIKA/DOPPLER’ package. A cubic or tetragonal supercell is used for the calculation. In the case of cubic, a supercell of  $(n \times n \times n, n \geq 3)$  size having a lattice constant  $a$  is used for the calculations. To perform the calculations in the presence of vacancy defects, atoms are removed from the lattice positions in the supercell. The resultant electron momentum distributions are convoluted with the detectors resolution function for their comparison with experimental ratio curves.

In the presence of vacancy defects, atoms in the vicinity of defects undergo relaxation which can change the free space available at the defect site. To calculate the positron lifetime as well as electron momentum distribution more precisely, relaxed coordinates of the atoms in the presence of defects are used for the calculations. The relaxed lattice structure in the presence of vacancy defects are calculated using first principle PAW pseudopotential methods within the LDA approximations implemented in Vienna *ab-initio* simulation package (VASP) [Kresse et al., 2001]. Same approach has also been used for the calculation of formation energy of defects in the lattice using VASP.

### **CHAPTER-III: Nanostructure and Glass Transition Behaviour of Starch/Sucrose Matrices**

This chapter deals with investigation of the effects of sucrose and water on nanostructure and glass transition process of starch matrix. In case of pure starch, it has been observed that glass transition temperature ( $T_g$ ) can not be directly determined by measuring the variation of *o*-Ps lifetime ( $\tau_3$ ) with temperature,  $T$ . This is because of decomposition of starch matrix well before  $T_g$ . The useful information gathered from pure starch study was that the normalized values of  $I_3$  and  $\tau_3$  are strongly correlated [Roudaut et al., 2009]. This was due to the fact that  $I_3$  varies in proportion to the surviving fraction,

$p$ , of the decomposing matrix, whereas  $R$ , the radius of the free volume nanoholes, and hence  $\tau_3$  (which is closely linear with  $R$  in the range 1–1.6 ns), decrease in proportion to  $p^{1/3}$  (this being the one-dimensional equivalent to a decrease in nanohole volume in proportion to  $p$ ). Determining  $T_g$  in biopolymers such as starch is very important, particularly in the context of food storage, and one way to improve our knowledge on the process of glass transition refers to the use of plasticizers, such as water or polyols, that reduces the  $T_g$  greatly [Mizuno et al., 1998; Levine and Slade, 1993 and Poirier-Brulez et al., 2006]. In this work, we chose sucrose as an adequate plasticizer to allow us to observe  $T_g$  in PALS experiments. For an efficient decrease in  $T_g$  the sucrose content used in the study was 20 w/w%. The present result show that the addition of sucrose in a starch matrix has a noticeable influence on its nanostructure in terms of both the density and size of the free volume nanoholes and confirmed that  $T_g$  is reduced greatly. This influence on nanostructure becomes even stronger when this plasticizer decomposes i.e. the starch matrix left after sucrose decomposition (state  $S_D$ ) displays properties very different from that of pure starch. The *o*-Ps intensity decreases greatly, from 26.2% in pure starch down to 6.8% in state  $S_D$ , denoting a much smaller free volume fraction in the latter case. Similarly, at 294 K,  $\tau_3$  passes from 1.32 ns in pure starch to 1.09 ns in state  $S_D$ , indicating a corresponding decrease in the free volume nanohole average radius, from 0.212 nm to 0.18 nm, respectively. Finally, the change in the slope of the  $\tau_3$  vs.  $T$  variation below  $T_g$ , points to a much lower thermal expansion coefficient in state  $S_D$  as compared to pure starch. These findings may open the way to the preparation of polymeric matrices possessing specific properties. Quite unexpectedly, from the quantitative approach used, the free volume fraction is found to be much less sensitive to  $T$  than the starch matrix volume fraction itself. This finding is made possible through our probe, *o*-Ps, which

serves as a lens to examine more closely the fate of the free volume nanoholes and their close environment.

As mentioned earlier, the nanostructure of biopolymers changes as a function of relative humidity due to the sorption of water which acts as a plasticizer. It has been observed by using various methods that the  $T_g$  of biopolymers decreases with the water content [Poirier-Brulez et al., 2006 and Kilburn et al., 2004]. Determining  $T_g$  in a hydrated biopolymer requires some special arrangement to avoid water evaporation during the PALS measurements. Moreover, moisture sorption of polymers (whether of biological origin or not) is a topic of great interest since many materials properties are sensitive to water, an effect which is yet to be understood. There are very few studies using PALS on hydrated biopolymers at different temperatures. Dlubek et al. (1999) investigated water in local free volume nanoholes of a polyimide but this study was limited to room temperature. There are [Kilburn et al., 2004 and Townrow et al., 2007] reports on polymer matrices as a function of temperature and moisture, the control of moisture content over the temperature treatment being different depending on the authors. The present study focuses on the use of PALS to investigate the effect of moisture on the nanostructure of starch-based material (hydrated starch having 10 and 20% sucrose,  $w/w\%$ ) in the region of the glass transition with a novel approach to control the moisture content of the studied sample over the temperature treatment. The present study confirms the usefulness of  $o$ -Ps as a probe to study nanostructural features of biopolymers, particularly as regards to the fate of the free volume nanoholes as a function of either temperature or the presence of additives. On the basis of a reasonable number of experiments, a quantitative approach can result in a general description of the behavior of the  $o$ -Ps lifetime,  $\tau_3$ , and hence, the nanohole average volume,  $V$ , as a function of temperature as well as sucrose and water contents. It is shown that, although some general



rules seem to apply to most (bio) polymers (e.g., plasticizing effect of selected additives), detailed observation of the results (e.g., the behavior of the gradient of  $V$  with temperature or water content, occupation of the nanoholes by water molecules) brings out some noticeable differences among them. Similarly, quantitative and qualitative differences are found in the results from conventional techniques as compared to PALS, such as the usual finding that  $T_g$  for a given matrix appears to be lower when studied through PALS as compared to DSC. The difficulty in maintaining constant water content upon heating while recording the PALS spectra is circumvented by letting the sample lose water regularly, at constant  $T$ . As compared to the usual establishment of  $\tau_3$  vs.  $T$  plots, the present method leads to satisfactory results regarding the determination of  $T_g$  and the various gradients. It is argued that in this system, water molecules do not block the preexisting free volume nanoholes in the matrices. Water molecules are uniformly distributed in the matrix and undergo hydrogen bonding with starch/sucrose molecule leading to smaller entities. This reduces the  $T_g$  of the matrix as energy associated with the movement of smaller entities is low. It would be interesting to carry out more studies in natural polymers using PALS to widen the scope of use for the different types of polymers and under different conditions.

#### **CHAPTER-IV: Nanostructures of Poly ethylene terephthalate (PET) Polymer: Effect of Grafting and Ion-Irradiation**

This chapter deals with the investigation of nanostructure of poly ethylene terephthalate (PET) grafted with acrylic acid, PET-g-AA, polymer. This chapter also describes the study of modification of nanostructure of surface and bulk in ion-irradiated PET film using slow positron beam based Doppler broadening annihilation spectroscopy. In the first study, PALS is used to characterize PET-g-AA copolymer films with the

degree of grafting in the range of 1.8–12.1 %. The PALS result have been correlated with the  $\tan \delta$  values for  $\beta$  relaxation of the samples obtained from the dynamic mechanical analysis (DMA) and the variation in the crystallinity evaluated from wide angle X-ray diffraction (WAXD). PALS was found to be a useful technique to study the free volume hole properties and packing at the molecular level for PET-g-AA copolymers at low degree of grafting. The variation in the free volume parameters had a direct correlation with structural transition from DMA up to 6.0 % grafting. The free volume parameters followed simple additive rule. At higher degree of grafting, a marked deviation in free positron intensity was observed with a sharp drop in fractional free volume. Thus, we believe that at higher degree of grafting, phase segregation occurs in the polymer matrix and these interfacial effects has a dominant role on positron behavior.

To study the effects of ion irradiation and etching on the polymer films, various techniques *viz.* Positron Annihilation Spectroscopy (PAS), Infrared (IR) spectroscopy and X-Ray Diffraction (XRD) are employed. The sensitivity of these techniques to the changes in the polymer nanostructure varies. Most of the studies on the changes in the polymer nanostructure by ion beam irradiation have been carried out at the fluences of  $10^{10}$  to  $10^{16}$  ions/cm<sup>2</sup> and the changes in the film properties like absorbance, crystallinity, capacitance and mechanical properties have been monitored. The present study aims at the study of nanostructural changes at lower fluence ( $7 \times 10^7$  ions/cm<sup>2</sup>). Surface studies or depth-selective measurements of free volume in polymer films are carried out by a mono energetic slow positron beam. Doppler broadening spectroscopy (DBS) using a slow positron beam has evolved as a useful technique to characterize the nanostructure of a polymer membrane as a function of depth. The depth-dependent  $S$ -parameter and  $(3\gamma/2\gamma)$  annihilation ratio measurements are two sensitive methods to characterize the architecture of the pores or free volumes, electron density and inter connectivity of the free volumes to

the surface of a polymer [Coleman, 2003]. In the present study, PET film has been irradiated by 100 MeV  $^{35}\text{Cl}$  beam ( $7 \times 10^7$  ions/cm<sup>2</sup>). The conventional PALS has been used to characterize the free volumes in the bulk of the polymer, and depth-dependent DBS using a slow positron beam has been used to characterize the surface and near surface region of the polymer membrane. FTIR and XRD measurements have also been carried out to supplement the positron studies. There is neither new phase formation initiated in the film nor any change in crystallinity after irradiation as observed from XRD. FTIR studies showed that no other major modification in the chemical structure has taken place after low fluence ion-irradiation and subsequent etching. The changes seen are primarily in the free volume fraction and size. It is observed through the positron annihilation characteristics that the ion-irradiation and etching result in the modification of nanostructure of the polymer membrane but the effect of etching on irradiated membranes is more pronounced at the surface and sub surface region.

## **CHAPTER-V: Nanostructure of Polymer Nanocomposite: Development and Applications of Age Momentum Correlation (AMOC)**

The present chapter deals with the development of AMOC facility and its application for the study of chemical environment of free volumes as well as positron states in a polymer nanocomposite. The correlated measurements of positron lifetime and annihilating electron momentum distribution provide more information about positron/Ps states in a system compared to uncorrelated measurements of positron lifetime and Doppler broadening [Jean et al., 2003]. These measurements are called age momentum correlation (AMOC) measurements. AMOC measurements are expected to provide information about the chemical environment of free volume nanoholes in polymer matrix. A positron source ( $^{22}\text{Na}$ , 40 Ci) deposited between two kapton foils of thickness 7  $\mu\text{m}$  is

used for AMOC measurements. The AMOC measurements are performed by acquiring positron lifetime and Doppler broadening radiation in coincidence. The details of development are given in this chapter. Positron lifetime spectra are acquired using coincidence set up having two BaF<sub>2</sub> scintillation detectors placed at 90<sup>0</sup>, one recording the birth signal (1.274 MeV,  $\gamma$ ) and other recording the annihilation signal (511 keV,  $\gamma$ ). Simultaneous measurements of Doppler broadening of annihilation radiation are carried out using an HPGe detector having resolution 2.0 keV at 1332 keV of <sup>60</sup>Co. The time resolution of the set up is ~290 Ps. The correlated events are recorded using a multi parameter acquisition system. Positron age dependent Doppler broadening spectra are obtained by summing the correlated events with in a time window ( $t_1$  to  $t_2$ ) on positron age axis. The positron age dependent Doppler broadening spectra are analyzed in term of age dependent line shape parameter  $S(t)$ ,  $t = (t_1+t_2)/2$ , which is determined as the ratio of central area (511 $\pm$  1.2 keV) to the total area of the photo peak [Jean et al., 2003]. There is only one positron component and no positronium formation in kapton. Hence, The fraction of positron annihilation in Kapton and source are not subtracted for the evaluation of  $S(t)$ . A routine has been developed for the evaluation of  $S(t)$  parameter for each state of positron in the system. The input parameters for the routine are discrete lifetime and intensity components as well as the time windows for determination of  $S(t)$ . This routine calculates the fraction of each component in a time window and fit  $S(t)$  parameter vs positron age assuming  $S(t)$  as weighted average of  $S$ -parameter of each lifetime component in the given positron age window.

Positron annihilation lifetime and positron age momentum correlation have been used to characterize the free volumes sizes, distribution and chemical environment in Phenol Formaldehyde (PF) resin and PF-multiwall carbon nanotubes (MWCNTs) nanocomposites having 2, 5, 10 and 20% (w/w%) MWCNTs. On incorporation of

MWCNTs, *o*-Ps lifetime increases with an irregular decrease in the corresponding intensity. The free volume size was observed to have a nonlinear increase with MWCNTs concentration indicating the agglomeration of MWCNTs in PF matrix. The chemical environment of free volumes in PF-MWCNTs nanocomposites was observed to be enriched in oxygen. AMOC data provides a direct evidence of free positron annihilation in MWCNTs in PF matrix which is also observed to be consistent with positron lifetime measurements. The present study should provide a backbone to further free volume characterization studies on polymer- carbon nanotubes (functionalized) nanocomposites.

## **CHAPTER-VI: Vacancy Defects in Semiconductor and Metal Nanoparticles**

This chapter deals with the studies of atomic defects in ZnO, CdSe and Au nanoparticles. Point defects in nanoparticles, semiconductor or metal, present in the bulk or at the surface are of great importance because they can tailor mechanical, as well as optical, electrical, catalytic properties of the nanoparticles. Zinc oxide (ZnO) is a semiconductor with a wide band gap of 3.437 eV at 2 K. It has attracted considerable attention over the years because of its possible applications in catalysis, UV light emitting diodes, blue luminescent devices, and gas sensors which has led to a large number of studies in polycrystalline as well as single crystals ZnO using a variety of techniques. ZnO being more radiation resistant compared to Si, GaN and GaAs, is considered to be a suitable material for use in high radiation areas such as space satellite electronics. CdSe nanoparticles are semiconductor in nature and can be considered as a model system for semiconductor nanoparticles, as its shape and size can be well tailored through different routes of synthesis. Synthesis of CdSe nanoparticles through chemical reactions, where the growth of nanoparticles is controlled by capping the particles with the organic ligands, has been established as a potential method to synthesize nearly mono dispersed

nanoparticles [Murray et al., 1993]. These nanoparticles have shown interesting opto-electronic properties based on their size and shape. The nanoparticles synthesized through different routes can have defects of various origins, e.g., the vacancy defects, stacking faults, surface disorder etc., which can modify the opto-electronic properties of the nanoparticles. In the last few years ZnO nanoparticles of various sizes (in the range of 15-140 nm) and CdSe nanoparticles in very small size range ( $< 6$  nm) have been subjected to positron annihilation studies [Mishra et al., 2007; Dutta et al., 2006; Sanyal et al., 2008; Eijt et al., 2006, and Weber et al., 2002]. These studies have found evidence for the presence of Zn vacancies in ZnO nanoparticles. In case of CdSe nanoparticles, the observed variations in electron momentum distribution have been explained in terms of quantum confinement of valence electrons and widening of electronic band gap with the decrease in size. The effects of positron annihilation from defect sites in CdSe nanoparticles have not been considered to explain the changes in positron parameters. Thus, characterization of the defects in ZnO and CdSe nanoparticles produced through various methods is important to identify the suitable methods for the synthesis of nanoparticles with desired properties. Keeping in mind these objectives, we have carried out positron annihilation lifetime and CDB measurements in zinc oxide (ZnO) nanoparticles in the range of 4 nm to 40 nm prepared by a solid state pyrolytic reaction and CDB measurements in CdSe nanoparticles having size range of 7 -17 nm prepared by chemical route. The shape, size and crystallinity of these nanoparticles were characterized with XRD and TEM. Experimental data are complemented by first principle calculations of positron lifetime and electron momentum distribution. In addition, photoluminescence (PL) studies have been carried out to observe the role played by the defects in the optical properties of the ZnO nanoparticles. Positron lifetime and momentum distribution in the ZnO nanoparticles are seen to have a strong dependence on the particle size in the range

of 4-40 nm. Similarly, a strong dependence in momentum distribution ratio curves is seen in case of CdSe nanoparticles. Comparison of experimental data with theoretical calculations strongly suggests the presence of Zn vacancies, similar to observations made in ZnO nanoparticles, and, Cd vacancies in the CdSe nanoparticles. The Zn vacancies are seen to migrate to the grain boundaries with the increase in particle size (by heating) and finally anneal out at higher temperatures. In the case of CdSe, concentration of the Cd vacancy defect reduces with the particles size. Photoluminescence measurements of the ZnO nanoparticles reveal that both Zn and O vacancies may be responsible for the origin of visible emission in ZnO. The present study also provides evidence of Se enrichment of the surface of CdSe nanoparticles with decrease in the particle size.

Gold nanoparticles of average size  $\sim 6$  nm have been synthesized using chemical route and characterized using XRD and TEM. For the characterization of point defects in terms of size and shape in gold nanoparticles, PALS measurements corroborated with theoretical calculations have been carried out. The gold supercell was relaxed in the presence of vacancy defects using Vienna *ab-initio* simulation package (VASP). The positron lifetimes were also calculated by considering the relaxed coordinates of the atoms in the supercell. To determine the probability of formation of vacancy defects in gold nanoparticles, VASP was also employed to calculate the formation energy and binding energy of the defects in the supercell. In the presence of vacancy defects depending on the configuration of the defects, both inward and outwards relaxations of the first nearest neighbours were observed leading to change in the calculated positron lifetimes. The formation energy calculations of the defects seem to be useful in the prediction of most probable defect in the nanoparticles. Our studies showed the presence of monovacancy and, pentavacancy defect in square pyramidal configuration in the gold nanoparticles prepared using the present synthesis procedure.

## Summary

The present work shows the usefulness of positronium and positron as probes for the molecular level defects (nanoholes) in polymers and atomic defects in nanoparticles, respectively. A noticeable change in the free volume size and density is measured on addition of sucrose in the starch matrix. A simple model has been proposed to measure the  $T_g$  in biopolymers when they undergo decomposition before reaching their  $T_g$ . The estimated  $T_g = 446$  K for starch/sucrose (20%) using PALS is very close to the DSC data. A significant difference has been observed in the nanostructure of starch left after decomposition of sucrose. Water acts as a strong plasticizer for starch/sucrose mixture. The new approach of measuring  $T_g$  in the presence of water i.e. measurement of *o*-Ps lifetime as a function of water concentration at constant  $T$ , was found satisfactory that circumvents the problem of evaporation of water during measurements. Water molecules undergo intermolecular hydrogen bonding with starch/sucrose molecules and do not block the preexisting nanoholes in the matrix. These studies may serve as backbone for the further PAS studies on natural polymers.

Positron annihilation spectroscopy corroborated with supplementary techniques like XRD, FTIR and DMA is found to be a suitable method for the characterization of free volume nanoholes (size, concentration and size distribution) and their effect on macroscopic properties in modified polymer systems. In PET-g-AA copolymer, positron parameters were observed to follow additive rule up to 6.0 % grafting. At higher degree of grafting phase segregation has been observed in the copolymer. Depth dependent Doppler broadening measurements in ion-irradiated (low fluence =  $7 \times 10^7$  ions/cm<sup>2</sup>) and etched PET films showed that free volume size and fraction in the film change mainly at the surface and subsurface region (~ 60 nm). No other major modifications have been observed after ion-irradiation and etching of the PET film at low fluence.



AMOC set up has been developed having a time resolution of 290 ps. From PALS and AMOC data in PF-MWCNTs nanocomposites, it is observed that chemical environment in PF-MWCNTs nanocomposite is enriched in oxygen which is different from pure PF resin.  $S(t)$  vs positron age could clearly show free positron annihilation in the MWCNTs incorporated in PF matrix which is consistent with the variation of positron lifetime components from PALS. More studies should be carried out in polymer nanocomposites using AMOC for the complete understanding of positron dynamics in the nanocomposites.

In ZnO nanoparticles, Zn vacancies are found as the dominant defects in the as prepared samples. The Zn vacancies become mobile and start migrating on annealing the sample. It is observed that these vacancies first agglomerate in the form of large vacancy cluster and then anneal out at higher temperature (800°C). Cd vacancies are found to be dominant defects in case of CdSe nanoparticles synthesized through present chemical route. The concentration of these defects is observed to decrease with increase in particle size. The CDB ratio curves for CdSe nanoparticles also suggest possible Se enrichment of surface in small size CdSe nanoparticles. Two types of vacancy defects i.e. monovacancy and, penta vacancy in square pyramidal configuration have been observed in Au nanoparticles. These studies revealed the presence of point defects in nanoparticles. PAS appears as a promising technique to characterize the point defects in nanoparticles. It would be interesting to carry out more PAS studies in different type of nanoparticles like core-shell and embedded nanoparticles for exploring and enhancing the capabilities of PAS as defect characterization techniques in the field of nanoparticles.

## References

1. Anderson, C.D., **1933**. *Phy. Rev.*, 43, 491.
2. Apel, P.Yu.; Blonskaya, I.V.; Dmitriev, S.N.; Orelovitch, O.L., and Sartowska, B., **2006**. *J. Mem. Sci.*, 282, 393.
3. Asoka-Kumar, P.; Alatalo, M.; Ghosh, V.J.; Kruseman, A.C.; Nielsen, B., and Lynn, K.G., **1996**. *Phys. Rev. Lett.*, 77, 2097.
4. Brandt W., and Dupasquier, A., (Eds.) **1981**. *Positron Solid State Physics: Proceedings of the International School of Physics “Enrico Fermi”, Course LXXXIII*, July 1981.
5. Chu, L-Q.; Tan, W-J.; Mao, H.Q., and Knoll, W., **2006**. *Macromolecules*, 39, 8742.
6. Coleman, P.G., **2003**. In *Principles and Applications of Positron and Positronium Chemistry*, Jean, Y.C.; Mallon, P.E., and Schrader, D.M., (Eds.) World Scientific Publishing, Singapore, 2002.
7. Dirac, P.A.M., **1930**. *Proc. Camb. Phil. Soc.*, 26, 361.
8. Dirac, P.A.M., **1935**. *The Principles of Quantum Mechanics*, Oxford University Press.
9. Dlubek, G.; Buchhold, R.; Hubner, Ch., and Nakladal, A., **1999**. *Macromolecules*, 32(7), 2348.
10. Dutta, S.; Chattopadhyay, S.; Jana, D.; Banerjee, A.; Manik, S.; Pradhan, S.K.; Sutradhar, M., and Sarkar, A., **2006**. *J. Appl. Phys.*, 100, 114328.
11. Eijt, S.W.H.; van Veen, A.; Schut, H.; Mijnders, P.E.; Denison, A.B.; Barbiellini, B., and Bansil, A., **2006**. *Nature Materials*, 5, 23.
12. Eldrup, M.; Lightbody, D., and Sherwood, J.N., **1981**. *Chem. Phys.*, 63, 51.
13. Ferain, E., and Legras, R., **1994**. *Nucl. Instrum. Method Phys. Res. Sect. B*, 84, 331.
14. Harrison, P., **1999**. *Quantum Wells, Wires and Dots*, Wiley, New York.
15. He, C., and Gu, Z., **2003**. *Rad. Phys. Chem.*, 68, 873.

16. Jean, Y.C.; Mallon, P.E., and Schrader, D.M., (Eds.) **2003**. *Principles and Applications of Positron and Positronium Chemistry*, World Scientific Publishing, Singapore.
17. Kirkegaard, P.; Eldrup, M.; Mogensen, O.E., and Pedersen, N.J., **1981**. *Comput. Phys. Commun.*, 23, 307.
18. Kresse G., and Furthmuller, J., **2001**. *VASP the guide* (Vienna University of Technology, Vienna).
19. Kilburn, D.; Claude, J.; Mezzenga, R.; Dlubek, G.; Alam, A., and Ubbink, J., **2004**. *J. Phys. Chem. B*, 108, 12436.
20. Lazea, A.; Kravets, L.I.; Dmitrev, S.N., and Dinescu, G., **2005**. *Rom. Rep. Phys.*, 57, 396.
21. Levine, H., and Slade, L., **1993**. In *The Glassy state in Foods*, Blanshard, J.M.V., and Lilliford, P.J., (Eds.) Nottingham University Press: Leicestershire, U. K.
22. Mattoussi, H.; Mauro, J.M.; Goldman, E.R.; Anderson, G.P.; Sundar, V.C.; Miculec, F.V., and Bawendi, M.G., **2000**. *J. Am. Chem. Soc.*, 122, 142.
23. Mishra, A.K.; Chaudhuri, S.K.; Mukherjee, S.; Priyam, A., and Das, D., **2007**. *J. Appl. Phys.*, 102, 103514.
24. Mizuno, A.; Mitsuiki, M., and Masao, M., **1998**. *J. Agric. Food Chem.*, 46, 98.
25. Murray, C.B.; Norris, D.J., and Bawendi, M.G., **1993**. *J. Am. Chem. Soc.*, 115, 8706.
26. Nagai, Y.; Hasegawa, M.; Tang, Z.; Hempel, A.; Yubuta, K.; Shimamura, T.; Kawazoe, Y.; Kawai, A., and Kano, F., **2000**. *Phys. Rev. B*, 61, 6574.
27. Nagai, Y.; Chiba, T.; Tang, Z.; Akahane, T.; Kanai, T.; Hasegawa, M.; Takenaka M., and Kuramoto, E., **2001**. *Phys. Rev. Lett.*, 87, 176402.
28. Puska, M.J., and Nieminen, R.M., **1994**. *Rev. Mod. Phys.*, 66, 841.

29. Poirier-Brulez, F.; Roudaut, G.; Champion, D.; Tanguy, M., and Simatos, D., **2006**. *Biopolymers*, 81, 63.
30. Provencher, S.W., **1982**. *Comput. Phys. Commun.*, 27, 213.
31. Roudaut, G., and Duplâtre, G., **2009**. *Phys. Chem. Chem. Phys.*, 11, 9556.
32. Sanyal, D.; Roy, K.T.; Chakrabarti, M.; Dechoudhary, S.; Bhowmick, D., and Chakrabati, A., **2008**. *J. Phys.: Condens. Matter.*, 20, 045217.
33. Schrader, D.M., and Jean, Y.C., (Eds.) **1988**. *Positron and Positronium Chemistry*, Elsevier, New York
34. Song, Y-W.; Do, H.S.; Joo, H.S.; Lim, D-H.; Kim, S., and Kim, H.J., **2006**. *J. Adhes. Sci. Technol.*, 20, 1357.
35. Tao S.J., **1972**. *J. Chem. Phys.*, 56, 5499.
36. Timp, G.L., **1998**. *Nanotechnology*, Springer-verlag, AIP press, NewYork.
37. Torsti, T.; Eirola, T.; Enkovaara, J.; Hakala, T.; Havu, P.; Havu, V.; Hoynalanmaa, T.; Ignatius, J.; Lyly, M.; Makkonen, I.; Rantala, T.T.; Ruokolainen, J.; Ruotsalainen, K.; Rasanen, E.; Saarikoski, H., and Puska, M.J., **2006**. *Phys. Status Solidi B*, 243, 1016.
38. Townrow, S.; Kilburn, D.; Alam, A., and Ubbink, J., **2007**. *J. Phys. Chem. B*, 111, 12643.
39. van Huis, M.A.; van Veen, A.; Schut, H.; Falub, C.V.; Eijt, S.W.H.; Mijnenarends, P.E., and Kuriplach, J., **2002**. *Phys. Rev. B*, 65, 085416.
40. van Veen, A.; Schut, H.; Vries, J.de; Hakvroot, R.A.; and Ijpma, M.R., **1990**. *AIP conf. Proc.*, 218, 171.
41. Weber, M.H.; Lynn, K.G.; Barbiellini, B.; Sterne, P.A., and Denison, A.B., **2002**. *Phys. Rev. B*, 66, 041305.

42. Xu, J.; Mills Jr., A.P.; Ueda, A.; Henderson, D.O.; Suzuki, R., and Ishibashi, S., **1999**.  
*Phys. Rev. Lett.*, 83, 4586.
43. Xu, J.; Moxom, J.; Somieski, B.; White, C.W.; Mills Jr., A.P.; Suzuki, R., and  
Ishibashi, S., **2001**. *Phys. Rev. B*, 64, 113404.

## LIST OF FIGURES

	Page No.
<b>CHAPTER-I</b>	<b>35</b>
<b>Figure 1.1:</b> A schematic of pair production	<b>37</b>
<b>Figure 1.2:</b> A schematic of electron-positron annihilation	<b>37</b>
<b>Figure 1.3:</b> Positron annihilation spectroscopy	<b>44</b>
<b>CHAPTER-II</b>	<b>54</b>
<b>Figure 2.1:</b> The decay scheme of $^{22}\text{Na}$	<b>56</b>
<b>Figure 2.2:</b> The positron energy spectrum in $^{22}\text{Na}$ decay	<b>57</b>
<b>Figure 2.3:</b> Slow Positron Beam at Radiochemistry Division, BARC	<b>59</b>
<b>Figure 2.4:</b> Block diagram of the positron lifetime spectrometer	<b>60</b>
<b>Figure 2.5:</b> The lifetime spectrum measured using $^{60}\text{Co}$ $\gamma$ -rays for obtaining the time resolution of the positron lifetime spectrometer	<b>62</b>
<b>Figure 2.6:</b> Positron annihilation lifetime spectrum of Silicon single crystals	<b>64</b>
<b>Figure 2.7:</b> $o$ -Ps annihilation rate distribution obtained from CONTIN analysis of the lifetime spectrum from a polymer sample	<b>66</b>
<b>Figure 2.8:</b> The block diagram of the Doppler broadening spectrometer	<b>66</b>
<b>Figure 2.9:</b> Typical Doppler broadened annihilation radiation spectrum for Si. The 514 keV $\gamma$ -ray spectrum from $^{85}\text{Sr}$ is shown after displacing its centroid to 511 keV on the energy axis for visualizing the broadening due to detector resolution.	<b>67</b>
<b>Figure 2.10:</b> Schematic representation of evaluation of Doppler broadening parameters from DBAR spectrum	<b>69</b>
<b>Fig. 2.11:</b> The block diagram for the used CDB set up.	<b>72</b>

**Figure 2.12:** The sum and difference spectra of the energy signals measured using CDB. The difference is plotted by shifting the origin to 1024 channels. **73**

**Figure 2.13:** The CDB and conventional Doppler spectra from a typical sample **74**

### **Chapter-III** **85**

**Figure 3.1:** TGA curves for STS20 ( $\square$ ) and crystalline sucrose ( $\circ$ ); two horizontal lines show the complete decomposition of sucrose in starch and pure sucrose **95**

**Figure 3.2:** Variation of the *o*-Ps intensity,  $I_3$  (%), with temperature,  $T$  (K), for the various experimental series. (a):  $\bullet$ , S1;  $\circ$ , S2;  $\square$ , S4. (b):  $\blacksquare$ , S3;  $\Delta$ , S5. The data in the decreasing part of  $I_3$  are shifted along the abscissa for S2 (+ 10 K), S4 (+ 30 K) and S5 (+ 10 K). The broken line is the extrapolation of the initial part ( $I_3$  constant at 24.5 %). The solid lines are fits to the data. The arrows indicate experimental points for which the *o*-Ps lifetime is high (about 1.4 ns, see Figure 3.4) but the associated  $I_3$  is low (about 15 %). **97**

**Figure 3.3:** Linear variation of  $\tau_3$  with temperature  $T$  before any decomposition. The symbols are as in figure 3.2. **98**

**Figure 3.4:** Variation of the *o*-Ps lifetime,  $\tau_3$  (ns), with temperature,  $T$  (K), in the region of decomposition, for the various experimental series. (a): S1, S2, S4; (b): S3 and S5; symbols as in figure 3.2. The data are shifted by + 10 K along the abscissa for S4 and S5. The broken line is the extrapolation of the initial linear variation of  $\tau_3$  (see Figure 3.3). The solid lines are fits to the data. **99**

**Figure 3.5:** Variation of  $\tau_3$  in the absence of decomposition with temperature,  $T$  **100**

- Figure 3.6:** Calculated variation with temperature of the surviving fraction of starch in the samples (solid line) and of the free volume (broken line). The latter and the last part of the former (rectangle) are magnified 50 times. **105**
- Figure 3.7:** Variation of *o*-Ps lifetime and average nanoholes volume in STS20 having 11.4% water as a function of temperature **108**
- Figure 3.8:** Typical variations of the *o*-Ps lifetime as a function of water content,  $c_w$  (%), in the starch/sucrose mixtures, at various temperatures. (A), for STS10,  $T = 311$  ( $\square$ ), 323.7 ( $\bullet$ ), 342 ( $\circ$ ), 353 ( $\blacksquare$ ) and 367 ( $\blacktriangle$ ) K; (B), for STS20,  $T = 294$  ( $\blacktriangledown$ ), 311 ( $\bullet$ ), 333 ( $\nabla$ ), 357 ( $\square$ ), 368 ( $\Delta$ ) and 373 ( $\circ$ ) K. **109**
- Figure 3.9:** Variation of the *o*-Ps lifetime as a function of temperature in STS20, having water contents,  $c_w$ , of 5.1 (upper) and 7.1% (lower), respectively, as derived from the various  $\tau_3$  vs  $c_w$  experimental plots: ( $\bullet$ ), interpolated, ( $\blacksquare$ ) extrapolated from the data (see text). **110**
- Figure 3.10:**  $T_g$  (K), STS20 ( $\bullet$ ) and STS10 ( $\blacksquare$ ), measured from *o*-Ps lifetime measurements as a function of water content,  $c_w$ . Previous data for STS20 from Differential Scanning Calorimetry (Poirier-Brulez et al. (2006) are also shown ( $\circ$ ) **112**
- Figure 3.11:** *o*-Ps lifetime at the glass transition temperature as a function of  $T_g$  (K) in hydrated STS10 ( $\blacksquare$ ), and STS20 ( $\bullet$ ). **113**
- Figure 3.12:** (A) and (B). *o*-Ps lifetime as a function of water content at the glass transition,  $c_g$  (%), STS20 ( $\bullet$ ) and STS10 ( $\circ$ ), respectively. **114**
- Figure 3.13:** Volume distribution of the nanoholes at 294 K in STS20 ( $c_w = 4.3\%$ ) **117**



<b>CHAPTER-IV</b>	<b>121</b>
<b>Figure 4.1:</b> Variation of the degree of grafting of acrylic acid with reaction temperature	<b>127</b>
<b>Figure 4.2:</b> Typical FTIR spectrum of PET-g-AA (12.1% degree of grafting)	<b>128</b>
<b>Figure 4.3:</b> $\tan\delta$ vs temperature plot of the neat PET and PET-g-AA copolymer	<b>129</b>
<b>Figure 4.4:</b> Storage modulus vs temperature plot of neat PET and PET-g-AA copolymers	<b>130</b>
<b>Figure 4.5:</b> WAXD plot of neat PET and grafted copolymers. Inset shows a typical peak fitting to evaluate the relative crystallinity	<b>131</b>
<b>Figure 4.6A:</b> <i>o</i> -Ps lifetime as a function of degree of grafting	<b>132</b>
<b>Figure 4.6B:</b> <i>o</i> -Ps intensity as a function of degree of grafting	<b>133</b>
<b>Figure 4.6C:</b> Fractional free volume as a function of degree of grafting	<b>134</b>
<b>Figure 4.7A:</b> Free positron lifetime as function of degree of grafting	<b>136</b>
<b>Figure 4.7B:</b> Free positron intensity as function of degree of grafting	<b>136</b>
<b>Figure 4.8:</b> FTIR spectra of the pristine, ion-irradiated and etched PET films	<b>138</b>
<b>Figure 4.9:</b> XRD spectra of the pristine, ion-irradiated and etched films	<b>139</b>
<b>Figure 4.10:</b> The free volume radius ( $\times 10$ nm) distributions in the bulk of pristine, ion-irradiated and etched PET films	<b>141</b>
<b>Figure 4.11:</b> The <i>S</i> -parameter as a function of positron energy, top axis shows the positron implantation energy; solid lines are the eye guides	<b>142</b>
<b>Figure 4.12:</b> The $3\gamma/2\gamma$ ratio as a function of positron energy, top axis shows the positron implantation depth	<b>142</b>

<b>CHAPTER-V</b>	<b>146</b>
<b>Figure 5.1:</b> The block diagram for the AMOC setup	<b>149</b>
<b>Figure 5.2:</b> A typical 2D AMOC spectrum for a polymer sample	<b>150</b>
<b>Figure 5.3:</b> The Y-projection of 2D AMOC spectrum; lifetime spectrum of the sample	<b>151</b>
<b>Figure 5.4:</b> The X-projection of 2D AMOC spectrum; Doppler broadening spectrum of polymer sample	<b>151</b>
<b>Figure 5.5a:</b> The regenerated AMOC relief spectrum for a polymer sample	<b>153</b>
<b>Figure 5.5b:</b> A typical $S$ -parameter vs positron age profile for a polymer	<b>153</b>
<b>Figure 5.6:</b> The HRTEM bright field images of MWCNTs	<b>160</b>
<b>Figure 5.7a:</b> The SEM images of surface of PF-2, PF-5, PF-10 and PF-20.	<b>161</b>
<b>Figure 5.7b:</b> The SEM images of the fractured surfaces of PF-2, PF-5, PF-10 and PF-20.	<b>161</b>
<b>Figure 5.8:</b> XRD patterns of PF-MWCNTs composites	<b>162</b>
<b>Figure 5.9:</b> The plot of difference in $I_2$ as a function of MWCNTs concentration. The symbols (●) and (○) are for experimental results and linear variation of $I_2$ respectively. The solid line is an eye guide.	<b>166</b>
<b>Figure 5.10:</b> The average volume of nanoholes as a function of MWCNTs concentration	<b>167</b>
<b>Figure 5.11:</b> The distribution of volume of nanoholes; the symbols (■, □, ●, ○ and ▲) are for PF-0, PF-2, PF-5, PF-10 and PF-20 respectively. The solid lines are Gaussian fit to data.	<b>168</b>
<b>Figure 5.12:</b> Positron age dependence of $S(t)$ parameters in PF-0 (■), PF-2 (●) and PF-10 (○). The solid lines are eye guides. For clarification, the error	<b>171</b>

bars are not shown on all the data. The variation of  $S(t)$  up to 1 ns is shown in the inset.

<b>CHAPTER-VI</b>	<b>173</b>
<b>Figure 6.1:</b> XRD pattern of as-prepared ZnO (a) and samples annealed at different temperatures; 200°C (b), 300°C (c), 400°C (d), 500°C (e) and 800°C (f).	<b>184</b>
<b>Figure 6.2:</b> The XRD pattern of CdSe nanoparticles samples (a'), (b'), (c') having average particles size 7, 11.5 and 15.5, respectively.	<b>185</b>
<b>Figure 6.3:</b> The TEM images of sample (a') and sample (d'). The bars at the bottom on the right hand side show the scale of the images. The encircled dots are the CdSe nanoparticles	<b>186</b>
<b>Figure 6.4:</b> Size distribution of Au nanoparticles	<b>186</b>
<b>Figure 6.5(a) and (b):</b> ZnO supercell and positron density in a plane having Zn vacancy, respectively	<b>188</b>
<b>Figure 6.6 (a) and (b):</b> $S$ -parameter and average positron lifetime ( $\tau_{av}$ ) as a function of size of ZnO nanoparticles, respectively	<b>190</b>
<b>Figure 6.7(a) and (b):</b> Ratio curves with respect to Si from CDB measurements on ZnO nanoparticles and calculated ratio curves in ZnO with different vacancies, respectively	<b>191</b>
<b>Figure 6.8:</b> $S$ - $W$ plot of ZnO nanoparticles	<b>192</b>
<b>Figure 6.9:</b> Ratio of the intensities of visible ( $I_{VIS}$ ) to UV ( $I_{UV}$ ) emission $R = (I_{VIS}/I_{UV})$ as a function of particle size	<b>194</b>
<b>Figure 6.10:</b> Ratio curves with respect to Si single crystal from coincidence Doppler broadening measurements on different CdSe nanoparticles, Cd and	

Se. The representative error bars are shown in the peak and back ground region.	<b>195</b>
<b>Figure 6.11:</b> The plot of peak position obtained from the Gaussian fit to the experimental momentum distribution ratio curves vs. the size of CdSe nanoparticles	<b>197</b>
<b>Figure 6.12:</b> Theoretically calculated momentum distribution ratio curves for CdSe, Cd and Se with respect to Si.	<b>199</b>
<b>Figure 6.13:</b> Vacancy defects in Gold lattice in two configurations A and B	<b>202</b>
<b>Figure 6.14:</b> Formation energy per vacancy as a function of number of vacancy, $n$ .	<b>206</b>
<b>Figure 6.15:</b> Binding energy per vacancy as a function of number of vacancy, $n$	<b>206</b>

## LIST OF TABLES

	Page No.
<b>CHAPTER-III</b>	<b>85</b>
<b>Table 3.1</b> Average values of the slopes of the variations of the <i>o</i> -Ps lifetime ( $\tau_3$ ) and nanohole average volume ( $V$ ) with water content ( $c_w$ ) below, ( $a_{\tau,w}$ , $a_{V,w}$ ), and above, ( $b_{\tau,w}$ , $b_{V,w}$ ), the break at $c_g$	<b>109</b>
<b>CHAPTER-IV</b>	<b>121</b>
<b>Table 4.1</b> The <i>o</i> -Ps <i>pick-off</i> lifetime ( $\tau_3$ ) and intensity ( $I_3$ ) evaluated from PATFIT	<b>140</b>
<b>CHAPTER -V</b>	<b>146</b>
<b>Table 5.1</b> Positron annihilation lifetime components with corresponding intensities for pure PF-resin and PF-MWCNTs composites	<b>163</b>
<b>CHAPTER-VI</b>	<b>173</b>
<b>Table 6.1.</b> Positron annihilation lifetimes and corresponding intensities in ZnO nanoparticles of different size.	<b>187</b>
<b>Table 6.2.</b> Calculated positron lifetime in ZnO wurtzite supercell bulk and having various combinations of vacancies.	<b>188</b>
<b>Table 6.3</b> The peak positions and area under the peak in the experimental ratio curves of CdSe nanoparticles of different sizes, and pure Cd and Se. $f_{Cd}$ and $f_{Se}$ are the fraction of positrons annihilating with semi core electrons from Cd and Se in CdSe nanoparticles, respectively.	<b>196</b>

**Table 6.4** The calculated positron lifetimes in vacancy defects in two different configurations  $A$  and  $B$  in gold supercell. Positron lifetime under Unrelaxed and Relaxed columns show the values using unrelaxed and relaxed gold atoms coordinate. (In configuration  $A$ , the schematic for  $V_n$  where  $n = 7, 8$  and  $9$  are not shown).

203

# **CHAPTER-I**

---

## **INTRODUCTION**

## 1.1. Positron and Positronium

### 1.1.1 Discovery

According to Dirac's theory [Dirac, 1930 and 1935], the relationship between the energy  $E$  and momentum  $\vec{p}$  of a free particle of rest mass  $m_0$  is given as

$$E^2 = p^2 c^2 + m_0^2 c^4 \quad (1.1)$$

where  $c$  is the velocity of light. This equation gives two solutions to the energy of electron as  $E = \pm c \sqrt{p^2 + m_0^2 c^2}$ . It shows two states of electrons separated by  $\geq 2m_0 c^2$ .

Under normal conditions, the negative energy states are completely filled with electrons. A negative energy electron gets excited to one of the positive energy states absorbing a photon of energy  $\geq 1.022$  MeV ( $2m_0 c^2 = 1.022$  MeV) as shown in Fig. 1.1. The process is called pair production and as a result an electron of charge  $-e$  and energy  $+E$  is produced along with a hole in the negative energy sea. This hole is the absence of electron of charge  $-e$  and energy  $-E$  in the negative energy sea which was described as a particle, positron, of charge  $+e$  and energy  $+E$  with respect to vacuum. The inverse of pair production i.e. emission of radiation as a result of trapping of an electron by a hole (positron) in the negative energy sea is termed as electron-positron pair annihilation. The schematic of electron-positron annihilation is shown in Fig. 1.2.

Few years later, positron was experimentally discovered by Anderson (1933) in his cloud chamber experiments. The cosmic rays tracks in the cloud chamber were observed from a particle having mass of electron and positive charge equal to an electron. It was immediately realized to be the anti-particle of electron predicted by Dirac.



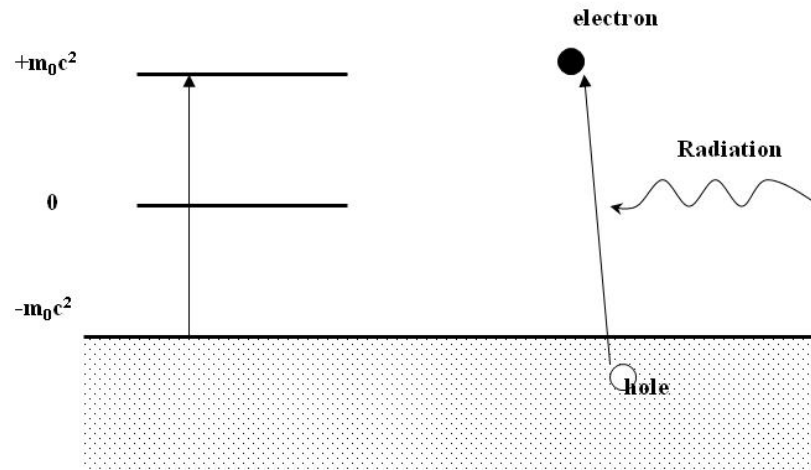


**Figure 1.1:** A schematic of pair production

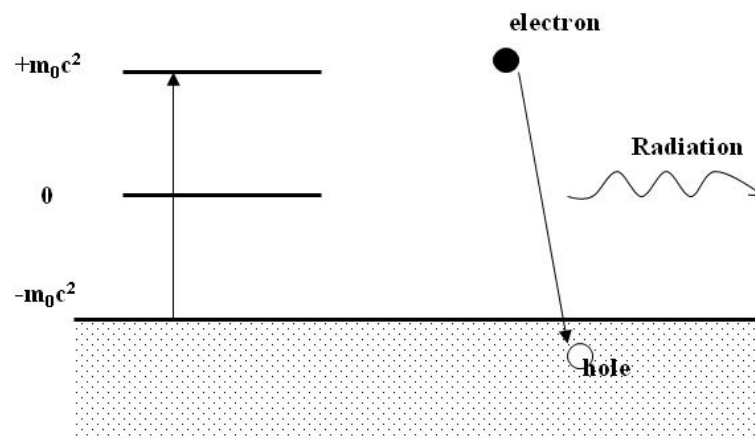


**Figure 1.2:** A schematic of electron-positron annihilation

### 1.1.2 Characteristics

The Positron belongs to “*leptons*” group of particles which consists of electron, muon, tauon, their corresponding neutrinos and respective anti-particles. Particles belonging to “*leptons*” group obey Fermi-Dirac statistics. They do not participate in strong interactions [Beiser, 2002] and participate only in gravitational, weak and electromagnetic interactions. The lepton number of positron is -1 (+1 for electron). The physical properties of positrons have been found to be little different from electrons [Schrader and Jean, 1988 and Schwinberg et al., 1981]. For most practical purpose, these two particles are considered equivalent. The only substantial differences between the two are the sign of their charge and attendant properties.

### 1.1.3 Annihilation

As discussed, the positron and electron are considered equivalent for most of the practical purposes but positron being the anti-particle of electron, can not survive for infinite time in a medium. Positron undergoes annihilation with an electron in a medium emitting the radiation photons. The annihilation event is governed by quantum electrodynamics. According to quantum electrodynamics, any number of photons can be emitted during positron-electron annihilation. The probabilities of zero photon and one photon emissions are very small due to the fact that two extra bodies for zero photon and one extra body for one photon annihilation are required for the momentum transfer. On the other hand, two photons emission is most favorable process as emission of two photons satisfies all the conservation laws themselves. The two photons annihilation cross-section of a positron- electron pair is [Schrader and Jean, 1988] given by

$$\sigma_2 = \frac{\pi r_0^2}{\gamma' + 1} \left[ \frac{\gamma'^2 + 4\gamma' + 1}{\gamma'^2 - 1} \ln(\gamma' + \sqrt{\gamma'^2 - 1}) - \frac{\gamma' + 3}{\sqrt{\gamma'^2 - 1}} \right] \quad (1.2)$$

where,  $\gamma' = \frac{E_+}{m_e c^2}$ ,  $E_+$  being the positron energy and  $r_0$  is the classical electron radius given by  $e^2/m_e c^2$  ( $e$  and  $m_e$  being the charge and mass of electron respectively and  $c$ , the velocity of light). Three photon cross-section is lower compared to two photons and is given by

$$\sigma_3 = \frac{4}{3\pi}(\pi^2 - 9)\alpha\sigma_2 \approx \frac{\sigma_2}{371.3} \quad (1.3)$$

where  $\alpha$  is the fine structure constant (1/137). In all condensed media, a high energy positron rapidly thermalizes by inelastic collisions before annihilation. At low energies of collisions the annihilation rate ( $\lambda$ ) of positron of velocity ' $v$ ' in an environment with electron density  $\rho$  is given by

$$\lambda = \sigma_2 v \rho = \pi r_0^2 c \rho \quad (1.4)$$

Thus measuring the lifetime (inverse of annihilation rate) of positron gives information about the electron density at the site of annihilation.

#### 1.1.4 Positronium atom

In molecular substances, a thermalized positron can form a quasi bound atom state called positronium, Ps, with an electron. Different models viz. "spur model" and "ore model" have been proposed for positronium formation mechanism [Ore and Powell, 1949, and Mogensen, 1974]. The Ps atom is analogous to hydrogen wherein proton is replaced by positron. Positronium, like hydrogen, can exist in two states i.e. singlet state (*para*-positronium, *p*-Ps) with anti parallel spin and triplet state (*ortho*-positronium, *o*-Ps) with parallel spin. The selection rules and cross-section for self annihilation of positronium are similar to that of a free positron. The relationship between the orbital

angular momentum  $l$  of the positronium state, the spin quantum number  $s$  and the number of photon emitted in self-annihilation,  $n$ , is given as

$$(-1)^{l+s} = (-1)^n \quad (1.5)$$

According to this selection rule, singlet state annihilates into an even number of photons and triplet state into odd number of photons. Therefore, in vacuum, the ground state  $p$ -Ps and  $o$ -Ps annihilate into two and three photons, respectively. The intrinsic lifetime of  $p$ -Ps and  $o$ -Ps in vacuum is 125 ps and 142 ns. In molecular solids, triplet state ( $o$ -Ps) can be trapped in low density regions like free volume nanoholes in polymers and geometrical cavities in zeolites where positron from  $o$ -Ps can annihilate with an opposite spin electron from the medium through two photons mode. The process is called “*pick-off*” annihilation. During this process,  $o$ -Ps lifetime is greatly reduced. The  $o$ -Ps *pick-off* lifetime is correlated with the size of free volume nanoholes in a polymer using the well known semi empirical Tao-Eldrup equation as given below [Tao, 1972 and Eldrup et al., 1981].

$$\begin{aligned} \lambda_{Pick-off} &= \left[ \frac{1}{4} \lambda_s + \frac{3}{4} \lambda_T \right] \cdot P \\ &= 2 \cdot \left[ 1 - \frac{R}{R + \Delta R} + \frac{1}{2\pi} \sin \left( \frac{2\pi R}{R + \Delta R} \right) \right] \end{aligned} \quad (1.6)$$

where  $\lambda_s$ ,  $\lambda_T$ ,  $R$  and  $\Delta R$  are the singlet and triplet positronium self-annihilation rates, radius of the free volume nanoholes (assuming spherical) and an empirical parameter, respectively. The value of the empirical parameter  $\Delta R$  has been determined as 0.166 nm.

Positronium like hydrogen can also undergo chemical reactions. Many reactions like oxidation, spin conversion and complex formation have been observed in case of positronium. In the presence of chemical reactions in a medium,  $o$ -Ps lifetime as well as positronium formation probability change depending on the type of chemical reaction. [Duplatre et al., 2003]

### 1.1.5 Sources of positron

Different sources have been considered for Positron Annihilation Spectroscopy (PAS) depending on the requirement. The largely used sources for laboratory based conventional studies are neutron deficient isotopes. The choice of radioisotope depends on the experimental technique of positron annihilation spectroscopy. In positron lifetime spectroscopy an isotope with a good yield of prompt gamma ray (birth signal of positron) following positron emission is required.  $^{22}\text{Na}$  is the most commonly used radioisotope in positron annihilation studies. Typical source strengths used are about few tens of micro-Curie and depend on the size of the sample and counting efficiency of the system.

The energy of positrons emitted in  $\beta^+$  decay of radioisotopes is not constant but ranges from zero to  $\beta_{\text{max}}$ . To obtain the depth dependent information on samples, mono energetic positrons are needed. The mono energetic positron beams are obtained by either monochromatizing the positrons emitted from radioisotopes or by using the accelerator based positron sources. A detailed account of the positron beams and their applications are reviewed by Schultz and Lynn (1988).

## 1.2 Positron and Positronium as probes in condensed matter

Positron annihilation spectroscopy (PAS) is a well established family of techniques to study the condensed matter. In PAS, positron and positronium are used as probes to characterize the materials. Positron and positronium have propensity to get trapped in low electron density regions (point defects in metals/alloys, free volume nanoholes in polymers, pores in zeolites etc.) and information about the size and concentration of these low density regions can be obtained. PAS has been extensively used to study positron trapping at mono vacancies, dislocations and vacancy clusters in metals [Dupasquier and Mills, Jr., 1995; and Dekhtyar, 1974] and type of vacancies and

electronic environment around the vacancies in semiconductor materials [Hautakangas et al., 2003; Gebauer et al., 2002; Slotte et al., 2003 and Krause-Rheberg et al., 1999]. PAS has been employed for the determinations of Fermi surface in materials [Smedskjaer et al., 1998; Bansil et al., 1988 and Chan et al., 1992]. It has been extensively used through *o*-Ps *pick-off* lifetime to study the free volume hole size distributions and nanostructural changes in polymers [Ito et al., 1998, 1999a and 2000; Bandzuch, 2000 and Mallon 2003]. The phase transitions in confined liquids [Dutta et al., 2006 and 2008], porous materials of technological importance like catalysts [Miranda et al., 1993], low-k dielectric materials [Gidley et al., 2006] and aerogels [Miranda et al., 2006] have been extensively studied using this technique. A review of general applications of positron and positronium in probing molecular substances can be found in literature [Jean et al., 2003]. In recent years, positron has also been identified as a sensitive and self seeking probe for the embedded and colloidal nanoparticles [Xu, 2003].

### 1.3. Positron annihilation spectroscopy

Positron annihilation spectroscopy consists of a number of techniques. Each technique provides specific information about the material under investigation. The techniques used for the studies presented in this thesis are (i) Positron annihilation lifetime spectroscopy, PALS (ii) Doppler broadening of annihilation radiation, DBAR (iii) Coincidence Doppler broadening (CDB) technique and (iv) Positron Age-momentum correlation, AMOC. The schematic of these techniques are shown in Fig. 1.3. The principle and experimental details of PALS, DBAR and CDB are given below. The instrumentation used in PALS, DBAR and CDB will be discussed in chapter II. AMOC development and its application for a polymer nanocomposite will be described in Chapter V.

### 1.3.1 Positron Annihilation Lifetime Spectroscopy (PALS)

The positron lifetime (inverse of annihilation rate) in a medium depends on the electron density at the site of annihilation. In PALS, the survival time of a positron in a material is measured by indexing the birth and annihilation signals of positron. In conventional measurements using radioisotope source, the prompt gamma ray emitted with positron is used to index the birth, and, the annihilation photon is used to index the “death” or annihilation of the positron. The typical positron annihilation lifetime spectrum consists of multi-exponential decay curve (corresponding to different positron states in the media) convoluted with time resolution function of the spectrometer. The resolution function for most of the set ups used in PALS is in the range of 200 -300 ps which can be further improved depending on the requirements. PALS is the main technique in positron annihilation spectroscopy to provide quantitative information about the size and concentration of defects in different media. The instrumentation of this technique is discussed in detail in Chapter II.

### 1.3.2 Doppler Broadening of Annihilation Radiation (DBAR)

As shown in Fig. 1.3, when a thermalized positron annihilates with an electron from the medium, the electron-positron pair carries the electron momentum. Due to the finite electron momentum, the energies and emission directions of the emitted photons are changed in laboratory reference of frame. The angle of deviation  $\delta\theta$  (Fig. 1.3) is related to transverse component ( $P_T$ ) of electron momentum  $P$  by eq. 1.7.

$$\delta\theta \approx \frac{P_T}{m_0 c} \quad (1.7)$$

where  $m_0$  and  $c$  are the rest mass of electron and velocity of light, respectively. Similarly, the energy of photons in laboratory frame is given as

$$E_\gamma = \frac{1}{2} E_T (1 \pm \frac{v}{c} \cos \theta) \quad (1.8)$$

The energy of annihilation photon (neglecting the small deviation) can be written in terms of its rest mass energy as

$$E_\gamma = E_0 \pm \delta E = m_0 c^2 \pm c \frac{P_L}{2} \quad (1.9)$$

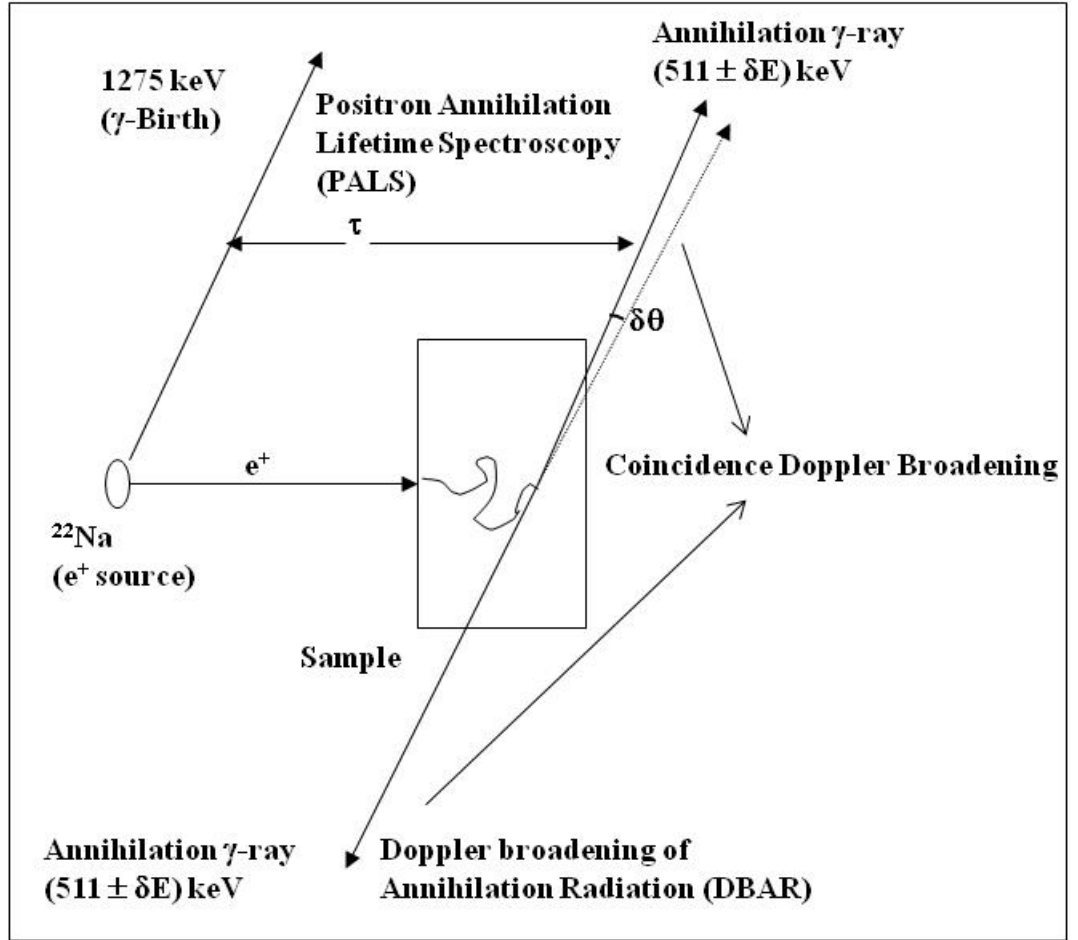


**Figure 1.3:** Positron annihilation spectroscopy

where,  $P_L$  is the momentum component along the emission direction of the annihilation photons (taken as  $z$  axis). The measurement of momentum distribution of the annihilating electrons by measuring the deviation from anti-collinearity is known as angular correlation of annihilation radiation (ACAR). In DBAR, momentum distribution of the



annihilating electrons is determined by measuring the energy of annihilation photons using high purity Ge detector. The Doppler broadening spectrum corresponds to longitudinal momentum density and is given by

$$W(E) = \text{const.} \iint \rho(p_x, p_y, p_z) dp_x dp_y \quad (1.10)$$

where  $\rho$  is the electron momentum space density and  $z$  axis is the line joining the detector and source. The spectrum is convoluted with detector resolution (a Gaussian distribution). The Doppler broadening spectrum is analyzed in terms of shape and wing parameters without deconvoluting the resolution function of the detector. The details are discussed in chapter II.

### 1.3.3 Coincidence Doppler Broadening (CDB)

This technique is superior version of DBAR. In this technique, both the annihilation gamma rays (of energies  $E_{\gamma 1}$  and  $E_{\gamma 2}$ ) are measured in coincidence. The coincidence measurements offer superior signal to background ratio compared to conventional Doppler broadening measurements in the higher momentum region of the Doppler broadened spectrum. This enables the identification of the elements surrounding the annihilation site by indexing the annihilations with the core electrons of these elements. In CDB measurements, if both detectors have same energy resolution then it leads to an improved resultant resolution by a factor of  $\sqrt{2}$ . The details are discussed in chapter II.

## 1.4 Nanostructures

Nanostructures studied in the present thesis are classified into two categories viz. the molecular level vacant spaces (free volume nanoholes) in polymers and atomic level vacancy defects in nanoscale crystalline materials. The free volume nanoholes can be

dynamic or static in nature and their size varies in the range of subnanometer. These free volume nanoholes govern various properties such as thermo-mechanical, optical, diffusion and perm selectivity etc. of the polymers. The size and concentration of these free volume nanoholes vary as a function of temperature, pressure, additives, cross-linking, heavy ion-irradiation and grafting . Thus, it is important to characterize these free volume nanoholes in polymer under different conditions to have correlation between macroscopic properties and their nanostructure. Free volume nanoholes in natural polymers like starch and sucrose is also of great importance because macroscopic properties of the natural polymers are governed by the packing of molecules which leads to a specific nanostructure characterized by free volume naoholes. The natural polymers have large molecular entities compared to synthetic polymers. As a result their glass transition temperature is higher compared to synthetic polymers. Water is an essential part of natural polymer products like food, pharmaceuticals and packaging materials. Water absorption by natural polymers and addition of small polyol molecules change the nanostructure of natural polymer and greatly reduce the glass transition temperature.

Nanoscale crystalline materials are of great importance because of their improved properties like mechanical, optical, electronic, and catalytic over the bulk counterpart. This is mainly because of their high surface to volume ratio. The evolved properties depend on the shape, size and size distribution of the nanoparticles. Various methods have been developed to control the shape, size and size distribution of nanoparticles. The synthesis of nanoparticles using chemical reaction is a potential method for producing nanoparticles with narrow size distribution. In case of semiconductor nanoparticles, their opto-electronic properties are tunable as the band gap of these nanoparticles varies with their size. In case of metal nanoparticles, collective oscillation of conduction electron known as “surface plasmon” is observed. The frequency of surface plasmon is a function

of electron density which again depends on the size of the nanoparticle. Hence, the optical properties of metal nanoparticles can be tuned by varying their size. In very small size nanoparticles,  $< 5$  nm, (quantum dots), nanoparticle acts as a potential well for the conduction electron and characteristics of quantum confinement of electron are observed. Defects viz. vacancy, vacancy cluster, interstitials, voids etc. are generally produced in the nanoparticles during the synthesis as they are thermodynamically stable. These defects can be present either in the bulk or at the surface (grain boundaries) of the nanoparticles. Defects in nanoparticles play an important role in governing various properties such as optical, electrical, and mechanical etc. Defects in semiconductor nanoparticles can act as trap for electron and hole which leads to change in their optical and electronic properties. In case of metal nanoparticles, presence of defects can alter the electron density at the surface which again modifies the frequency of surface plasmon and leads to modified optical properties. To develop a method for synthesis of nanoparticles of desirable properties, it is essential to characterize the defects in the nanoparticles.

### **1.5 Positron annihilation spectroscopy in nanostructures and scope of present work**

Positronium is the smallest probe (1.059 Å) and sensitive to small holes of the order of subnanometer size called free volume nanoholes. The triplet state of positronium (*o*-Ps) has been used as a probe to characterize free volume nanoholes in various types of polymers. PAS in polymers can provide information about the size, concentration and size distribution of the free volume nanoholes. Due to its short lifetime (2- 4 ns), it can be used to probe the holes due to molecular motion from  $10^{-10}$ s and longer. PAS also gives information about the local environment of the free volume nanoholes [Mallon, 2003 and Jean et al., 1986]. The *o*-Ps lifetime in a polymer is related to size of free volume nanoholes using the well documented Tao-Eldrup equation (eq. 1.6). Whenever the hole

size is bigger, a fraction of *o*-Ps can annihilate via three gamma photon mode. Several models have been proposed to correlate the *o*-Ps lifetime with hole size considering three gamma annihilation in the free volume nanoholes [Gowrek et al., 1997 and 1998; Ciesielski et al., 1998; Wawryszczuk et al., 2003; Ito et al., 1999b, Dutta et al., 2004 and Sudarshan et al., 2007]. The fractional free volume,  $f_v$  in a polymer is calculated using average volume of nanoholes and *o*-Ps intensity as

$$f_v = CI_3 \langle v_f(\tau_3) \rangle \quad (1.11)$$

where  $C$  is a constant,  $I_3$  is *o*-Ps intensity and  $\langle v_f(\tau_3) \rangle$  is the average volume of nanoholes [Wang et al., 1990]. The nanostructure of polymers has been found deterministic for their thermo-mechanical properties. The glass transition temperature,  $T_g$ , of polymers is determined by measuring *o*-Ps lifetime as a function of temperature. This method has been extensively used for determination of  $T_g$  of different polymers under different conditions [Mallon 2003, Jean et al., 1986]. In glassy state, *o*-Ps lifetime increases linearly with temperature and the gradient of change sharply increases at glass transition temperature followed by a linear increase in rubbery phase. The point of inflexion gives the glass transition temperature,  $T_g$ , of the polymer. Similar trends have been reported in *o*-Ps intensity and line shape parameter,  $S$ , as a function of temperature.

In case of natural polymers, use of *o*-Ps as a probe for the nanostructure study is limited in literature [Kilburn et al, 2004 and 2006; Townrow et al., 2007 and Roudaut et al., 2009]. One of the issues of working with these polymers lies in their sensitivity to both temperature and relative humidity. It has been reported in the literature that measuring  $T_g$  of natural polymers using PALS is a cumbersome process as their decomposition starts before reaching the glass transition region. One way to improve our knowledge on the process of glass transition refers to the use of plasticizers, such as water or polyols (sucrose), that reduce greatly the  $T_g$  [Mizuno et al., 1998 and Poirier-Brulez et

al., 2006]. In the presence of water, determination of  $T_g$  becomes more difficult as water evaporates from the sample during PALS measurements. Hence, measurement of  $T_g$  in natural polymers using PALS requires new strategies. In the present thesis, the changes in the nanostructure of starch matrix on addition of sucrose and water are reported. The variations in nanoholes size and concentration as a function of temperature have been measured to gain insight into the nanostructure of the starch matrices. The measurement of the  $T_g$  of starch/sucrose matrix using PALS is reported where a model has been developed to determine the  $T_g$  even when the matrix is undergoing decomposition. For the measurement of glass transition temperature of hydrated starch/sucrose matrix, a new approach has been developed where  $T_g$  can be measured in the presence of evaporation of water from the sample. These studies provide useful information about the nanostructure of natural polymers and its effect on their thermal properties.

Modifications of polymers by graft copolymerization of functional monomers, and by ion-irradiation followed by etching are well established techniques to impart favorable physical and chemical properties to given polymers. These modifications induce changes (variation in size, density and size distribution of nanoholes) in the nanostructure of polymer matrix. A large number of studies have been reported where the changes in nanostructure of polymer have been correlated to the macroscopic properties of polymers [Jean et al., 2003]. Radiation induced graft copolymerization is advantageous because of its extensive penetration into the polymer matrix, and its ability to form radicals rapidly and uniformly for initiating the grafting in various kinds of polymers.

Poly ethylene terephthalate (PET) films are characterized by determining its properties like high crystallinity, thermal stability and hydrophobicity and presence of chemically inert functional groups [Karagianidis et al., 2008]. Radiation induced graft copolymerization of PET with various vinyl monomers such as styrene [Nasef, 2000 and

Nasef, 2002], acrylic acid [Huglin et al., 1973], methacrylic acid [Uchida et al., 2000], 2-methyl 5-vinyl pyridine [Helbeish et al., 1978] etc. has been reported. Ion-irradiation of PET films followed by etching with alkaline medium is known to change the pores size, distribution and their interconnectivity which leads to modified transport properties of the polymer. Most of the studies on the changes in the nanostructure of polymers by ion beam irradiation have been carried at the fluences of  $10^{10}$ -  $10^{17}$  ions/cm<sup>2</sup> and changes in the properties like absorbance, crystallinity, capacitance and mechanical properties have been monitored [Singh et al., 2006 and 2008 and Sun et al., 2003]. In the present thesis, nanostructure of PET (i) grafted with Acrylic acid (PET-g-AA) using radiation grafting, and (ii) irradiated with 100 MeV <sup>35</sup>Cl beam in low fluence ( $7 \times 10^7$  ions/cm<sup>2</sup>) have been studied using positron annihilation spectroscopy. The changes observed in the nanostructure have been correlated with structural changes observed from supplementary techniques. These studies showed that phase segregation occurs in PET-g-AA samples at higher degree of grafting and positron annihilation occurs at the interfaces without forming positronium. Depth dependent Doppler broadening measurement in ion-irradiated samples showed the predominant changes in nanostructure at surface and sub surface region at low fluence ion-irradiation. These studies confirmed that positron annihilation spectroscopy is a very sensitive technique to evaluate the changes in the nanostructure of modified polymers even when conventional techniques do not show any changes.

Polymers are also modified by nanocomposite formation for which a nanoscale crystalline phase is well dispersed in polymer matrix. Polymer nanocomposites possess modified mechanical, thermal and electrical properties compared to pristine polymer. PAS is used as a primary technique for the evaluation of the changes in nanostructure of polymers on nanocomposite formation. In the presence of nanoscale crystalline phase

distributed in the polymer matrix, new positron/Ps trapping/annihilation sites like interfaces and nanophase itself become available. Hence, it becomes essential to study the positron systematics in polymer nanocomposites to elucidate the positron states. The correlated measurements of positron lifetime and Doppler broadening provide information about different positron states in the system. This method is called age momentum correlation (AMOC) [Dauwe et al., 2003; Suzuki et al., 2003 and Schneider et al., 1997]. A set up has been developed for AMOC measurements and has been used to study the poly (phenol formaldehyde) PF resin -multi-wall carbon nanotube (MWCNTs) composite. AMOC measurements showed that positronium annihilation occur from PF-MWCNTs interfaces. Free positron annihilation from MWCNTs distributed in the polymer matrix is observed and its fraction increases with the concentration of MWCNTs. This study provides experimental evidence for the positron trapping at nanoscale crystalline phase dispersed in the polymer matrix.

Positron annihilation spectroscopy has been extensively used for the characterization of defects in metals, alloys and semiconductor in their bulk forms. Extensive reviews are available in the literature for these studies [Krause-Rheberg and Lipner, 1999 and Brandt and Dupasquier, 1981]. In the recent years, positron annihilation spectroscopy has been used for study of metal and semiconductor nanoparticles [Schaefer et al., 1988; Xu et al., 1999; Nagai et al., 2000; Xu et al., 2001; Nagai et al., 2001; van Huis et al., 2002; Weber et al., 20002 and Eijt et al., 2006]. Positron lifetime is related to the size of defects in the materials and corresponding intensity gives the concentration of the defects. Positron lifetime is calculated in the defects using first principle calculations to compare with the experimental results [Torsti et al., 2006]. This approach has evolved during the years to characterize the defect size as well as types in different type of materials. Doppler broadening measurements also gives information complementary to

positron lifetime measurements. In the presence of defects, overlap between trapped positron with valance and core electron reduces but the reduction in the core part is more. This effectively leads an increase in the low momentum region in the normalized Doppler broadening spectrum. This increase depends on the size and concentration of the defects in the material. Coincidence Doppler broadening is used to get information about the local chemical environment of the defects. First principle calculations are also employed for electron momentum distribution calculations for comparison with experimentally obtained data from CDB measurements [Torsti et al., 2006]. When positrons are implanted into the nanoparticles, a fraction of positrons diffuses to and annihilates from the surface. This is because the positron diffusion length is comparable to the size of the nanoparticles. Thus, positron annihilation spectroscopic studies in nanoparticles give information about the bulk as well as the surface. In recent years, positron has been identified as a sensitive and self seeking probe for the embedded and colloidal nanoparticles. The local structural properties and electronic structure of the nanoparticles can be revealed via the measurement of electron momentum density using positron annihilation techniques. [Schaefer et al., 1988; Xu et al., 1999; Nagai et al., 2000; Xu et al., 2001; Nagai et al., 2001; van Huis et al., 2002; Weber et al., 2002 and Eijt et al., 2006]. Positron annihilation spectroscopy has been used to study different type of nanoparticles e.g. nanocrystalline Fe [Schaefer et al., 1988], embedded nanoparticles [Xu et al., 1999; Nagai et al., 2000; Xu et al., 2001 and Nagai et al., 2001] and semiconductor nanoparticles [Weber et al., 2002 and Eijt et al., 2006]. The variation in positron parameters as a function of size has been correlated to electron quantum confinement, widening of band gap, presence of different type of defects, enrichment of surface by particular element etc. However, it may be mentioned that positron systematics in nanoparticles is well not understood. Extensive PAS studies in nanoparticles having



different size range are required to improve the understanding on positron systematics. In the present thesis, the focus is on the elucidation of positron states in the nanoparticles. The trapping of positrons at the defect sites present in the bulk and at the surface (grain boundaries) explains well the changes observed in the positron parameters like positron lifetime and CDB ratio curves. Defect characterization studies of semiconductor nanoparticles like ZnO and CdSe in the size range of 4 -40 nm are reported. Positron annihilation lifetime spectroscopy, Coincidence Doppler broadening techniques along with conventional techniques like X-ray diffraction, transmission electron microscopy have been employed for the characterization. Defect characterization using PAS is well corroborated by theoretical calculations of positron lifetime and electron momentum distribution. Gold nanoparticles of average size  $\sim 6$  nm have been characterized using PALS corroborated with positron lifetime calculations. Theoretical calculations of defect site relaxation in the presence of vacancy defects and formation energy of the defects have been carried out.

In the subsequent chapters, experimental details and observations are presented. In addition, the results obtained in the present investigations, both experimental and theoretical are presented. A summary of the thesis is given after the last chapter. The references are listed in the Bibliography.

## **CHAPTER-II**

---

# **EXPERIMENTAL TECHNIQUES AND THEORETICAL CALCULATIONS**

## 2.1. Experimental techniques

Positron annihilation spectroscopy consists of different techniques. The techniques used for the studies reported in this thesis using conventional  $^{22}\text{Na}$  positron source are (i) Positron annihilation lifetime spectroscopy (PALS) (ii) Doppler Broadening of annihilation radiation (DBAR) (iii) Coincidence Doppler Broadening (CDB) measurements of annihilation radiation and (iv) Age Momentum correlation (AMOC). Depth dependent DBAR and  $3\gamma/2\gamma$  measurements have been carried out using a slow positron beam. The details of these techniques excluding AMOC are described in this chapter. The details of development of AMOC and its application for characterization of polymer nanocomposite are described in chapter V. The conventional techniques such as X-ray diffraction (XRD), Fourier Transform Infra Red (FTIR), Thermal gravimetric analysis (TGA), Dynamical mechanical analysis (DMA) etc. used for the studies will be described in the respective chapters.

### 2.1.1. Positron source

#### 2.1.1.1 Conventional measurements

Sodium-22 ( $^{22}\text{Na}$ ) is the most common choice of radioisotope positron source in PALS and AMOC due to its relatively high positron yield of 90.4%, fairly long half-life (2.57 years) and appearance of 1275 keV prompt  $\gamma$ -ray almost simultaneously with the emission of positron that serves as start signal in the PALS and AMOC experiments. The decay scheme of  $^{22}\text{Na}$  is shown in Fig. 2.1 [Firestone et al., 1999]. Though,  $^{22}\text{Na}$  is not the ideal positron source for Doppler broadening measurements (prompt gamma ray not required), it is commonly used for both lifetime and DBAR measurements.

For the present work, the carrier free solution of  $^{22}\text{NaCl}$  was obtained from the Board of Radiation and Isotope Technology (BRIT), India. Required aliquot of this

carrier free solution was dried on a 7  $\mu\text{m}$  polyimide film (kapton<sup>®</sup>). When the required activity was achieved, the source was covered with identical kapton film and sealed with araldite, so as to isolate the radioactivity from the surroundings. The source activity for PALS and DBAR was  $\sim 10$  Ci but for AMOC measurements source activity was  $\sim 40$  Ci. The active diameter of the positron source was about 3 mm. The preparation of source used for natural polymer samples is discussed in chapter III.

Like any radioisotope source, the positrons emitted from  $^{22}\text{Na}$  have continuous energy from 0 to  $\beta_{\text{max}}^+$ . The energy distribution ranges from 0 to 0.547 MeV and has a maximum intensity at 0.19 MeV as shown in Fig. 2.2. Since the energy distribution of positrons emitted by radioisotope is continuous, the positron implantation profiles in the medium have to be considered while choosing the sample size. The number of positrons in the sample decreases exponentially with the depth of penetration in the sample.

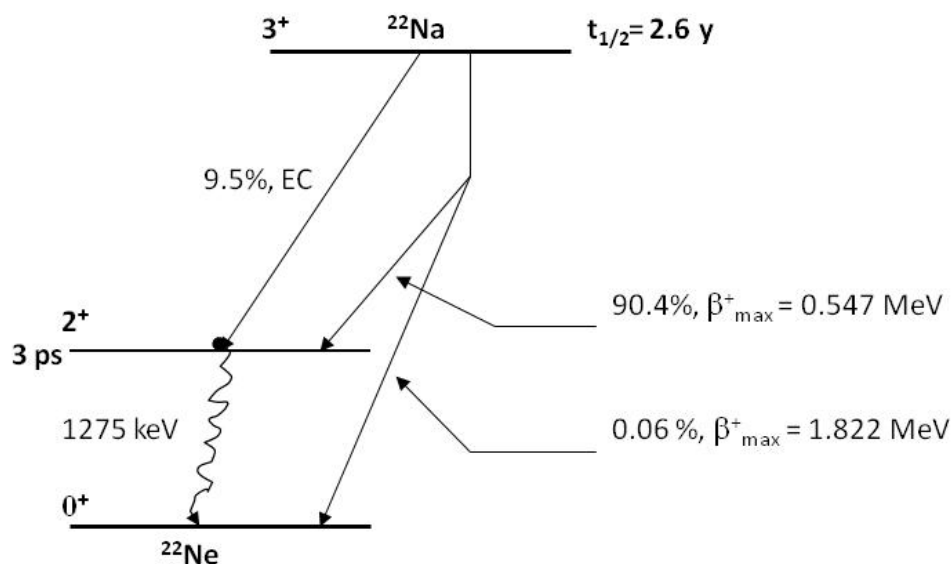


**Figure 2.1:** The decay scheme of  $^{22}\text{Na}$

The intensity of positrons at a depth  $x$  in the sample is given by  $I_x = I_0 e^{-\alpha x}$  where  $\alpha$  is the absorption coefficient of the material for positrons and is given by  $\alpha = (16 \pm 1) \rho E_{\max}^{-1.43} \text{ cm}^{-1}$  [Brandt and Paulin, 1977]. Here  $\rho$  is the density of the material in g/cc and  $E_{\max}$  ( $\beta_{\max}$ ) is in MeV. The mean implantation depth of positron in the material is  $\alpha^{-1}$ . The sample thickness surrounding the positron source is always kept much higher than this depth so that most of the positrons emitted by the radioisotope source get annihilated in the sample under study.

In the present studies of nanoparticles, positron source was embedded in sufficient powder samples ensuring the complete positron annihilation within the samples. In the case of natural polymer studies, pellets of 1 mm thickness sufficient to stop the positrons within the samples were taken for the study. For polymer films, positron source was sandwiched between stacks of polymer films on either side.

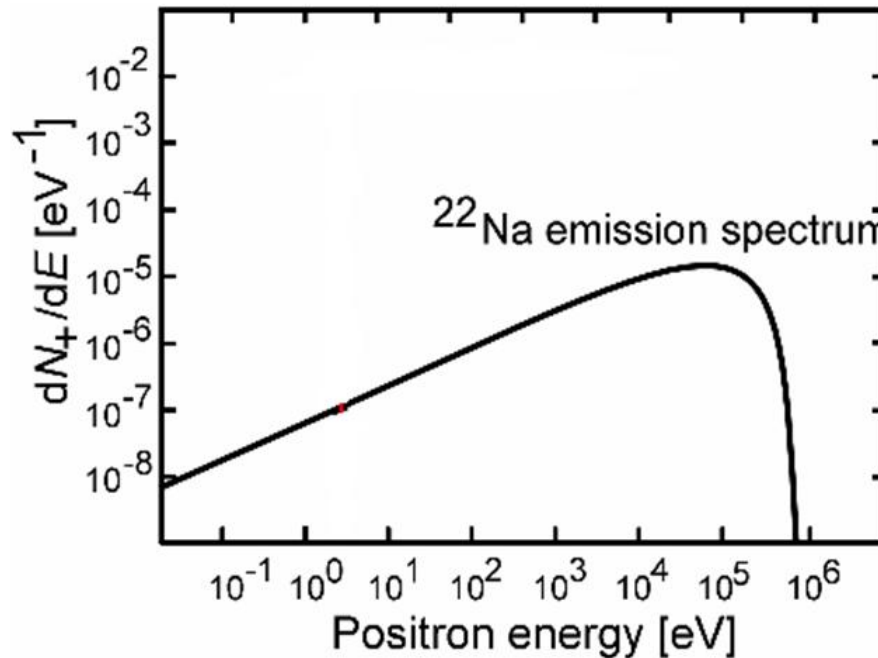


**Figure 2.2:** The positron energy spectrum in <sup>22</sup>Na Decay

### 2.1.1.2 Depth dependent measurements

As mentioned before, PAS studies using conventional source gives information about the bulk of the material. For depth dependent measurements, slow positron beam is used which can provide variable energy monoenergetic positrons. In the present work, radioisotope  $^{22}\text{Na}$  (50 mCi) based slow positron beam at Radiochemistry Division, BARC, Mumbai (Fig. 2.3.) has been used as monoenergetic positron source. Positrons emitted from  $^{22}\text{Na}$  are moderated using tungsten, W [0 0 1], 1 mm thick single crystal. The moderated positrons are emitted from the surface of W crystal which is positively biased (200V). The extracted positrons are focused to the entry of a solenoid using a symmetrical Einzel lens. The voltages to the three electrodes of the einzel lens are 190, 0 and 190 V, respectively. These positrons are transported through solenoid using magnetic field to the target chamber. Two Helmholtz coils are used to transport the positrons from the exit of solenoid to the sample. The positrons are accelerated to desired energy by applying negative voltage to the target. This beam can provide positrons in the energy range of 200 eV to 50 keV. The beam set up is kept under vacuum of  $10^{-8}$  mbar.

The implantation profile of monoenergetic positrons follows the Makhovian distribution,

$$P(z) = mz^{m-1} \exp[-(z/z_0)^m]/z_0^m \quad (2.1)$$

and the mean implantation depth of monoenergetic positrons of energy  $E$  is given as

$$\langle Z \rangle = \frac{A}{\rho} E^n \quad (2.2)$$

where  $\langle Z \rangle$  is the mean implantation depth (nm) and  $\rho$  is the density of material (g/cc).

The parameters  $A$  and  $n$  are material dependent constants. The parameters  $A$  and  $n$  are usually taken as 40 and 1.6, respectively.

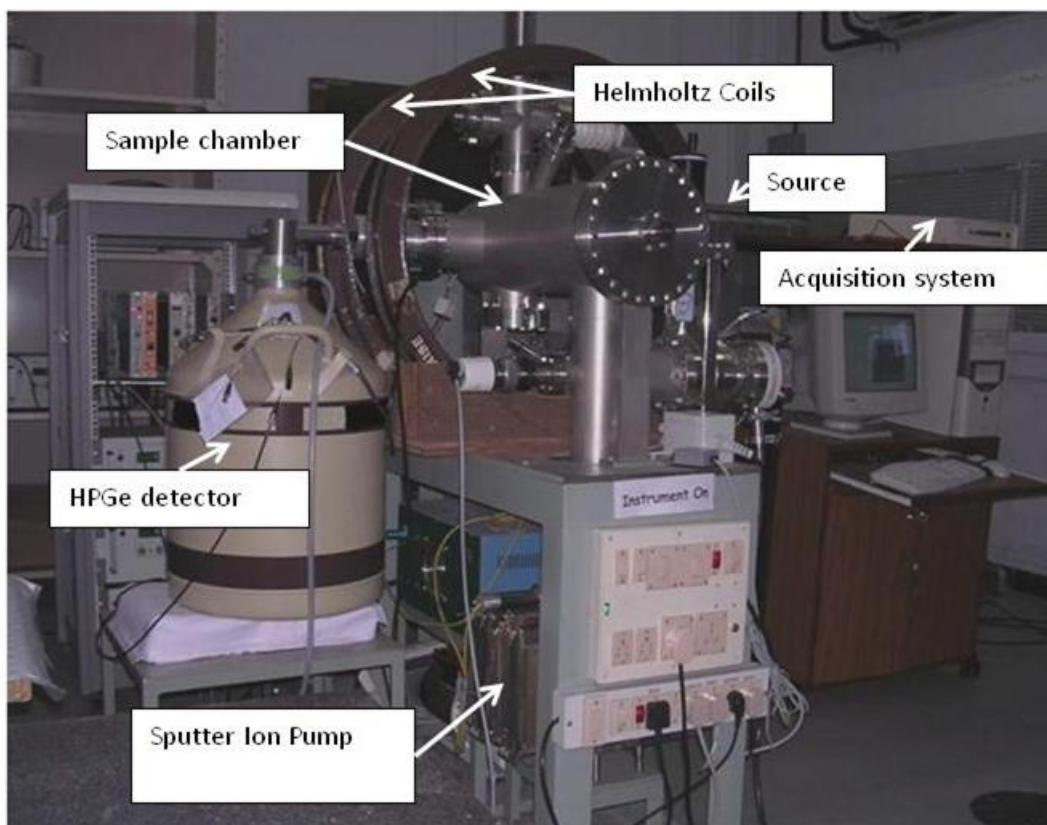


**Figure 2.3:** Slow Positron Beam at Radiochemistry Division, BARC

### 2.1.2. Positron annihilation lifetime spectroscopy

#### 2.1.2.1 Positron lifetime spectrometer

The positron lifetime spectrum in a material is measured as time distribution of events, each event being the time interval between the birth,  $t_1$ , (1275 keV prompt  $\gamma$  ray from  $^{22}\text{Na}$ ) and annihilation,  $t_2$ , of positrons (511 keV  $\gamma$  ray). The time difference between these two processes ( $t = t_1 - t_2$ ) which is equal to the survival time of each positron is measured using a fast-fast coincidence setup. A schematic of the fast-fast coincidence setup is shown in Fig. 2.4. The fast-fast coincident setup employs a pair of scintillation detectors along with photo multiplier tubes (PMT), two constant fraction differential discriminators (CFDD), a time delay unit, a fast coincidence unit and a time-to-amplitude converter (TAC).

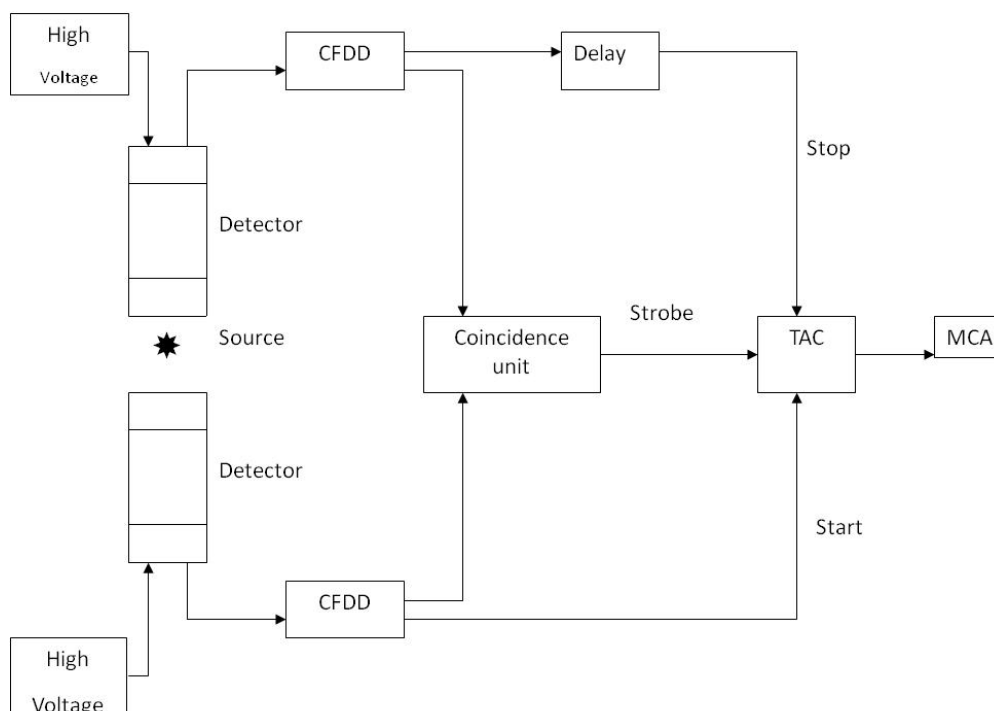


**Figure 2.4:** Block diagram of the positron lifetime spectrometer

The energy and timing information are obtained from the same output of the PMTs using the CFDD. The 1275 keV and 511 keV  $\gamma$ -rays signifying the birth and annihilation of positron, respectively, are picked up by two scintillation detectors. The timing *pick-off* signals are communicated to the TAC through CFDDs and the respective energy signals reach the coincidence unit through the single channel analyzers (SCAs) of CFDD. The coincidence unit checks for the ‘genuineness’ of the events and in the case of true coincident events, the TAC is strobed by the output pulse of coincidence unit to produce a signal which is equivalent to time difference between the detection of 1275 keV and 511 keV  $\gamma$ -rays. The magnitude of this signal is converted to pulse height and recorded in a multi-channel analyzer [Pujari et al., 1992].

The time calibration of the multi channel analyzer was chosen depending on the range of the lifetimes required to be measured. Since most of the work included in the thesis focused on measuring the positron lifetime components ( $< 500$  ps) in nanoparticles



and *o*-Ps lifetime component in polymers, natural or synthetic, (1- 3 ns) , time calibration was chosen 12.5 or 25 ps/channel. The time calibration of the spectrometer was performed from the measured lifetime spectrum of  $^{60}\text{Co}$   $\gamma$ -rays, keeping the discriminator levels of the CFDDs same as required for positron lifetime measurements using a  $^{22}\text{Na}$  source. The delay on the stop detector signal was varied systematically using a nano second delay unit. The centroids of these peaks are plotted as a function of delay time introduced on the stop detector and slope of this line gives the time calibration of the spectrometer. The time calibration can also be calculated by dividing the TAC range (e.g. 50 ns) with number of channels in MCAs (e.g. 2K or 4K).

The  $^{60}\text{Co}$  emits the two gamma rays of 1173 keV and 1332 keV within a time of less than 1 ps. These two gamma rays are assumed to be emitted simultaneously and the peak shape of the lifetime spectrum acquired for these two gamma rays is assumed to be Gaussian. The response function (time resolution) of the spectrometer is obtained by measuring the times difference between these two gamma rays. The lifetime spectrum of  $^{60}\text{Co}$  is shown in Fig. 2.5. The time resolution of the spectrometer is estimated from the width of this peak. The time resolution of present spectrometer was of the order 240 ps with plastic scintillations detectors. For the PALS measurements of natural polymers and AMOC measurements, time resolution was inferior due to wider CFDDs windows.

#### **2.1.2.2 Lifetime data analysis**

The positron lifetime spectrum is a sum of decaying exponentials convoluted with time resolution of the spectrometer. The number of exponentials depends on the positron states in the sample under study.

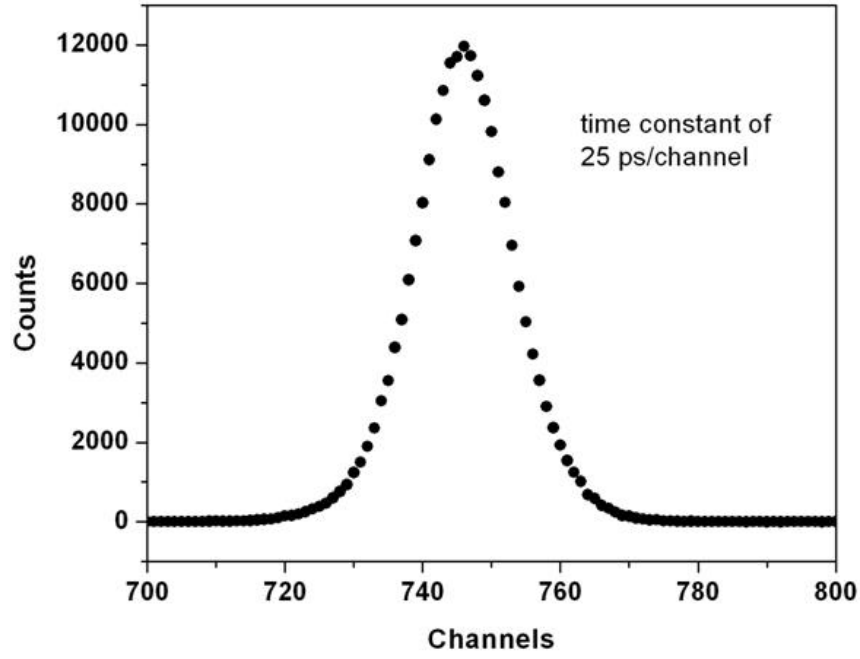


**Figure 2.5:** The lifetime spectrum measured using  $^{60}\text{Co}$   $\gamma$ -rays for obtaining the time resolution of the positron lifetime spectrometer

The routine PATFIT-88 having programs RESOLUTION and POSITRONFIT have been used for the discrete lifetime components analysis [Kirkegaard et al., 1981 and 1989; Kirkegaard and Eldrup, 1972]. The positron lifetime spectrum is given by

$$F(t) = \sum_{i=1}^k \frac{I_i}{\tau_i} e^{-\frac{t}{\tau_i}} \quad (2.3)$$

where  $k$  is the number of exponential decays,  $\tau_i$  is the lifetime of the  $i^{\text{th}}$  component and  $I_i$  is the corresponding intensity. The spectrum is shifted on the time scale by a fixed delay introduced on the stop detector signal to a time  $t_0$  and consequently the time  $t$  in the eq. 2.3 would change to  $(t-t_0)$ . A typical positron lifetime spectrum of silicon sample is shown in Fig. 2.6. The experimentally obtained spectrum is a convoluted spectrum of actual lifetime spectrum defined by eq. 2.3 with the time resolution function of the spectrometer. The time resolution function of the spectrometer is approximated by a sum of Gaussians

or a Gaussian with exponential tails. In general, a single Gaussian distribution,  $G(t)$ , centered at  $t_0$  is used for the deconvolution and solves the purpose,

$$G(t) = \frac{1}{\sigma\sqrt{2\pi}} \exp\left[-\left(\frac{t-t_0}{2\sigma}\right)^2\right] \quad (2.4)$$

The standard deviation  $\sigma$  of the Gaussian distribution is related to its full width at half maximum (FWHM) by

$$FWHM = 2\sqrt{2 \ln 2} \sigma \quad (2.5)$$

The convoluted lifetime spectrum containing  $k$  components is represented as

$$F(t) = \sum_{i=1}^k \frac{I_i}{2} \cdot \exp\left[-\frac{t-t_0 - \frac{\sigma^2}{4\tau_i}}{\tau_i}\right] \left[1 - \operatorname{erf}\left(\frac{1}{2\sigma\tau_i} - \frac{t-t_0}{\sigma}\right)\right] \quad (2.6)$$

The actual spectrum is recorded on discrete channels and it is not a continuous function of time. The whole spectrum has a constant background throughout its time range. The count distribution in lifetime spectrum is integration of the time interval into one fixed channel

$$N(t) = \int_{t-\Delta t}^{t+\Delta t} F(t)dt + B \quad (2.7)$$

where  $N(t)$  is the number of counts in the channel corresponding to time ' $t$ ',  $2\Delta t$  is the channel constant and  $B$  is the constant background. The model POSITRONFIT [Kirkegaard et al., 1989] contains a list of parameters  $\tau_i$ ,  $I_i$ ,  $t_0$ ,  $\sigma$  and  $B$ . The value of  $\sigma$  is taken from the fitted resolution function of  $^{60}\text{Co}$  spectrum or it is determined using the routine RESOLUTION for a reference spectrum like Silicon single crystal having a well defined positron lifetime (218 ps). The background in the above model is taken as the average counts per channel at the far end (no contribution from decaying exponential) of the lifetime spectrum.

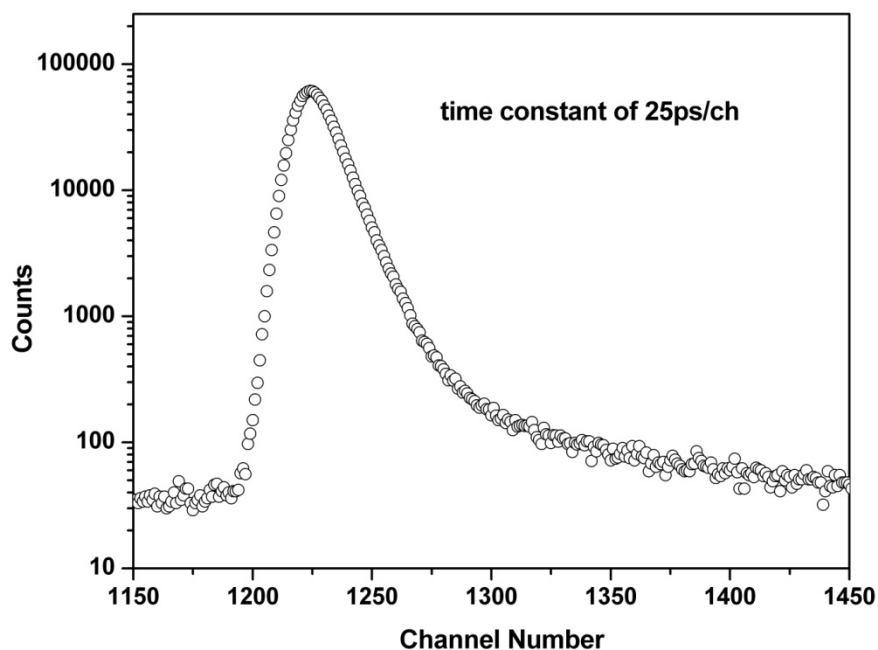


**Figure 2.6:** Positron annihilation lifetime spectrum of Silicon single crystals

### 2.1.2.3 Source correction

In conventional positron studies, positron source (carrier free NaCl solution) is sandwiched between two kapton films and a fraction of positrons is expected to annihilate in these kapton films as well as within the source material itself. The scattering of positrons from the samples also contribute to the fraction of positrons annihilating within the source [Djourellov and Misheva, 1996]. Kapton (7  $\mu\text{m}$  thickness) has one positron lifetime 390 ps with 7 % intensity. The actual fraction of positrons annihilating within the source in different sources used for the study was determined by analyzing the silicon spectrum using the routine RESOLUTION. The resolution function (free parameter in analysis) obtained from Si spectrum analysis was used as fixed input parameter in samples lifetime analysis using POSITRONFIT.

#### 2.1.2.4 CONTIN analysis

It is assumed in routine CONTIN that positron lifetimes follow a distribution over  $\tau$  and the lifetime spectrum may be described by a continuous form as given in eq. 2.8.

$$F(t) = \int_0^{\infty} \frac{I(\tau)}{\tau} \cdot \exp[-t/\tau] \cdot d\tau \quad (2.8)$$

where  $\int I(\tau) d\tau = 1$ . The CONTIN-PALS routine calculates the annihilation rate distribution function,  $\lambda\alpha(\lambda)$ , via Laplace inversion technique [Provencher, 1982; Van Resandt et al., 1982 and Deng et al., 1998] where  $\lambda=1/\tau$ .

The intensities are related to the annihilation rate distribution function as

$$I(\tau) = \lambda^2 \alpha(\lambda) \quad (2.9)$$

A reference spectrum e.g. Si is used for the deconvolution of experimental resolution in this procedure. The fixed inputs parameters for CONTIN analysis are annihilation rates and fractions in the source as well as in reference Si [Gregory, 1991a and 1991b; Gregory and Zhu, 1990]. A typical distribution over annihilation rate obtained from CONTIN analysis is shown in Fig. 2.7. The distribution over annihilation rate or lifetime can be translated to radius or volume distribution through the Tao-Eldrup equation.

#### 2.1.3. Doppler broadening of annihilation radiation

##### 2.1.3.1 Doppler broadening spectrometer

A typical block diagram of Doppler broadening spectrometer is shown in Fig. 2.8. High purity Ge (HPGe) detectors have best energy resolution and are employed for Doppler broadening measurements. It is to be noted that broadening in 511 keV annihilation peak is of the same order as of energy resolution of HPGe.

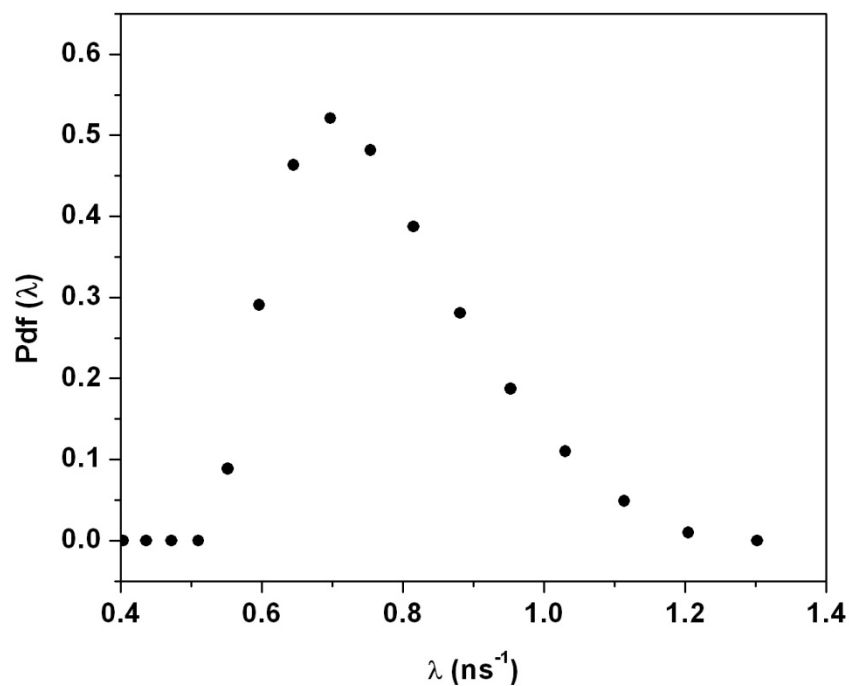


**Figure 2.7:** *o*-Ps positronium annihilation rate distribution obtained from CONTIN analysis of the lifetime spectrum from a polymer sample.

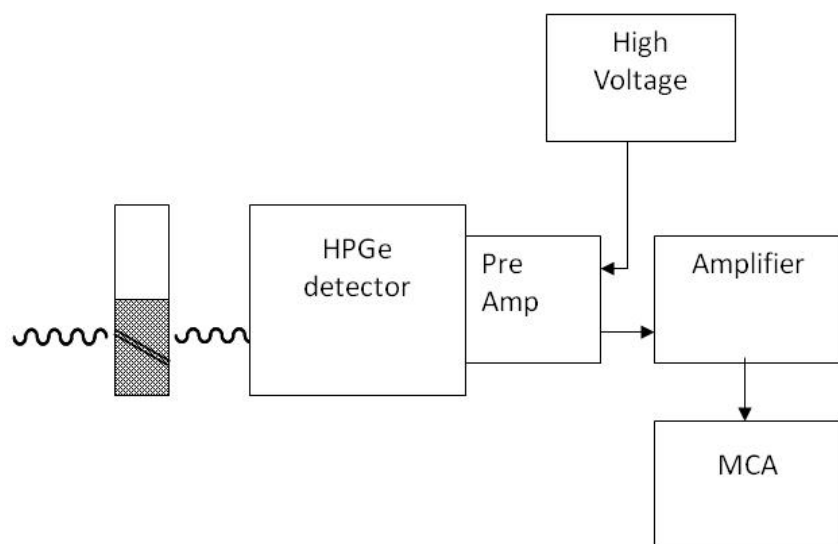


**Figure 2.8:** The block diagram of the Doppler broadening spectrometer

The signal is passed through preamplifier followed by spectroscopy amplifier and recorded in multichannel analyzer (MCA). The used MCA was energy calibrated using the standard multi gamma ray sources of  $^{152}\text{Eu}$  and  $^{133}\text{Ba}$ . The energy resolution of the detection system was 2.1 keV at 1332 keV and 1.1 keV around 511 keV. A typical Doppler broadened annihilation  $\gamma$ -ray spectrum from silicon sample is shown in Fig. 2.9. The gamma ray spectrum of 514 keV from  $^{85}\text{Sr}$  source which is not Doppler broadened is also shown in Fig. 2.9. The energy spectrum of 514 keV placed at the centroid of the annihilation photo peak (511 keV) shows the broadening due to detector resolution.

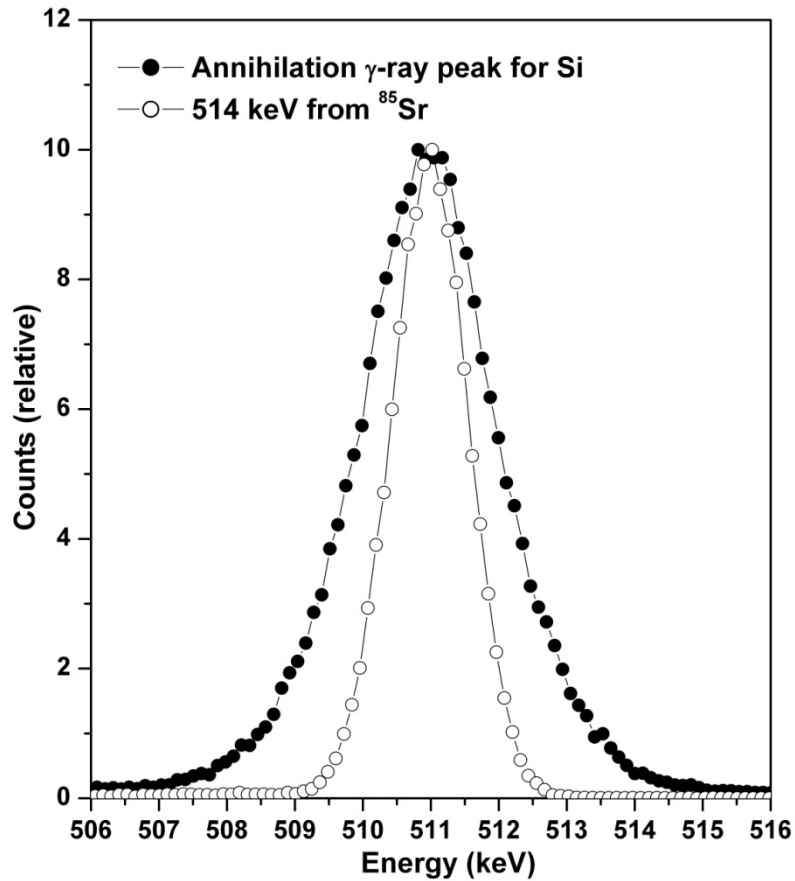


**Figure 2.9:** Typical Doppler broadened annihilation radiation spectrum for Si. The 514 keV  $\gamma$ -ray spectrum from  $^{85}\text{Sr}$  is shown after displacing its centroid to 511 keV on the energy axis for visualizing the broadening due to detector resolution.

### 2.1.3.2 Data analysis

The Doppler broadened spectrum is a convoluted spectrum of Doppler broadened annihilation photon spectrum with the detector resolution (a Gaussian distribution). In the present work, the deconvolution of the detector resolution function was not performed. The spectrum is analyzed in terms of *line shape* and *wing* parameters. The line shape parameter  $S$  and wing parameter  $W$  were evaluated from the measured spectra using the program SP version 1.0 [SP-1] [Dryzek, SP 1.0; Dryzek and Quarles, 1996]. The apparent background on left of 511 keV is more compared to right, partly because of incomplete charge collection and scattering in the sample. Additional background contribution comes from the Compton scattering of 1275 keV gamma ray.

In this program, the background is taken as a step function. The line shape parameter  $S$  is defined as the ratio of the central area ( $A_s$ ) to the total area under the spectrum ( $A_t$ ) as

$$S = \frac{A_s}{A_t} = \frac{\int_{511-\Delta E}^{511+\Delta E} N(E)dE}{\int_{-\infty}^{+\infty} N(E)dE} \quad (2.10)$$

where  $N(E)$  represents the counts in the spectrum at energy  $E$ . The  $W$  parameter is defined as the fractional area in the wing region of the Doppler broadened spectrum and it is a signature of the annihilations with core electrons of the surrounding medium. It is defined as

$$W = \frac{A_w}{A_t} = \frac{\int_{511-E_1}^{511-E_2} N(E)dE + \int_{511+E_2}^{511+E_1} N(E)dE}{\int_{-\infty}^{+\infty} N(E)dE} \quad (2.11)$$



The values of  $\Delta E$ ,  $E_1$  and  $E_2$  for evaluating  $S$  and  $W$  parameters were chosen in such a way that the value of  $S$  parameter is in the range of 0.50 and the value of  $W$  is in the range of  $10^{-2}$  [Campbell, 1977]. A schematic representation of evaluating the line shape parameters in the Doppler broadening spectroscopy is shown in Fig. 2.10.

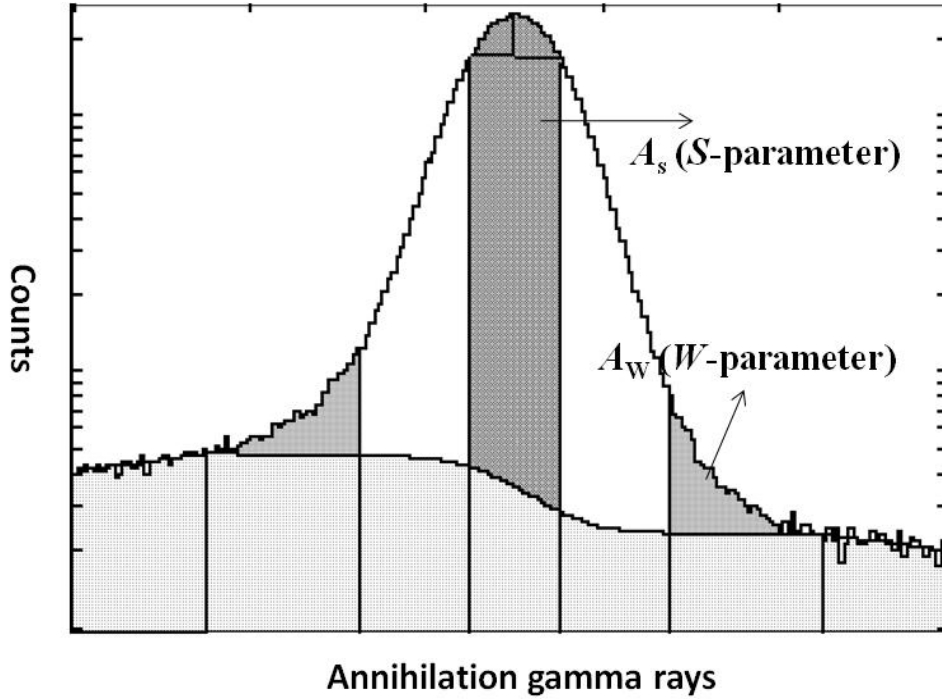


**Figure 2.10:** Schematic representation of evaluation of Doppler broadening parameters from DBAR spectrum

#### 2.1.4. Coincidence Doppler broadening measurements

In one detector Doppler broadening measurements, signal to noise ( $S/N$ ) ratio is in the order of  $10^2$ . The tail part of the photo peak where core electrons mainly contribute is buried under the background and reliable  $W$  parameter cannot be evaluated. In two detectors Doppler broadening measurements both annihilation gamma rays (of energies  $E_{\gamma 1}$  and  $E_{\gamma 2}$ ) are measured in coincidence using two HPGe detectors placed at  $180^\circ$ .

The sum of these annihilation gamma energies,  $E_s = E_{\gamma 1} + E_{\gamma 2}$ , and their difference,  $E_d = E_{\gamma 1} - E_{\gamma 2}$ , are usually recorded. Assuming that the kinetic energy of the thermalized

positron is negligible and  $E_B$  is the binding energy of the annihilating electron, the energy difference between the two annihilation gamma photons can be written as

$$\begin{aligned} E_d &= E_{\gamma 1} - E_{\gamma 2} \\ &= m_0 c^2 - \frac{1}{2}(E_B \pm cP_L) - (m_0 c^2 - \frac{1}{2}(E_B \mp cP_L)) \\ &= \pm cP_L \end{aligned} \quad (2.12)$$

where  $c$  is the velocity of light,  $m_0$  is the rest mass of electron and  $P_L$  is the momentum component of electron-positron pair in the direction of the detectors. During the measurement using single detector Doppler broadening, the spread in the annihilation energy,  $\Delta E$ , would be half of the CDB measurements i.e.  $\Delta E = \pm cP_L/2$ . The resolution of the coincidence set up is also better than the single detector Doppler broadening measurements. Assuming the energy resolution of the two detectors used in CDB set up to be  $\sigma_1$  and  $\sigma_2$  respectively, the resolution of the energy difference spectrum would be  $\sqrt{\sigma_1^2 + \sigma_2^2}$ . If two identical detectors are used in the measurement ( $\sigma_1 = \sigma_2 = \sigma$ ), the relative resolutions of CDB and single detector Doppler broadening would be  $\sqrt{2}\sigma/cP_L$  and  $2\sigma/cP_L$ , respectively. Thus the resolution improves by a factor of  $\sqrt{2}$  in CDB measurements. The sum of the energies of two annihilation gamma rays is given by

$$\begin{aligned} E_s &= E_{\gamma 1} + E_{\gamma 2} \\ &= m_0 c^2 - \frac{1}{2}(E_B \pm cP_L) + (m_0 c^2 - \frac{1}{2}(E_B \mp cP_L)) \\ &= 2m_0 c^2 - E_B \end{aligned} \quad (2.13)$$

The difference spectrum is taken with a gate on sum of the energies  $E_s$ . By measuring two annihilation photons in coincidence, the background in the high momentum region, where annihilation with core electrons mainly contributes is reduced. Typically, a peak to back ground ratio of  $10^5$ -  $10^6$  enabling extraction of information about the core electrons momentum is obtained. Since core electrons do not participate in chemical bonding, they are element specific. Therefore, the chemical surrounding of the

annihilation site or elemental specificity is obtained from the shape and magnitude of the high momentum core component which carries the signature of the atom. The intensity of momentum distribution curve extends over a few orders of magnitude. Hence, the ratio of momentum distribution curve of the sample with a reference material like Si is taken to magnify the changes in the momentum distribution curve and they are referred to as ratio curves.

Figure 2.11 shows the set up for the CDB measurements. Two HPGe detectors having 30% efficiency and  $\sim 1.1$  keV resolutions at 514 keV ( $^{85}\text{Sr}$ ) are used for the coincidence measurement of annihilation photons from the same event. The energy signals from the detectors are passed through the spectroscopy amplifiers and recorded using a Computer Automated Measurement and Control (CAMAC). The ‘genuineness’ for these signals to be in coincidence is checked using the circuit which produces a gate for the recording of energy signal. For this, timing signals from two detectors are amplified using Timing Filter Amplifier (TFA), passed through Constant Fractional Discriminator (CFD) to record the timing for 511 keV signals. The coincidence signal between the two detectors is used as master gate to trigger the multi parameter data acquisition system. The 511 keV signals from spectroscopy amplifiers which come within the master gate are recorded as true coincidence event and recorded in two 4k MCAs with energy dispersion of 140 eV/ch.

From these coincident events a two dimension spectrum  $E_1 + E_2$  vs  $E_1 - E_2$  is generated over  $(2k \times 2k)$  channels, a typical spectrum of which is shown in Fig. 2.12. To generate this spectrum, two pseudo parameter equivalents to ‘difference’ and ‘sum’ of individual spectrum is used. As the difference  $(E_1 - E_2)$  can be negative, the difference spectrum is shifted by 1024 channels to have the coincidence events in the centre of 2-D spectrum. To obtain the annihilating electron momentum distribution, coincidence events

are selected in the range of  $2m_0c^2 - 2.4 \text{ keV} < E_s < 2m_0c^2 + 2.4 \text{ keV}$  which resulted in the peak to background ratio equal to  $> 10^5$ . A comparison of peak normalized spectra acquired using single detector and two detectors are shown in Fig. 2.13. It clearly shows that signal to background ratio is greatly improved in the wing region in CDB spectrum.

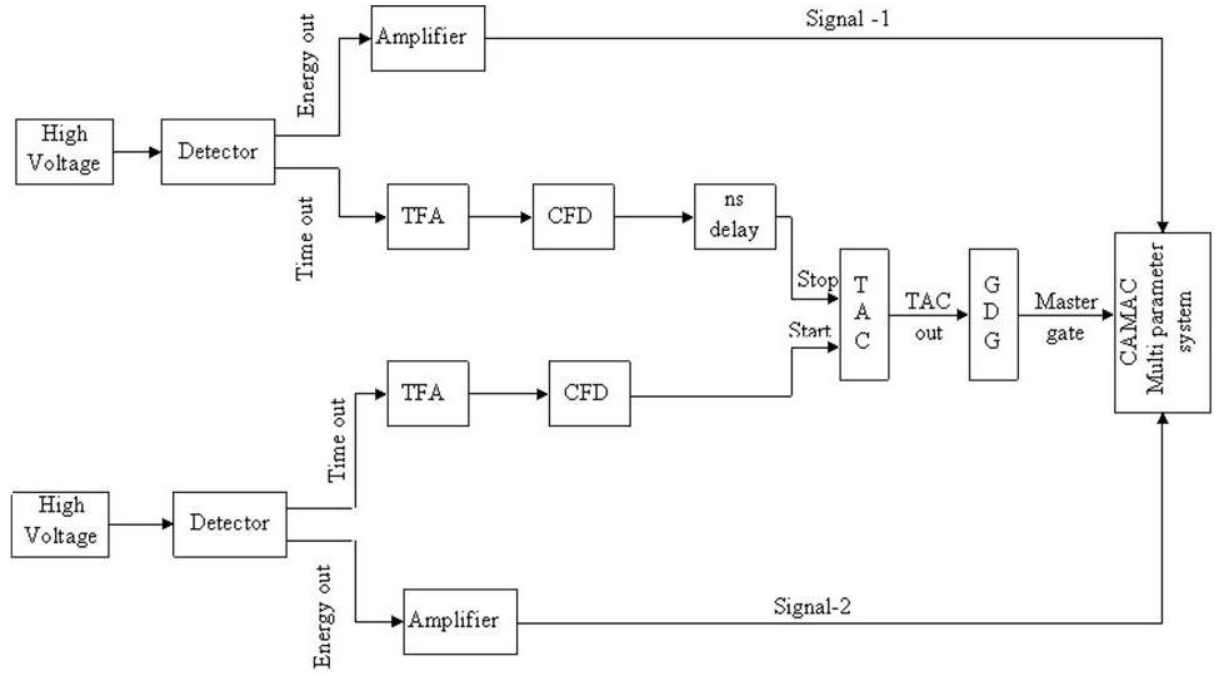


**Fig. 2.11** The block diagram for the used CDB set up.

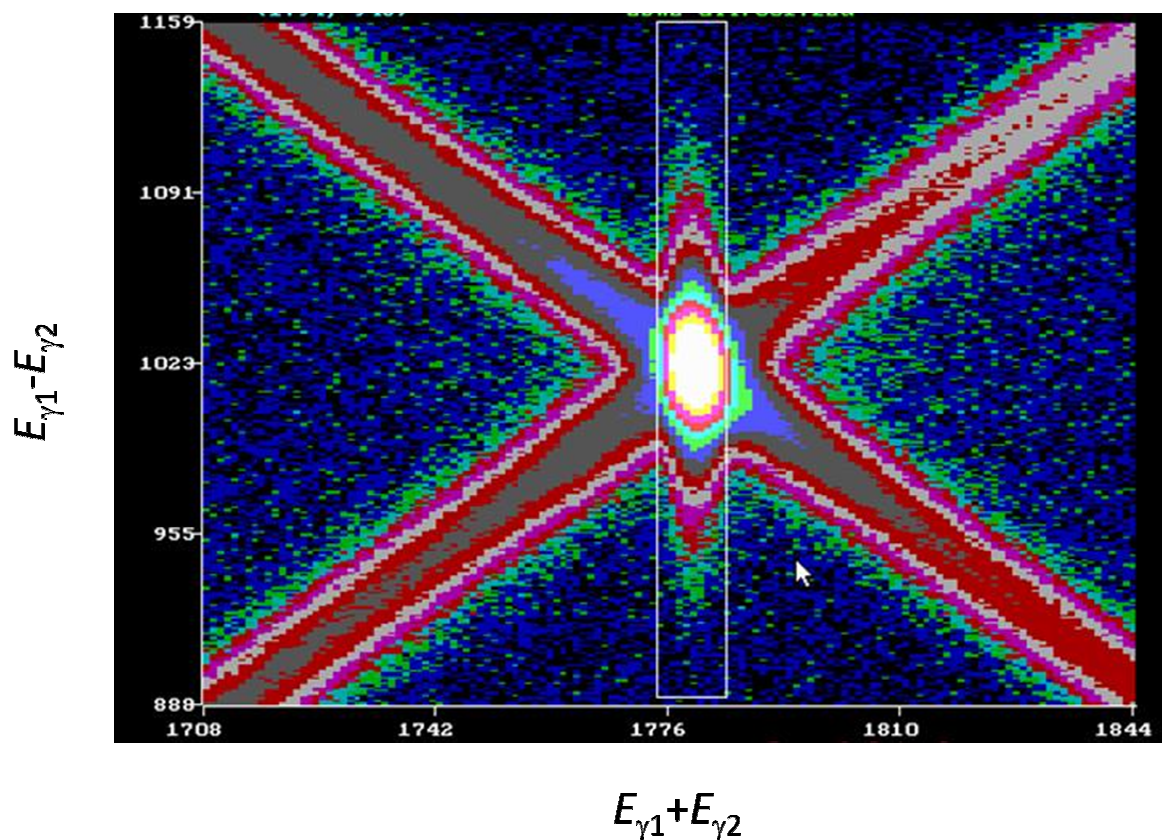


**Figure 2.12:** The sum and difference spectra of the energy signals measured using CDB. The difference is plotted by shifting the origin to 1024 channels.

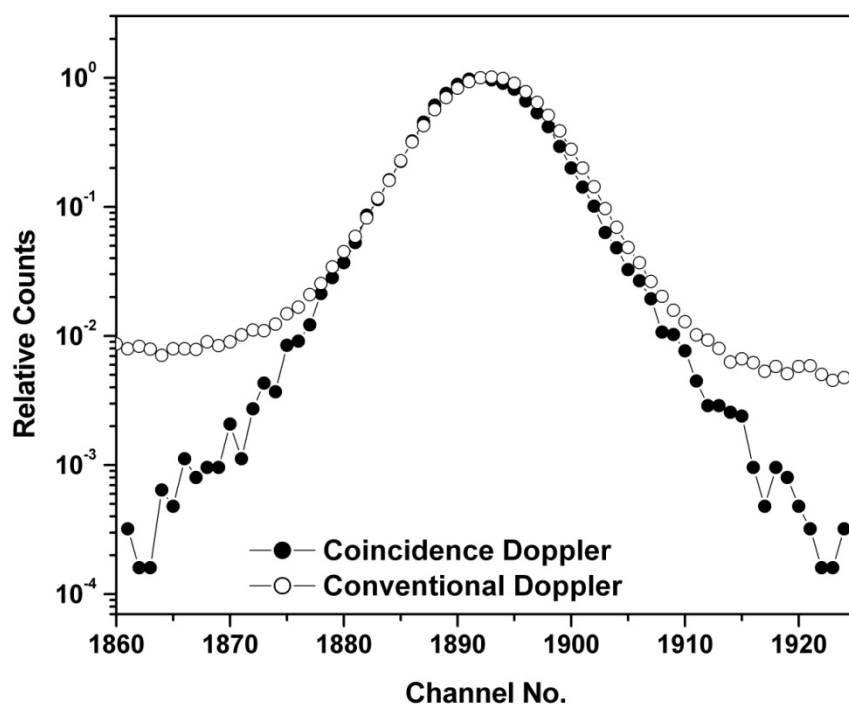


**Figure 2.13:** The CDB and conventional Doppler spectra from a typical sample

#### 2.1.4.1 Data Analysis

For energy calibrations of MCAs a multi gamma reference of  $^{152}\text{Eu}$  source is used. From eq. 2.12, the energy difference between the annihilation gamma rays can be expressed as

$$\begin{aligned} E_d &= \pm cP_L \\ \frac{E_d}{m_0c^2} &= \frac{cP_L}{m_0c^2} \Rightarrow \frac{E_d}{511} = \frac{P_L}{m_0c} \\ \Rightarrow 1 \text{ keV of } E_d &= 1.96 \times 10^{-3} m_0c \text{ of } P_L \end{aligned} \quad (2.14)$$

The momentum distribution curves are represented in momentum units. For this, the difference in the energies can be converted to the momentum units using eq. 2.14. For comparison of CDB spectra from different samples, the spectra are normalized to unit area and the  $S$  and  $W$  parameters are evaluated. To magnify the differences in normalized momentum distribution curves, ratio of CDB spectrum of the sample with respect to a chosen reference spectrum like Si is plotted.

#### 2.1.5. Depth dependent measurements using slow positron beam

The slow positron beam (Fig. 2.3) at Radiochemistry Division, BARC, has been used for the depth dependent Doppler broadening measurements in polymer films. Monoenergetic positrons are implanted on the sample which is negatively biased at desired potential to vary the energy of implanted positrons. The positrons implantation follows the Makhovian distribution (eq. 2.1) in the sample. Positrons are diffused in the sample prior to annihilation either via positronium formation or free positron modes. The average distance of positron diffusion in a material is termed as positron diffusion length,  $L_+$ . To evaluate the positron diffusion length in a sample, Doppler broadening measurements as a function of depth are carried out in the sample. These measurements provide information about the pore (free volume) size, pores interconnectivity as well as

pores connectivity to the surface as a function of depth. An HPGe detector having 30% efficiency and 2.1 keV resolution at 1332 keV ( $^{60}\text{Co}$ ) placed at  $90^\circ$  to the target position and coupled to a 4k MCA is used for the measurements. The voltage applied to the target is varied and Doppler spectra at different positron energy (implantation depth) are recorded. The line shape  $S$ -parameter is evaluated as a function of positron energy. The  $S$ -parameter as a function of positron energy is termed as  $S$ - $E$  profiles of the sample. Other important parameter i.e. ratio of  $3\gamma/2\gamma$  annihilation is evaluated as a function of depth from the annihilation gamma spectrum. For evaluation of  $3\gamma/2\gamma$ , the ratio of integrated counts in the range 375 to 460 keV to total area under the photo peak of 511 keV is calculated. The variation of  $3\gamma/2\gamma$  with positron energy gives information about the reemission of implanted positron from different depths. These profiles can also be used for the evaluation of the positron diffusion length in the studied sample.

### 2.1.5.1 Variable Energy Positron Fit (VEPFIT) analysis

The obtained ( $S$ - $E$  or  $3\gamma/2\gamma$ - $E$ ) profiles from the depth dependent Doppler broadening measurements are fitted using the routine VEPFIT [van Veen et al., 1990]. This involves solving of positron diffusion equation (eq. 2.15) taking into account the positron diffusion, trapping and annihilation in the medium.

$$D^+ \frac{d^2 c(z)}{dz^2} - \frac{d}{dz} (v_d c(z)) + I(z) - \kappa_t n_t c(z) - \lambda_b c(z) = 0 \quad (2.15)$$

where,  $c(z)$  is the time averaged positron density at a certain depth  $z$  below the solid surface,  $v_d$  is the drift velocity of positrons,  $I(z)$  is the positron stopping rate at depth  $z$ ,  $n_t$  is defect density,  $\kappa_t$  is rate constant for positron trapping at defects,  $\lambda_b$  is the bulk annihilation rate and  $D^+$  is positron diffusion coefficient. The drift velocity,  $v_d = \mu E$ , is the function of electric field  $E$  present in the sample and mobility  $\mu$  of positron in the sample. The fast non-iterative calculation scheme is used to solve the diffusion equation to

calculate the time averaged positron density in the medium. The average positron density is then used to extract diffusion length and the fraction of positrons annihilating at various depths taking into account the various boundary conditions for the diffusing positrons. The VEPFIT analysis provides different models for fitting the data under different scenarios. The model mainly used for fitting the (S-E or  $3\gamma/2\gamma$ -E) profiles in polymers considers multi layers (maximum 5) with different bulk  $S$ -parameter as well as diffusion lengths. In the present study, only single layer fitting has been carried out. The input parameters to fit a (S-E) profile are  $S$ -parameter at the surface,  $S$ -parameters and diffusion lengths corresponding to layers, boundaries of different layers and the densities of the layers. With these input parameters, an S-E profile is fitted using VEPFIT to evaluate the diffusion lengths and  $S$ -parameters corresponding to bulk of different layers. For the fitting of ( $3\gamma/2\gamma$ -E) profile, the input  $S$ -parameters for surface as well as for the bulk of the layers are replaced by corresponding  $3\gamma/2\gamma$  fraction,  $f$ , keeping other parameters unchanged. In most of the polymers, diffusion length is in the order of few nanometers due to presence of free volume nanoholes which act as trap for positron and positronium.

## 2.2. Theoretical Calculations

Positron lifetimes and annihilation electron momentum distribution in bulk solids and in the presence of defects have been calculated using computer program “Doppler: A program to model positron states and annihilation in solids” (in short MIKA DOPPLER) developed by Laboratory of Physics, Helsinki University of technology. This program is used for the calculations in periodic lattice. A brief description of the theory involved in the calculations is described.



### 2.2.1 Positron lifetime

The positron annihilation rate, inverse of positron lifetime, is proportional to the electronic density at the positron in a lattice and can be calculated from the overlap integral as

$$\lambda = \frac{1}{\tau} = \pi r_0^2 c \int dr n_+(r) n_-(r) g(0; n_+, n_-) \quad (2.16)$$

where  $r_0$  is the classical electron radius,  $c$  is the speed of light,  $n_+$  and  $n_-$  are the positron and electron densities and  $g(0; n_+, n_-)$  is the electron-positron pair correlation functional evaluated at the positron in the solid [Saarinen et al., 1997]. To solve the eq. (2.16), positron and electron densities and, electron-positron pair correlation function are required. The electron and positron densities are calculated using two-component generalization of the density functional theory (TCDFT)

$$E[n_+, n_-] = F[n_-] + F[n_+] + \int dr V_{ext}(r) [n_-(r) - n_+(r)] - \int dr \int dr' \frac{n_-(r) n_+(r')}{|r - r'|} + E_c^{e-p}[n_+, n_-]$$

with

$$F[n] = T[n] + \frac{1}{2} \int dr \int dr' \frac{n(r) n(r')}{|r - r'|} + E_{xc}[n] \quad (2.17)$$

Where  $E[n_+, n_-]$  is the total electron-positron functional for electron positron system under the external potential,  $V_{ext}$ ,  $F[n]$  is the one component functional for electron/positron [Puska et al., 1994],  $T[n]$  is the kinetic energy functional for noninteracting positron and electrons,  $E_{xc}$  is the exchange correlation potential and  $E_c^{e-p}[n_+, n_-]$  is the positron-electron correlation energy functional. To obtain the ground state positron and electron densities, generalized Kohn-Sham variation method is used. The one-particle Schrödinger equations for positrons and electrons wavefunctions are required for this.

The equation for positron is as follows

$$-\frac{1}{2}\nabla^2\psi_i^+(r)+V_{eff}(r)\psi_i^+=\varepsilon_i\psi_i^+(r) \quad (2.18)$$

with effective potential as

$$V_{eff}(r)=\phi(r)+\frac{\delta E_{xc}[n_+]}{\delta n_+(r)}+\frac{\delta E_c^{e-p}[n_+,n_-]}{\delta n_+(r)} \quad (2.19)$$

$$\phi(r)=\int dr' \frac{-n_-(r')+n_+(r')+n_0(r')}{|r-r'|} \quad (2.20)$$

Where  $\Phi(r)$  is the total Coulomb potential and  $n_0$  is the charge density from which the external potential  $V_{ext}$  arises. For electron, the effective potential is the same as of electron with  $n_-$  and  $n_+$  swapped and the sign of Coulomb potential reversed. The positron and electron densities using corresponding wavefunctions are written as

$$n_-(r)=\sum_{\varepsilon_i\leq\varepsilon_f}|\psi_i(r)|^2, n_+(r)=\sum_i^{N_+}|\psi_i^+(r)|^2 \quad (2.21)$$

The summation on electron states is taken up to Fermi level but for positron only one state is considered in the calculation. The Kohn-Sham equations are solved consistently using iterative scheme simultaneously for both positron and electron.

The terms  $E_{xc}$  and  $E_c^{e-p}[n_+,n_-]$  in eq. (2.19) are unknown. To evaluate these two terms, approximations are called and the results may depend heavily on the approximations used for the solutions. The usual way to calculate the  $E_{xc}$  is using Local Density Approximation (LDA) [Dreizler et al., 1990]. Using LDA,  $E_{xc}$  is written as

$$E_{xc}^{LDA}[n]=\int dr n(r)\varepsilon_{xc}^{hom}(n(r)) \quad (2.22)$$

In this way, the exchange correlation,  $E_{xc}$ , is approximated by exchange-correlation energy of the homogenous electron gas  $\varepsilon_{xc}^{hom}$  per electron with the replacement of the constant density  $n_0$  by the local density  $n(r)$  of the inhomogeneous system, known from quantum Monte Carlo simulations. LDA does not consider the inhomogeneous feature of

the electron gas. To take care of the inhomogeneous nature, Generalized Gradient Approximation (GGA) which takes into account the gradient of electron density in the system is used for the calculations [Barbiellini et al., 1995].

The electron-positron correlation energy is calculated on the limit of the vanishing positron density. For computation, the simplification for the above mentioned method is required and an approximation called ‘Conventional Scheme’ (CONV) is used [Puska et al., 1994]. For this, the electron density is calculated in the absence of positron in the system. This is justified in the case of a perfect lattice where positron is delocalized and positron density everywhere in the system is negligibly small. In such case, the positron density and electron part of positron-electron correlation can be omitted from the above mentioned equations. Whenever defects are present in the lattice, positrons get trapped in the defects and positron density can be quite high in these defects, which affects the electron density distribution in the system. Nevertheless, positron parameters calculated using CONV match well with the TCDFT and experimental values. This is mainly because the enhancement factor  $g$  decreases with increasing of both positron as well as electron densities, thus countering the large positron and electron overlap.

The parameter,  $g(0, n_-, n_+)$ , positron-electron pair correlation function under zero positron density limit is denoted by  $\gamma$  and called enhancement factor of the electron density at positron. The most trivial form is simply  $\gamma = 1$  and called ‘Independent Particle Model’ (IPM) but it is not the perfect form to be used. In the calculations using program, different expression for  $\gamma$  can be selected for either LDA or GGA calculations [Ranki 1999].

For conventional scheme, within LDA, Lantto, Boronski and Nieminen have suggested the following form [Boronski and Nieminen, 1986]

$$g_{LDA-BN} = 1 + 1.23r_s + 0.8295r_s^{3/2} - 1.26r_s^2 + 0.3286r_s^{5/2} + \frac{1}{6}r_s^3 \quad (2.23)$$

where  $r_s$  is calculated from electron density as

$$r_s = \sqrt[3]{\frac{3}{4\pi n_-}} \quad (2.24)$$

Another two forms of enhancement factor is given by Arponen, Pajanne (1979) and Barbiellini (1995) as

$$g_{LDA-AP1} = 1 + 1.23r_s - 0.0742r_s^2 + \frac{1}{6}r_s^3 \quad (2.25)$$

$$g_{LDA-AP2} = 1 + 1.23r_s - 0.91657r_s^{3/2} + 1.0564r_s^2 - 0.3455r_s^{5/2} + \frac{1}{6}r_s^3 \quad (2.26)$$

Any of these forms can be chosen for the calculation using the appropriate input parameters in the input file for the calculations.

In GGA [Barbiellini et al., 1995], the variation in electron density is given as

$$\varepsilon = \frac{|\nabla n_-|^2}{(n_- qTF)^2} \quad (2.27)$$

where  $qTF$  being the total Thomas-Fermi screening length

$$qTF = \left(\frac{4}{\pi}(3\pi^2 n_-)^{\frac{1}{3}}\right)^{\frac{1}{2}} \quad (2.28)$$

The corrected enhancement factor is then

$$g_{GGA} = 1 + (g_{LDA} - 1)e^{-\alpha\varepsilon} \quad (2.29)$$

where  $\alpha$  is an empirical parameter and the value which provides lifetime in agreement with most of the solid is 0.22.

It is to be noted that further simplifications in the calculation can be achieved by calculating the electron density and the Coulomb potential non-self consistently by Atomic Super Position Method (ATSUP). This means superimposing free-atom densities

and potentials. This method is very simple even in case of complex systems [Puska, 1997].

### 2.2.2 Electron momentum distribution

The momentum distribution are calculated separately for each electron state described by  $\psi_j$  according to following equation

$$\rho_j(P) = \pi r_e^2 c u_j^2(0) \left| \int dr e^{-ip \cdot r} \psi_+(r) \psi_j(r) \right|^2 \quad (2.30)$$

where  $r_e$  is the classical radius for electron and  $\psi_+$  is the positron wave function [Alatalo et al., 1996]. The term  $u_j^2$  is called the state dependent enhancement factor and it is a constant related to annihilation rate of the  $j^{\text{th}}$  state as

$$u_j^2 = \frac{\lambda_j}{\lambda_j^{\text{IPM}}} \quad (2.31)$$

In this equation, the annihilation rate is calculated with in LDA or GGA through

$$\lambda_j = \pi r_0^2 c \int dr \gamma^{\text{LDA,GGA}}(r) |\psi_+(r)|^2 |\psi_j(r)|^2 \quad (2.32)$$

where  $\gamma$  is the corresponding enhancement factor. The  $\lambda^{\text{IPM}}$  is the annihilation rate with  $\gamma = 1$  i.e. using IPM model. The final momentum distribution is then obtained by summing  $\rho_j(p)$  in eq. (2.30) over all electron states. The positron wave function used in this equation is a parameterized wave function given as

$$|\psi_+\rangle \approx a_0 + a_1 \left( \text{erf} \left( \frac{r}{a_2} \right) \right)^{a_3} = a_0 + a_1 \left( \frac{1}{\sqrt{2\pi}} \int_{-\infty}^r e^{-\left( \frac{r}{\sqrt{2}a_2} \right)^2} dr \right)^{a_3} \quad (2.33)$$

where  $r$  is the distance from the centre of the atomic sphere and  $a_i$  are the fitted parameters,  $i \in \{0, \dots, 3\}$ . The parameters have been calculated using LMTO-ASO method.

In the presence of defects, the lattice undergoes relaxation either inward or outward depending on the forces acting on the atoms. The relaxation of the atoms in the

vicinity of defects is predominant. To mimic the experimental condition more precisely, relaxed coordinates of the atoms are used for the positron lifetime and electron momentum distribution calculations. The formation energy calculations of the defects are also calculated to supplement the positron annihilation results. In the present studies, Vienna *ab-initio* simulation package (VASP) has been employed to calculate the relaxed coordinates and formation energy of defects in gold lattice. The details of the calculations are given in Chapter VI

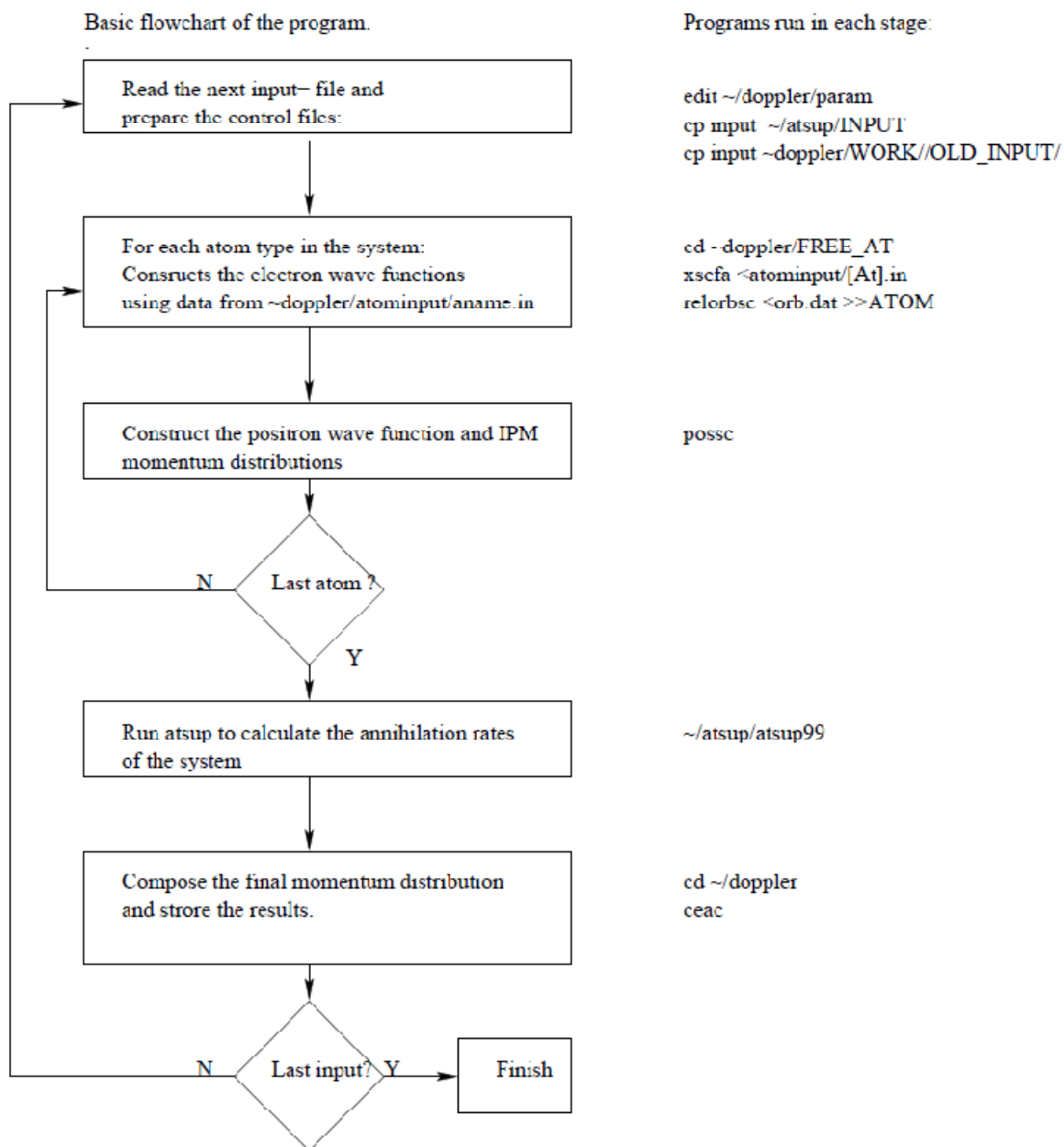
### **2.2.3 Execution of calculations using MIKA DOPPLER**

The program uses efficiently ‘Rayleigh Quotient Multigrid (RQMG)’ method programmed by MIKA Heiskanen for solving the Schrödinger equations [Heiskanen et al., 1999 and 2001]. The idea behind multigrid method is that the discretized eigenvalue problem is first solved iteratively on fine grids and then moving to coarser grids. The reason for this is that when using local discretization the equation can be locally satisfied at the discretization points but the errors may not be reduced on bigger scale. This problem is overcome using multiple grids.

The software requires a UNIX environment and is usable in any platform equipped with Fortran90 compiler. The program is compiled using the script ‘compile\_doppler’ in the MIKA/directory. The main requirement for a calculation is the input file which contains all the required information about the calculation. The main input parameters are the number of atoms in the lattice, type of atoms in the lattice, lattice constant and the relative position of the atoms in the lattice. The point defects in the lattice are created by removing the atoms from the lattice positions. The input file provides options to consider the approximations like LDA or GGA as well as the solver like RQMG or CG solver for the calculations. The expression for the enhancement factor

$\gamma$  can also be chosen from the input file. The details of all the input parameters are provided in the manual of MIKA DOPPLER package. To calculate the electron momentum distribution a parameterized positron wave function (eq 2.33) is used. The values of parameters for different atoms are listed in `~/doppler/atominputs/pospara`. The string in the file having the appropriate parameters are selected by writing the atomic number in the beginning of the string and keeping the value 99 in the beginning of all other strings for the same atom.

The main outputs of calculations are positron lifetime, momentum distribution (total as well as orbital), positron density, positron binding energy and potential felt by positron. The electron momentum distribution are plotted in the form of ratio curves for that the electron momentum distribution for the lattice under study is divided by the momentum distribution of a reference material. To compare with experimentally obtained ratio curves from CDB measurements, the calculated electron momentum distributions of sample and reference are convoluted with combined resolution of the detectors before taking the ratio. The positron density and potential felt by positron in a particular plane can be obtained using the appropriate input parameters defining the desired plane. For example, the input parameter '*nwave*' (-1, -1, -2) defines a plane [0 0 1] for the calculations of positron density and potential felt by positrons. The positron density and potential felt by positron in a particular plane clearly show the positron states either delocalized or trapped in the plane. The basic flow chart of the program is shown by scheme 2.1.



**Scheme 2.1:** The basic flow chart of the program “MIKA DOPPLER” for the calculations



## **CHAPTER-III**

---

# **NANOSTRUCTURE AND GLASS TRANSITION BEHAVIOUR OF STARCH/SUCROSE MATRICES**

Natural polymers are of utmost importance in a number of fields (e.g., food and packaging industries, pharmaceuticals) in which they are increasingly being used. Literature provides one with a large wealth of data accumulated in the last decades on their physical properties [Ferry, 1980; Farhat et al., 2003 and Valles Pamies et al., 2000]. Much attention has not been given to their nanostructures in terms of free volume nanoholes and its effects on the physical properties of these polymers. Study of the nanostructures of these matrices appears also quite promising towards a better understanding of the origins of their macroscopic properties. Determining glass transition temperature,  $T_g$ , in such natural polymers like starch or starch based products is very important, particularly in the context of food storage [Mizuno et al., 1998 and Levine and Slade, 1993]. One way to improve our knowledge on the process of glass transition refers to the use of plasticizers, such as water or polyols (sucrose), whose effect is to reduce greatly  $T_g$  [Mizuno et al., 1998 and Poirier-Brulez et al., 2006]. One of the issues of working with these polymers lies in their sensitivity to both temperature and relative humidity. Besides, as many natural polymers undergo decomposition before reaching their  $T_g$ , measuring  $T_g$  through positron annihilation lifetime spectroscopy (PALS) may become cumbersome.

Recently, a study has been reported with the initial aim to study the nanostructure as a function of temperature and determining the glass transition temperature,  $T_g$ , of pure starch using PALS [Roudaut et al., 2009]. In this study, it was discovered that nanostructure of starch changes due to decomposition of the starch matrices and this would hamper the quest of measuring the  $T_g$ , by inducing a pronounced decrease in both  $\tau_3$  and  $I_3$  before reaching the  $T_g$ .  $\tau_3$  was found to increase linearly with  $T$  up to the region of decomposition, without any sign of enhancement in the gradient and the data merely indicated that  $T_g$  should lie above about 501 K, in qualitative agreement with previous

data on starch of various origins with variable water contents [Mizuno et al., 1998]. The useful information gathered was that the normalized values of  $I_3$  and  $\tau_3$  were strongly correlated. This was due to the fact that  $I_3$  varies in proportion to the surviving fraction,  $p$ , of the decomposing matrix, whereas  $R$ , the radius of the free volume nanoholes, and hence  $\tau_3$  (which is closely linear with  $R$  in the range 1 – 1.6 ns), decrease in proportion to  $p^{1/3}$  (this being the one-dimensional equivalent to a decrease of the nanoholes volume in proportion to  $p$ ) [Roudaut et al., 2009].

The corresponding equations were as follows:

$$I_3/I_3^0 = p \quad (3.1)$$

$$R = (R_0 - R_{\min})p^{1/3} + R_{\min} \quad (3.2)$$

where  $I_3^0$  and  $R_0$  are the *o*-Ps intensity and nanohole radius in the absence of decomposition ( $p = 1$ ), respectively, and  $R_{\min}$  is the nanohole radius reached when decomposition is completed ( $p = 0$ ). Finally, a value of  $\tau_3^0$  is associated to  $R_0$  through the Tao-Eldrup equation.

The nanostructure of natural polymers changes as a function of relative humidity due to the sorption of water which acts as a plasticizer. It has been observed by using various methods that the  $T_g$  of biopolymers decreases with the increase in water content [Kilburn et al., 2004 and Poirier-Brulez et al., 2006]. Determining  $T_g$  in a hydrated natural polymer requires some special arrangement to avoid water evaporation during the PALS measurements [Kilburn et al., 2004 and Townrow et al., 2007]. Moreover, moisture sorption of polymers (whether from biological origin or not) is a topic of great interest since many materials properties are sensitive to water, an effect which still requires to be understood. There are very few studies using PALS on hydrated biopolymers at different temperature. Dlubek *et al.* (1999) investigated water in local free volume nanoholes of a polyimide but this study was limited to room temperature. Some papers [Dlubek et al.,

2002; Kilburn et al., 2004; Hu et al., 2005 and Townrow et al., 2007] report studies on polymer matrices as a function of temperature and moisture, the control of moisture content over the temperature treatment being different depending on the authors.

The present study focuses on the use of PALS to investigate the effect of sucrose and moisture (water absorption) on the nanostructure of starch-based material in the region of the glass transition.

### 3.1 Sample preparations

Pregelatinized waxy maize starch (PregeFlow CH 20: adipic acid-reticulated, acetic anhydride-stabilized and drum drying-gelatinized) was supplied by Roquette Frères, France. This biopolymer is mainly (>95%) constituted by amylopectin ( $\alpha$  1-4, 1-6 glucose). A 1.16 % (dry basis) sucrose solution was prepared and starch was added to this solution so that the sucrose w/w ratio was 10 and 20% of the total dry matter (sucrose + starch). The dry matter of the prepared solution was equal to 5.5% of the total weight. This preparation was thoroughly mixed in order to obtain homogenous systems which were then freeze-dried. Starch + 20% sucrose (STS20) was chosen for the study of effects of sucrose in starch matrix, and both STS20 and starch+ 10% sucrose (STS10) were considered for the study of effects of water.

The freeze-dried material was ground to a powder with a household grinder. The powder starch/sucrose matrices were kept to equilibrate for at least 15 days, most usually a month, at 294 K in desiccators, in the presence of saturated salt solutions of known relative humidity:  $\text{MgCl}_2$  (33%),  $\text{K}_2\text{CO}_3$  (45%) and  $\text{NaCl}$  (75%). The dry or water equilibrated powder samples, as required, was compressed for 5 minutes under  $3 \times 10^8$  Pa at 298 K into disk-shaped tablets. The dry tablets were stored in closed environments above a desiccant and the water equilibrated tablets have been used in PALS

measurements without any delay. The size of the tablets (1 – 1.5 mm thick, 8 mm diameter) was such as to ensure complete stopping of the positrons inside the tablets.

From the nominal weight fractions ( $W$ ) and assuming an ideal behaviour of the mixture, the volume fraction of sucrose ( $V_f$ ) in the dried samples can be estimated from the specific weights (subscripts 1 and 2 are for sucrose and starch, respectively):

$$V_{f1} = (W_1/d_1)/(W_1/d_1 + W_2/d_2) \quad (3.3)$$

With  $W_1 = 0.2$ ,  $W_2 = 0.8$ ,  $d_1 = 1.588 \text{ g/cm}^3$ ,  $d_2 = 1.50 \text{ g/cm}^3$ , eq. 3.3 gives  $V_{f1} = 19.1 \%$ , a value similar to that of the sucrose weight fraction.

Amorphous sucrose was prepared from an analytical grade batch (Sigma). A 5% w/w (wet basis) sucrose water solution was prepared with deionised water, then frozen at 193 K and freeze-dried. The dried sample was next stored in dry atmosphere in a closed desiccator containing silica gel until use.

## 3.2. Experiments

### 3.2.1 Thermal Gravimetric Analysis (TGA)

TGA measurements were run in a nitrogen atmosphere using a TA SDT 2960 instrument from 298 K up to about 573 – 623 K at a heating rate of 1 K/min, with sample weights in the range of 4 – 6 mg. An additional TGA experiment was run for pure crystalline sucrose, with a sample weight of about 40 mg.

### 3.2.2. Positron annihilation lifetime measurements

#### 3.2.2.1 Sample holder and PALS devices

The positron source was a 20  $\mu\text{Ci}$   $^{22}\text{Na}$  droplet dried and sandwiched between two 7  $\mu\text{m}$  thick Kapton<sup>®</sup> foils. The foils were kept stuck by two brass rings (0.8 cm diameter) that were stamped together, resulting in a compact source-holder (0.8 cm height). This

source-holder was kept inside a closed copper cylinder (sample-holder) consisting of two similar parts, the upper one with a rimmed top, which could be screwed into one another. The lower tablet was placed inside the lower part of the cylinder. The source-holder was put upon it and the upper tablet deposited on top of the upper Kapton<sup>®</sup> foil. The upper part of the cylinder was then screwed, close contact between the tablets and the Kapton<sup>®</sup> foils being assured by means of a set of very thin copper discs inserted at both ends of the tablet/source-holder assembly.

The heating system was a metallic cylinder (3 cm height, 2 cm diameter) with a copper coil running along its inner surface and providing temperatures up to about 620 K. The sample-holder was introduced in this cylinder, in thermal contact with the heating coil, the upper rim of the source-holder lying on the top of the coil. An additional outer cylinder with a cooled water flow running in a coil along its external surface and separated from the heating cylinder by a 2 mm thick insulating ring, was used to avoid any heating of the scintillators. The total diameter of the heating system was 3.2 cm. The temperature was measured through a thermocouple placed close to the samples through a cavity from the top of the sample-holder. To avoid sticking of the tablets onto the Kapton<sup>®</sup> foils after decomposition, an additional layer of the same foils was added, yielding a source correction of 14 %. The PALS setup was a conventional fast-fast coincidence circuit with BaF<sub>2</sub> scintillators. The windows of the constant fraction discriminators (CFDD) had to be rather wide open for the high counting rates needed to avoid excessive weight loss from the samples. The time resolution was ~ 310-350 ps for different measurements depending on the CFDDs windows.

### 3.2.2.2 Sample handling, heating and PALS counting

#### (i) *Dry samples*

The sample tablets were systematically dried in vacuum overnight before counting. Five series of measurements (S1 through S5) were carried out, each consisting successive heatings of the samples at selected  $T$ . Each  $T$  was reached within 2 - 4 min, during which time counting was hampered, and then kept constant within 0.1 K. Series S1, 2 and 3 lasted 3 hours at each  $T$  step, with an integral of 1.1 million counts; S4 and S5 lasted 2h. S3, S4 and S5 were conducted by jumping directly from low  $T$  up to the region of decomposition, in order to be able to witness the crossing of  $T_g$  with a minimum interference of decomposition.

#### (ii) *Hydrated samples*

Preliminary experiments have shown that, although the samples were confined in the air-tight sample-holder, [Roudaut et al., 2009] loss of water was seen particularly at high temperatures (353 – 373 K). The same would most probably be true when using the procedure developed by the Bristol group, [Kilburn et al., 2004 and 2006] through which the loss of moisture would be minimized by filling the space around the tablets in the sample-holder with the original equilibrated powder. Therefore, we decided to use a different strategy by which, instead of seeking for  $T_g$  through the usual  $\tau_3$  versus temperature ( $T$ ) experimental plots, the temperature would be kept constant and the water content ( $c_w$ , w/w %) of the samples be varied. Any abrupt change in the  $\tau_3$  vs  $c_w$  plots would hopefully denote the specific  $c_w$  value,  $c_g$ , at which the glass transition occurs for the chosen  $T$  ( $= T_g$ ). To implement this method, two experimental difficulties i.e. the knowledge of the initial  $c_w$  of the samples and of the loss of water per unit heating time, had to be overcome.

To determine the initial  $c_w$ , the weight of the samples was measured before and after dehydration and this method is noted (Water Dehydration, WD) in the present study. Using this method, when a series of PALS measurements was finished, the samples were kept to dry overnight under vacuum at 366 K, until constant weight. The absolute experimental errors were below 0.02 % for WD measurements for samples having  $c_w$  in the range of 3 -12 %. Although WD is such that the initial water content can be known only after the samples have been run in PALS, we chose this method for the whole study. The next step consisted of examining the water loss per unit heating time and establishing the protocol for the PALS experiments. Three different regions of  $T$  were defined in preliminary experiments, resulting into three protocols to carry out the PALS measurements. (i) Below about 296 K, a sample in the sample-holder hardly loses or gains any weight over several days, within experimental error (0.01 – 0.02 mg). Therefore, the series conducted below 294 K was run in the form of the usual plot of  $\tau_3$  (and  $I_3$ ) vs  $T$  through successive 1 h heating steps at increasing temperatures, this providing about 1 million counts per PALS spectrum. (ii) For the series at 294 K, the sample was alternately counted in PALS then heated for about 1 h at 318 K, its weight being carefully measured before and after heating. (iii) Above 294 K, trials showed the occurrence of a significant weight loss. Specific WD measurements, where the weight loss of the sample was measured after each PALS counting for a fixed time, were carried out which verified the constancy of the weight loss at a given  $T$ , within experimental errors. Using the same protocol as described for 294 K appeared unsafe and too much time consuming, because of the need to measure the sample weight at the beginning and end of each step (this requiring cooling, with possible change in weight, and re-equilibrating the sample temperature for each step). Therefore, the series above 294 K were run by a number,  $n$ , of successive heating/counting steps at a constant  $T$ , to provide



the  $\tau_3$  (and  $I_3$ ) vs  $c_w$  plots. For this, a sample was heated to and equilibrated (typically, 5 min) at a chosen temperature  $T$ . The recording of the  $n$  PALS spectra ( $n$  steps) was started immediately after equilibration, each spectrum being counted for a given time (typically, 1h). Several series have thus been carried out at different  $T$ .

As the water loss is a continuous process, the average water content during a counting step was calculated as explained in the following. The weight of the tablets was measured at the beginning,  $w_1$ , and at the end of a series having  $n$  steps,  $w_2$ , this providing the absolute loss of weight per step:  $\Delta w = (w_1 - w_2)/n$ . At the end of a series, the weight of the fully dehydrated sample ( $w_D$ ) was determined through WD, providing the initial water weight ( $w_0 = w_1 - w_D$ ) and initial  $c_w$  (before any heating). The weight loss at the end of a step is  $\Delta w$ , while the *average* weight loss during a given step is  $\Delta w/2$ . Therefore, the *average* water content for the first step is given by  $c_{w,1} = (w_0 - \Delta w/2)/(w_1 - \Delta w/2)$ . For the  $i$ th of the remaining ( $n-1$ ) steps, the water content,  $c_{w,i}$ , is obtained by subtracting  $i\Delta w$  in both the nominator and denominator. From all series, it appears that the loss of weight per hour of heating increased smoothly from about 0.3 to 0.5 mg in the range 303 – 357 K, then more abruptly to reach 1.11 mg at 473 K. Due to this, the number of experimental points was about 16 – 24 below 357 K, decreasing to only 8 at 473 K.

At the beginning of the experiment, neither the initial  $c_w$  (for a given sample) nor  $\Delta w$  (at a given  $T$ ) were known. The range of  $c_w$  values in which  $c_g$  would be found could be only roughly guessed from previous results on  $T_g$ , for STS20 measured by using Differential Scanning Calorimetry (DSC) [Poirier-Brulez et al., 2006]. As a result, some measured series were incomplete as  $c_g$  was not crossed and only the slope,  $d\tau_3/dc_w$ , above or below  $c_g$  could be determined. For two series, the water content of the sample after it had been run at low  $T$  was still high enough to carry out an additional series at higher  $T$ .

Thus, the same sample from batch STS20, first studied at 294 K was run thereafter at 318 K, and, for STS10, two successive series were run at 323.7 K and 367 K.

### 3.2.2.3 PALS analysis

The PALS spectra were analysed as a sum of 3 decaying exponential components with lifetimes,  $\tau_i$ , and intensities,  $I_i$ , in the order of increasing lifetimes; subscripts  $i = 1, 2$  and 3 are ascribed to *p*-Ps, free positrons and *o*-Ps, respectively. All values of  $\tau_1$  and  $\tau_2$  could be averaged, at all  $T$ , to  $(121 \pm 6)$  ps and  $(363 \pm 4)$  ps, respectively. For the sake of a better consistency, all data ( $\tau_3$  and  $I_3$ ) were derived with  $\tau_2$  set at 363 ps. The PALS absolute errors were 0.02 ns for  $\tau_3$  and 0.2 % for  $I_3$  for time resolution  $\sim 310$  ps. For time resolution  $\sim 350$  ps, the errors on  $\tau_3$  and  $I_3$  increased to 0.035 ns and 0.4 %, respectively.

## 3.3. Effect of sucrose in starch matrix

### 3.3.1 Decomposition study of STS20 using TGA

A typical variation of the starch/sucrose matrix weight with  $T$  is shown in Fig. 3.1. The data clearly show two steps, attributable to the successive decompositions of the sucrose (subscript 1 in the following), next of the starch (subscript 2) molecules. They were analyzed on the basis of two first order reactions with reaction rate constants  $k_1$  and  $k_2$ , defined through the Arrhenius equation. [Roudaut et al., 2009] The corresponding differential equations, in terms of the weights, were thus:

$$dw_1/dt = -k_1(T).(1-\alpha).w_1 \quad (3.4)$$

$$dw_2/dt = -k_2(T).(1-\beta).w_2 \quad (3.5)$$

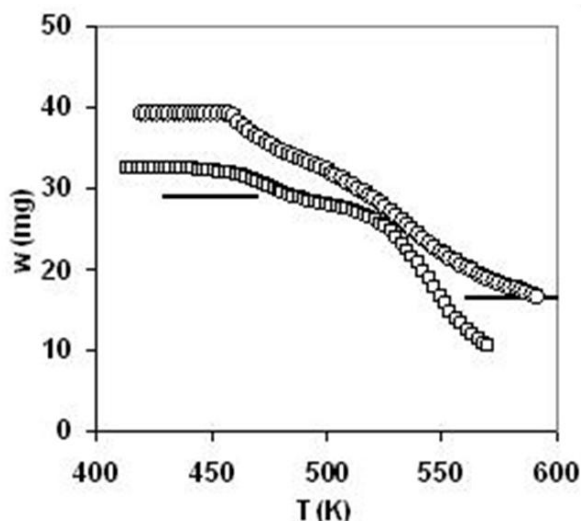


**Figure 3.1:** TGA curves for STS20 (□) and crystalline sucrose (○); two horizontal lines show the complete decomposition of sucrose in starch and pure sucrose

Here,  $w_1$  and  $w_2$  are the sucrose and starch weights, respectively, and  $\alpha$  and  $\beta$  are the weight fractions of the nonvolatile products produced by the decomposition of these two substances, respectively. The measured weight is the sum of  $w_1$  and  $w_2$ . The heating rate,  $\nu$ , was introduced in the above equations through  $dt = dT/\nu$  and these were numerically fitted to the TGA data. A good fit was obtained, as shown from the solid line in (indiscernible from data points) Fig. 3.1 and the relative average deviation,  $\sigma_w = 0.28 \%$ , with the parameters to follow.

- Activation energies:  $E_1 = (1.54 \pm 0.05) \text{ eV}$  and  $E_2 = (1.52 \pm 0.05) \text{ eV}$ . These values are very close, the value of  $E_2$  being the same as previously found for pure starch [Roudaut et al., 2009].

- Frequency factors ( $\text{s}^{-1}$ ):  $\ln(k_{01}) = 30.8 \pm 0.3$  and  $\ln(k_{02}) = 25.3 \pm 0.3$ , this latter value also coinciding with that found in pure starch [Roudaut et al., 2009].

- Initial weights:  $w_{01} = (0.805 \text{ mg} \pm 0.004)$  and  $w_{02} = (3.28 \pm 0.002) \text{ mg}$ , this giving a weight fraction of sucrose in the sample of 19.7%, in agreement with the nominal ratio of 20%.

- Weight fractions of the non-volatile residuals (carbon):  $\alpha = 0.421 \pm 0.004$  and  $\beta = 0.279 \pm 0.005$ . The value of  $\alpha$  corresponds closely to what would be expected if all 12 carbons in sucrose would remain after complete decomposition (i.e., loss of the 11 H<sub>2</sub>O molecules), whereas  $\beta$  indicates the loss of a significant fraction of the carbons from starch.

Complementary information was sought by examining the fate of pure sucrose, as shown in Fig. 3.1. Thermolysis of sucrose is a complex process [Richards et al., 1978]. Since it is known that 95 % of the sucrose decomposition relates to the loss of water, [Scheer et al., 1982] for the present purpose the data in Fig. 3.1 were analyzed on the hypothesis that the weight loss was due to that of the 11 H<sub>2</sub>O molecules per sucrose molecule. Therefore, a fitting was successfully carried out (solid line indiscernible from data points in Fig. 3.1), in a way similar to that used just above, including 11 first order consecutive steps of equal magnitudes. To limit the number of fitting parameters, a single frequency factor was used for all reactions. The resulting values for the 11 activation energies (eV) were 1.54, 1.54, 1.59, 1.67, 1.70, 1.75, 1.76, 1.77, 1.82, 1.88 and 1.88 together with  $\ln(k_0, \text{s}^{-1}) = 31.2$ . It may be seen that the activation energies of the two first steps and the frequency factor are very close to those found in the case of sucrose decomposition in starch. In Fig. 3.1, the horizontal bars denote the level at which all water molecules become lost for pure sucrose and sucrose in starch, accordingly. Clearly, sucrose decomposition reaches an end at a much lower temperature when in starch than in pure form.

### 3.3.2 *o*-Ps lifetime, $\tau_3$ , and intensity, $I_3$

Fig 3.2 shows the variation of  $I_3$  with  $T$  for all experimental series.  $I_3$  remains constant at  $I_3^0 = (24.5 \pm 0.2) \%$  up to about 440 K.  $I_3$  appears to be a little higher at about 313 K, possibly due to the uptake of moisture by the samples during counting.

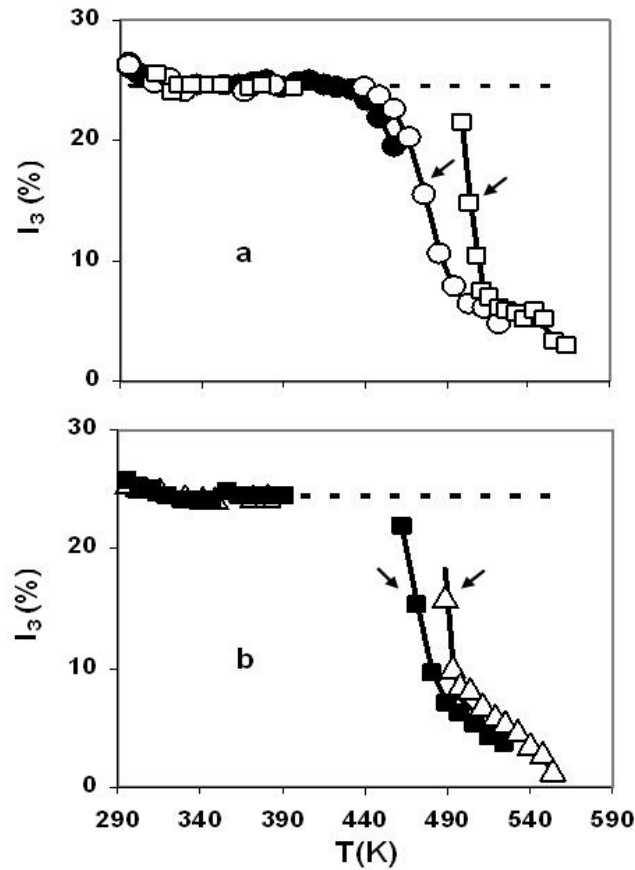


**Figure 3.2:** Variation of the *o*-Ps intensity,  $I_3$  (%), with temperature,  $T$  (K), for the various experimental series. (a): ●, S1; ○, S2; □, S4. (b): ■, S3; △, S5. The data in the decreasing part of  $I_3$  are shifted along the abscissa for S2 (+ 10 K), S4 (+ 30 K) and S5 (+ 10 K). The broken line is the extrapolation of the initial part ( $I_3$  constant at 24.5 %). The solid lines are fits to the data. The arrows indicate experimental points for which the *o*-Ps lifetime is high (about 1.4 ns, see Figure 3.4) but the associated  $I_3$  is low (about 15 %).

Above 440 K,  $I_3$  suffers two successive decreases in a way which is strongly reminiscent of the two decomposition steps observed through TGA (Fig. 3.1). However, the relative magnitudes of the two steps are clearly different in either type of experiments.

The first step in PALS represents some 73 % of  $I_3^0$ ,  $I_3$  decreasing from 24.5 down to about 6.8 % as observed around 500 K, before the second step occurs.

Fig. 3.3 shows the linear variation observed for  $\tau_3$  with  $T$  below about 440 K, for all series, yielding the following equation (solid line in the Figure):

$$\tau_3 \text{ (ns)} = 9.44 \times 10^{-4} T \text{ (K)} + 0.964 \quad (3.6)$$

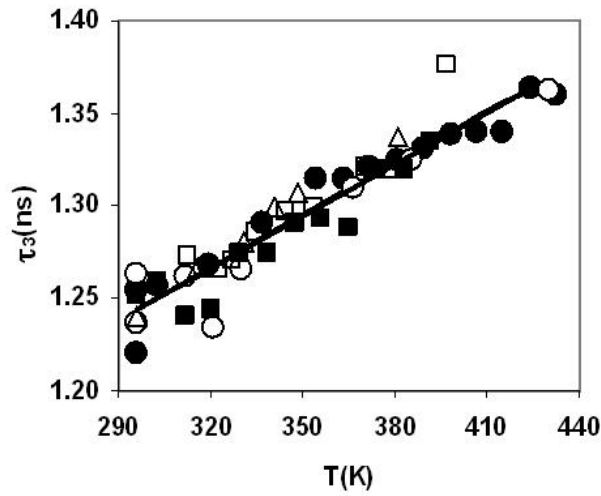


**Figure 3.3:** Linear variation of  $\tau_3$  with temperature  $T$  before any decomposition. The symbols are as in figure 3.2

Such a change is typical of what is expected from the thermal expansion of a polymeric matrix [Mallon, 2003 and Dlubek et al., 2006]. Above 440 K, as shown in Fig. 3.4, the changes in  $\tau_3$  denote the existence of two successive regions of decrease, as found for  $I_3$  in Fig. 3.2. A first strong decrease, starting from a value higher than expected from the data given in Fig. 3.3 (extrapolated by the broken line in Fig. 3.4) is observed. Such high values are indicative of the fact that  $T_g$  has been reached at some  $T$  above about 440 K (Fig. 3.3). This clue becomes even more convincing when noting that some of the experimental points, denoted by an arrow in Fig. 3.2 and 3.4, have a lifetime close to or

higher than that expected from the linear trend in Fig. 3.3, together with a  $I_3/I_3^0$  ratio situated at about half of the first step in Fig. 3.2.

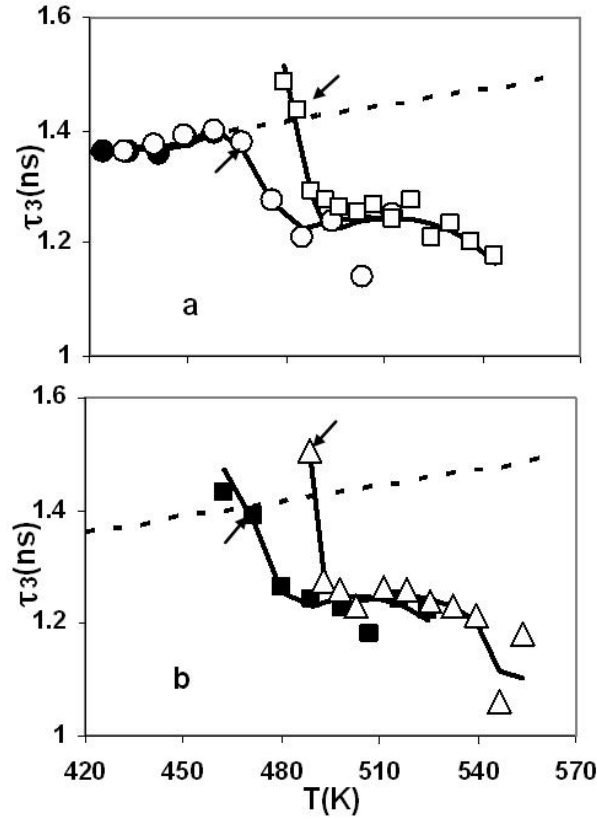


**Figure 3.4:** Variation of the *o*-Ps lifetime,  $\tau_3$  (ns), with temperature,  $T$  (K), in the region of decomposition, for the various experimental series. (a): S1, S2, S4; (b): S3 and S5; symbols as in figure 3.2. The data are shifted by + 10 K along the abscissa for S4 and S5. The broken line is the extrapolation of the initial linear variation of  $\tau_3$  (see Figure 3.3). The solid lines are fits to the data.

A simple approach can help visualize the crossing of  $T_g$  by  $\tau_3^0$ , the *o*-Ps lifetime in the absence of any decomposition, from the experimental data as explained in the following. On the basis of eq. 3.1, the values of  $I_3$  in Fig. 3.2 provide  $p$ , the surviving fraction for the first step, for which  $I_3^0 = (24.5 - 6.8) \%$ . Next, the values of  $\tau_3$  in Fig. 3.4 provide those of the corresponding  $R$  through the Tao-Eldrup equation, then, those of  $R_0$ , through eq. 3.2 and finally, the values of  $\tau_3^0$  again from the Tao-Eldrup equation. Note that since  $\tau_3$  for  $I_3 = 0$  can be estimated to be a little below 1 ns in this work and for pure

starch [Roudaut et al., 2009],  $R_{\min} = 1.5\text{\AA}$  was adopted in eq. 3.2. The variation of  $\tau_3^0$  with  $T$  thus obtained is displayed in Fig. 3.5, showing a neat increase of gradient at about 450 K. This simple semi-empirical method to derive a reasonable estimate of  $T_g$  can most probably be applied to other polymeric systems undergoing decomposition in a temperature range that would include  $T_g$ .

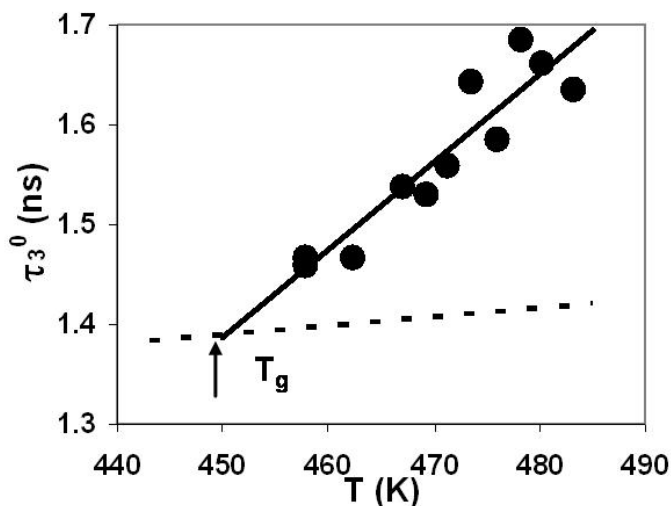


**Figure 3.5:** Variation of  $\tau_3$  in the absence of decomposition with temperature,  $T$

At the end of the first step in Fig 3.4, there appears a very slight increase in  $\tau_3$  before the second decrease becomes efficient. All PALS data thus point to the implication of two states for the matrix and two possibilities are open and examined in the following. Hypothesis 1: the system studied is a mere mixture of starch and sucrose. To evaluate this possibility, PALS measurements at 296 K were carried out in pure sucrose samples either purely crystalline or largely amorphous.

For crystalline sucrose, the results were  $I_3 = (42.6 \pm 1) \%$ ,  $\tau_2 = (335 \pm 8) \text{ ps}$  and  $\tau_3 = (728 \pm 5) \text{ ps}$ . The presence of crystalline sucrose in a mixture with starch could only increase  $I_3$  above 26.2 %. It is worth noting that  $\tau_3 = 0.728 \text{ ns}$  corresponds closely to what is expected from the size of the crystallographic voids present in sucrose. The volume of a



unit cell, containing two sucrose molecules, [Hynes et al., 1991] is  $0.7154 \text{ nm}^3$  and the intrinsic volume of a sucrose molecule [Banipal et al., 1997] has been reported to be very close to  $0.3519 \text{ nm}^3$ , leaving a void of  $0.0058 \text{ nm}^3$  volume or  $0.1115 \text{ nm}$  radius which, through Tao-Eldrup equation corresponds to an expected lifetime of  $0.725 \text{ ns}$ .

For amorphous sucrose, the PALS spectra give  $I_3 = (26.5 \pm 0.3) \%$ ,  $\tau_2 = (342 \pm 3) \text{ ps}$  and  $\tau_3 = (1008 \pm 6) \text{ ps}$ . As such, these results would yield  $\tau_3 = 1.26 \text{ ns}$  and  $I_3 = 26.3 \%$  for the starch/sucrose mixture.  $\tau_3$  ( $1.26 \text{ ns}$ ) is consistent with the value expected from eq. 3.6, but  $I_3$  ( $26.3 \%$ ) appears too high. The amorphicity of this sucrose is high, but quantitatively uncertain. Considering that the sucrose sample would not be purely amorphous, the PALS spectra were analyzed with two long-lived components for *o*-Ps decay in either the crystalline ( $\tau_{3C}$ ,  $I_{3C}$ ) or amorphous ( $\tau_{3A}$ ,  $I_{3A}$ ) phases, with  $\tau_{3C}$  set at  $728 \text{ ps}$ . The resulting PALS parameters were  $I_{3C} = (7.8 \pm 0.4) \%$ ,  $I_{3A} = (20.7 \pm 0.3) \%$  and  $\tau_{3A} = (1070 \pm 7) \text{ ps}$ . From these values, the amorphicity should be  $100 \times (1 - 7.8/42.6) = (81.6 \pm 0.8) \%$ , and the *o*-Ps intensity in purely amorphous sucrose should reach  $25.4 \%$ . Note that  $\tau_{3A} = 1070 \text{ ps}$  is quite consistent with  $1090 \text{ ps}$ , the *o*-Ps lifetime found for another amorphous disaccharide, maltose [Townrow et al., 2007]. The PALS data from this 4-component analysis lead to the same conclusions, as regards the nature of the sucrose/starch matrix, as those from the 3-component analysis.

Thus, from the PALS results, the studied matrix must be considered as a solid solution, in agreement with what can be inferred from data on maltose/maltopolymer matrices [Townrow et al., 2007]. In addition, a mixture should exhibit two glass transitions, one around  $343 \text{ K}$  for the sucrose-rich phase, and the other above  $519 \text{ K}$ , [Orford et al., 1989] for the starch-rich phase. However, in Differential Scanning Calorimetry experiments, a single glass transition has been observed for starch/sucrose matrices [Poirier-Brulez et al., 2006].

Hypothesis 2: the system is originally a solid solution (state  $A$ ) which, upon sucrose decomposition, turns into a matrix of starch with carbon atoms (decomposed sucrose) dispersed in it, the latter eventually undergoing decomposition (state  $B$ ).

Since the PALS data are in the form of a single pair of parameters,  $I_3$  and  $\tau_3$ . These necessarily result from an average when the two states are coexisting (essentially in the region 440 – 490 K). The corresponding chemical scheme, supposing first order decomposition reactions, is as follows (the volatile products are not noted):



The reaction constant  $k_A$  ( $k_B$ ) is defined through the Arrhenius equation, with activation energy  $E_A$  ( $E_B$ ) and frequency factor  $k_{0A}$  ( $k_{0B}$ ). Note that state  $A$  keeps its intrinsic properties all throughout the sucrose decomposition process. This is true, in particular, for the presence of  $T_g$ , as suggested by the data with an arrow in Figs. 3.2 and 3.4. Although the overall volume fraction of sucrose through decomposition has dropped importantly, the sucrose nominal volume fraction still holds for state  $A$ . Previously, the glass transition (or more precisely the primary relaxation associated with it) of this 20% sucrose-plasticized starch has been studied by mechanical spectroscopy [Poirier-Brulez et al., 2006]. The transition of the solid solution appears not to be affected by sucrose decomposition since it was observed in the expected temperature range (about 433 K), i.e., at a lower temperature than for a pure starch sample.

On the present hypothesis, a simple model could be built that leads to a good fitting of all data. Reference is made to the work on pure starch [Roudaut et al., 2009] for the definition of the surviving fractions of the two states at a given  $T$ ,  $p_A$  and  $p_B$ . From eq. 3.7, and following eq. 3.1, the  $o$ -Ps intensities in the two states read:

$$I_{3A} = I_{3A}^0 p_A \quad (3.8)$$

$$I_{3B} = I_{3B}^0 (p_A - p_B) k_A / (k_B - k_A) \quad (3.9)$$

The measured intensity should be the sum of the individual intensities:

$$I_3 = I_{3A} + I_{3B} \quad (3.10)$$

For the lifetimes, we first define the variation with  $T$  of  $\tau_{3A}^0$  and  $\tau_{3B}^0$ , the *o*-Ps lifetimes in the absence of any decomposition. Below  $T_g$ ,  $\tau_{3A}^0$  is given by eq 3.6. Above  $T_g$ , its gradient should increase as follows:

$$\tau_{3A}^0 (\text{ns}) = a_A T(\text{K}) + b_A \quad (3.11)$$

with  $b_A = 0.964 + (9.44 \times 10^{-4} - a_A)T_g$ .

For state *B*, the data in Fig. 3.4 do not show any sign of a particular abrupt increase in  $\tau_3$  upon heating as expected for the present system. This is because only one  $T_g$  is found in this system and no other transition appears at about 519 K, the value for  $T_g$  in pure starch [Roudaut et al., 2009]. Therefore, the equation for  $\tau_{3B}^0$  is

$$\tau_{3B}^0 (\text{ns}) = a_B T(\text{K}) + b_B \quad (3.12)$$

Then, the radii of the intact free volume nanoholes,  $R_{0A}$  and  $R_{0B}$ , can be calculated from  $\tau_{3A}^0$  and  $\tau_{3B}^0$ , respectively using the Tao-Eldrup equation. Next, the radii affected by decomposition are obtained through eq. 3.2 and finally, the lifetimes  $\tau_{3A}$  and  $\tau_{3B}$ , again using Tao-Eldrup equation. The measured lifetime should be the average of  $\tau_{3A}$  and  $\tau_{3B}$ :

$$\tau_3 = (I_{3A} \tau_{3A} + I_{3B} \tau_{3B}) / I_3 \quad (3.13)$$

All data on  $I_3$  and  $\tau_3$  shown in Figs. 3.2, 3.3 and 3.4 were successfully fitted together by using eqs 3.10 and 3.13, as shown by the solid lines in these figures and the low average deviations obtained,  $\sigma_I = 0.23 \%$  and  $\sigma_\tau = 0.014 \text{ ns}$  for  $I_3$  and  $\tau_3$ , respectively. The fitting parameters are listed in the following.

(i) Activation energies:  $E_A$  ( $E_B$ ) and  $k_{0A}$  ( $k_{0B}$ ) were soon found to be strongly correlated within a rather broad range (e.g., 1.45 - 1.65 eV for  $E_A$ ). Therefore, to limit the number of free parameters and taking it that the thermodynamically important step would be the

breaking of the bonds in either sucrose or starch, the values of  $E_A$  and  $E_B$  were set to those derived from the TGA experiments (Fig. 3.1):  $E_A = 1.54$  eV and  $E_B = 1.52$  eV.

(ii) Frequency factors ( $s^{-1}$ ):  $\ln(k_{0A}) = 28.3 \pm 0.3$  and  $\ln(k_{0B}) = 23.3 \pm 0.6$ . Both values are significantly lower than those derived from the TGA experiments (Fig. 3.1), 30.8 and 25.3, respectively.  $k_{0B}$  is not well defined due to the fact that, at the highest  $T$  studied,  $I_3$  becomes very low. All values are typical for molecular solids, but the differences are large enough to conclude that the associated  $p_A$  and  $p_B$  values should not be identified with the surviving fraction of the matrix. They should relate, more strictly, to the surviving fraction of the free volume nanoholes. Since the  $k_0$ 's as seen by our probe are lower than those found through TGA, whereas they were the same in pure starch, [Roudaut et al., 2009]. It appears that the presence of sucrose and/or carbon result in some stabilization of the nanoholes inside the matrix.

This is illustrated in Fig. 3.6, which shows the isochronal variation with  $T$  for 3 h heatings of the surviving fraction of starch in the matrix, as expected from the TGA data, together with that of the free volume,  $F_v$ , as estimated from the following empirical equation [Jean et al., 2003]. The parameters,  $I_3$  and  $\tau_3$ , used in the equation are calculated using the parameters derived from the present model.

$$F_v (\%) = 0.0018I_3(\%)(4\pi R^3/3) \quad (3.14)$$

where  $R$  is the nanohole radius associated to  $\tau_3$ .

One might note that the frequency factors could be lower in the vicinity of the nanoholes, considered as a disordered region of the matrix, than in the bulk. However, the fact that there is no difference between  $k_0$  from PALS and from TGA in pure starch would remain enigmatic.

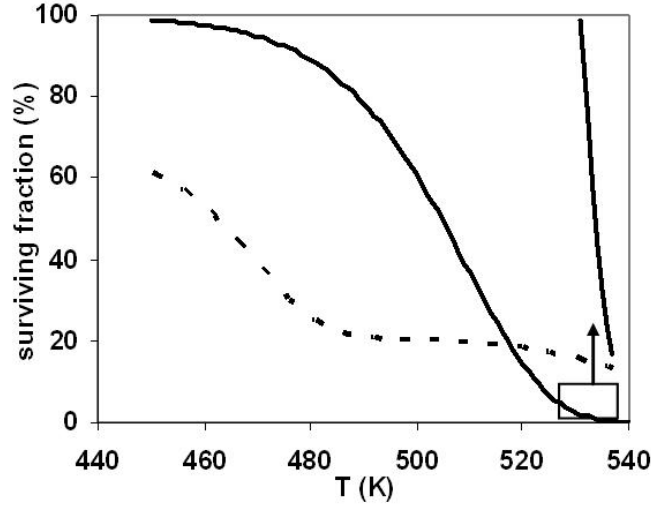


**Figure 3.6:** Calculated variation with temperature of the surviving fraction of starch in the samples (solid line) and of the free volume (broken line). The latter and the last part of the former (rectangle) are magnified 50 times.

At this level, one may note that eq. 3.1 implies that  $I_3$  decreases in proportion to the matrix survival fraction, more specifically, to the available density of free volume holes at a given  $T$ , this being in agreement with the concepts of the various free volume models [Jean et al., 2003; Kobayashi et al., 1989 and Wang et al., 1990]. However, as underlined in work on pure starch [Roudaut et al., 2009], other processes can be responsible for a decrease in  $I_3$ , namely, spur processes [Jean et al., 2003]. Thus, in the present case, the carbon clusters produced upon sucrose (and starch) decomposition might be supposed to act as traps for either of the particles of the initial  $e^+/e^-$  pair, before positronium formation. This kind of inhibition has been observed in solid solutions and should result in the following variation of  $I_3$  [Magalhaes et al., 1989]

$$I_3 = I_3^0 / (1 + kC) \quad (3.15)$$

where  $C$  is the concentration of the inhibiting species and  $k$  its inhibition constant. The carbon clusters concentration,  $C$ , should be proportional to  $(1 - p)$ . Eq. 3.15 was

tentatively used instead of eq. 3.1, this resulting in a rather bad fitting of the data. Hence, the possibility of inhibition is abandoned.

(iii) *o*-Ps intensities:  $I_{3A}^0 = (17.7 \pm 0.1) \%$  and  $I_{3B}^0 = (6.8 \pm 0.1) \%$ , in good agreement with visual observation (Fig. 3.2).

(iv) Variation of the *o*-Ps lifetimes in the intact states: For  $\tau_{3A}^0$ , above  $T_g$ , and for  $\tau_{3B}^0$  in the whole range of  $T$ , the variations come as follows.

$$\tau_{3A}^0 (\text{ns}) = 8.16 \times 10^{-3} T(\text{K}) - 2.255 \quad (3.16)$$

The change in the slope for  $\tau_{3A}^0$  at  $T_g$ , from  $9.44 \times 10^{-4} \text{ K}^{-1}$  to  $8.16 \times 10^{-3} \text{ K}^{-1}$ , is abrupt, but this is not uncommon in polymers studies [Hsu et al., 1990 and Dlubek et al., 2006].

$$\tau_{3B}^0 (\text{ns}) = 8.10 \times 10^{-4} T(\text{K}) + 0.845 \quad (3.17)$$

The gradient for starch decreases importantly, from  $1.525 \times 10^{-3} \text{ K}^{-1}$  in pure starch [Roudaut et al., 2009] to  $8.10 \times 10^{-4} \text{ K}^{-1}$  in state *B*, thus denoting a much lesser lattice thermal expansion coefficient in the latter case. The validity of eq. 3.17 is corroborated by the fact that the samples of series S2 and S3 were counted at 296 K, after the completion of the heating runs, when only state *B* is present, both yielding  $\tau_3 = 1.08 \text{ ns}$ , in excellent agreement with eq. (3.17). The radius reached in either state upon complete decomposition ( $p_A$  or  $p_B = 0$ ) was  $R_{\min} = 0.160 \text{ nm}$ , corresponding to a lifetime of 0.97 ns.

(v) Glass transition temperature:  $T_g = (446 \pm 2) \text{ K}$ . This value is higher than expected from the linear variation previously found for starch + 20% w/w sucrose matrices as a function of water content, denoting a strong increase in the value of  $T_g$  for water contents below 3.1 % [Poirier-Brulez et al., 2006]. However, a linear extrapolation may not be appropriate. One of the most employed empirical equation to predict the glass transition temperature of complex compatible mixture is the Couchman-Karas equation: [Couchman et al., 1978]

$$T_g = \frac{W_1 \Delta C_{p1} T_{g1} + W_2 \Delta C_{p2} T_{g2} + W_3 \Delta C_{p3} T_{g3}}{W_1 \Delta C_{p1} + W_2 \Delta C_{p2} + W_3 \Delta C_{p3}} \quad (3.18)$$

Here, subscripts  $i = 1, 2, 3$  stand for water, sucrose and starch respectively;  $W_i$ ,  $\Delta C_{pi}$  and  $T_{gi}$  are the weight fraction, heat capacity change at the glass transition and glass transition temperature of the pure components. From the literature, the relevant parameters are:

For water: [Kalichevsky et al., 1992]  $\Delta C_p = 1.11 \text{ J/g/K}$ ;  $T_g = 134 \text{ K}$

For waxy starch: [Orford et al., 1989]  $\Delta C_p = 0.47 \text{ J/g/K}$ ;  $T_g = 519 \text{ K}$

For sucrose: [Kalichevsky et al., 1992]  $\Delta C_p = 0.76 \text{ J/g/K}$ ;  $T_g = 343 \text{ K}$ .

From eq. 3.18, the calculated  $T_g$  for the studied mixture is then 456 K, which is slightly higher than that determined from PALS.

### 3.4. Effect of water on starch/sucrose matrices

#### 3.4.1 $\sigma$ -Ps lifetime, $\tau_3$ , and nanohole average volume, $V$

Fig. 3.7 shows the changes in  $\tau_3$  measured as a function of  $T$  below room temperature (294 K) for a constant water content of 11.4 % as confirmed by WD. The shape is the same as observed in numerous works on polymers, the break denoting the occurrence of the glass transition [Kilburn et al., 2004; Hsu et al., 1990; Mallon, 2003; Dlubek et al., 2006; and Townrow et al., 2007]. It is observed that  $\tau_3$  and therefore the average volume of the nanoholes,  $V$ , increase with  $T$  as a result of molecular vibrations in the vicinity of the nanoholes in the glassy phase and after crossing  $T_g$ , this increase becomes sharper in the rubbery phase as a result of molecular and segmental relaxations in the matrix [Hsu et al., 1990; Mallon, 2003 and Dlubek et al., 2006]. The average nanoholes radii,  $R$ , were derived from the experimental  $\tau_3$  values by using the Tao-Eldrup equation and the average volumes were obtained as  $V = 4\pi R^3/3$ . It is to be noted that one can express  $V$  in terms of  $R$  only when the distribution of the nanohole size is narrow,

[Roudaut et al., 2009] this being true in the present case, as verified *a posteriori* (see section 3.4.3). The average volumes  $V$  behaves linearly with  $T$  similar to  $\tau_3$  due to the narrow range of  $\tau_3$  values explored. As illustrated in Fig. 3.7, fitting either  $\tau_3$  or  $V$  in terms of two straight lines of different slopes results in the same value of  $T_g$  for all series.

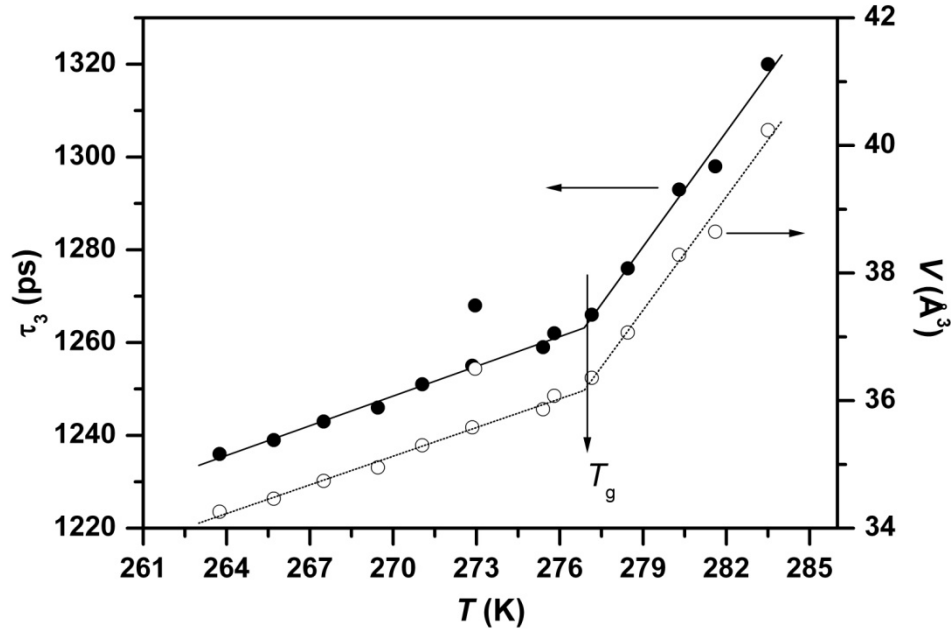


**Figure 3.7:** Variation of *o*-Ps lifetime and average nanoholes volume in STS20 having 11.4% water as a function of temperature

Fig. 3.8 shows some typical variations of  $\tau_3$  (ps) with the water content,  $c_w$  (%), for STS10 and STS20 at various  $T$ . The behaviour is similar to that observed in the usual  $\tau_3$  vs  $T$  curves [Hsu et al., 1990; Mallon et al., 2003 and Dlubek et al., 2006] (see Fig. 3.7), with a smooth linear variation in the lower  $c_w$  region, then a break at  $c_g$  followed by a sharper linear increase. It is observed that at critical water content,  $c_g$ , both matrices, STS10 and STS20, undergo a transition from glassy to rubbery phase at a fixed  $T$ . The  $c_g$  values expectedly decrease with increasing temperature. The slopes of the various lines appear to be very similar, whatever  $T$ , before and after  $c_g$ , respectively. Although there is some spread due to the difficulty in determining the slopes precisely, these can be averaged as shown in Table 3.1.



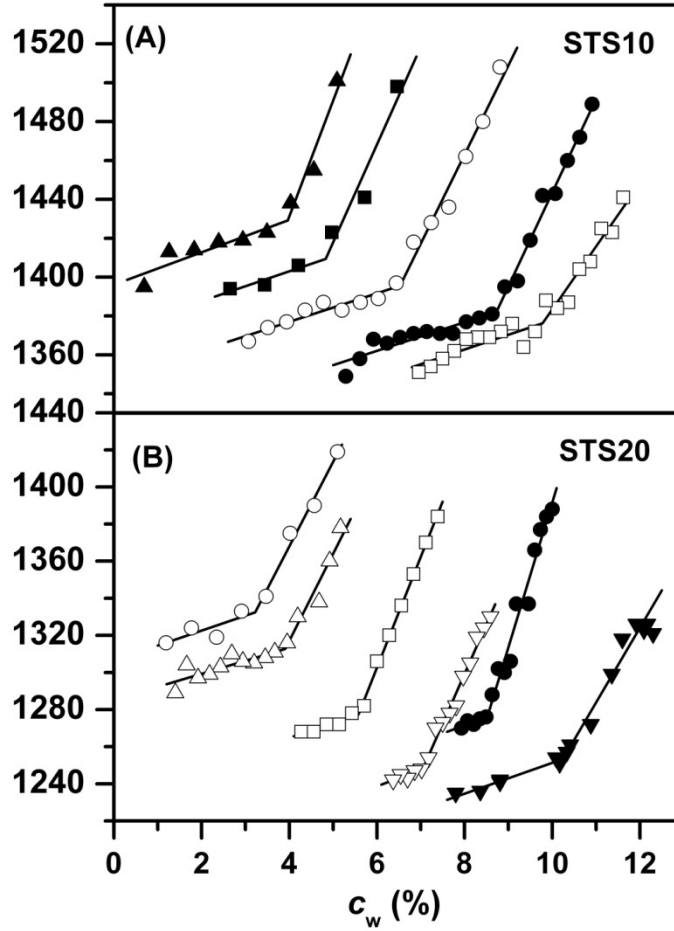


**Figure 3.8:** Typical variations of the *o*-Ps lifetime as a function of water content,  $c_w$  (%), in the starch/sucrose mixtures, at various temperatures. (A), for STS10,  $T = 311$  ( $\square$ ), 323.7 ( $\bullet$ ), 342 ( $\circ$ ), 353 ( $\blacksquare$ ) and 367 ( $\blacktriangle$ ) K; (B), for STS20,  $T = 294$  ( $\blacktriangledown$ ), 311 ( $\bullet$ ), 333 ( $\nabla$ ), 357 ( $\square$ ), 368 ( $\Delta$ ) and 373 ( $\circ$ ) K.

**Table 3.1** Average values of the slopes of the variations of the *o*-Ps lifetime ( $\tau_3$ ) and nanohole average volume ( $V$ ) with water content ( $c_w$ ) below, ( $a_{\tau,w}$ ,  $a_{V,w}$ ), and above, ( $b_{\tau,w}$ ,  $b_{V,w}$ ), the break at  $c_g$

batch	$a_{\tau,w}$ (ps/%)	$b_{\tau,w}$ (ps/%)	$a_{V,w}$ ( $\text{\AA}^3/\%$ )	$b_{V,w}$ ( $\text{\AA}^3/\%$ )
STS20	$7.97 \pm 0.55$	$48 \pm 6$	$0.56 \pm 0.03$	$3.60 \pm 0.38$
STS10	$7.66 \pm 0.28$	$47 \pm 6$	$0.57 \pm 0.03$	$3.64 \pm 0.52$

From the wealth of data on  $\tau_3$  vs  $c_w$  at various temperatures, it is possible to build other  $\tau_3$  vs  $T$  variations by considering the experimental values of  $\tau_3$  at a constant  $c_w$  value. This is illustrated in Fig. 3.9 for  $c_w = 5.1$  and 7.1 %.

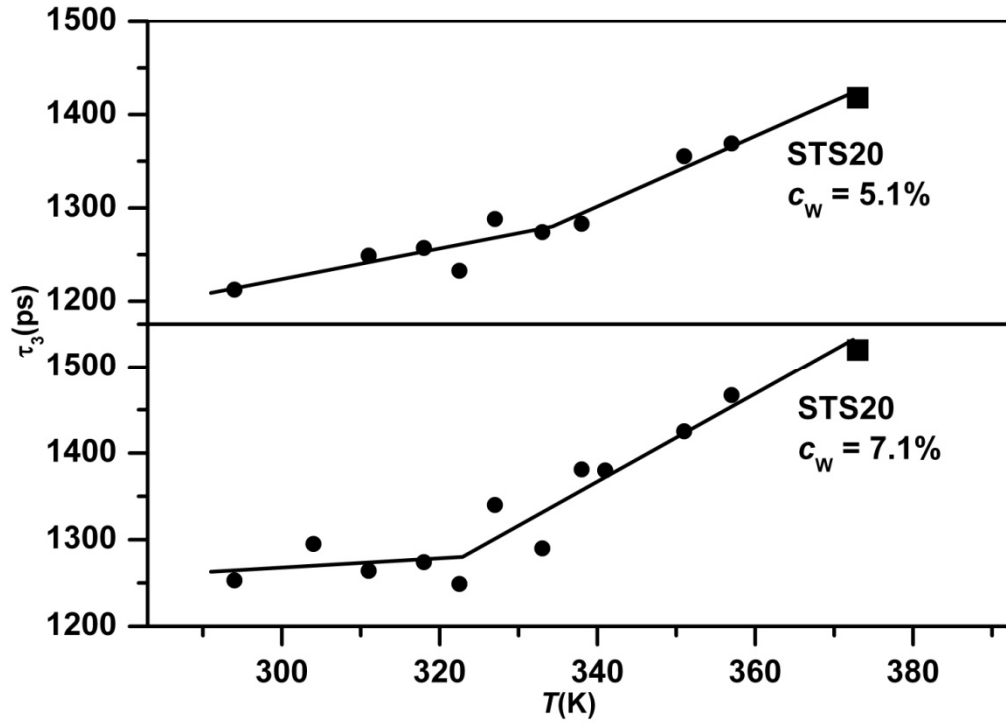


**Figure 3.9:** Variation of the o-Ps lifetime as a function of temperature in STS20, having water contents,  $c_w$ , of 5.1 (upper) and 7.1% (lower), respectively, as derived from the various  $\tau_3$  vs  $c_w$  experimental plots: (●), interpolated, (■) extrapolated from the data (see text).

The curves were built in the following manner,  $c_{w0}$  denoting the value of  $c_w$  chosen: (i) for those curves such as shown in Fig. 3.8, where  $T$  is known and constant, which would include  $c_{w0}$ , the corresponding  $\tau_3$  value was directly interpolated from experimental data; when  $c_{w0}$  would lie outside the range of  $c_w$  values studied at a given  $T$ , either below or above, the corresponding  $\tau_3$  value was extrapolated from the value of  $\tau_3$  at  $c_g$  through the use of the average slopes given in Table 3.1 (either  $a_{\tau,w}$  or  $b_{\tau,w}$  accordingly). In this way, the  $\tau_3$  vs  $c_w$  plots at various temperatures can be drawn in the form of the usual PALS  $\tau_3$  vs  $T$  plots for a fixed  $c_w$  thus circumventing the problem of important loss of water from the samples.

### 3.4.2 $T_g$ as a function of the water content, $c_w$

Fig. 3.10 collects all data for STS20 and STS10. The most detailed curve, for STS20, shows a broad sigmoidal shape. Linear extrapolation of the last 4 points at low  $c_w$  values down to  $c_w = 0$  yields a value of  $T_g = 450$  K, in good agreement with the experimental  $(446 \pm 2)$  K previously found for dry STS20. The values of  $T_g$  derived from the extrapolated  $\tau_3$  vs  $T$  curves (Fig. 3.9) are also included, showing good agreement with the other data. It is interesting to note that the data derived by using a sample that was previously used at a lower  $T$  insert very well in the correlation (see Experimental section). This clearly indicates that a similar type of changes occur in the nanostructure of the matrices during the glass transition process either as a function of  $T$  or as a function of  $c_w$ . The curve for STS10 is grossly parallel, with higher  $T_g$  values for a given  $c_w$ , confirming the plasticising effect of sucrose. The figure also shows the changes in  $T_g$ , the glass transition temperature of STS20 measured by using DSC in a previous work [Poirier-Brulez et al., 2006]. The average nanohole size in a polymer increases with  $T$  as a result of thermal expansion in the glassy phase due to the molecular vibrations in the vicinity of nanoholes and the rate of change depends on the thermal expansion coefficient of the polymer. With the increase in  $T$ , molecular and segmental relaxations begin and polymers undergo a transition from glassy to rubbery phase which has larger size free volume nanoholes. In the rubbery phase, the energy associated with the relaxation of the chain segments is lower and, consequently, the rate of change of the free volume nanoholes size with  $T$  is higher as compared to the glassy phase. DSC measures the change in heat capacity at the glass transition, a second order transition in nature. Most of polymers are poor heat conductors and DSC measurements are run at a very high speed (e.g. 10K/min) which results in observing the glass transition as occurring at a higher temperature compared to the actual  $T_g$  of the polymer because thermal equilibrium is not reached at a

particular temperature during the run. Now, *o*-Ps being a nanoscopic probe directly measures the change in the size of the nanoholes of the polymers which are equilibrated at a given temperature due to the long duration of *o*-Ps lifetime measurements. Thus,  $T_g$  measured through PALS is much closer to the actual  $T_g$  of the polymers and always lower than  $T_g$  measured when using DSC [Jean et al., 2003].

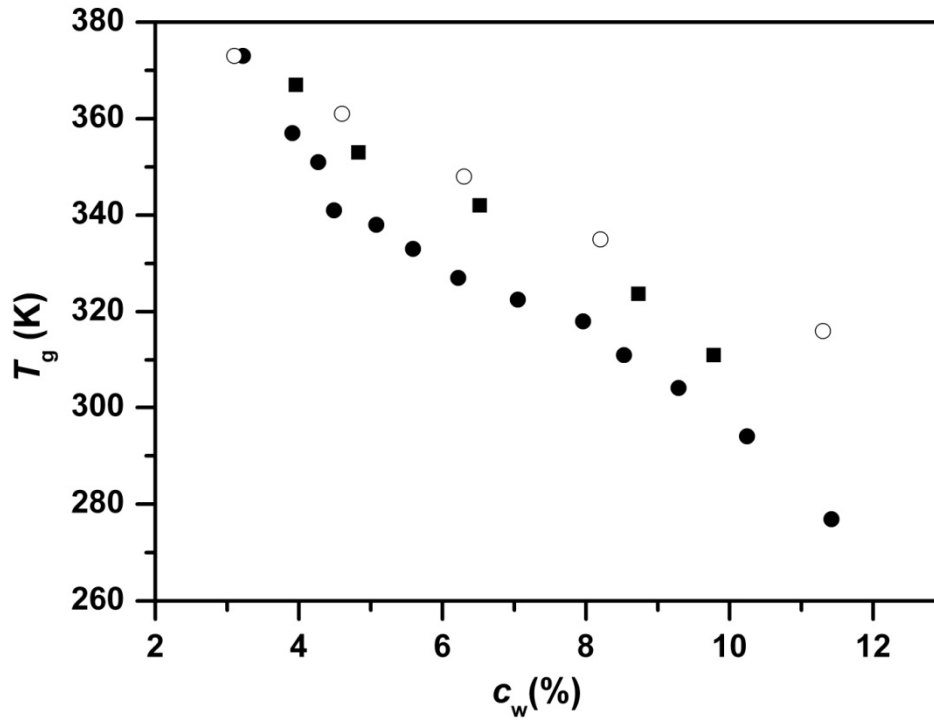


**Figure 3.10:**  $T_g$  (K), STS20 (●) and STS10 (■), measured from *o*-Ps lifetime measurements as a function of water content,  $c_w$ . Previous data for STS20 from Differential Scanning Calorimetry (Poirier-Brulez et al. (2006) are also shown (○)

Fig. 3.11 collects the values of  $\tau_3$  at  $T_g$  as a function of  $T_g$  for STS20 and STS10. For STS10 at  $c_w = 0\%$ , one expects  $\tau_3$  at  $T_g$  to be close to 1520 ps, as may be inferred from the corresponding values in STS20 (1384 ps at  $T_g = 446$  K) and STS0 (1660 ps), the latter being calculated from the data reported by Roudaut et al. [2009] for  $T_g = 519$  K; [Orford et al., 1989]. This value is well in line with the experimental data in Fig. 3.11. It is observed that a higher  $T_g$  is associated with a larger  $\tau_3$ , i.e., a higher nanoholes average volume, in both STS20 and STS10. A matrix having a higher  $T_g$  would require a large

free volume fraction to undergo the glass transition and, consequently, larger free volume nanoholes (longer  $\tau_3$ ) are produced at the transition. [Srithawatpong et al., 1999] It is seen that STS10 possesses larger nanoholes at a given  $T_g$  as compared to STS20; this is due to the fact that STS10 requires more water as compared to STS20 to have the same  $T_g$  as observed from Fig. 3.10 and  $\tau_3$  increases as a function of water content.

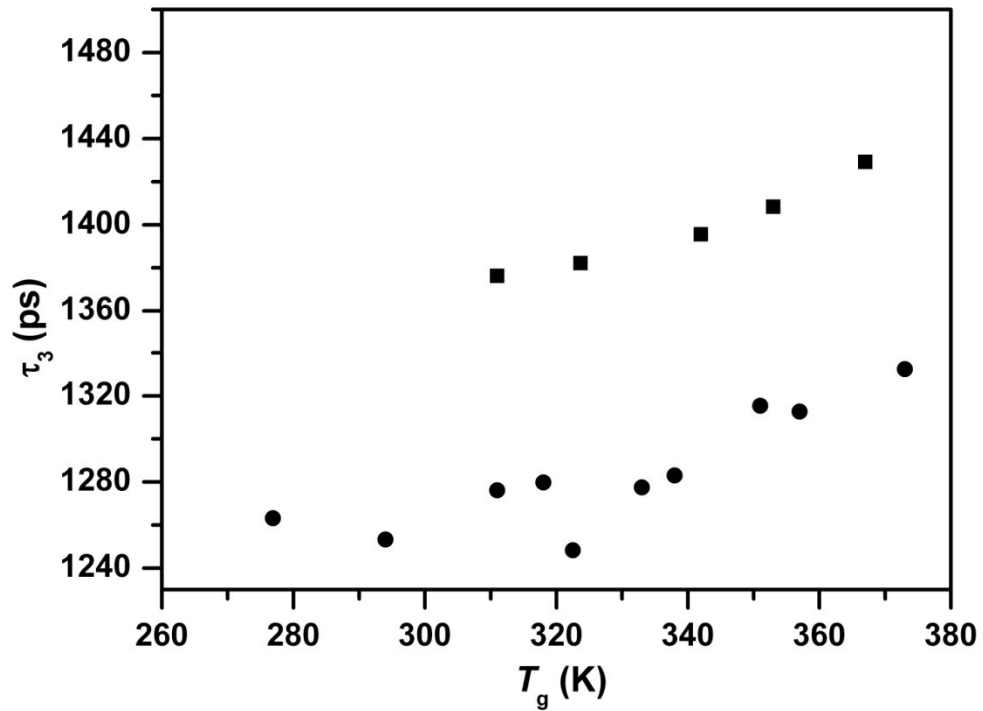


**Figure 3.11:** *o*-Ps lifetime at the glass transition temperature as a function of  $T_g$ (K) in hydrated STS10 (■), and STS20 (●).

Fig. 3.12 shows the variations of  $\tau_3$  vs  $c_g$ , at the transition for STS20 and STS10.  $\tau_3$  is seen to decrease with  $c_g$  indicating a decrease in the critical free volume fraction required for the transition of STS20 and STS10 from glassy phase to rubbery phase. This shows that the addition of water enhances the free volume fractions in STS20 and STS10 by reforming their nanostructure and it is speculated that water molecules do not block the pre-existing nanoholes.

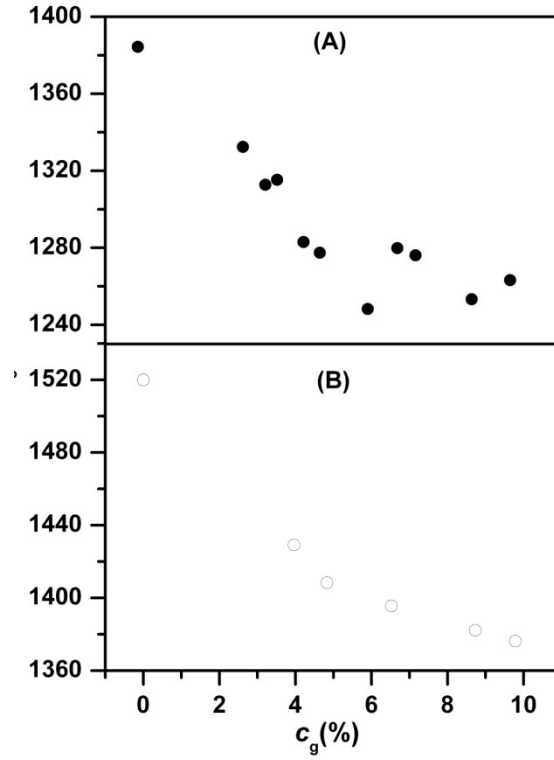


**Figure 3.12: (A) and (B).** *o*-Ps lifetime as a function of water content at the glass transition,  $c_g$  (%), STS20 (●) and STS10 (○), respectively.

Quantitatively, on the experimental observation that  $\tau_3$  varies linearly with  $T$  below (slope,  $a_{\tau,T}$ ) and above ( $b_{\tau,T}$ )  $T_g$ , and also linearly with  $c_w$  below  $c_g$  (slope,  $a_{\tau,w}$ ), the general equations relating  $\tau_3$  to  $T$  and  $c_w$  are as follows:

$$\text{For } T < T_g \quad \tau_3(T, c_w) = \tau_3(T_0, c_0) + a_{\tau,T}(T - T_0) + a_{\tau,w}c_w \quad (3.19)$$

$$\text{For } T > T_g \quad \tau_3(T, c_w) = \tau_3(T_0, c_0) + a_{\tau,T}(T_g - T_0) + a_{\tau,w}c_w + b_{\tau,T}(T - T_g) \quad (3.20)$$

Here,  $\tau_3(T_0, c_0)$  is an arbitrary value of  $\tau_3$  taken as an origin of the plot at a given temperature  $T_0$  (typically, 294 K) and water content  $c_0$  (typically, 0 %). It is noteworthy that eqs. (3.19) and (3.20) do not depend explicitly on  $b_{\tau,w}$ , the slope of the  $\tau_3$  vs  $c_w$  variation above  $c_g$ . Supposing that the variation of  $T_g$  with  $c_w$  is linear, which is true for the central part of the sigmoid in Fig. 3.10 and certainly a good approximation on a short range of  $c_w$  values such as explored in the plots of Fig. 3.8, eqs.(3.19) and (3.20) confirm the experimental observation that the plots of  $\tau_3$  with  $c_w$  should resemble those with  $T$  in

the form of two intersecting straight lines. By definition, the slope of  $\tau_3$  with  $c_w$  below  $c_g$  is  $a_{\tau,w}$  (eq. 3.20). Denoting  $\alpha$  the slope of variation of  $T_g$  with  $c_w$ , eq. (3.21) expresses that the slope of the  $\tau_3$  vs  $c_w$  plot for  $T > T_g$  should be given by:

$$b_{\tau,w} = a_{\tau,w} + \alpha(a_{\tau,T} - b_{\tau,T}) \quad (3.21)$$

In the present case, from several plots of  $\tau_3$  vs  $T$  derived as shown in Fig. 3.9 and from previous work on STS0, [Roudaut et al., 2009] the slopes below and above  $T_g$  may be estimated to be  $a_{\tau,T} = 1$  ps/K and  $b_{\tau,T} = 5$  ps/K respectively. In addition,  $\alpha$  for the central part of the sigmoid in Fig. 3.10 is about -9.5 K/%. Together with the average value of  $a_{\tau,w}$  given in Table 3.1, about 8 ps/%, these figures lead to expect  $b_{\tau,w}$  at about 46 ps/%, in good agreement with the experimental average value given in Table 3.1, thus demonstrating the consistency of our results.

### 3.4.3 Distribution of $\tau_3$ (and $V$ )

It is common use, in PALS studies on polymeric materials, to produce some distributions or probability density functions of  $\tau_3$  (and therefore of  $R$  or  $V$ ) as extracted from the PALS spectra [Mallon, 2003]. Two main routes can be used for this, either a given mathematical equation is hypothesised for the distribution such as is the case for the program [Kansy et al., 1996] LT9, or a grid of  $\tau_3$  values is imposed in the fitting program e.g., CONTIN or MELT programs [Provencher et al., 1982 and Shukla et al., 1993]. In the present case, a sequence of 21 spectra was acquired on a STS20 sample containing 4.3 % water. Each spectrum was counted for 3 h, yielding about 3 million counts. The spectra were next summed 3 by 3, giving an integer of 9 million counts. The results to follow were extracted from the summed spectra. To analyse these spectra, a very simple procedure was chosen: (i) each spectrum was analysed first in terms of 3 discrete decaying exponentials, yielding the usual average  $\tau_i$  and  $I_i$  parameters with a good

variance ( $<1.1$ ); (ii) in a second analysis, the parameters of the short lifetimes ( $\tau_1$ ,  $\tau_2$  – these being much shorter than  $\tau_3$ ) were fixed at the values thus obtained, and a grid of “i” values of  $\tau_3$ ,  $\tau_{3i}$ , was submitted to the fitting program (with  $I_{3i}$  as fitting parameters), distributed above and below the average value,  $\tau_{3av}$ , previously determined as a discrete component; typically, there was a total of 11  $\tau_{3i}$  values, separated by 15 ps steps. The distributions derived for the various summed spectra were all similar, peaking at the same value of  $V$ , corresponding to  $\tau_{3av}$ . We consider that the information extracted from the spectra with this simple approach is neither better nor coarser than with the other conventional methods.

The resulting distribution is shown in Fig. 3.13. It was verified that the sum of the intensities of the  $\tau_{3i}$  components was exactly the same as  $I_{3av}$ , associated to  $\tau_{3av}$ . The probabilities shown in Fig. 3.13 are the average values of the  $I_{3i}$  values from the 7 summed spectra, normalised to  $I_{3av}$  of each of them and the error bars denote the average deviation between these normalised probabilities and their average. Note that, from all spectra, one has  $\tau_2 = (363 \pm 6)$  ps, in good agreement with all previous values measured for this parameter in STS samples, furthermore, the ratio  $I_{3av}/I_1$  is found to be  $2.9 \pm 0.1$ , in good agreement with the expected theoretical value of 3, showing that the short-lived components with lifetimes  $\tau_1$  and  $\tau_2$  are well analysed through our procedure.

It may be seen that the distribution is very narrow; however, the general shape, with a somewhat abrupt increase at low  $\tau_{3i}$  and a tail in the higher  $\tau_{3i}$  range, is very similar to what has been observed in other polymers [Kristiak et al., 1993 and Dlubek et al., 2004]. From Fig. 3.13, it comes out that to the average nanoholes volume of  $30.3 \text{ \AA}^3$  ( $\tau_3 = 1182$  ps) corresponds a fwhm of  $3.4 \text{ \AA}^3$  (51 ps). These values are small, but the *o*-Ps lifetime (and associated  $V$ ) in STS20 is also among the lowest found in literature [Mallon,



2003, Kristiak et al., 1993 and Dlubek et al., 2004, Zhang et al., 2007 and He et al., 2001].

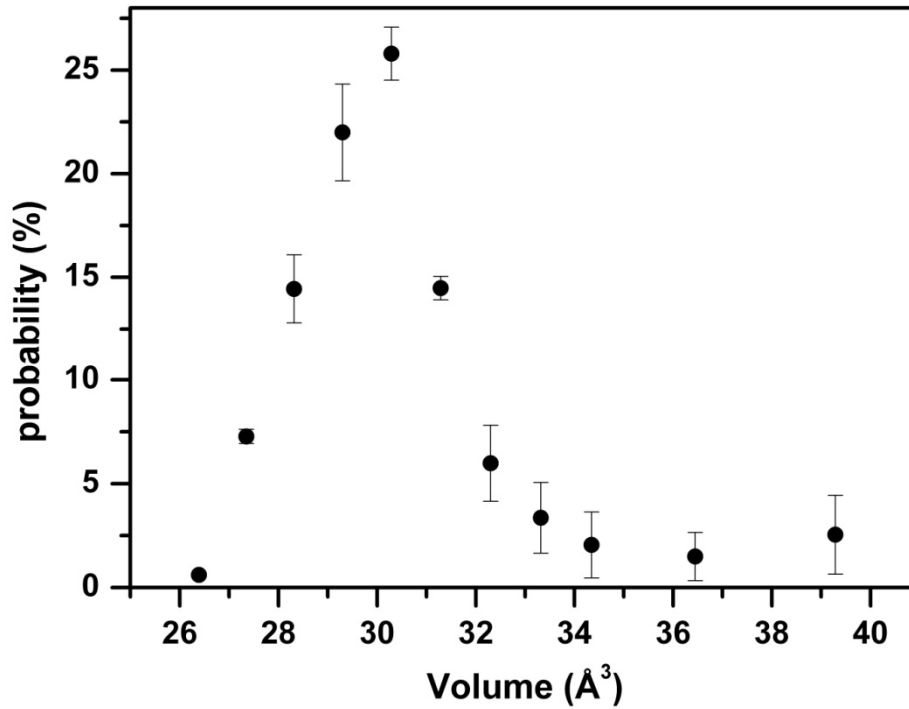


**Figure 3.13:** Volume distribution of the nanoholes at 294 K in STS20, ( $c_w = 4.3\%$ )

#### 3.4.4 Location and role of the water molecules

Figure 3.8 shows the effect of water absorption on the *o*-Ps lifetime in STS20 and STS10 at constant  $T$ .  $\tau_3$  monotonously increases with an average gradient,  $a_{\tau,w}$  (Table 3.1), as a function of water content,  $c_w$ , up to a value,  $c_g$ , and then further increases with a higher gradient,  $b_{\tau,w}$  (Table 3.1). This indicates that the nanoholes present in STS20 and STS10 open up with the absorption of water in both the glassy and rubbery states. Biomolecules have been reported in literature to exhibit a denser structure with the absorption of water, indicating that water is closely associated most probably through intermolecular hydrogen bonding [Kilburn et al., 2004 and Benczedi et al., 1998].

Water can influence the nanoholes in two ways in the glassy state (i) by occupying the nanoholes and (ii) by making intermolecular hydrogen bonding. Townrow et al. (2007) have reported a reduction in the average nanoholes volume due to the filling of nanoholes in an amorphous carbohydrate matrix at very low water content and Dlubek et al. (1999) have reported the filling of nanoholes by water in polyimides up to very high water content. In the present study, the average size of the nanoholes ( $30.3 \text{ \AA}^3$ ) is such that they could hardly accommodate more than a single water molecule whose average volume is about  $30 \text{ \AA}^3$ . Blocking of the nanoholes by water molecules should result in a regular decrease in  $I_3$  as  $c_w$  increases. However, this is not the case and an abrupt decrease in  $I_3$  at  $c_g$  has been observed in this study which rules out the possibility of the occupation of the nanoholes by water molecules. Furthermore, that the free positron lifetime  $\tau_2$  remains constant at  $(363 \pm 6) \text{ ps}$  whatever the water content strongly points to the non-aggregative behaviour of water in STS20 and STS10 which otherwise would have resulted in an increase in  $\tau_2$  with water content, since  $\tau_2$  in water is about  $400 \text{ ps}$  at  $294 \text{ K}$ , increasing with  $T$  [Talamoni et al., 1981]. This confirms that the water molecules are well dispersed in both matrices, STS20 and STS10.

Figure 3.10 shows the expected increase in  $T_g$  with decreasing  $c_w$  for STS20 and STS10. The extrapolated value of  $T_g$  for  $c_w = 0$  for STS20 and STS10 is higher than that of the synthetic polymers of similar molecular weights [van Krevelen et al., 1990]. In the glassy state, biopolymers undergo hydrogen bonding, leading to larger molecular entities which require large amount of heat energy for the segmental fluctuation making their  $T_g$  higher compared to synthetic polymers. On water absorption, water molecules form hydrogen bonds with the hydroxyl groups present in starch and sucrose, disrupting the original structure of STS20 and STS10 and enhancing the molecular vibrations in the vicinity of the nanoholes leading to increase in the nanohole size. This increase in the free

volume fraction in the glassy states of STS20 and STS10 after water absorption reduces their glass transition temperature (plasticising effect of water). With the increase in water content at constant  $T$  in STS20 and STS10, the disruption in the matrices becomes significant and large molecular entities of starch and sucrose are converted into smaller ones which have lower heat energy associated with their molecular and segmental motions and consequently, the matrix is transformed from glassy to rubbery phase.

### 3.5 Conclusion

The present studies provide the information about the changes in the nanostructure of starch matrix on addition of sucrose and water. These studies show that the addition of sucrose in a starch matrix has noticeable influence on both the density and size of nanoholes and confirm that it reduces greatly the  $T_g$ . These influence even become stronger after decomposition of sucrose in the starch matrix, the starch matrix left displaying the properties like density, size of nanoholes and thermal expansion of the polymer below  $T_g$  entirely different from the pure starch. These findings may open the way to the preparation of polymeric matrices possessing some specific properties not initially available. It appears as if some general rules can be applied to most of the biopolymers regarding the role of plasticizers (like water and polyols) but the detailed investigation of the results are required to bring out some noticeable difference among them. It is shown that water molecules are well dispersed in the matrix. Water molecules do not block the pre-existing nanoholes in the matrix and undergo hydrogen bonding.

In these studies, new methods have been developed for the determination of  $T_g$  using PALS. In the presence of sucrose decomposition,  $T_g$  has been determined using a simple model. A new approach has been used to determine the  $T_g$  in the presence of water. A quantitative description has been given for the variation of  $o$ -Ps lifetime or size

of nanoholes as a function of water concentration and temperature. These studies may provide a backbone for the further studies on biopolymers nanostructure and thermal mechanical properties.

## **CHAPTER-IV**

---

# **NANOSTRUCTURE OF POLY ETHYLENE TEREPHTHALATE (PET) POLYMER: EFFECT OF GRAFTING AND ION-IRRADIATION**

Modifications of polymers by graft copolymerization of functional monomers and by ion-irradiation followed by etching are well established techniques to impart favorable physical and chemical properties to given polymers. Several techniques have been used to initiate the graft copolymerization including ion-radiation [He et al., 2003], ultraviolet light [Song et al., 2006 and Chu et al., 2006], plasma treatment [Lazea et al., 2005 and Gupta et al., 2002] etc. Among these techniques radiation induced graft copolymerization is advantageous because of its extensive penetration into the polymer matrix, and its ability to form radicals rapidly and uniformly for initiating the grafting in various kinds of polymers. Hence, the nanostructure of polymers is uniformly modified by radiation induced graft copolymerization in terms of its physical and chemical properties. Such changes have a strong impact on the structural and hence thermo-mechanical properties of the polymers.

The irradiation of the polymers by energetic heavy ions leads to the modification in the nanostructure due to chain scission and new bonds formation which change the porosity or transport properties of the polymers. These properties are further modified by etching the irradiated polymers in acidic or alkaline medium [Itoh et al., 1994 and Trautmann, 1995]. These polymers (ion-irradiated and etched) having controlled and well defined pores are widely used as templates for the synthesis of nano-materials [Apel et al., 2006] and in nano-filtration [Ferain et al., 1994]. They are also useful as *in vitro* substrates in cell biology [Sergent-Engelen et al., 1990 and Ferain et al., 1994] and in the development of new sensor devices [Tahara et al., 1997; Zhang et al., 1997 and Singh et al., 2006]. It is, therefore, important to study the nanostructural changes of the polymeric membranes under different experimental conditions for their technological applications.

Poly ethylene terephthalate (PET) films are characterized by determining its properties like high crystallinity, thermal stability, hydrophobicity and presence of

chemically inert functional groups [Karagianidis et al., 2008]. To get desirable properties, various functional monomers can be grafted onto PET [Avny et al., 1978]. Radiation induced graft copolymerization of PET with various vinyl monomers such as styrene [Nasef, 2000 and 2002], acrylic acid [Huglin et al., 1973], methacrylic acid [Uchida et al., 2000], 2-methyl 5-vinyl pyridine [Helbeish et al., 1978] etc. has been reported. Radiation induced graft copolymerization is well known to induce the chemical and physical changes in the host polymer matrix [Charlesby, 1960; Nasef, 2000]. Ion-irradiation of PET films followed by etching with alkaline medium is known to change the pores size, distribution and their interconnectivity which leads to modified transport properties of the polymer. Therefore, monitoring of these structural changes is important to evaluate the applicability of the grafted and ion-irradiated PET films for various applications.

In the present study positron annihilation spectroscopy (bulk and depth dependent measurements) has been used for the characterization of the nanostructure of grafted and ion-irradiated PET films. Techniques like dynamical mechanical analysis (DMA), X-ray diffraction (XRD) and Fourier transform infra red (*FTIR*) have been used to supplement the positron data.

## **4.1. Experiments**

### **4.1.1. Sample preparation and characterization**

#### **4.1.1.1 Grafted samples**

PET films of 50  $\mu$ m thickness (DU PONT) were washed with methanol to remove any impurities adhering to the surface. The films were dried under vacuum at 60°C before using them for grafting. Acrylic acid (Merck India Ltd.) was distilled under vacuum before using for the experiments. Mohr's salt was supplied by Qualigens, India. Distilled water was used for all the experiments. Irradiation of PET films was carried out in air by

using a  $^{60}\text{Co}$  gamma radiation source at a dose rate (0.18 kGy/h) to give a total dose of 40 kGy to the samples. Graft copolymerization of acrylic acid onto PET was carried out by pre-irradiation method. The grafting was carried out in glass ampoules of  $2 \times 10 \text{ cm}^2$  size. A weighed amount of the irradiated PET films (~600 mg) were placed into the ampoules containing aqueous monomer (acrylic acid) solution having monomer concentration of 40 % (vol %) along with Mohr's salt of 0.1% (wt %) to prevent the homopolymerization of the monomer. Nitrogen gas was purged into the ampoules to remove air trapped inside the reaction mixture. The ampoules were subsequently placed in a water bath maintained at 50, 60, 70 and 80°C for a constant reaction time of 10 hours. After the reaction, the ampoules were removed and the samples were washed with boiling water to remove any homopolymer adhering to the sample surface. The samples were dried in an oven at 60°C under vacuum and the degree of grafting was determined using the following expression.

$$\text{Degree of grafting (D. G)} = \frac{W_g - W_i}{W_i} \times 100 \quad (4.1)$$

where,  $W_i$  and  $W_g$  are the weight of the ungrafted PET and grafted PET copolymer films, respectively.

These samples were characterized using positron annihilation spectroscopy supplemented by FTIR, XRD and DMA measurements. PALS measurements were carried out by using a fast-fast coincidence system with plastic scintillation detectors (chapter II). The results for each sample reported are the average of three measurements.

FTIR spectra of the neat PET and the graft copolymer samples were recorded with a Nicolet Omnic 3 Fourier transform infrared spectrometer with a resolution of  $4 \text{ cm}^{-1}$ . Signals from 16 scans of the same sample were averaged before performing Fourier transform. The measurements of dynamic mechanical properties of the neat PET and PET-g-AA samples were carried out at a frequency of 1 Hz and a heating rate of 5°C/min



on a Rheometric Scientific DMTA. The temperature range of the measurements was from -130°C to 200°C. The crystallinity of the neat PET and the graft copolymer samples were evaluated using wide angle XRD measurements. For these measurements, the XRD patterns for the samples were recorded using a Cu K $\alpha$  ray of wavelength 1.54 Å between 2 $\theta$  range of 3-90° at 0.2°/10 S with a Phillips x-ray diffractometer.

#### 4.1.1.2 Ion-irradiated and etched samples

PET polymer films of 25  $\mu\text{m}$  thickness and 1.39  $\text{g}/\text{cm}^2$  density were irradiated by 100 MeV  $^{35}\text{Cl}$  beam ( $7 \times 10^7$  ions/ $\text{cm}^2$ ) in the presence of air at BARC-TIFR pelletron accelerator facility in India. The beam energy was sufficiently high for the ions to pass through the polymer film. The ion-irradiated film was etched with 6N NaOH solution for 45 minutes. The positron annihilation measurements were carried out using the same set up as for grafted samples but the time resolution for these measurements was 250 ps for the used discriminators window settings. The lifetime spectra were analyzed using PATFIT-88 [Kirkegaard et al., 1989] and CONTIN [Provencher et al., 1982] routines in terms of discrete positron lifetime components and lifetime distribution, respectively.

Depth profiling of the surface of the pristine, irradiated and etched samples, as the case may be, was carried out using the slow positron beam coupled with Doppler broadening set up (details in chapter II). The mean implantation depth  $\langle Z \rangle$  of the mono energetic positron beam having incident energy  $E$  (keV) in a material of density  $\rho$  (g/cc) is given as

$$\langle Z \rangle = \frac{A}{\rho} E^n \quad (4.2)$$

where,  $\langle Z \rangle$  is expressed in nm. The parameters,  $A$  and  $n$ , are the material dependent constants [Schultz et al., 1998 and Coleman, 2003]. For polymers, the values of  $A$  and  $n$

are generally taken as 40 and 1.6, respectively [Xie et al., 1995 and Myler et al., 1998]. The depth-dependent  $S$ -parameter and the three photon to two photon ( $3\gamma/2\gamma$ ) annihilation ratio measurements are the sensitive probes to characterize the architecture of the pores or nanoholes, electron density and inter connectivity of the nanoholes to the surface of a polymer [Coleman, 2003]. The Doppler broadening measurements were carried out in the energy range of 200 eV to 6 keV which corresponds to a depth upto  $\sim 500$  nm. The  $S$ -parameter was evaluated as the fractional peak area in the region of  $511 \pm 0.75$  keV. The  $S$ - $E$  curves were fitted using the VEPFIT program to evaluate  $e^+$ /Ps diffusion length [van Veen et al., 1990]. The  $o$ -Ps  $3\gamma/2\gamma$  annihilation ratio was also calculated by taking the ratio of the integrated counts in the range of 375 keV to 460 keV to the integrated counts under 511 keV full-energy peak.

All the samples studied were also characterized by FTIR (in transmission mode) using JASCO FT-IR-420 spectrometer and XRD using Philips X'pert Pro XRD unit.

## 4.2. Results and Discussion

### 4.2.1. PET-g-AA samples

#### 4.2.1.1 Radiation grafting mechanism

The grafting of acrylic acid onto PET films was accomplished in two consecutive steps i.e., radiation activation of the PET backbone followed by the grafting of the monomer (acrylic acid) onto the activated surface. The irradiation of the base polymer, PET, in the presence of oxygen induces formation of hydro peroxide groups along the polymer chains [Botelho et al., 2001]. The latter is then subsequently used for initiation of polymerization of acrylic acid onto it. The various parameters to control the degree of grafting are the reaction temperature, monomer concentration, total dose to the base polymer and the additives. In the present study, the degree of grafting was varied by

carrying out the reaction for 10 hours at different temperatures. The variation of the degree of grafting of AA with reaction temperature is shown in Fig. 4.1. The degree of grafting increases with the increase of the reaction temperature. It may be mentioned that Mohr's salt concentration for the graft copolymerization has been selected on the basis of the reported values for effective suppression of homopolymer formation [Gupta et al., 2008] during graft copolymerization. The graft copolymers were found to be translucent compared to the neat PET films, which were perfectly transparent.

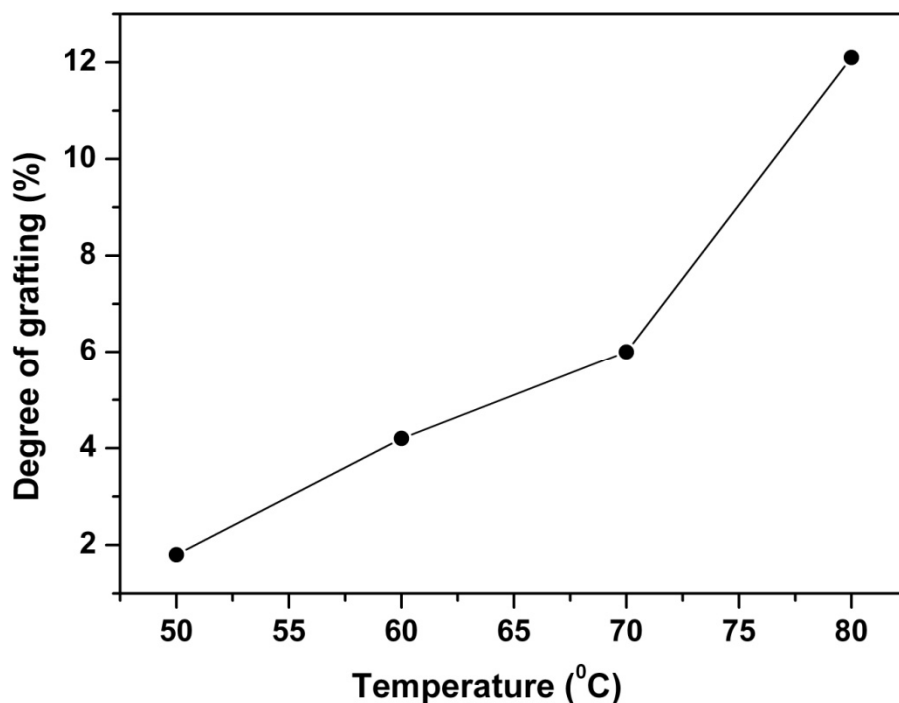


**Figure 4.1:** Variation of the degree of grafting of acrylic acid with reaction temperature

#### 4.2.1.2 FTIR, XRD and DMA measurements

The graft copolymers were identified by FTIR spectral analysis. Figure 4.2 shows a typical FTIR spectrum of the PET-g-AA graft copolymer with 12.1% degree of grafting. A broad band in the range of 2300-3400  $\text{cm}^{-1}$  is observed in the PET-g-AA polymers.

This broad absorption corresponds to the stretching vibrations of -OH of grafted acrylic acid.

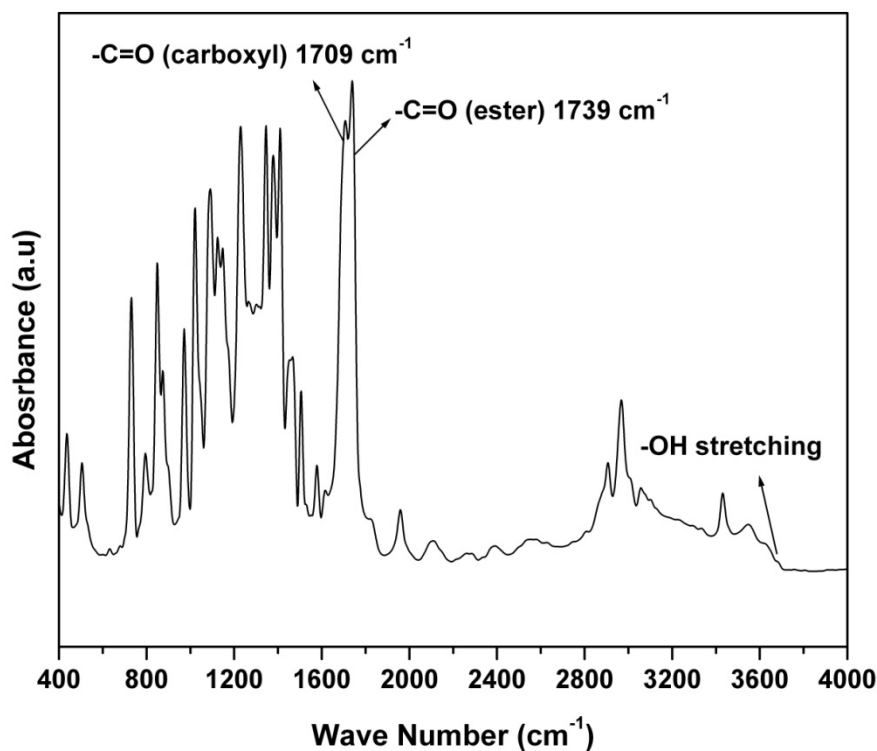


**Figure 4.2:** Typical FTIR spectrum of PET-g-AA (12.1% degree of grafting)

Figure 4.3 shows the  $\tan\delta$  values, from DMA measurement, vs. temperature plot of the neat PET and the graft copolymer samples. From the results, two different relaxation peaks are noticed for the neat PET as well as the PET-g-AA graft copolymers. Thus, the grafting of AA onto PET does not introduce any new relaxation behavior. However, the peak positions and the corresponding magnitude of the relaxation peaks are affected even at low degree of grafting. The relaxation peak positions for PET observed in the present work are matching with those observed by McGonigle et al.,(2000) in their study of the influence of physical ageing on the structural relaxation and molecular motion in PET and related materials.

The glass transition temperature or the  $\alpha$ -relaxation of the samples are observed in the temperature range of 100 to 130°C, while the sub room temperature secondary relaxations are observed in the range of -130 to 25°C (Fig. 4.3). The glass transition temperature ( $\alpha$  relaxation) increases monotonically with the increase in the degree of grafting. This can be attributed to the incorporation of glassy acrylic acid graft chains onto PET matrix. The  $\beta$  relaxation (subroom temperature transition) position does not shift with the increase in the degree of grafting. The magnitude of the  $\beta$ -relaxation peak decreases marginally in 1.8% grafting while it marginally increases at 4 and 6 % grafting. A discernible increase in the  $\beta$  relaxation is observed for 12.1% grafting. This suggests that the introduction of acrylic acid grafts increase the molecular motion in the PET base polymer.

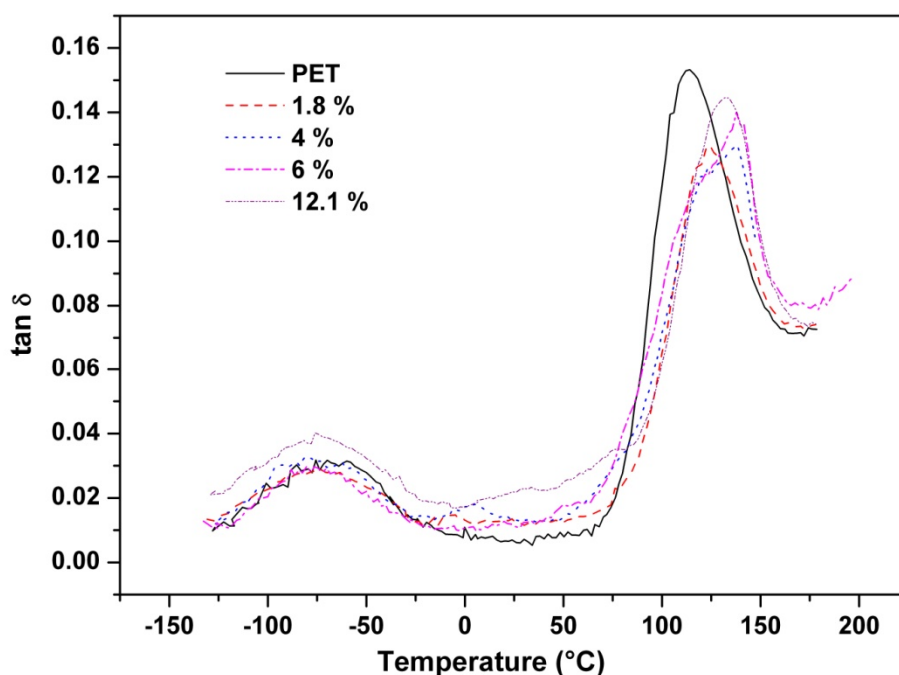


**Figure 4.3:**  $\tan\delta$  vs temperature plot of the neat PET and PET-g-AA copolymer

Figure 4.4 shows the storage modulus vs. temperature plot for the neat PET and the PET-g-AA samples. From the figure, it is seen that the graft copolymers have lower moduli compared to the base polymer. However, no particular trend in the variation of the modulus with the degree of grafting is observed. The 12.1% grafted sample, contrary to our expectation, has the highest modulus value among the graft copolymers followed by the 6% graft copolymer, while the 4% graft copolymer has the lowest modulus.

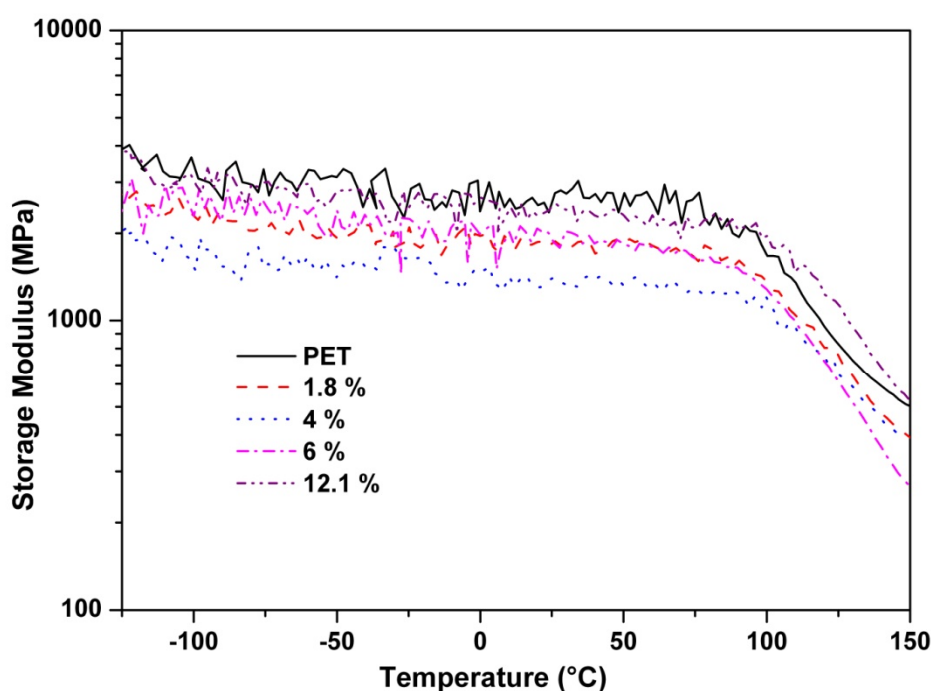


**Figure 4.4:** Storage modulus vs temperature plot of neat PET and PET-g-AA copolymers

The variation in the degree of crystallinity induced by the structural changes during radiation induced grafting of AA onto PET was investigated by using wide angle x-ray diffraction (WAXD). Figure 4.5 shows the diffractograms of the PET-g-AA samples compared to the neat PET film. The relative crystallinity of all the samples was evaluated from the WAXD plots. The peaks were fitted to the Lorentzian distribution and the relative crystallinity was calculated from the area under the crystalline and amorphous peaks. Only a marginal change (decrease) in the relative crystallinity of the graft

copolymers was observed compared to neat PET which can be well within the error limits of the peak fitting procedure. However, with the increase in the degree of grafting, a slight shift of the diffractograms to higher Bragg angles is observed compared to the base polymer. Since grafting occurs only in the amorphous region of the semicrystalline base polymer. Since grafting occurs only in the amorphous region of the semicrystalline base polymers and the present degree of grafting extends only upto 12.1%, the alteration of the crystal structure of PET with the degree of grafting is not expected.

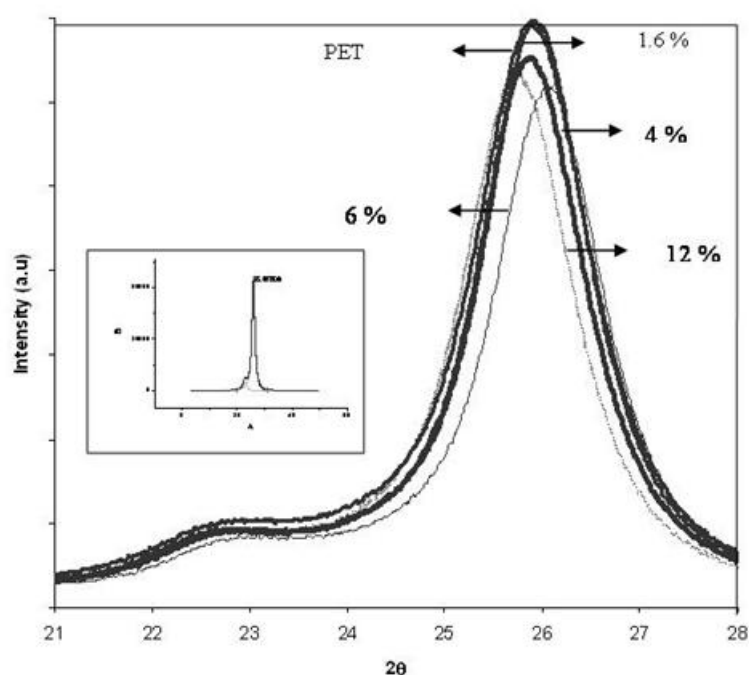


**Figure 4.5:** WAXD plot of neat PET and grafted copolymers. Inset shows a typical peak fitting to evaluate the relative crystallinity

#### 4.2.1.3 Positron annihilation measurements

The *o*-Ps lifetime and intensity ( $\tau_3$  and  $I_3$ ), as a function of the degree of grafting are shown in Figs. 4.6 A and B, respectively. The *o*-Ps lifetime,  $\tau_3$ , is correlated to the free volume holes radius through the Tao-Eldrup equation and the intensity,  $I_3$ , is proportion to the concentration of these free volume holes present in polymer. The  $\tau_3$  and  $I_3$  values of the base polymer, PET, were 1.68 ns and 15.4%, respectively. The  $\tau_3$  and  $I_3$

values of the graft copolymers were higher compared to the base polymer. However, the variation is not smooth. At 1.8 % grafting the *o*-Ps lifetime remains unchanged compared to the base polymer followed by an increase upto 6% grafting, while 12.1% grafting registers a sharp drop in the *o*-Ps lifetime. From the variation of the intensity with the degree of grafting, we observe that the graft copolymers have lower  $I_3$  values compared to the base polymer, however, the decreasing pattern is not continuous. A sharp drop of intensity at 1.8% grafting is followed by an increase for 4% and 6% and subsequently the lowest value is registered for the 12.1% graft copolymer.

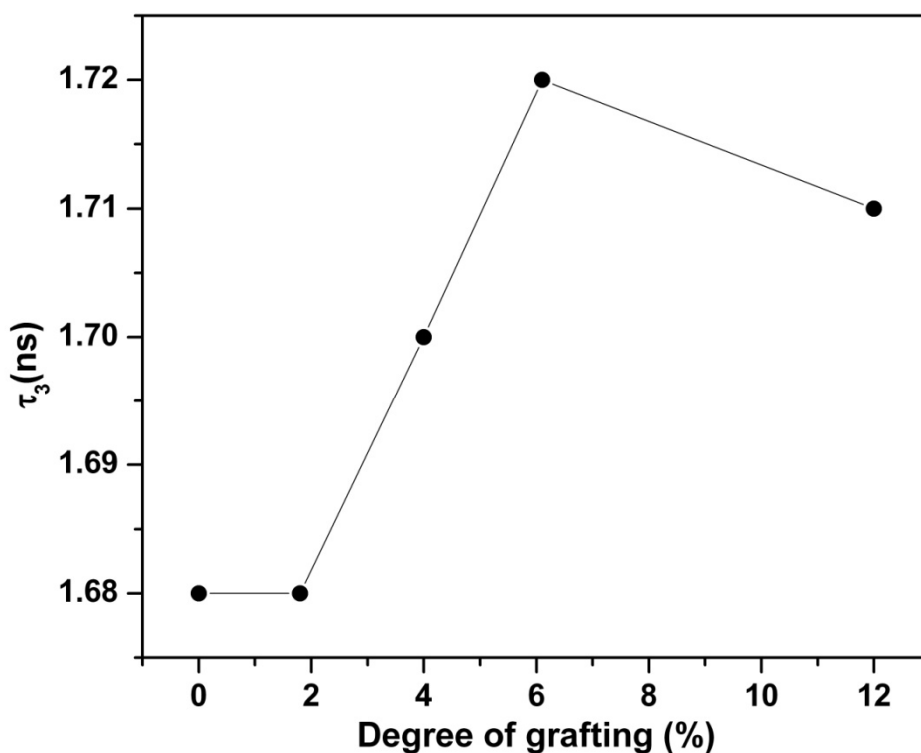


**Figure 4.6A:** *o*-Ps lifetime as a function of degree of grafting



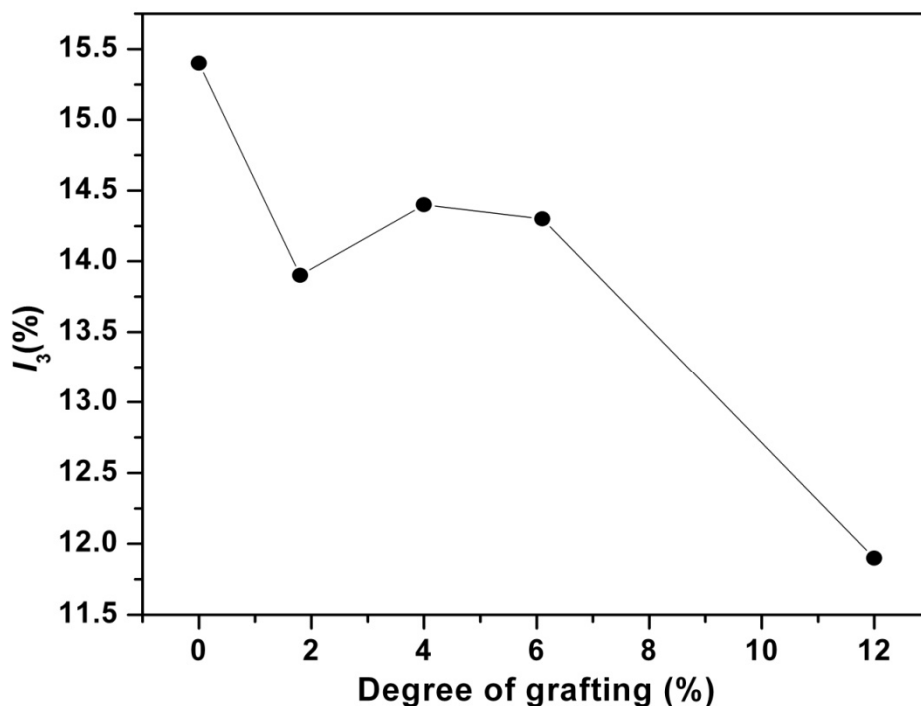


**Figure 4.6B:** *o*-Ps intensity as a function of degree of grafting

The variation of the fractional free volume ( $f_v$ ) with the degree of grafting is presented in Fig. 4.6C. The fractional free volume ( $f_v$ ) has been calculated using the equation [Wang et al., 1990]

$$f_v(\%) = C \langle V_f \rangle I_3 \quad (4.3)$$

where,  $\langle V_f \rangle$  is the volume ( $4\pi r^3/3$ ) of spherical free volume holes calculated using radius obtained from Tao-Eldrup equation,  $I_3$  (%) is the *o*-Ps intensity, and  $C$  is taken as  $0.0018 \text{ nm}^{-3}$  from the specific volume data [Wang et al., 1990]. The fractional free volume variation follows the same trend as the intensity, with the increase in the degree of grafting.

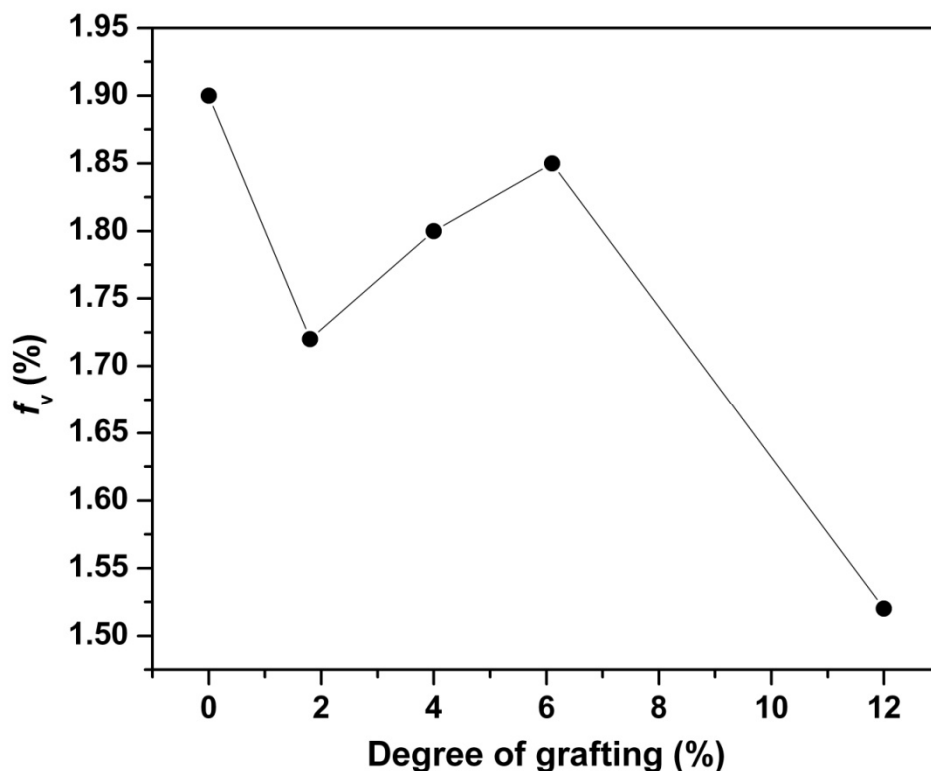


**Figure 4.6C:** Fractional free volume as a function of degree of grafting

Thus, there is a complex variation in the free volume parameters with the degree of grafting. However, strictly on qualitative terms, an increase in *o*-Ps lifetime with a decrease in intensity is observed for the graft copolymers, compared to the base polymer (Fig. 4.6). It must be noted that the reported values of  $\tau_3$  and  $I_3$  for polyacrylic acid are 1.95 ns and 7.6%, respectively [Gomma, 2007]. Thus, the base polymer, PET, has more number of smaller holes, while the acrylic acid has lesser number of bigger holes. Purely on additive terms, graft copolymerization should result in expansion of the average hole size and reduction in the number of holes in the graft copolymers.

Until 6% grafting the trend seems to follow the simple additive rule, with an increase in the *o*-Ps lifetime and a decrease in the intensity (Fig. 4.6). This is also supported by the subroom temperature secondary relaxation behaviour of the graft copolymers observed from DMA (Fig. 4.3) as a definitive relation between free volume

properties and secondary relaxations has already been reported [Chen et al., 1999; Sudarshan et al., 2007]. However, at 12.1% grafting there is a simultaneous decrease in the  $\tau_3$  and  $I_3$  values (Fig 4.6), though it shows maximum increase in the secondary  $\tan\delta$  relaxation (Fig. 4.3). It seems dynamic transition alone cannot account for the trend reversal. The complicated variation of free volume parameters in the graft copolymers can be due to the sensitivity of positron/Ps not only to the preexisting free volume holes in the PET backbone and the AA grafts but also to any interfacial spaces, such as those created between boundaries of two phases viz. PET backbone and AA grafts. This phenomenon has been reported especially for immiscible blends [Liu et al., 1995]. The graft copolymers of hydrophobic PET base polymer and the hydrophilic acrylic acid are expected to have a complex phase separated morphology. The effect of the newly formed interfacial spaces on the variation of the free volume parameters can be observed from the variation of the intermediate lifetime and intensity components,  $\tau_2$  and  $I_2$ , with the degree of grafting, as shown in Figs. 4.7A and B, respectively. The intermediate lifetime component is attributed to the annihilation characteristics of free or trapped positrons in interfacial spaces.

The sharp increase in  $\tau_2$  at the higher degree of grafting substantiate our contention that there is trapping of positrons in the interfacial spaces which do not form positronium and it is more evident with the increase in the degree of grafting. Thus, the complicated variation in PALS parameters can be reasonably likened to similar behaviour in the immiscible blends [Liu et al., 1995]. However, the free volume hole properties obtained in these systems of more than one phases can be further interpreted only after studying the graft copolymers at higher degree of grafting with different base and graft copolymers.

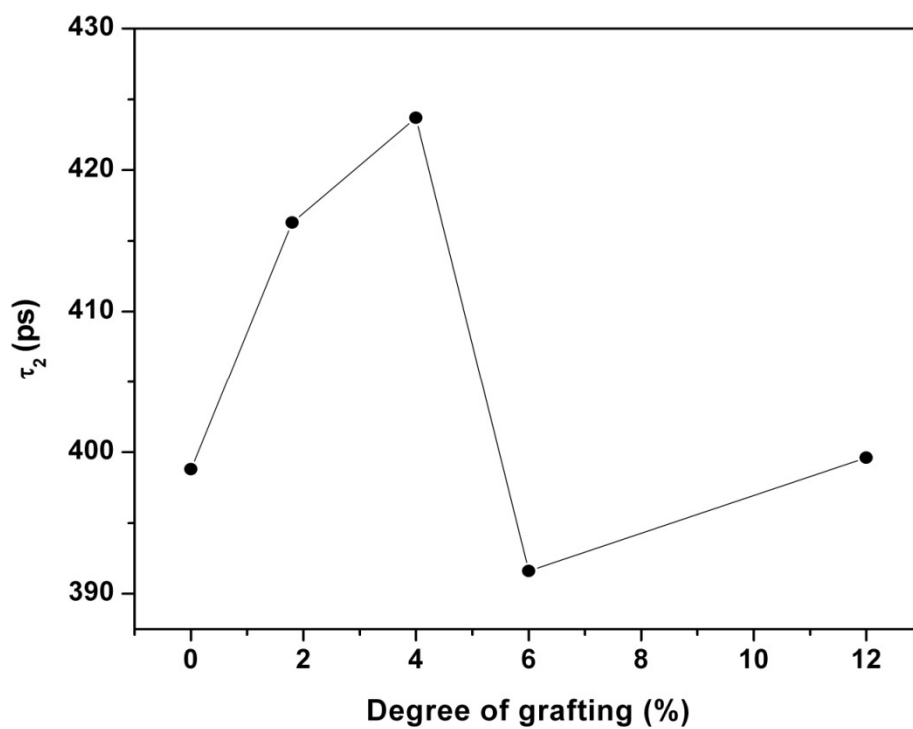


Figure 4.7A: Free positron lifetime as function of degree of grafting

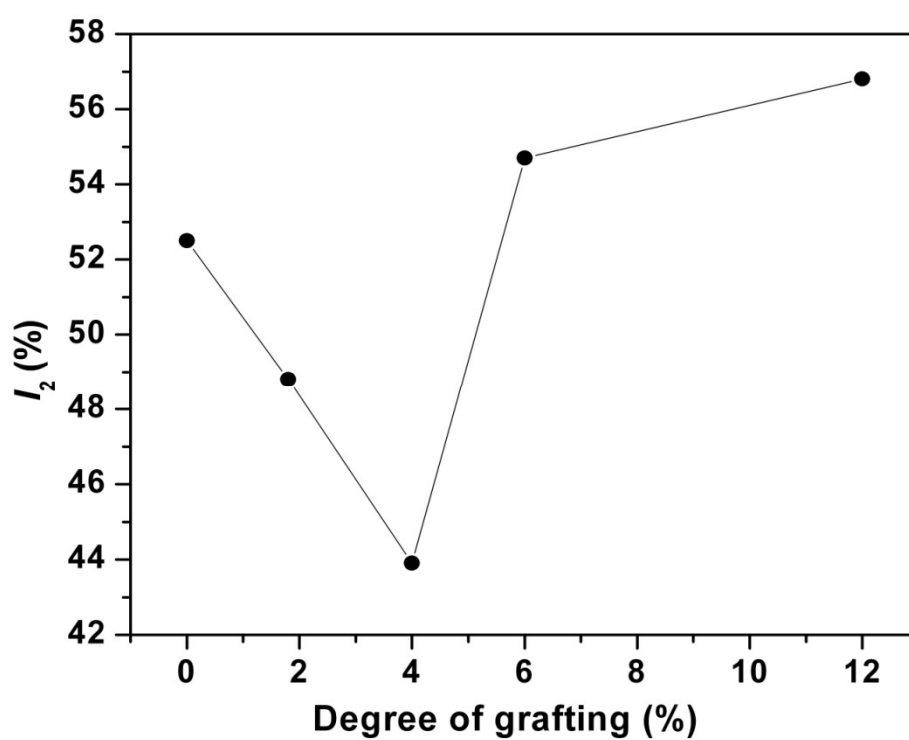
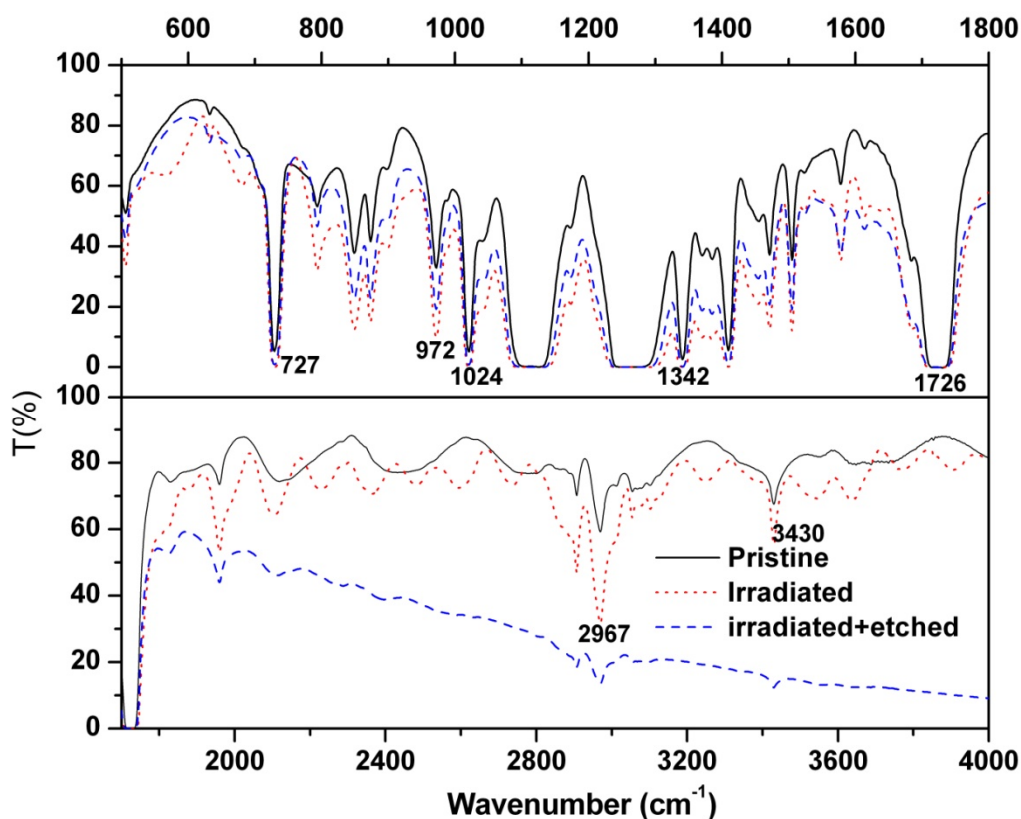


Figure 4.7B: Free positron intensity as function of degree of grafting

## 4.2.2. Ion-irradiated and etched samples

### 4.2.2.1 FTIR and XRD measurements

FTIR spectra of the pristine, ion-irradiated and etched PET samples are shown in Fig. 4.8. The observed characteristic peaks are as follows: (i)  $727\text{ cm}^{-1}$ : deformation of phenyl ring and bending vibration of  $\text{CH}_2$  group, (ii)  $972\text{ cm}^{-1}$ : C-H deformation out of plane, (iii)  $1024\text{ cm}^{-1}$ : C-O-C stretching, (iv)  $1342\text{ cm}^{-1}$ : C-C stretching of phenyl ring and vibration band of para substituted benzene ring, (v)  $1726\text{ cm}^{-1}$ : stretching vibration of C=O, (vi)  $2967\text{ cm}^{-1}$ : C-H stretching of  $\text{CH}_2$  group and (vii)  $3430\text{ cm}^{-1}$ : O-H group. All these characteristic bands are present in the pristine, ion-irradiated and etched samples. No new peaks are observed after ion-irradiation and etching. It may be mentioned that there is a report of the formation of  $\text{-C=C-}$  double bonds when PET is irradiated with energetic Cu ions (120 MeV) [Singh et al., 2008] while similar chemical changes are not seen for energetic C ion (70 MeV) irradiation in the PET. Singh and Prasher (2006) have reported that the IR transmittance through various functional groups changes after the Li (50 MeV) ion-irradiation on the PET. In the present study too, we have observed a decrease in the transmittance of the peaks like  $972\text{ cm}^{-1}$ ,  $2967\text{ cm}^{-1}$  and  $3430\text{ cm}^{-1}$  corresponding to C-H and C-OH groups, in the irradiated membrane. This might be due to the chain scission upon irradiation, and reaction of oxygen (from air) with radicals. On etching, the polymer becomes translucent and the transmittance in the range of  $1800\text{-}4000\text{ cm}^{-1}$  decreases considerably. We have not observed any new peak in the FTIR spectra, which indicates that no other major modification in the chemical structure has taken place after low fluence ion-irradiation and subsequent etching in our samples.



**Figure 4.8:** FTIR spectra of the pristine, ion-irradiated and etched PET films

X-ray diffraction spectra of the pristine, ion-irradiated and etched PET are shown in Fig. 4.9. XRD spectrum of the pristine sample shows that it is highly crystalline. Singh et al. (2008) reported a decrease in the crystallinity of PET by irradiation with copper and carbon ions to the fluence of  $10^{13}$  to  $10^{14}$  ions/cm<sup>2</sup>. In the present study, no new phase formation is observed in XRD spectra upon ion-irradiation and etching probably due to the low fluence of irradiation ( $10^7$  ions/cm<sup>2</sup>). Also, FWHM of XRD peak shows that there is no change in the crystallinity of the sample after ion-irradiation and etching.

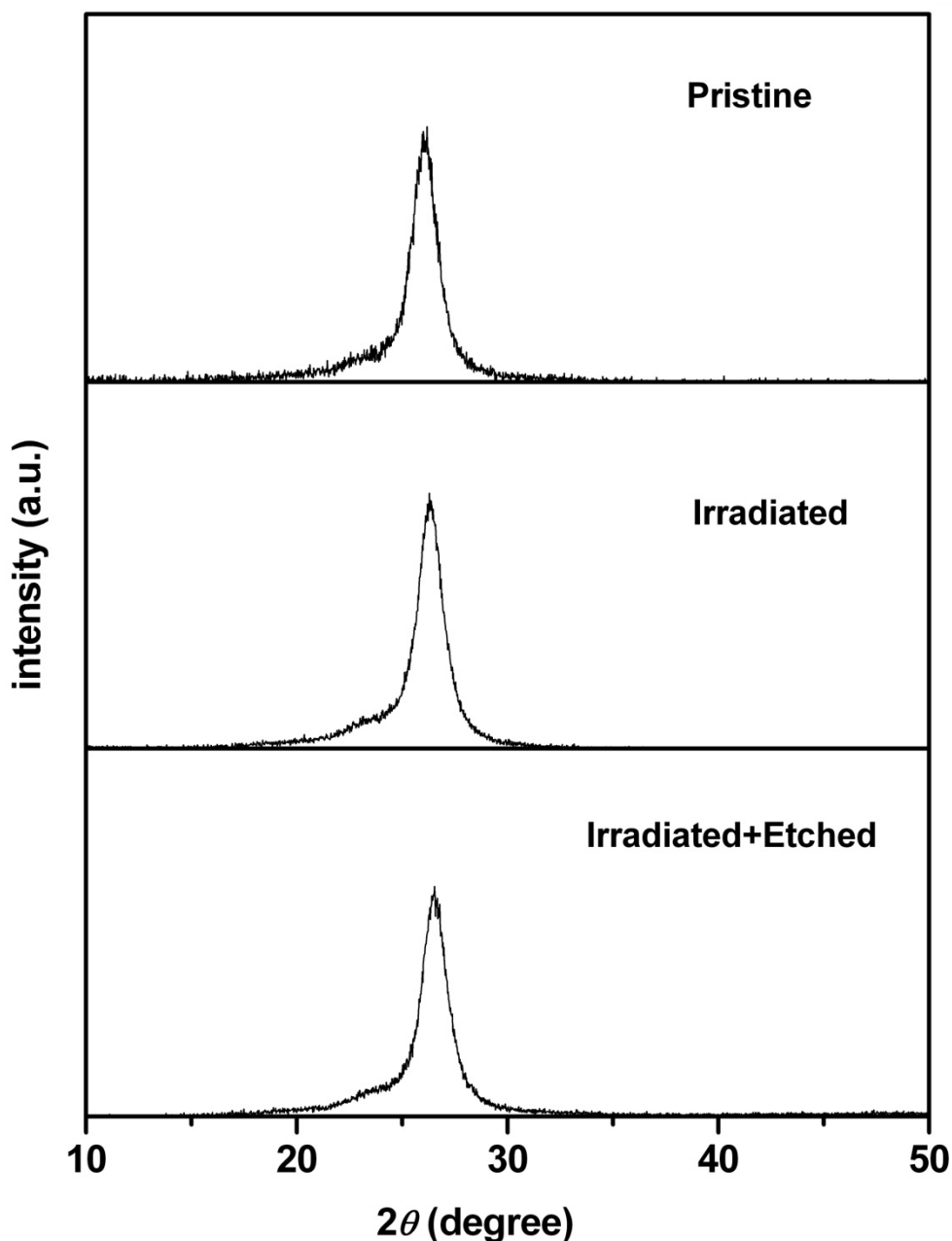


**Figure 4.9:** XRD spectra of the pristine, ion-irradiated and etched films

#### 4.2.2.2 Positron annihilation measurements

The *o*-Ps *pick-off* lifetime ( $\tau_3$ ) and the corresponding intensity ( $I_3$ ) in the pristine, ion-irradiated and etched PET films are listed in Table 4.1. On irradiation,  $\tau_3$  decreases indicating the reduction in the size of the free volumes in the bulk of the polymer. On ion-irradiation, the degree of cross-linking increases in the polymer due to

the formation of radicals which undergo new bonds formation. As a result of cross-linking, the size of the free volumes decreases which results in the reduction of  $\tau_3$ . The intensity  $I_3$  decreases upon ion-irradiation of the polymer which indicates the overall reduction in the fraction of available free volumes in the bulk. The presence of some inhibitor species in the irradiated polymer sample is also possible, which may be responsible for the inhibition of Ps formation and hence, the reduction in  $I_3$ .

**Table 4.1** The *o*-Ps *pick-off* lifetime ( $\tau_3$ ) and intensity ( $I_3$ ) evaluated from PATFIT

Sample	PATFIT analysis	
	$\tau_3$ (ns)	$I_3$ (%)
Pristine	1.95	15
Ion-irradiated	1.68	10
Etched	1.61	13

On etching, no significant change in  $\tau_3$  was observed as compared to ion-irradiated PET. This shows that etching by NaOH has not changed the average nanostructure of the bulk of the polymer. The *pick-off* intensity  $I_3$ , on the other hand, is observed to increase on etching of the ion-irradiated PET films. The increase in  $I_3$  can be attributed to either the increase in fractional free volume or the removal of scission products and the inhibitor species due to the etching. The nature of the pore size distribution shows that the latter is more probable.

The free volume size distribution as shown in Fig. 4.10 has been evaluated from the Tao-Eldrup equation using the *o*-Ps *pick-off* lifetime distribution obtained from the CONTIN analysis. The peak positions of the size distribution are in agreement with the



values obtained from the PATFIT (Table 4.1). FWHM of the size distribution curves for the pristine, ion-irradiated and etched polymer were observed to be 0.36 nm, 0.24 nm and 0.23 nm respectively, which illustrates that the free volume size distribution becomes narrower on ion-irradiation.

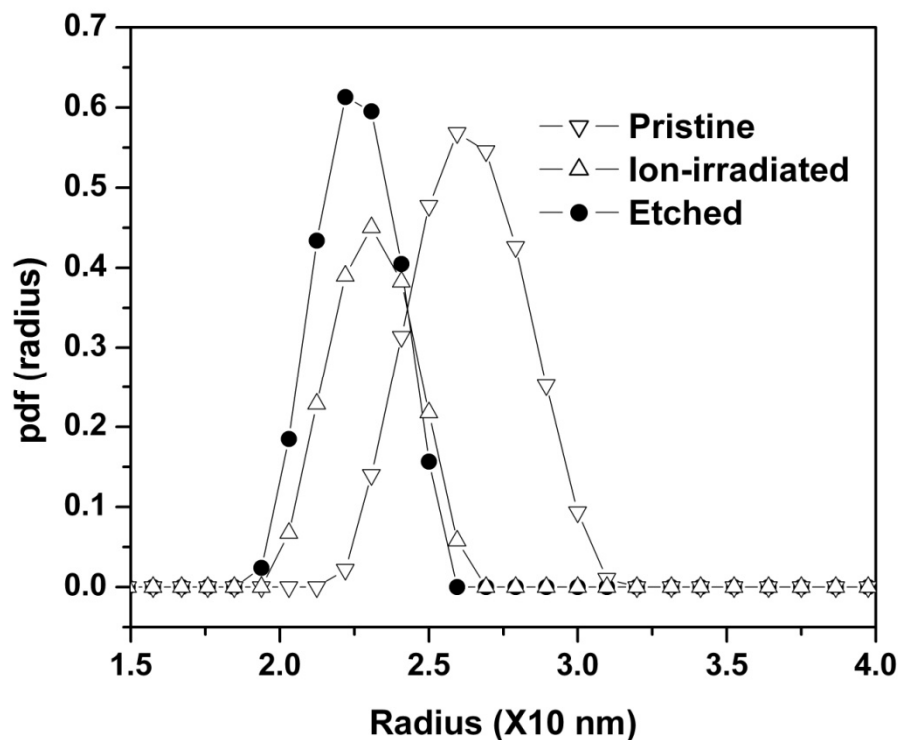


**Figure 4.10:** The free volume radius ( $\times 10$  nm) distributions in the bulk of pristine, ion-irradiated and etched PET films

#### 4.2.2.3 Depth dependent Doppler broadening measurements

The modification at the surface and near surface region due to the ion-irradiation and etching on the PET membranes was probed by Doppler-broadened  $S$ -parameter measurement and  $3\gamma/2\gamma$  annihilation ratio using the slow positron beam. The plots,  $S$ -parameter and  $3\gamma/2\gamma$  ratio as a function of the positron implantation energy ( $E$ ) of the pristine, ion-irradiated and etched PET films, are shown in Figs. 4.11 and 4.12, respectively.

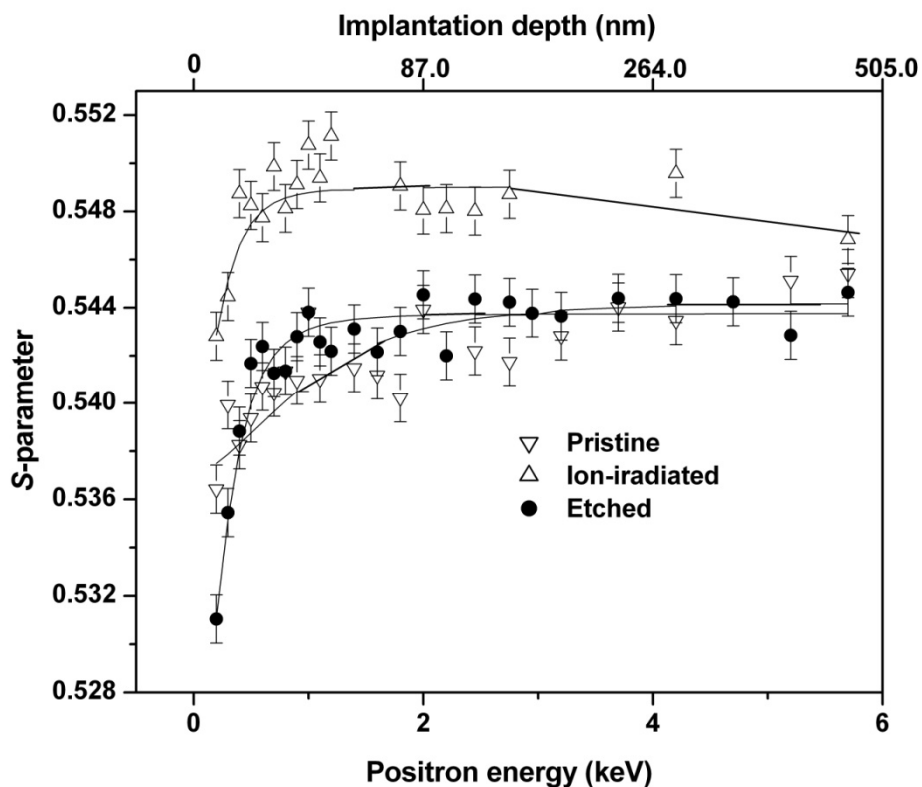


**Figure 4.11:** The S-parameter as a function of positron energy, top axis shows the positron implantation energy; solid lines are the eye guides

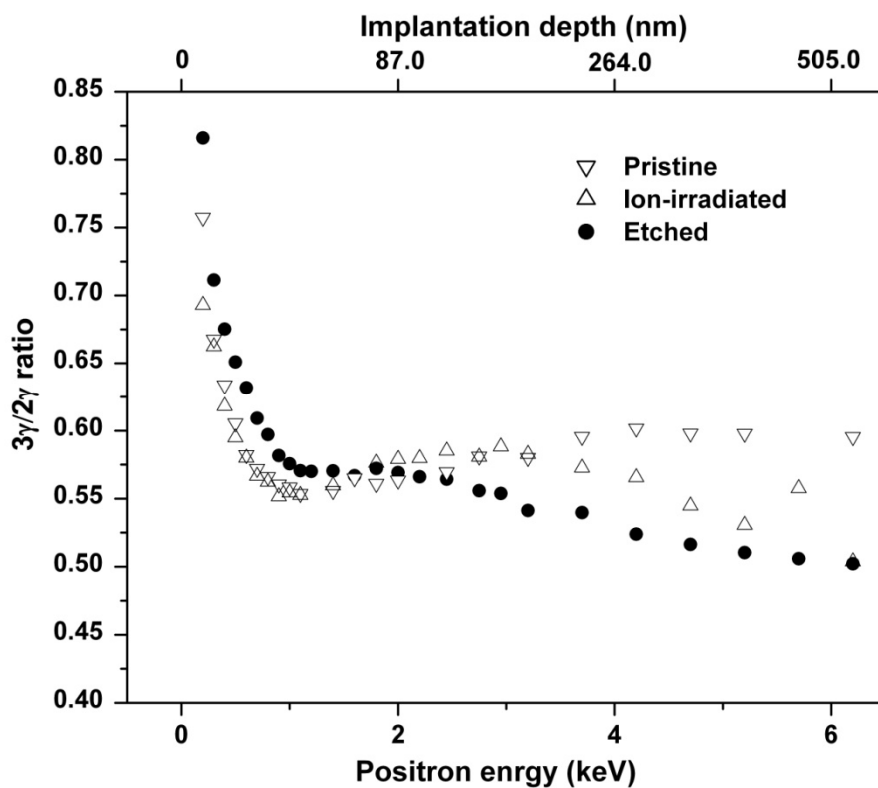


**Figure 4.12:** The  $3\gamma/2\gamma$  ratio as a function of positron energy, top axis shows the positron implantation depth

The  $S$ - $E$  curves of the pristine, ion-irradiated and etched PET were fitted using the VEPFIT (details given in chapter II) and the diffusion lengths of Ps were evaluated. The Ps diffusion lengths for the pristine, ion-irradiated and etched PET are  $34.2 \pm 9.3$  nm,  $3.4 \pm 0.5$  nm and  $4.3 \pm 0.5$  nm, respectively. The dramatic reduction of diffusion length upon irradiation shows the formation of excess free volumes in the surface of the film caused due to the chain scission. A number of positron annihilation spectroscopic studies [Hsu et al., 1971; Suzuki et al., 1992; Kobayashi et al., 1995; Dlubek et al., 2000 and Saito et al., 2007] have been carried out to observe the effect of irradiation on the polymer membranes. All these studies have reported (i) the formation of excess free volumes or the change in the size of the free volumes due to the fragmentation of the long molecular chains along with the formation of new chemical bonds (change in the degrees of cross-linking) and (ii) the formation of radicals and ions (paramagnetic species) due to the breaking of bonds, which finally get converted into peroxides, carboxy groups in the presence of oxygen. The attendant changes in the polymer are reflected on the positron annihilation characteristics. In the present study, the surface  $S$ -parameter for the irradiated-polymer is observed to be higher than the pristine PET (Fig. 4.11) and dramatically reduces even below the pristine value in the case of the etched sample.

The higher value of  $S$ -parameter for the irradiated polymer membrane indicates the presence of the excess free volume or defects created as a result of the chain scissioning due to the irradiation. However, for the etched membrane, the surface  $S$ -parameter reduces dramatically even below the pristine membrane. The reduction of the surface  $S$ -parameter as compared to the irradiated membrane can be understood from the  $3\gamma/2\gamma$  profiles for the membranes. The  $3\gamma/2\gamma$  ratio signifying the Ps re-emission probability, is found to be the highest in the case of the etched sample and lowest in the ion-irradiated sample (Fig. 4.12). The increase in the  $3\gamma/2\gamma$  ratio at the surface reflects

high surface open porosity which may be due to the removal of chemical species formed during the irradiation by etching treatment. The re-emission of Ps from the surface of etched samples due to the surface open porosity resulted in the decrease of the surface  $S$ -parameter in this case (Fig. 4.11). However, the effect of the etching is more predominant at the surface and near surface region which is reflected from the large difference in the  $S$ -parameter and  $3\gamma/2\gamma$  ratio at the surface than in the bulk. The  $3\gamma/2\gamma$  ratio decreases from the surface to the bulk showing the decrease in the Ps re-emission from deep inside the membranes.

It is noticeable that the effect of ion-irradiation and etching is different on the surface from that of the bulk. From the positron lifetime studies using isotope source, where the contribution to the spectra is principally from the bulk of the polymer, the free volumes were seen to decrease on irradiation (Table 4.1). On the other hand, the free volume and porosity of the surface is increased as seen by the enhanced Ps re-emission from the etched sample (Figs. 4.11 and 4.12). These results together show that the chain scission is the principal mechanism on the surface and near surface regions on ion-irradiation while cross-linking seems to be the major affect in the bulk of the polymer. The chain scission in the surface layers might be favored due to the presence of air during the irradiation of the membrane.

### 4.3 Conclusion

Positron annihilation lifetime spectroscopy supplemented by conventional techniques was found to be a useful method to study the nanostructure of PET-g-AA copolymers and ion-irradiated PET films. The variation in the free volume parameters had a direct correlation with structural transition from DMA up to 6% grafting. The free volume parameters followed simple mixture rule. At higher degree of grafting, a marked

deviation in  $I_2$  was observed with a sharp drop in fractional free volume. Thus, we speculate that at higher degree of grafting, interfacial effects has a dominant role on positron behavior. There is a need to investigate graft copolymers with a wider range of grafting and on different base polymers by PALS to gain more insight into their positron dynamics.

In case of ion-irradiated PET films, neither new phase formation nor any change in the crystallinity is observed. FTIR studies showed that no other major modification in the chemical structure has taken place after low fluence ion-irradiation and subsequent etching. The changes seen are primarily in the free volume fraction and size. It is observed through the positron annihilation characteristics that the ion-irradiation and etching result in the nanostructure changes of the polymer membrane but the effect of etching on the irradiated membranes is more pronounced at the surface. Positron annihilation spectroscopy is seen to be a very sensitive technique to evaluate the nanostructural changes selectively on the surface as well as bulk of the membrane even at very low fluence.

## **CHAPTER-V**

---

# **NANOSTRUCTURE OF POLYMER NANOCOMPOSITE: DEVELOPMENT AND APPLICATION OF AGE MOMENTUM CORRELATION (AMOC)**

Positron annihilation spectroscopy consists of PALS, DBAR, CDB and ACAR as the commonly used techniques dealing with the measurement of positron lifetime and annihilating electron momentum distribution in a material. These measurements provide essential information about the defects size, concentration and electronic environment of the defects in the crystalline material. In molecular solids, information about the free volumes sizes and concentration are obtained from positron annihilation spectroscopy measurements. It is expected that the correlated measurements of positron lifetime and momentum distribution can provide more information about positron states and positron dynamics in a system compared to their uncorrelated measurements. This becomes more important when more than one positron state can have similar lifetime and different momentum distribution or vice versa. The correlated measurements of lifetime and Doppler broadening are called Age MOmentum Correlation (AMOC) measurements [Dauwe et al., 2003; Suzuki et al., 2003; and Schneider et al., 1997]. From AMOC measurements, momentum distribution as a function of positron age in a medium can be obtained. AMOC has been extensively used to differentiate the positron states in liquids where positron as well positronium undergo different chemical reactions like spin conversion, complex formation and oxidation in the presence of solutes leading to changes in *o*-Ps lifetime and intensity [Stoll et al., 2003]. AMOC measurements have been found very useful for the investigation of chemical environment of free volume nanoholes in various polymers [Sato et al. 2009] as well as positron dynamics in alloys samples [Inoue et al., 2011]. A set up for AMOC measurements has been developed and used to study a polymer nanocomposite as detailed in the following sections.

## 5.1. Development of Age momentum correlation (AMOC) facility

### 5.1.1 Principle

In AMOC, positron lifetime and Doppler broadening are measured for the same positron. For this, positron lifetime and Doppler broadening measurements are carried out in coincidence using a 3- $\gamma$  coincidence set up. The line shape parameters obtained from Doppler broadening spectra is plotted as a function of positron age. The variations in line shape parameter as a function of positron age give information about the electron momentum distribution at annihilation sites corresponding to different positron ages. Doppler spectra in AMOC measurements are recorded using  $\gamma$ - $\gamma$  coincidence using a BaF<sub>2</sub> and an HPGe detector such as in CDB measurements where two HPGe detectors are used in coincidence. Hence, the Doppler broadening spectra obtained from AMOC have better signal to noise ratio compared to single detector Doppler broadening measurements but inferior compared to CDB.

### 5.1.2 Setting up of AMOC system

For AMOC measurements, positron lifetime and Doppler broadening spectra are recorded in coincidence using a 3- $\gamma$  coincidence set up. For lifetime measurements, two BaF<sub>2</sub> scintillation detectors were used in fast-fast coincidence and for Doppler broadening measurements, an HPGe detector (efficiency 30%) having resolution (2.1 keV at 1332 <sup>60</sup>Co) was used. The block diagram of the set up is shown in Fig. 5.1. The lifetime spectrum is generated using a Time to Amplitude Converter TAC which receives start and stop inputs from two Constant Fractional Differential Discriminators CFDDs connected to the anodes of two BaF<sub>2</sub> detectors placed at 90° relative to each other. The stop signal (annihilation  $\gamma$ , 511 keV) is delayed by a fixed time before feeding it to TAC to shift the lifetime spectrum in higher channels of multi channel analyzer (MCA). The



energy windows of CFDDs are set to select the energies of gamma photons for start (1275 keV) and stop (511 keV) signals. The Doppler broadening spectrum is recorded using HPGe detector placed at  $180^\circ$  relative to the stop ( $\text{BaF}_2$ ) detector. The energy signal from HPGe is passed through a spectroscopy amplifier and recorded in coincidence with lifetime signal from TAC using a Computer Automated Measurement and Control (CAMAC) system. The coincidence between all three detectors with suitable energy windows is taken as the master gate to record lifetime (from TAC) and Doppler broadening (spectroscopy amplifier) signals.

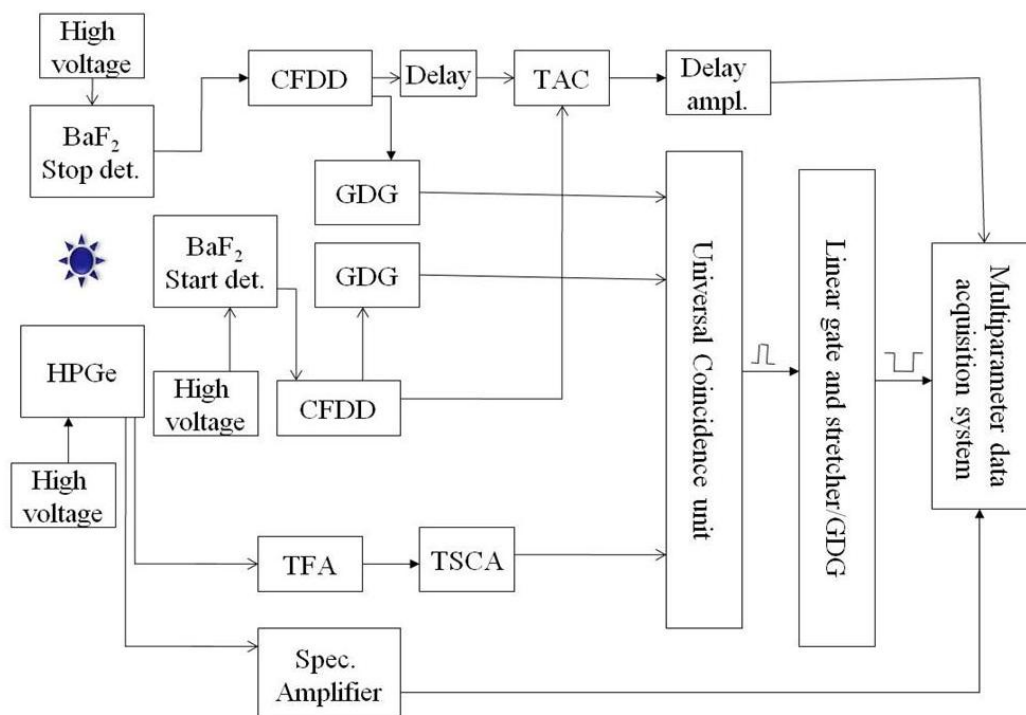


**Figure 5.1:** The block diagram for the AMOC setup

The lifetime and Doppler spectra are recorded on 4k MCAs in list mode using LINUX based advanced multiparameter acquisition systems ‘LAMPS’ data acquisition and analysis software. This software allows one to generate different spectra using pseudo parameters which in turn are functions of original parameters such as lifetime and

Doppler broadening in the present case. Fig. 5.2 shows a typical two dimensional AMOC spectrum having positron lifetime spectrum on Y axis and Doppler broadening spectrum on X axis. The Y and X projections from 2D spectrum are shown in Figs. 5.3 and 5.4 showing the typical positron lifetime and Doppler broadening spectrum, respectively. The time resolution of the lifetime spectrometer was 290 ps and time constant was 25 ps/channel. The energy calibration for Doppler spectra was 170 eV/channel.

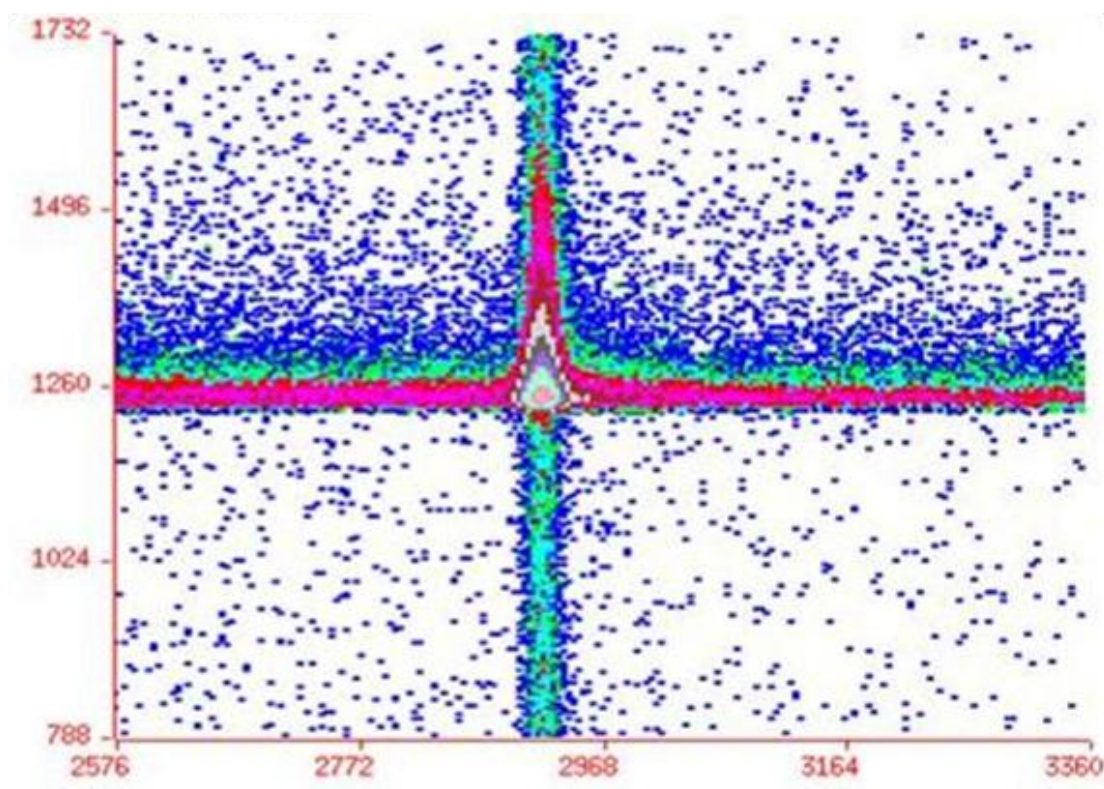


**Figure 5.2:** A typical 2D AMOC spectrum for a polymer sample

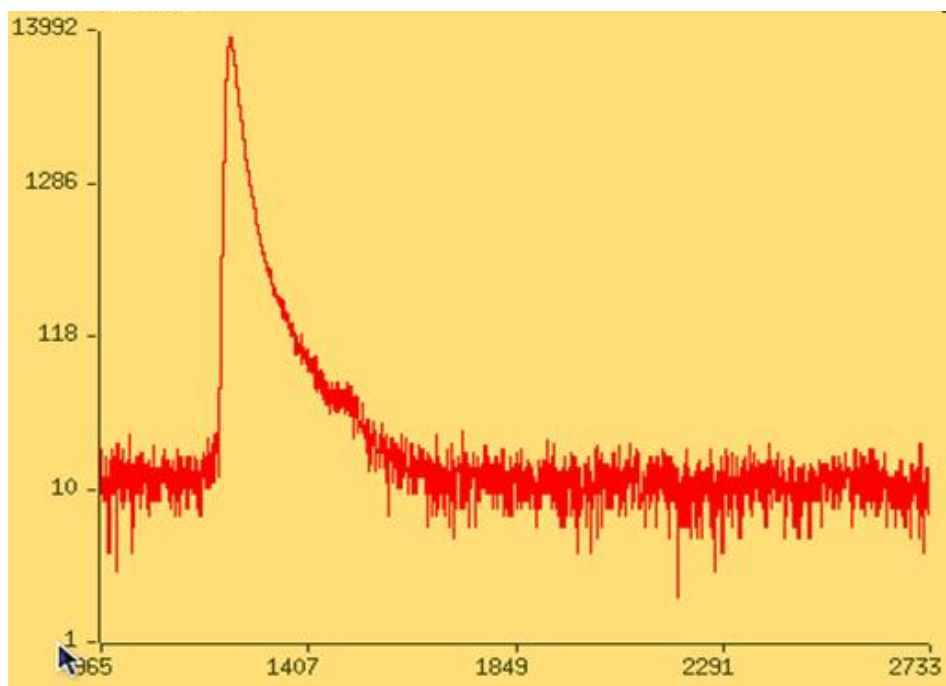


**Figure 5.3:** The Y-projection of 2D AMOC spectrum; lifetime spectrum of a polymer sample

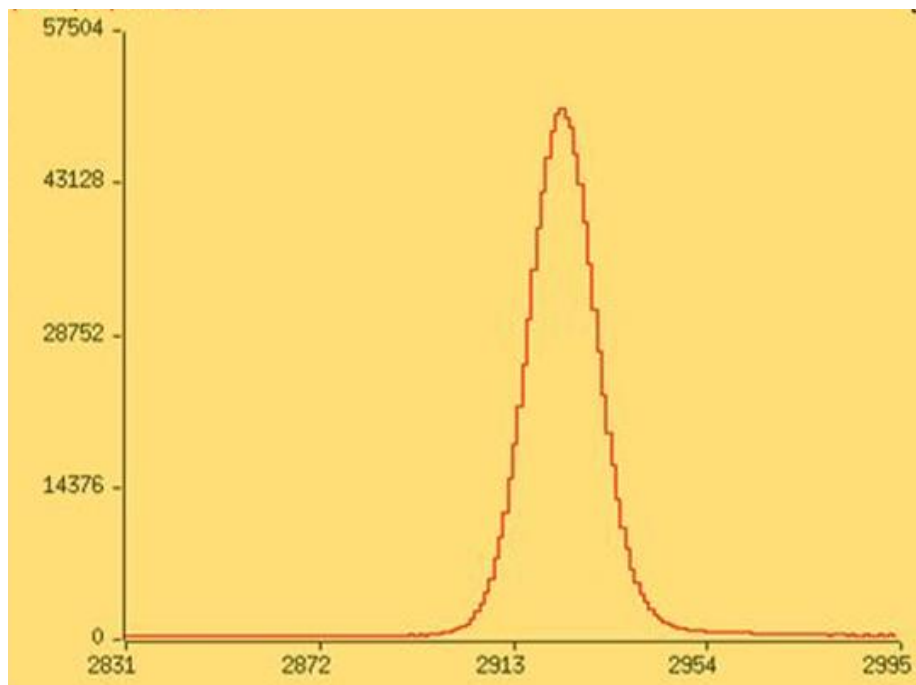


**Figure 5.4:** The X-projection of 2D AMOC spectrum; Doppler broadening spectrum of a polymer sample

### 5.1.3 Data analysis

The  $S$ -parameter profile as a function of positron age is evaluated as follows: The lifetime spectrum is analyzed using PATFIT to find the zero time,  $t_0$  (equivalent to positron age = 0), and the corresponding channel of MCA  $ch_0$ . The X axis for the lifetime spectrum can be converted from channels to real positron age using the relation,  $t_i = (ch_i - ch_0) * t'$ , where  $t_i$  is positron age corresponding to  $i^{\text{th}}$  channel,  $ch_i$ , and  $t'$  is the time/channel of MCA. The lifetime spectrum is divided in  $n$  number of time windows (Y axis of 2 D spectrum) and the Doppler spectrum within these  $n$  time windows are generated (X axis of 2 D spectrum) using the list mode analysis. The time window on the lifetime axis or positron age axis is chosen to increase with age to get reasonable counts in the Doppler spectra at higher positron ages (exponential decay nature of lifetime spectrum). Thus,  $n$  numbers of Doppler spectra corresponding to different positron ages are obtained. The corresponding positron age for a Doppler spectrum is taken as midpoint of the time window over which that Doppler spectrum has been generated. Fig. 5.5a shows the typical AMOC relief obtained from the current set up for a polymer sample. This figure clearly shows the Doppler spectra lying over lifetime spectrum at different positron ages. The line shape parameter  $S$  is evaluated from these Doppler broadening spectra using the program SP-1 [Dryzek, SP 1.0; Dryzek and Quarles, 1996].

Fig. 5.5b shows the typical  $S$ -parameter profile as a function of positron age in a polymer sample. The  $S$ -parameter is higher in the beginning (positron age  $\sim 0$  ns) due to contribution from  $p$ -Ps annihilation. The  $S$ -parameter reduces at higher age (positron age  $\sim 500$  ns), where major contribution is from free positron annihilation, and further increases to a plateau region at the end (positron age  $> 2$  ns) due to contribution from  $o$ -Ps *pick-off* annihilation.

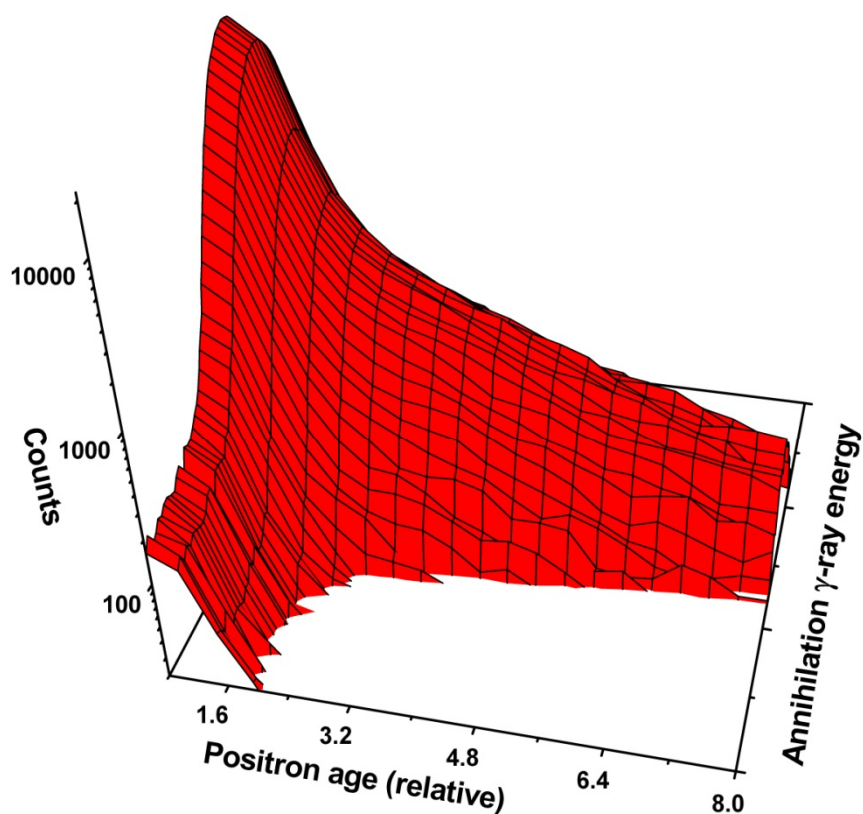


Figure 5.5a: The regenerated AMOC relief spectrum for a polymer sample

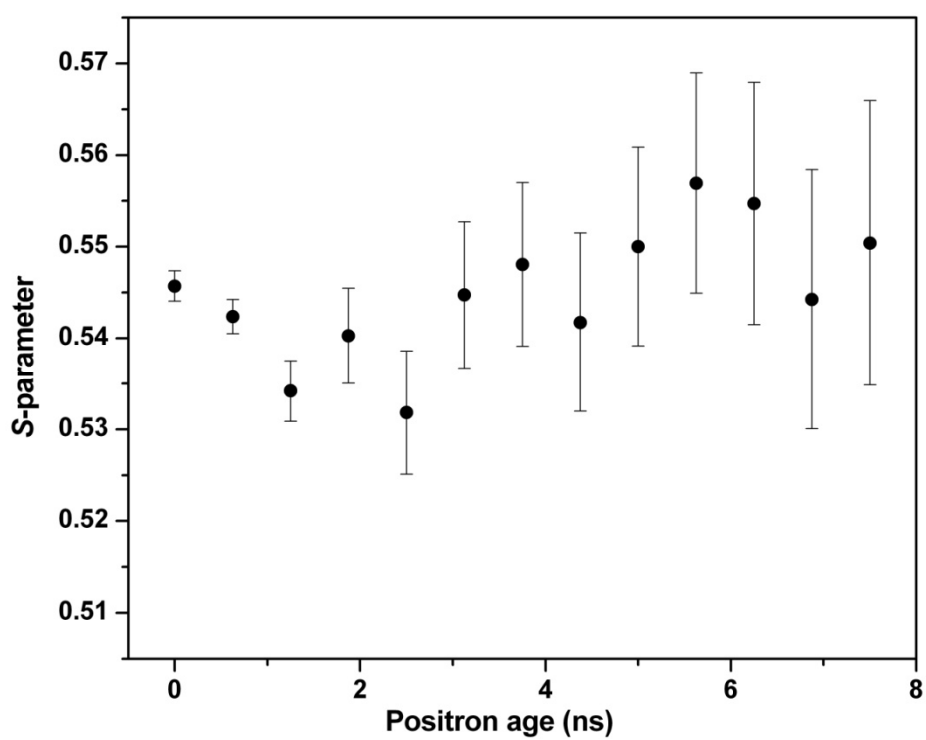


Figure 5.5b: A typical S-parameter vs positron age profile for a polymer

The variations in the  $S$ -parameter as a function of positron age are correlated to different positron states in the polymer. In this profile, contribution from each positron state (more or less) is present at all data points due to exponential decay in lifetime spectrum. The contribution from  $p$ -Ps and free positron at the end of the curve [positron age = 4 \* ( $o$ -Ps *pick-off* lifetime)] will be very small and the data points in this range can be taken as solely from  $o$ -Ps *pick-off* annihilation.

The individual  $S$ -parameter corresponding to different positron states can be evaluated from  $S$ -parameter vs positron age profile using the following methodology.  $S$ -parameter at positron age ( $t$ ),  $S(t)$ , is the weighted average of  $S$ -parameters from all positron states and written as

$$S(\tau) = \sum_{i=1}^k f(\tau, i) S(i) \quad (5.1)$$

where  $f(t, i)$  and  $S(i)$  are the fraction of  $i^{\text{th}}$  state at positron age ( $t$ ) and  $S$ -parameter for  $i^{\text{th}}$  state, respectively. The fraction of  $i^{\text{th}}$  state at positron age ( $t$ ),  $f(t, i)$ , is the contribution from  $i^{\text{th}}$  state within a time window averaging over positron age ( $t$ ) in the lifetime spectrum. These fractions, contribution from a component in a fixed time window, can be calculated using the lifetime and intensity components obtained from the lifetime spectrum. The  $S$ -parameter as a function of positron age is fitted to eq. (5.1) using non linear square fitting program with well-defined  $f(t, i)$  and keeping  $S(i)$  as free parameters. A computer program in FORTRAN has been developed for these fitting.

## 5.2 Nanostructure of polymer nanocomposite: Application of AMOC

Polymer nanocomposites are multiphase materials having one phase in nanometer scale (filler) which is well dispersed in the matrix [Vilgis et al., 2009]. Polymer nanocomposites are known to have modified properties such as mechanical, electrical, thermal, gas permselectivity, photovoltaic etc. [Chatterjee, 2010; Liou et al., 2010; Yang

et al., 2006; Karaman et al., 2008; De Sitter et al., 2006; Liu et al., 2010 and Kuan et al., 2009] Polymer nanocomposites having various nanophases like metal oxide nanoparticles, metal nanoparticles, clays and silica powders have been studied using different techniques to establish some correlation between their nanostructure and macroscopic properties [Zhang et al., 2011; Harms et al., 2010; Zaleski et al., 2011 and Awad et al., 2011]. In case of organic polymers, carbon nanotubes, generally, multiwall carbon nanotubes (MWCNTs), are considered suitable material for preparing polymer nanocomposites as carbon is the main constituent of organic polymers as well as carbon nanotubes. The new properties of the polymer nanocomposites mainly depend on interaction between polymer molecules and nanophase material [Pirlot et al., 2002 and Sreekumar et al., 2002]. This interaction can be easily varied in case of polymer-carbon nanotubes composites as it is possible to functionalize the carbon nanotubes with different functional groups having different type of interaction with polymer molecule.

Positron annihilation lifetime spectroscopy (PALS) is a well established technique for probing the local free volume nanoholes in polymers [Mallon, 2003 and Schrader et al., 1988]. In recent years, PALS has been employed to characterize free volume nanoholes in polymer nanocomposites [Zhang et al., 2011; Harms et al., 2010; Zaleski et al., 2011 and Awad et al., 2011]. *o*-Ps *pick-off* lifetime,  $\tau_3$ , in a polymer is correlated with the radius of free volume nanoholes using the Tao-Eldrup equation. *o*-Ps intensity,  $I_3$ , is used to obtain the fractional free volume, and a distribution over *o*-Ps lifetime provides free volume size distribution in the polymers. Polymer nanocomposites are multiphase systems and new trapping/annihilation sites like matrix-nanophase interfaces and nanophase itself for positron/Ps become available in the nanocomposites. Thus, it becomes essential to investigate the positron/Ps trapping/annihilation sites in polymer nanocomposites for its free volume characterization. AMOC measurements are expected

to provide more information about the free volume nanoholes as compared to uncorrelated measurements of lifetime and Doppler broadening [Sato et al., 2009].

Phenol formaldehyde (PF) resins include synthetic thermosetting resins and obtained by the reaction of phenol and formaldehyde. These resins have a large number of applications such as coatings, adhesives, pool balls and laboratory countertops etc. Carbon nanotubes composites of PF resin show improved properties over pure PF resin. This chapter describes the free volume characterization of PF-MWCNTs composites using positron annihilation spectroscopy. PALS has been used to characterize the free volume nanoholes in Pure PF resin and having MWCNTs (2, 5, 10 and 20 %, w/w). To investigate the positron/Ps states in the nanocomposites, AMOC measurements have been carried. The MWCNTs have been characterized using high resolution transmission electron microscopy (HRTEM). The PF resin-MWCNTs composites have also been characterized using X-ray diffraction (XRD) and scanning electron microscopy (SEM) for the changes in the crystallinity and morphology.

### **5.2.1. Experiments**

#### **5.2.1.1 Sample preparation and characterization**

The MWCNTs used in the present study were synthesized using catalytic chemical vapor deposition method. The supported catalyst, Nickel formate, 10 wt%, dispersed on magnesia powder (surface area 100 m<sup>2</sup>/g) was used for the synthesis. Supported catalyst weighing 0.5 g was taken in an Inconel boat and kept inside a horizontal quartz tube of diameter 50 mm. The heating was carried out in an electrical resistance furnace with an effective heating zone of 30 cm. Initially the boat with the supported catalyst was kept outside the heating zone and only nitrogen gas was passed to create inert atmosphere. Once the desired temperature was achieved the boat was placed



in the heated zone and the reagent gas flow started simultaneously. Carbon nanotubes (CNTs) were synthesized at 850°C using acetylene (flow rate 100 cc min<sup>-1</sup>) diluted with nitrogen (flow rate 1000 cc/min) for 30 minutes. A two-stage oxidative purification procedure was adapted. In this method, the as-synthesized CNTs sample was refluxed in 3M HNO<sub>3</sub> for 16 h. The mixture was then filtered through a Fluoropore- PTFE membrane filter. The filter cake was rinsed with deionized water until the pH of the filtrate became neutral. The sample was then dried overnight and air oxidized at 500°C for 1 h in a capped crucible. The polymer resin used in this study as base material was a novolac type phenol-formaldehyde (PF) condensation resin. Para toluene sulphonic acid (PTSA) was used as the cross linking agent. Novolac– PTSA was mixed with MWCNTs (2, 5, 10 and 20 wt%) and homogenized in methanol with continuous stirring for 1 h. To avoid the formation of bubbles the evaporation of alcohol and settling of resin was done in controlled manner. The alcohol evaporation was done by heating the homogenized mixture for 12 h at 40°C. The settling of CNT suspended resin mixture was done by keeping it at 50°C for 36 hrs. The controlled pyrolysis of the mixture provided bubble free solid films. The mixture was deposited in the form of films of thickness ~ 10 mm. The pure resin and PF-MWCNTs nanocomposites are named as PF-0, PF-2, PF-5, PF-10 and PF-20. The carbon nanotubes samples have been characterized using 2000FX JEOL transmission electron microscope. XRD patterns of the samples were obtained on Philips X pert pro XRD unit using Cu K<sub>α</sub> radiation. The SEM images of PF-MWCNTs nanocomposites surface and fractured surfaces were taken using SEM- Camscan MV2300CT/100, UK.

### 5.2.1.2 Positron annihilation lifetime measurements

All the positron lifetime measurements have been carried out at room temperature in laboratory atmosphere using a fast-fast coincidence set up coupled with plastic scintillation detectors with a time resolution of 240 ps (fwhm of a Gaussian resolution function for  $^{60}\text{Co}$ ) and channel width of 25 ps/channel. The samples were in the form of 10 mm thick films having area of  $5\text{ cm}^2$ . The positron source ( $^{22}\text{Na}$ , 10 Ci) was prepared by evaporating carrier free NaCl solution on 7  $\mu\text{m}$  thick kapton foil. For each experiment, the positron source was sandwiched between two identical pieces of a sample and area under the spectrum was  $1 \times 10^6$ . Lifetime spectrum for the MWCNTs was recorded by embedding the positron source in the powder. Silicon was used as reference material to calculate the fraction of positrons annihilating within the source and kapton films. All the spectra were analyzed using the routine PATFIT-88 [Kirkgaard et al., 1991] as a sum of decaying exponential components. For PF resin and PF-MWCNTs nanocomposites, three decaying exponential components with lifetime  $\tau_i$ , and intensities,  $I_i$ ; in the order of increasing lifetimes, subscripts  $i = 1, 2$  and  $3$ , are ascribed to singlet Ps ( $p$ -Ps), free positrons and  $o$ -Ps, respectively. In case of MWCNTs, only two positron lifetime components are observed. The reduced variance of the fit for all the spectra was in the range of 0.97 -1.05. The routine CONTIN [Provencher et al., 1982] was used to evaluate the distribution function of annihilation rate from lifetime spectrum for pure PF resin and the nanocoposites. Instead of sum of decaying exponentials, CONTIN assumes a continuous decay form where the annihilation decay integral is a Laplace transformation of  $\lambda_a(\lambda)$ . The fraction of positrons annihilating with rates between  $\lambda$  and  $\lambda+d\lambda$  is  $\alpha(\lambda) d\lambda$  and  $\int(\alpha(\lambda)d\lambda) = 1$  (integration from 0 to  $\infty$ ). The procedure also includes the deconvolution of the experimental resolution using a well characterized reference spectrum (Si spectrum in the present case). The annihilation rate (lifetime) distribution can be converted to

radius or volume distribution using appropriate algorithms through the Tao-Eldrup equation [Dlubek et al., 1998].

### 5.2.1.3 Age Momentum Correlation measurements

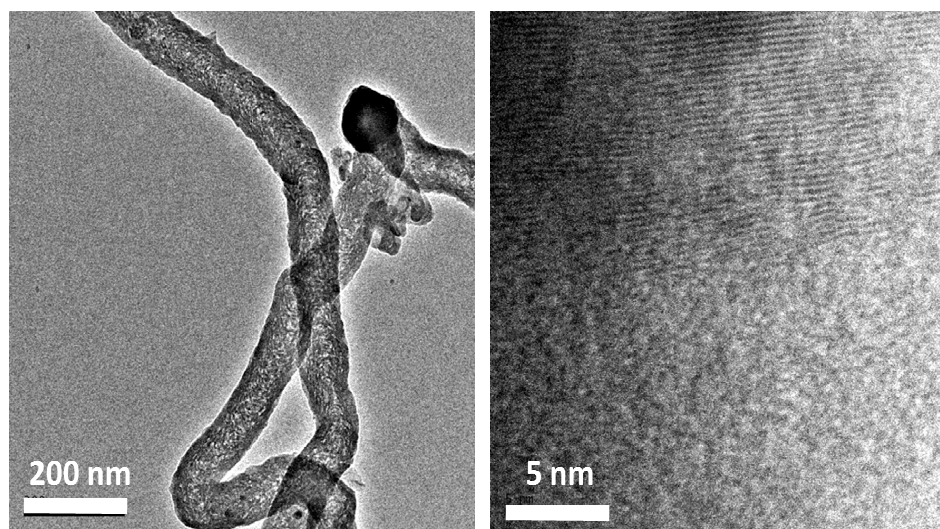
A positron source ( $^{22}\text{Na}$ , 40 Ci) sandwiched between two kapton films of thickness 7  $\mu\text{m}$  was used for AMOC measurements. The AMOC measurements were performed by acquiring positron lifetime and Doppler broadening spectra in coincidence as described before in the present chapter. The positron age dependent Doppler broadening spectra are analyzed in term of age dependent line shape parameter  $S(t)$ , which is determined as the ratio of central area ( $511 \pm 1.2$  keV) to the total area of the photo peak. There is only one positron component and no positronium formation in kapton. The fraction of positron annihilation in Kapton and source are not subtracted for the evaluation of  $S(t)$ .

## 5.2.2. Results and Discussion

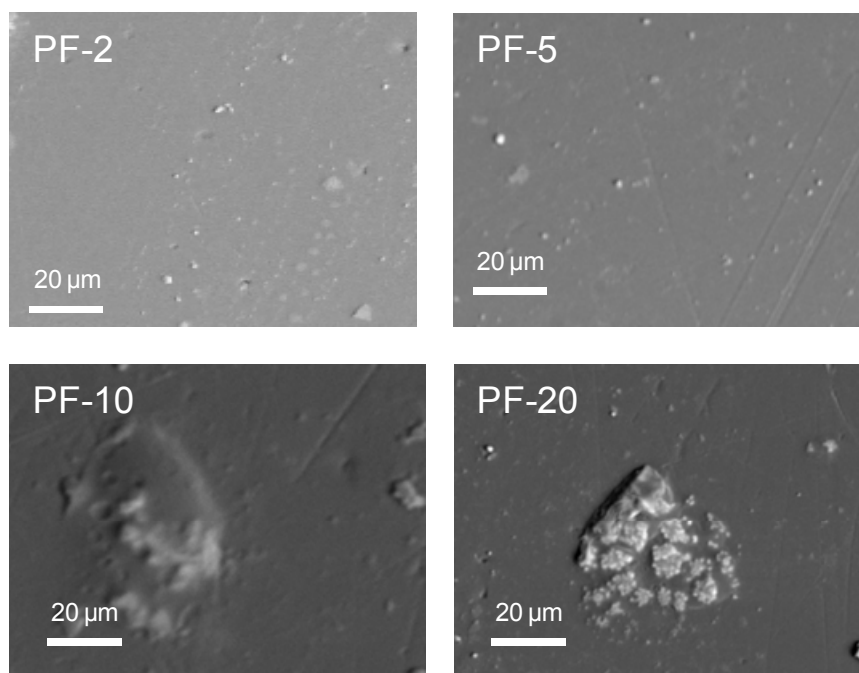
### 5.2.2.1 TEM, SEM and XRD

Fig. 5.6 shows the HRTEM bright field image of the synthesized carbon nanotubes. It is widely accepted that size of the carbon nanotubes can be determined by measuring the distance between two dark lines observed in TEM overviews [Branca et al., 2004]. The carbon nanotubes length was of micrometer range and average outer diameter measured from the images was  $\sim 93$  nm. The figure also shows that these carbon nanotubes are multiwall carbon nanotubes (MWCNTs). Fig. 5.7a shows the SEM images of the surfaces of PF-MWCNTs nanocomposites. The SEM images of the surfaces show that the MWCNTs are uniformly distributed at lower concentrations and start to aggregate at higher concentrations. The aggregation is evidently seen in the PF-10 and PF-20

samples. Fig. 5.7b shows the SEM images of the fractured surface of PF-MWCNTs composites. The lateral surface was fractured for all the samples and observed under microscope at same magnification to compare the fracture behavior with respect to different percentage of MWCNTs. The predominant fracture mode for PF-2 and PF-5 composites was transgranular cleavage which basically indicates brittle fracture mode. But there was a significant percentage of intergranular fracture in the PF-10 and PF-20 samples that increase the fracture toughness by incorporating the small amount of plastic deformation. Fracture toughness is basically the ability of the motif to absorb energy. The incorporation of MWCNTs in PF matrix improves the toughness by changing the fracture mode. Due to the presence of MWCNTs, micro/nano cracks appear during fracture and in the process of creating these nano-cracks, energy is absorbed in the system which is expected to increase the fracture toughness.



**Figure 5.6:** The HRTEM bright field images of MWCNTs



**Figure 5.7a:** The SEM images of surface of PF-2, PF-5, PF-10 and PF-20.

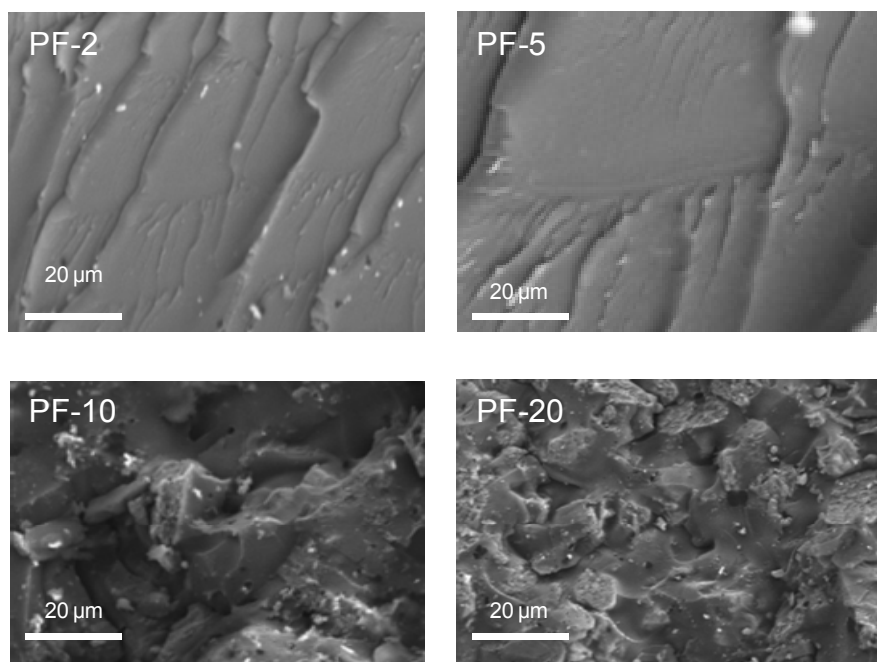


**Figure 5.7b:** The SEM images of the fractured surfaces of PF-2, PF-5, PF-10 and PF-20.

Fig 5.8 shows the XRD patterns for pure PF resin and PF-MWCNTs nanocomposites. The XRD pattern for pure PF resin shows a broad reflection in the range of 10 to 30 degree, which is caused by the repeating units of chain molecules in the region with laterally arranged “stretched” chains. On incorporation of MWCNTs, there were no crystalline peaks observed in the XRD patterns of PF-MWCNTs composites indicating no change in the crystallinity of the samples.

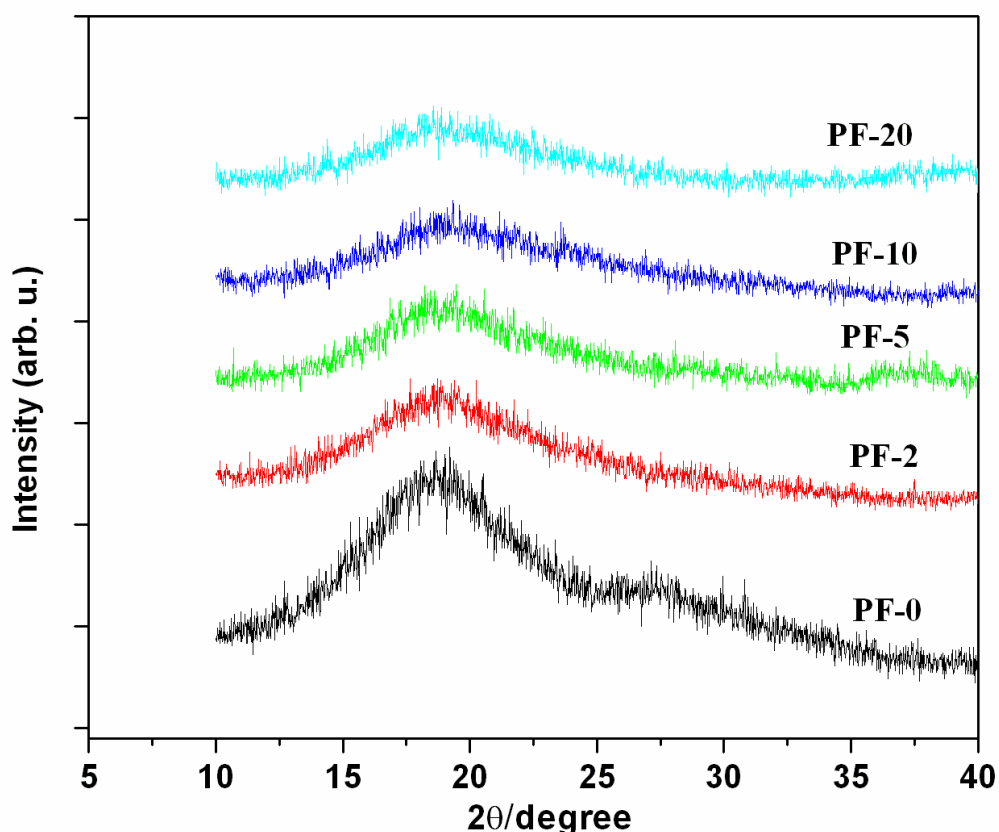


**Figure 5.8:** XRD patterns of PF-MWCNTs composites

#### 5.2.2.2 Positron annihilation lifetime measurements

Two positron lifetime components were observed in pure MWCNTs and the results are shown in Table 5.1. In the present study, no positronium component was observed. It is consistent with the reports in literature where no positronium formation (or negligible) has been reported in carbon nanotubes. The positron trapping and annihilation sites in carbon nanotubes have been discussed in details in these reports.[Ito et al., 1999;

Fukutomi et al., 2001; Ohdaria et al., 2002 and Chakrabarti et al., 2006]. Ishibashi et al. (2002) has shown from *ab-initio* calculations that trapping/annihilation of positrons in the single wall carbon nanotube varies as a function of diameter. In the present case, the diameter of nanotubes is quite large (outer diameter  $\sim 93$  nm) and positrons are expected to get trapped within the interstitials or inside the tubes. The positron lifetime components ( $\tau_1 = 137.4$  ps and  $\tau_2 = 338.3$  ps) in MWCNTs are typical of those reported in graphite. [Dryzek et al., 1995] The shorter component (137.4 ps) is ascribed to the positron annihilation from delocalized states in the graphene sheets and the longer component (338.3 ps) is ascribed to the trapped state within the interstitials or inside the tubes [Chakrabarti et al., 2006]. The positron lifetime observed in CNTs ranging from 140 to 225 ps have been attributed to free positron annihilation with  $\pi$  electrons in whole volume [Chakrabarti et al., 2006]. The lower value observed for  $\tau_1$  (137.4 ps) in the present case indicate the reduced bulk lifetime due to trapping of a fraction of positrons in open volume defects corresponding to  $\tau_2$ .

**Table 5.1** Positron annihilation lifetime components with corresponding intensities for pure PF-resin and PF-MWCNTs composites

Sample	$\tau_1(\text{ps})$	$I_1(\%)$	$\tau_2(\text{ps})$	$I_2(\%)$	$\tau_3(\text{ns})$	$I_3(\%)$
MWCNTs	137.4 $\pm$ 2.2	11.3 $\pm$ 1.2	338.3 $\pm$ 1.2	89.2 $\pm$ 1.9		
PF-0	117.2 $\pm$ 2.1	8.06 $\pm$ 1.5	329.0 $\pm$ 1.1	73.64 $\pm$ 1.1	1.378 $\pm$ 0.04	18.28 $\pm$ 0.25
PF-2	116.6 $\pm$ 2.0	12.40 $\pm$ 1.5	322.2 $\pm$ 1.1	71.19 $\pm$ 1.5	1.520 $\pm$ 0.03	16.40 $\pm$ 0.29
PF-5	122.1 $\pm$ 1.9	18.01 $\pm$ 1.7	316.7 $\pm$ 1.2	67.46 $\pm$ 1.6	1.523 $\pm$ 0.03	14.52 $\pm$ 0.32
PF-10	150.5 $\pm$ 1.7	21.37 $\pm$ 2.8	332.9 $\pm$ 1.0	64.28 $\pm$ 2.7	1.602 $\pm$ 0.03	14.34 $\pm$ 0.30
PF-20	144.4 $\pm$ 1.6	14.83 $\pm$ 2.3	340.6 $\pm$ 1.0	69.17 $\pm$ 2.1	1.696 $\pm$ 0.03	15.98 $\pm$ 0.32

The discrete positron lifetime components for PF-0 and PF-MWCNTs nanocomposites are given in Table 5.1. The results reported are obtained keeping all parameters (lifetimes and their corresponding intensities) free in PATFIT analysis. It is observed that *o*-Ps *pick-off* lifetime,  $\tau_3$ , increases with the incorporation of MWCNTs in PF resin with a decrease in the corresponding intensity with the exception of PF-20 sample. It shows that the nanostructure of PF resin has changed with the incorporation of MWCNTs. The reduction in  $I_3$  is not proportional to the weight fraction of MWCNTs in PF matrix which means that  $I_3$  in PF-MWCNTs nanocomposites is not the weighted average of *o*-Ps intensities in PF-0 (18.28 %) and MWCNTs (0.0 %). This indicates that concentration of free volume nanoholes in PF matrix changes with incorporation of MWCNTs. The increase in *o*-Ps lifetime with a decrease in intensity can be observed either due to (i) opening up of a fraction,  $f$  (proportional to MWCNTs concentration), of preexisting nanoholes ( $I_3$ ) with the occupancy or “*annihilation*” of the remaining fraction,  $(1-f)$ , by nanotubes, or (ii) nanoholes of larger sizes are produced in the matrix with the “*annihilation*” of preexisting nanoholes in the polymer matrix in the vicinity of MWCNTs (interphase region). In the first case, there is no role of interphase and a linear increase for average *o*-Ps lifetime along with a linear decrease in intensity is expected with MWCNTs concentration. In such a case, the upper limit of *o*-Ps lifetime would be decided by the maximum loading of nanotubes in the polymer matrix which can be well dispersed in the matrix without agglomeration. However, the MWCNTs are merely physically dispersed in the PF matrix as there is no chemical bonding between PF matrix and MWCNTs. To elucidate the nature of interaction between polymer and nanotubes, the difference in positron intensity ( $I_2$ ) of nanocomposite with pure polymer as a function of MWCNTs concentration, which is related to interfacial interaction, has been plotted and shown in Fig. 5.9 [Zhou et al., 2008]. The figure also shows the linear variation of  $I_2$



based on the weight fraction ( $\phi_w$ ) assuming there is no interfacial interaction between the polymer and nanotubes. The liner variation of  $I_2$  is given by following equation.

$$I_2^c = I_2^M \phi_w + I_2^P (1 - \phi_w) \quad (5.2)$$

Where  $c$ ,  $M$  and  $p$  represent composite, MWCNTs and polymer, respectively. It is clear that experimental results show negative deviation indicating the weak interfacial interactions between polymer and nanotubes. The reverse trend in case of PF-20 indicates the presence of MWCNTs aggregates and in such a case free positron annihilation may occur from the MWCNTs itself. Due to weak interfacial interaction, large interfaces (open space) are created at the surface of MWCNTs in polymer matrix. Thus, the nanostructure of the polymer matrix in the vicinity of the MWCNTs has to change to accommodate the MWCNTs and some preexisting free volume nanoholes in the vicinity of MWCNTs in PF matrix disappear with the creation of large size PF-MWCNTs interface. An interphase in the vicinity of filler particles (i.e starting from the filler surface) having higher or lower density than bulk of polymer has been reported depending on polymer-filler interaction [Vilgis et al., 2009]. It appears that a fraction of formed Ps annihilates from these large size interfaces which results in an increase in average  $o$ -Ps lifetime (weighted average of  $o$ -Ps lifetimes from preexisting nanoholes and new interfaces) along with a decrease in corresponding intensity.

The average volume,  $V(nm^3)$  of free volume nanoholes is calculated as  $4\pi R^3/3$  where  $R$  is radius of the nanoholes and calculated through the Tao-Eldrup equation. Fig. 5.10. shows the variation of  $V$  in the range of 0.044 to 0.070  $nm^3$  as a function of MWCNTs concentration. Mean hole size in this range has been reported in literature for various resins/polymers [Jean et al., 1986; Wang et al., 1990; Jeffrey et al., 1994 and Venditti et al., 1995]. It is observed that  $V$  has a nonlinear variation with MWCNTs concentration indicating the agglomeration of MWCNTs in the matrix at higehr MWCNT

concentration. The agglomeration of nanotubes in other polymer systems has been reported in literature with the increase in filler loading [Zhou et al., 2009, Venditti et al., 1995]. The SEM images also showed the agglomeration of MWCNTs in PF-10 and PF-20 nanocomposites. The variation of  $V$  with MWCNTs concentration  $c_n$  was fitted to  $V = A + Bc_n + Cc_n^2$ , where  $A$ ,  $B$  and  $C$  are evaluated as 0.0474, 0.0021 and  $-4.60 \times 10^{-5}$ . The increase in  $o$ -Ps intensity at higher MWCNTs concentration also supported the possibility of agglomeration by irregular decrease in  $o$ -Ps intensity with MWCNTs concentration (Table 5.1).

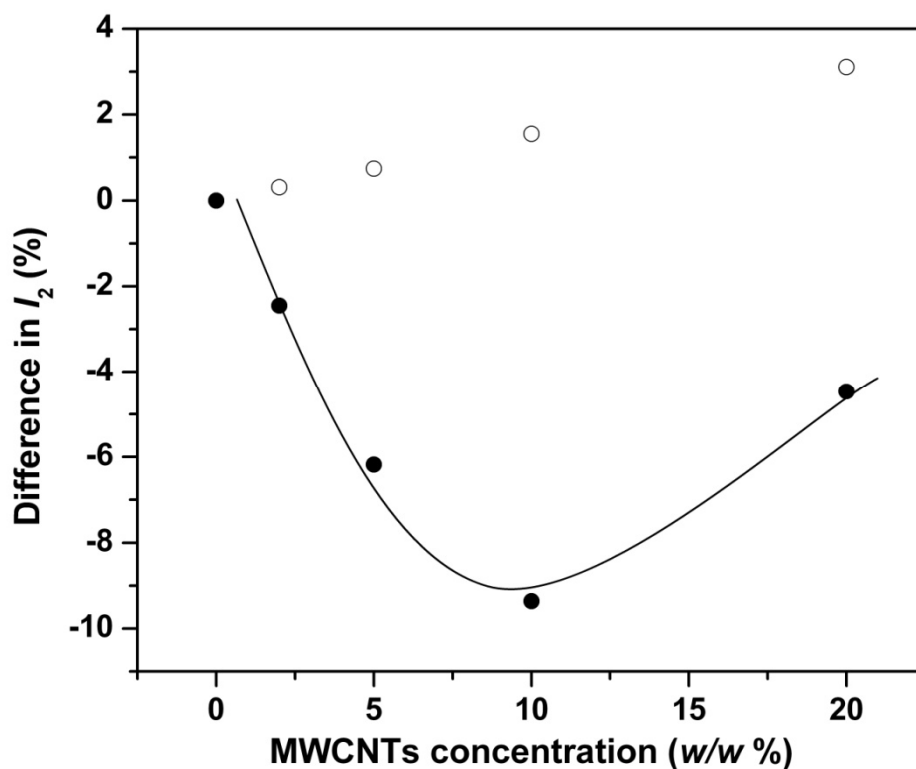


**Figure 5.9:** The plot of difference in  $I_2$  as a function of MWCNTs concentration. The symbols (●) and (○) are for experimental results and linear variation of  $I_2$  respectively. The solid line is an eye guide.

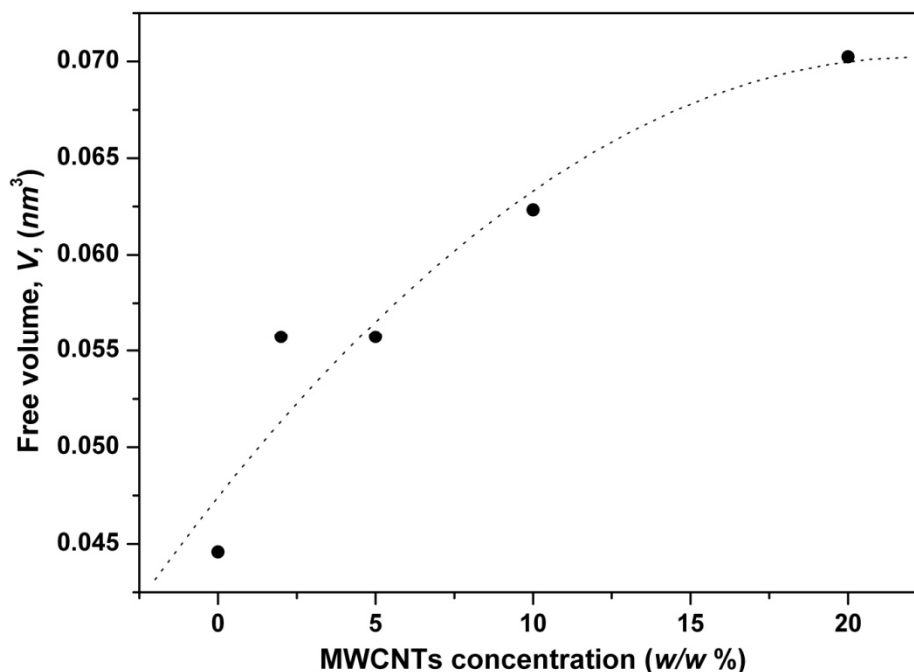


**Figure 5.10:** The average volume of nanoholes as a function of MWCNTs concentration

From CONTIN analysis, continuous *o*-Ps lifetime distributions were observed for all PF samples. The *o*-Ps average lifetime and intensity from continuous distributions are in good agreement with the discrete component analysis. The *o*-Ps annihilation rate distribution obtained from CONTIN analysis has been transformed to free volume distribution using algorithms based on the Tau-Eldrup equation [Dlubek et al., 1994]. The distribution of size,  $V(\text{nm}^3)$ , of free volume nanoholes is shown in Fig. 5.11. The peak position of the distribution shifts to higher value with incorporation of MWCNTs which is consistent with discrete component analysis [Fig. 5.10]. Zhou et al., (2009) have reported the presence of two peaks (second one peaking at higher value compared to pristine polymer) in the lifetime distribution on incorporation of MWCNTs in epoxy matrix which indicated an enhancement in the degree of local ordered regions.

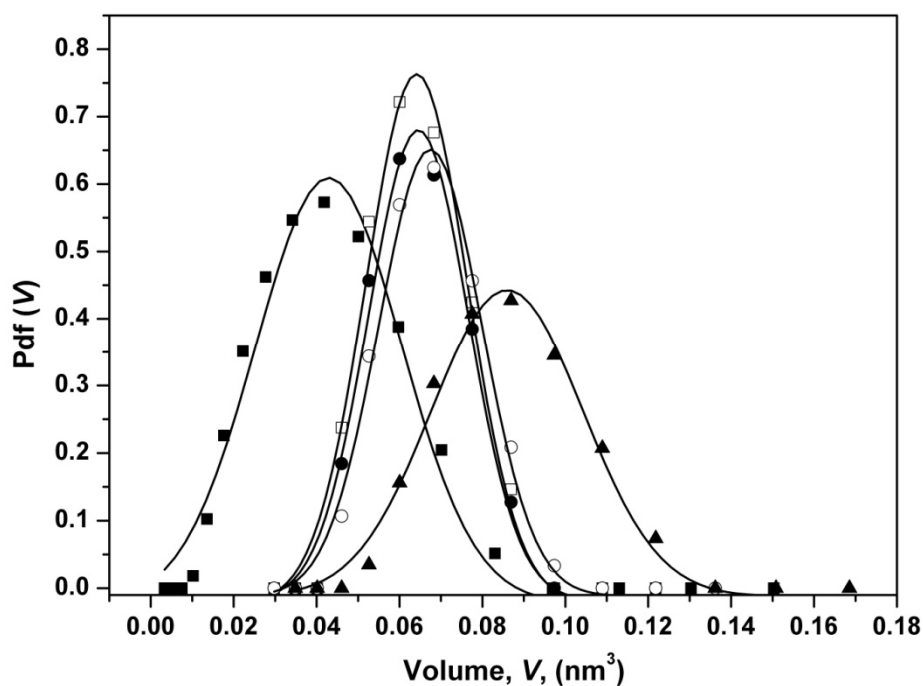


**Figure 5.11:** The distribution of volume of nanoholes; the symbols (■, □, ●, ○ and ▲) are for PF-0, PF-2, PF-5, PF-10 and PF-20 respectively. The solid lines are Gaussian fit to data.

In the present case of PF-MWCNTs composites, only one peak has been observed showing the overall distribution of nanoholes in PF-nanocomposites. It shows that the interfaces formed in the present case are not very different in size compared to pre-existing nanoholes. The free volume size distributions were fitted to Gaussian distribution and full width at half maximum, (fwhm) for PF-0, PF-2, PF-5, PF-10 and PF-20 were 0.041, 0.029, 0.028, 0.029 and 0.043 ( $\text{nm}^3$ ), respectively. On incorporation of MWCNTs (2 wt.%) the free volume size distribution (fwhm = 0.029  $\text{nm}^3$ ) becomes narrower compared to PF-0 (fwhm = 0.029  $\text{nm}^3$ ) which does not change significantly upto 10 wt.% MWCNTs. The reduction in fwhm after incorporating 2 wt.% MWCNTs again indicates that the nanotubes can lead to variation in packing density of chains in the vicinity of nanotubes creating large size interfaces with the “*annihilation*” of smaller size nanoholes in the interphase region and exclude the possibility of opening of a fraction,  $f$ , of

preexisting nanoholes. The constant value of fwhm up to 10 wt.% loading indicate that there is no significant difference in the dispersion of MWCNTs in PF resin up to 10 wt.%. On incorporation of 20 wt.% MWCNTs, a broader distribution (fwhm =  $0.043 \text{ nm}^3$ ) of free volume size centered at higher value is observed indicating the presence of larger interfaces as a result of agglomeration of MWCNTs in PF matrix. An increase in *o*-Ps intensity (Table 5.1) is also observed in this case showing the higher fractional free volume in this sample.

### 5.2.2.3 Age Momentum Correlation Measurements

To elucidate the positron/Ps trapping/annihilation sites in the PF-MWCNTs nanocomposites, AMOC measurements have been carried out in (PF-0, PF-2, PF-5 and PF-10) and positron age dependent  $S(t)$ -parameter is shown in Fig 5.12. The  $S(t)$  vs. positron age for PF-0 resin shows a typical profile as observed for various polymers [Sato et al., 2009]. The  $S(t)$ -parameter is highest in the beginning (0- 0.1 ns) where *p*-Ps has maximum contribution then it falls and reaches a minimum (  $\sim 0.8 \text{ ns}$ ) where the contribution from free positron annihilation nearly ends and it further increases with the contribution from *o*-Ps *pick-off* annihilation. In the positron age  $>2.0 \text{ ns}$  range, the contribution is solely from *o*-Ps *pick-off* annihilation and  $S(t)$  remains nearly constant in this region. The  $S(t)$  parameter in higher ages ( $> 2.0 \text{ ns}$ ) for PF-MWCNTs nanocomposites is nearly constant (average value from 2 ns to 4 ns =  $0.506 \pm 0.002$ ) which is lower compared to PF-0 (average value from 2 ns to 4 ns =  $0.517 \pm 0.002$ ). This shows that chemical environment around the free volumes is similar in PF-MWCNTs nanocomposites but different from pure PF resin. In PF-MWCNTs nanocomposites, a large fraction ( $\sim 100\%$ ) of formed *o*-Ps annihilates from PF matrix –MWCNTs interfaces. It appears as if the chemical environment around these new free volumes (interfaces) is

rich in oxygen which is not the case for pure PF resin where *o*-Ps annihilation with constituent elements (C, O and H) is weighted average. It is known that *pick-off* annihilation with oxygen electrons would produce more broadening in Doppler spectrum (lower *S*-parameter) compared to carbon [Sato et al., 2009]. It is to be noted that a reproducible increase in *S*(*t*) for PF-2 is observed in the positron age range of  $\sim 2$  ns. This shows that at lower concentration of MWCNTs, *o*-Ps annihilation is not solely from the interfaces and a fraction of *o*-Ps also annihilates from pre-existing nanoholes.

*S*(*t*) parameter in the positron age ( $< 0.8$  ns) is lower for PF-MWCNTs nanocomposites as compared to PF-0. In the presence of MWCNTs in polymers, a fraction of free positrons may annihilate from MWCNTs with lower *S*-value which will reduce the *S*(*t*) in positron age ( $< 0.8$  ns). In positron age range (0- 0.2 ns) where maximum contribution comes from *p*-Ps, a sharp decrease (insert in fig. 5.12) in *S*(*t*) is observed with MWCNTs concentration. With incorporation of MWCNTs, a fraction of positrons annihilate from MWCNTs aggregates and this fraction increases with MWCNTs concentration in the matrix. In MWCNTs, a positron lifetime component of 137.4 ps (Table 5.1) indistinguishable from *p*-Ps (125 ps) is observed as a result of annihilation from delocalized state in MWCNTs. This will contribute in the same range of positron age as of *p*-Ps and will reduce the *S*-parameter as observed in the figure. It is noteworthy that a decrease in *S*(*t*) has been observed for the positronium forming materials in young positron age range ( $\sim 0$  ns) because of hot positronium. This is called juvenile broadening of Doppler spectra. In the present case, no juvenile broadening has been observed in PF-0 and, hence, it is not expected in PF-MWCNTs nanocomposites [Stoll et al., 2003]. It is to be noted that first two lifetime components in PF-0 (117.2 and 329.0 ps) increase to 144.4 and 340.6 ps for PF-20. These two components in PF-20 are very close to positron lifetime components observed in pure MWCNTs (137.4 and 338.3

ps). An increase in  $I_1$  from 8.06 % in PF-0 to 14.23% in PF-20 is also observed. These observations are well consistent with AMOC data and confirm the annihilation of free positrons in MWCNTs dispersed in the matrix.

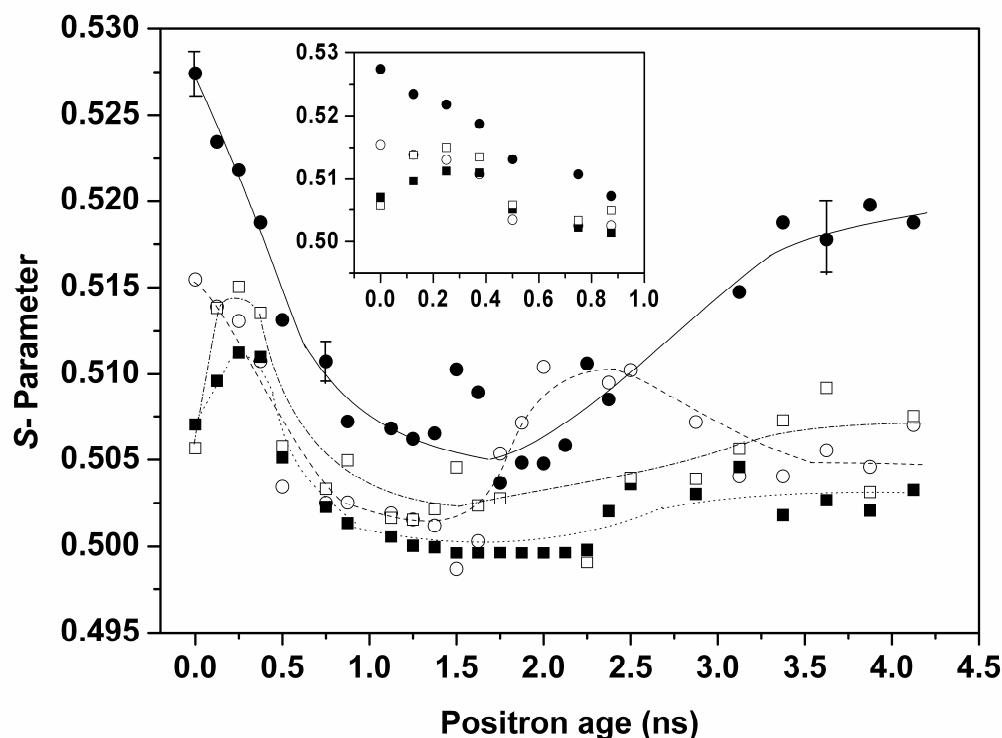


**Figure 5.12:** Positron age dependence of  $S(t)$  parameters in PF-0 (■), PF-2 (●) and PF-10 (○). The solid lines are eye guides. For clarification, the error bars are not shown on all the data. The variation of  $S(t)$  up to 1 ns is shown in the inset.

### 5.3 Conclusion

A set up for Age momentum correlation measurements has been developed with time resolution of 290 ps. Positron annihilation lifetime and positron age momentum correlation have been used to characterize the free volumes sizes, distribution and chemical environment in PF resin and PF-MWCNTs nanocomposites having MWCNTs concentration (w/w %) 2, 5, 10 and 20%. On incorporation of MWCNTs,  $o$ -Ps lifetime was observed to increase with a concomitant decrease in the corresponding intensity. The

free volume size was observed to increase with MWCNTs concentration with saturation at higher loadings indicating the agglomeration of MWCNTs in PF matrix. AMOC measurements along with PALS studies showed that *o*-Ps mainly annihilate from the interfaces. These interfaces are seen to be larger free volumes due to weak interaction between polymer and nanotubes. The chemical environment of free volumes (interfaces) in PF-MWCNTs nanocomposites was observed to be enriched in oxygen. AMOC data provided a direct evidence of free positron annihilation in MWCNTs incorporated in polymer matrix which was seen to be consistent with positron lifetime measurements. The present study confirms that the presence of crystalline nanophases in polymer matrix alters the positron systematics and an insight into nanophase role in positron systematics is essential for free volume characterization of a polymer nanocomposite using PALS. The present study should provide a backbone to further free volume characterization studies on polymer- CNTs (functionalized) nanocomposites.



## **CHAPTER-VI**

---

# **VACANCY DEFECTS IN SEMICONDUCTOR AND METAL NANOPARTICLES**

The properties of nanoscale crystalline materials are investigated extensively today, theoretically and experimentally, due to their scientific and industrial applications [Gleiter, 2000 and Richman et al., 2009]. Nanoparticles exhibit unique electronic and optical properties due to their size effects [Budai et al., 1997], quantum confinement [Gea et al., 1999], and quantum tunnelling [Chan et al., 1998]. The physical properties of the nanomaterials depend on the particle size, inter-particle distance, nature of the protecting organic shell and shape of nanoparticles [Brust et al., 2002]. Defects as vacancies play an important role in the electrical, optical, thermal as well as mechanical behaviour of the material. During the nucleation and growth, vacancy defects are produced either in the bulk or at the surface of the nanoparticles. These vacancy defects are thermodynamically stable as they increase the entropy of the system. The nanoparticles synthesized through different routes can have defects of various origins, *e.g.*, the vacancy defects, stacking faults, surface disorder etc., which can modify the opto-electronic properties of the nanoparticles. Thus, characterization of the defects in nanoparticles produced through various methods is important to identify the suitable methods for the synthesis of nanoparticles with desired properties.

A wide range of techniques have been employed to characterize the defects present in various nanoparticles. In recent years, positron has been identified as a sensitive and self seeking probe for the embedded and colloidal nanoparticles [Xu et al., 1999; Nagai et al., 2000; Xu et al., 2001; Nagai et al., 2001; van Huis et al., 2002; Eijt et al., 2006 and Weber et al., 2002]. The local structural properties and electronic structure of the nanoparticles can be revealed via the measurement of electron momentum density using positron annihilation techniques. This is primarily due to the fact that the diffusion length of positrons is larger than the size of the nanoparticles which renders them localized on the particle surface. When positron is implanted in the material, after

thermalization it diffuses in the medium followed by annihilation with electron. Positrons have high propensity for defects in the material that leads to a longer lifetime due to lower electron density. Thus positron lifetimes and corresponding intensities can be directly correlated to the size and concentration of defects. The electron momentum distribution, on the other hand, is obtained by Doppler broadening measurements. Coincidence Doppler Broadening (CDB), a relatively new technique, involves coincidence measurement of two 511 keV annihilation photons at  $180^\circ$  that improves the peak to background ratio up to  $\sim 10^5$  and enables unambiguous extraction of the shape and magnitude of the high momentum (core electrons) component of the Doppler spectrum. The chemical surrounding of the annihilation site is obtained from the magnitude of the high momentum core component which carries the signature of the specific atom. Positron annihilation spectroscopy has been used to study different type of nanoparticles e.g. nanocrystalline Fe [Schaefer et al., 1998], embedded nanoparticles [Xu et al., 1999; Nagai et al., 2000, Xu et al., 2001; Nagai et al., 2001 and van Huis et al., 2002] and semiconductor nanoparticles [Eijt et al., 2006 and Weber et al., 2002] in different size ranges. These studies demonstrate positron annihilation spectroscopy to be a sensitive technique to correlate the size effects, quantum effects, and surface defects of the nanoparticles to their electronic and optical properties. However, it may be mentioned that the physics of positron systematic in different type of nanoparticles is far from understood and requires extensive studies in different type of materials. Keeping this objective in mind, the positron annihilation spectroscopic studies corroborated with first principle calculation of positron lifetime and electron momentum distributions have been carried out in semiconductor (ZnO, CdSe) and metal (Au) nanoparticles. In these studies, the size of ZnO nanoparticles were varied by annealing the as prepared nanoparticles and different size CdSe nanoparticles were prepared by taking different ratio of Cd and Se

precursors. Gold nanoparticles of average size 6 nm were studied for the characterization of vacancy defects in terms of its shape and size as well.

Zinc Oxide (ZnO) is a semiconductor with a wide band gap of 3.437 eV at 2 K [Tuomisto et al., 2003]. It has attracted considerable attention over the years because of its possible applications in catalysis [Chopra et al., 1983], UV light emitting diodes, blue luminescent devices, and gas sensors [Look et al., 1999a and Reynolds et al., 1996] which has led to a large number of studies in polycrystalline as well as single crystals of ZnO using a variety of techniques. ZnO being more radiation resistant compared to Si, GaN, GaAs, it is considered to be a suitable material for use in high radiation area such as space satellite electronics [Look et al., 1999b]. ZnO nanoparticles are expected to exhibit tunable optical and electronic properties based on the size as the surface contribution becomes dominant. Positron annihilation spectroscopy has been extensively used for the defect characterization of ZnO single crystal [Tuomisto et al., 2003, Look et al., 1999b, Brauer et al., 2006, de la Cruz et al., 1992 and Chen et al., 2004]. Theoretical calculations of positron lifetimes have also been carried out in rigid and relaxed ZnO wurtzite lattice to explain the experimentally observed defects in as grown as well as ion implanted ZnO [Brauer et al., 2006 and Chen et al., 2004]. In the last few years ZnO nanoparticles of various sizes (in the range of 15-140 nm) have been subjected to positron annihilation studies [Mishra et al., 2007, Dutta et al., 2006, Sanyal et al., 2008, Dutta et al., 2005 and Ghosal et al., 2008]. These studies have found evidence for the presence of Zn vacancies in ZnO nanoparticles. Significantly, the vacancies produced in these nanoparticles are seen to be dependent on the synthesis procedure e.g. mechanical milling and/or wet chemical route, as the case may be. It is, therefore, interesting to carry out positron annihilation studies on ZnO nanoparticles prepared by methods not reported so far which

is solid state pyrolytic reaction method. In addition, it is interesting to examine the vacancies present in nanoparticles of smaller dimension.

CdSe nanoparticles can be considered as a model system for semiconductor nanoparticles, as its shape and size can be well tailored through different routes of synthesis [Murray et al., 2000 and Alivisatos et al., 1996]. Synthesis of CdSe nanoparticles through chemical reactions, where the growth of nanoparticles is controlled by capping the particles with the organic ligands, has been established as a potential method to synthesize nearly mono dispersed nanoparticles [Murray et al., 1993]. Positron annihilation spectroscopy techniques have been employed to study the CdSe nanoparticles in very small size range ( $< 6$  nm) [Eijt et al., 2006 and Weber et al., 2002]. In these studies, it has been shown that positrons annihilate from CdSe nanoparticles and probe its electronic structure. The observed variations in electron momentum distribution have been explained in terms of quantum confinement of valence electrons in CdSe nanoparticles having size smaller than 5 nm as well as widening of electronic band gap with the decrease in size [Eijt et al., 2006 and Weber et al., 2002]. As mentioned earlier, positrons are trapped at the structural defects, e.g. vacancy defects present in the nanoparticles and annihilate with the electrons from the surrounding. The variation in the electron momentum distribution due to the structural defects present in the nanoparticles has not been addressed in detail. The present study focuses on the role of structural defects present in CdSe nanoparticles in the variation of electron momentum distribution.

The optical properties of metal nanoparticles strongly depend on the particle size i.e. on the surface electron density. Vacancy defects present in the nanoparticles particularly on the surface may alter the surface electron density and consequently change the optical properties. Synthesis of gold nanoparticles capped with organic ligands through chemical routes has been established to produce the stable nanoparticles with

narrow size dispersion. To elucidate the shape and the size of the vacancy defects in thus produced nanoparticles, positron annihilation lifetime spectroscopy has been used.

The present study focuses on the defect characterization of ZnO, CdSe and gold nanoparticles using positron annihilation lifetime spectroscopy and Coincidence Doppler broadening (CDB) spectroscopy. The experimental results are corroborated with the first principle calculations of positron lifetime and electron momentum distribution calculations. In the case of Au nanoparticles, Vienna *ab-initio* simulation package (VASP) has been employed to calculate the relaxation of the lattice in the presence of vacancy defects and formation energy of defects. The details are discussed.

## **6.1. Experiments**

### **6.1.1. Synthesis**

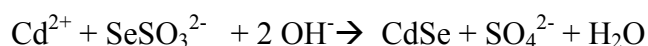
#### **6.1.1.1 ZnO nanoparticles**

ZnO nanoparticles were prepared by a solid state pyrolytic reaction of analytical grade  $\text{Zn}(\text{CH}_3\text{COO})_2$  and  $\text{NaHCO}_3$  at  $170^\circ\text{C}$ . The as-prepared nanoparticles, sample (a), were annealed at  $200^\circ\text{C}$ ,  $300^\circ\text{C}$ ,  $400^\circ\text{C}$ ,  $500^\circ\text{C}$  and  $800^\circ\text{C}$  for two hours which are referred to sample (b), (c), (d), (e) and (f) respectively in the text.

#### **6.1.1.2 CdSe nanoparticles**

Polyvinyl alcohol (PVA) (molecular weight 125,000) and cadmium acetate  $\text{Cd}(\text{OAc})_2$  were obtained from s. d. fine chemicals, and were used as received. All other chemicals used in the synthesis were of AR grade. Water from water purification system, Millipore-Q water, (conductivity of  $0.6 \mu\text{S cm}^{-1}$ , or lower) was used for preparation of the solutions. Sodium selenosulphate ( $\text{Na}_2\text{SeSO}_3$ ) was prepared using  $\text{Na}_2\text{SO}_3$  and Se powder [Shah et al., 2007].

PVA-capped CdSe nanoparticles were synthesized by following the procedure reported by Shah et al. (2010). The measured volumes of the aqueous solutions of the precursors,  $\text{Cd}(\text{OAc})_2$  and  $\text{Na}_2\text{SeSO}_3$ , of various concentrations were mixed in the presence of 9.2% (w/v) PVA and the mixture was stirred constantly at low temperature (below  $20^\circ\text{C}$ ) till the completion of the reaction. The chemical reaction may be represented as follows.



A beautiful greenish or orange-coloured, sol was obtained, depending on the concentrations of cadmium and selenium precursors. CdSe nanoparticles were separated from the aqueous sol using a high speed centrifuge followed by several washings with water to remove the excess PVA. Four samples namely sample (a'), (b'), (c'), and (d') were synthesized using this method by taking  $\text{Cd}(\text{OAc})_2$  and  $\text{Na}_2\text{SeSO}_3$  in 8:1, 4:1, 1:2 and 1:4 ratio, respectively.

### 6.1.1.3 Gold nanoparticles

Gold nanoparticles were synthesized by reducing hydrogen tetrachloroaurate ( $\text{HAuCl}_4$ ) in the presence of dodecanthiol ( $\text{C}_{12}\text{H}_{25}\text{SH}$ ) with lithium triethylborohydride. Tetra Hydro Furan (THF) was used as solvent for the reaction. The concentration ratio of  $\text{HAuCl}_4$  and RSH used for the synthesis was 1:1. The Au nanoparticles sample in the powder form from colloidal solution was collected using high speed centrifugation.

### 6.1.2 XRD, TEM and photoluminescence characterization

The X-ray diffraction patterns (XRD) of the samples were obtained on Philips PW 1710 automatic diffractometer using monochromatized  $\text{Cu } K_\alpha$  radiation. For each sample, a scan was carried out from  $10^\circ$  to  $90^\circ$  with a step of  $0.20^\circ$ . TEM characterization was

carried out with a JEOL-2000 FX electron microscope operating at 200 kV. The bright field images of the nanoparticles samples were collected by re-dispersing the synthesized nanoparticles in dilute ethyl alcohol medium, using a sonicator, and drying a drop of the dispersed solution on a copper grid coated with a thin amorphous carbon film. The average particle sizes were determined by Debye-Scherrer equation from the fwhm of XRD peaks and confirmed from TEM images. Photoluminescence spectra of all the ZnO samples were recorded using a fluorescence spectrometer (Hitachi F2000) with xenon flash lamp  $\lambda_{\text{ex}}$  of 248 nm and laser  $\lambda_{\text{ex}}$  of 345 nm.

### 6.1.3 Positron annihilation measurements

PALS and CDB measurements were carried out using a  $^{22}\text{Na}$  (10  $\mu\text{Ci}$ ) isotope sandwiched between two kapton foils of thickness 7  $\mu\text{m}$ . The samples were used in powder form and the source was covered adequately with the sample so that all the positrons annihilate within the sample. Positron lifetime spectra were recorded using plastic scintillation detectors coupled with fast-fast coincidence circuit with a resolution of 220 and 280 ps for ZnO and Au nanoparticles, respectively. The source correction was carried out using Silicon single crystal as reference. The lifetime spectra were best fitted to two or three lifetime components depending on the samples using PATFIT program [Kirkegaard et al., 1991]. CDB measurements were carried out using two HPGe detectors (resolution 1.1 keV at 514 keV of  $^{85}\text{Sr}$ ) located at  $180^\circ$  relative to each other; the details of which are described in chapter II. CDB measurements were carried out in ZnO and CdSe nanoparticles as well as in pure Cd and Se. Silicon crystal was used as reference for the calculation of CDB ratio curves. In case of ZnO nanoparticles samples, the line shape parameter ( $S$ ) and the wing parameter ( $W$ ) were calculated by taking the ratio of central



region ( $511 \pm 1.0$  keV), and, the wing region ( $511 \pm 5.1$  to  $10.2$  keV) to the total area of the photo peak ( $511 \pm 15.3$  keV), respectively.

## 6.2. Theoretical calculations

### 6.2.1 Positron lifetime and electron momentum distribution calculation

Positron lifetime and electron momentum distributions in bulk lattice of ZnO, CdSe and Gold and in the presence of defects, monovacancies as well as vacancy cluster as the case may be, were evaluated using MIKA Doppler code [Torsti et al., 2006]. The calculations were also carried out in pure Cd, Se and Si as well. The ‘conventional scheme’ was used in the calculations where electron density of the solid is approximated by non-self consistent superposition of free atoms in the absence of positron and the potential felt by the positron is also generated in a similar way [Puska et al., 1994]. The electron positron enhancement factors were parameterized using gradient-corrected scheme and correlation potential developed by Arponen-Pajanne as well as Boronski-Nieminen were used in the calculations [Arponen et al., 1979 and Boronski et al., 1986]. The positron wave function is obtained by solving the Schrodinger equation using a three-dimensional real space solver [Heiskanen et al., 2001]. The positron lifetime and electron momentum distribution is calculated using the positron wave function as described in ‘MIKA/DOPPLER’ package.

The ZnO nanoparticles have hexagonal wurtzite structure. For calculations lattice parameters of ZnO single crystal,  $a = 0.32501$  nm and  $c = 0.52071$  nm were used [Brauer et al., 2006 and references therein]. A supercell having 64 ZnO molecules were used for the calculations. To calculate the positron parameters in the vacancy defects, atoms Zn, O and combinations of (Zn,O) were removed from the lattice positions.

In the case of CdSe, a supercell of  $3 \times 3 \times 3$  of CdSe in zinc blende structure having a lattice constant  $a = 6.05 \text{ \AA}$  was used for the calculations. CdSe has two lattice structure viz. wurtzite and zinc blende. It has been reported in literature that the calculation in zinc blende lattice also serves as a good approximation to wurtzite structure [Eijt et al., 2006]. Cd and Se atoms were removed from the lattice positions to create the vacancy defects in the lattice. Silicon single crystal was used as reference. For calculation of ratio curves, calculated momentum distribution was convoluted with detectors combined response function.

A 256 atoms FCC lattice having lattice parameter  $4.08 \text{ \AA}$  was used for the calculation of positron lifetime in bulk gold. Gold atoms were removed from the lattice positions to create the vacancy defects in the lattice. Two configurations (see Table 6.4) of the defects were considered for larger defects ( $n \geq 3$ ,  $n$  is the number of vacancies in a defect). In the presence of defects, the atoms (neighbouring to the defect site) undergo relaxations. Positron lifetimes were also calculated using the relaxed coordinates of the atoms in the gold lattice.

### 6.2.2 Calculation of relaxation of lattice and formation energy of defects

The formation energy of the vacancy defects in gold super cell of 108 atoms as well as the relaxed lattice structure in the presence of vacancy defects were calculated using first principle PAW pseudopotential methods with in the LDA approximations implemented in VASP [Kresse et al., 1996 and 1999]. The Vanderbilt-type ultrasoft pseudopotentials were employed in the calculation [Vanderbilt 1990]. The  $4 \times 4 \times 4$  Monkhorst-pack k-point set was used to sample the Brillouin zone. The *energy cut-off* for the plane wave basis was 230 eV. The constant volume relaxation method was employed to get the relaxed coordinates of the first nearest neighbours of the atoms constituting the

vacancy defect. The formation energy and the binding energy of a defect of  $n$  vacancies were calculated. The formation energy was defined as follows.

$$E_f(V_n) = E_{\text{tot}}(N) - [E_{\text{tot}}(N-n) + n.E_{\text{Au}}] \quad (6.1)$$

Where,  $E_f(V_n)$ ,  $E_{\text{tot}}(N)$ ,  $E_{\text{tot}}(N-n)$  and  $E_{\text{Au}}$  are the formation energy of vacancy defect constituted by  $n$  atoms, total energy of bulk supercell having  $N$  atoms, total energy of supercell having  $N-n$  atoms and one Au atom in reference state. In general, the formation energy per vacancy is reported which is calculated using  $E_f(V_n) = n \cdot \hat{E}_f(V_n)$ , where  $\hat{E}_f(V_n)$  is the formation energy per vacancy. The Domain method [Domain, 2006] was used to calculate the binding energy of vacancy defects which is defined as the energy difference between the formation energy of a state containing two interacted defects and sum of that of two states containing respective single defect. For example, the binding energy of  $V_n$  defect is calculated as follows.

$$E_B(V_n) = E_f(V_n) - [E_f(V_{n-1}) + E_f(V_1)] \quad (6.2)$$

Where  $E_B(V_n)$ ,  $E_f(V_n)$ ,  $E_f(V_{n-1})$  and  $E_f(V_1)$  are the binding energy of defect  $V_n$ , formation energies of defects  $V_n$ ,  $V_{n-1}$  and  $V_1$  in the gold supercell, respectively.

### 6.3. Results and Discussion

#### 6.3.1. XRD and TEM

##### 6.3.1.1 ZnO nanoparticles

The XRD patterns of all the samples are shown in Fig. 6.1. The observed peaks were in good agreement with the hexagonal wurtzite structure of ZnO. On annealing at different temperatures, no new peak was observed in the XRD pattern, which showed that there was no new phase evolution by two hours annealing in the temperature range of 200°C to 800°C. The average particle sizes of all the ZnO samples were calculated from XRD pattern using Debye-Scherrer equation. The average size of the samples (a), (b), (c),

(d), (e) and (f) calculated from the XRD pattern were 4, 11, 15, 20, 30 and 40 nm, respectively. The particle size data agreed well with TEM data for sample (a) and (b) on which TEM measurements were carried out.

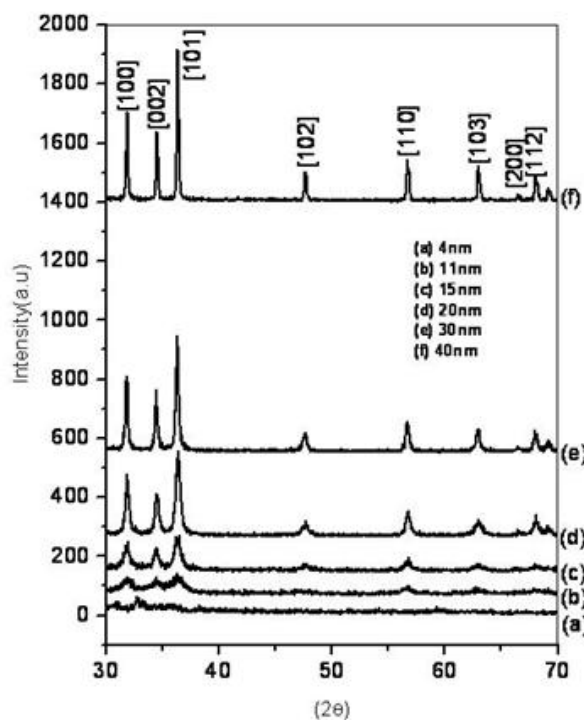


**Figure 6.1:** XRD pattern of as-prepared ZnO (a) and samples annealed at different temperatures; 200°C (b), 300°C (c), 400°C (d), 500°C (e) and 800°C (f).

### 6.3.1.2 CdSe nanoparticles

The XRD patterns of three CdSe nanoparticles samples are shown in Fig. 6.2. The XRD diffraction pattern of sample (c') shows three characteristic peaks at  $2\theta \sim 25^\circ$ ,  $42^\circ$  and  $50^\circ$ , corresponding to a cubic cell of CdSe [Murray et al., 1993]. The peaks at  $2\theta \sim 42^\circ$  and  $50^\circ$  are much broader in the case of sample (b') and they nearly merge in the case of sample (a') indicative of reduction in particle size. However, no new peak is observed in sample (a') showing that its crystal structure is identical to other samples. This shows that higher concentration of Cd precursor results in the small size of the nanoparticles as the Cd (OAc)<sub>2</sub> concentration reduces from sample (a') to sample (c'). The XRD diffraction

pattern of sample ( $d'$ ) is not measured but it is expected to have much sharper peaks as it was synthesized by using lower  $\text{Cd}(\text{OAc})_2$  concentration compared to sample ( $c'$ ). Murray et al. (1993) have reported the XRD characterization of CdSe nanoparticles in the size range of 1.2 nm to 11.5 nm, where the same type of XRD pattern in the range of  $2\theta \sim 42^\circ$  and  $50^\circ$  has been shown. It has been reported that the stacking faults affect the XRD pattern in the range of  $2\theta \sim 30^\circ$  and  $50^\circ$ , the prolate shape and the reduction in the particle size affect the peak position of the first diffraction feature at  $2\theta \sim 25^\circ$  and the surface disorder affects the shape of the first diffraction feature [Murray et al., 1993].

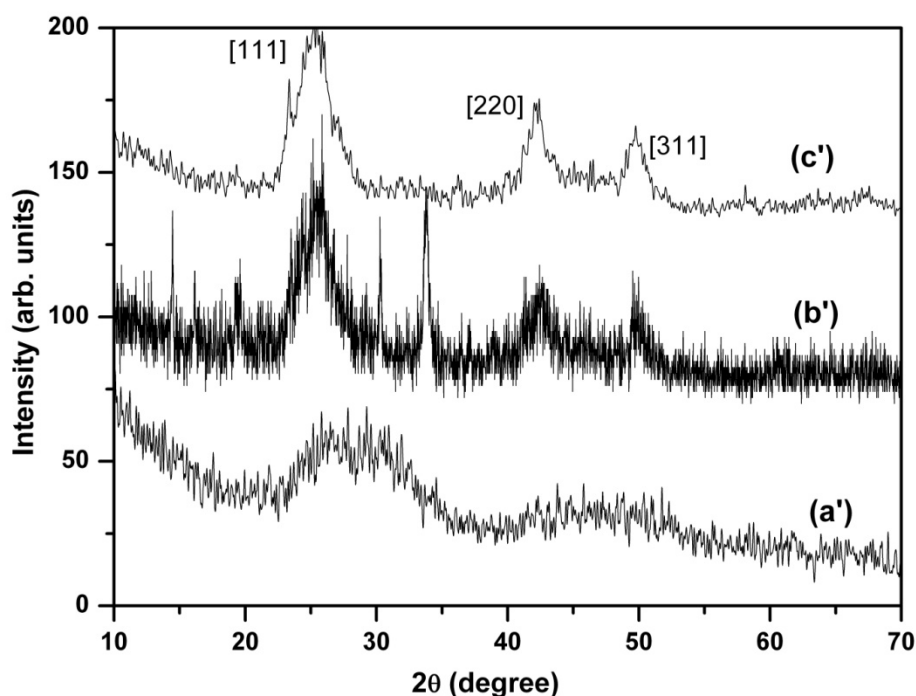


**Figure 6.2:** The XRD pattern of CdSe nanoparticles samples ( $a'$ ), ( $b'$ ), ( $c'$ ) having average particles size 7, 11.5 and 15.5, respectively.

TEM is a very important technique for providing the information about particles size, shape and surface topography etc. Therefore, morphology and structure of the synthesized CdSe nanoparticles were also investigated using TEM technique. The TEM images of samples ( $a'$ ) and ( $d'$ ) are shown in Fig. 6.3. From the TEM images, it is observed that the size of the nanoparticles increases from sample ( $a'$ ) to ( $d'$ ). The average

size of the samples ( $a'$ ), ( $b'$ ), ( $c'$ ) and ( $d'$ ) measured from the TEM images were 7, 11.5, 15.5 and 17.0 nm, respectively. The particles seen in the TEM images are not completely spherical. The particles have elongated shape which modifies the XRD pattern of the samples as discussed before.

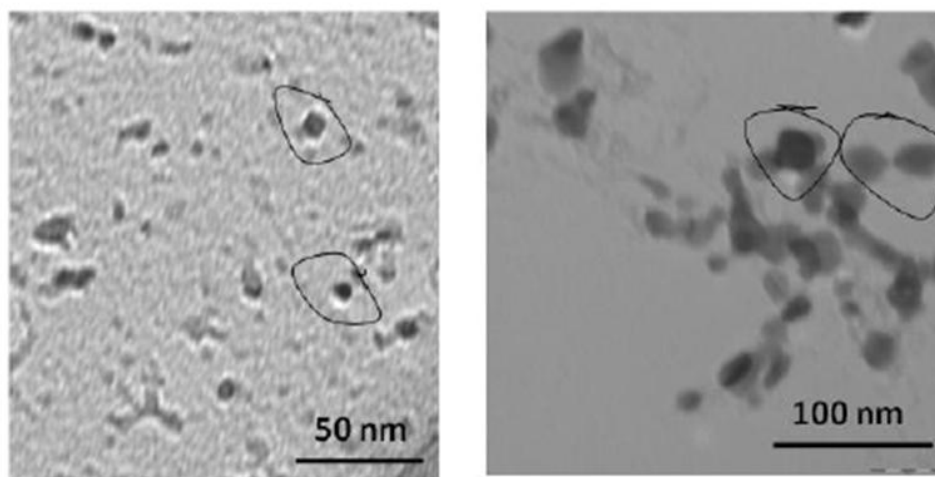


**Figure 6.3:** The TEM images of sample ( $a'$ ) and sample ( $d'$ ). The bars at the bottom on the right hand side show the scale of the images. The encircled dots are the CdSe nanoparticles.

### 6.3.1.3 Gold nanoparticles

Fig. 6.4 shows the size distribution of the gold nanoparticles obtained from TEM images. The average size of the nanoparticles is  $\sim 6$  nm.

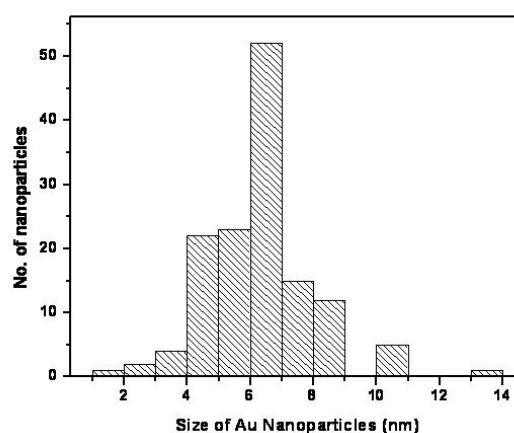


**Figure 6.4:** Size distribution of Au nanoparticles

### 6.3.2. PALS, CDB measurements and theoretical calculations

#### 6.3.2.1 ZnO nanoparticles

##### (i) Defects in ZnO nanoparticles

Two positron lifetime components were observed in all the samples as shown in Table 6.1. The shorter lived component,  $\tau_1$ , is expected to be originating from the bulk and on the particle surface referred to as grain boundary. The longer lived second component,  $\tau_2$  arises from the positrons trapped in the nanovoids available at the intersection of the grain boundaries [Schaefer et al., 1988 and Mishra et al., 2007]. It may, however, be mentioned that this component may also contain the signature of *pick-off* annihilation of *ortho*- positronium (*o*-Ps) formed in the trapped air with in the grains.

**Table 6.1.** Positron annihilation lifetimes and corresponding intensities in ZnO nanoparticles of different size.

Sample	Average particle size (nm)	$\tau_1(\text{ps}) \pm 1 \text{ ps}$	$I_1(\%)$	$\tau_2(\text{ps}) \pm 3 \text{ ps}$	$I_2(\%)$
(a)	4	261	$83.0 \pm 0.6$	803	$16.9 \pm 0.6$
(b)	11	306	$94.3 \pm 1.0$	739	$5.6 \pm 1.0$
(c)	15	299	$94.4 \pm 0.8$	765	$5.5 \pm 0.8$
(d)	20	283	$91.5 \pm 1.0$	650	$8.4 \pm 1.0$
(e)	30	274	$89.0 \pm 1.0$	592	$10.9 \pm 1.0$
(f)	40	201	$95.7 \pm 0.3$	746	$4.2 \pm 0.3$

Theoretically calculated positron lifetime using atomic superposition method with Boronski-Nieminen approximation (ATSUP-BN) in ZnO wurtzite supercell and with  $V_{\text{Zn1}}$  (mono vacancy of zinc),  $V_{\text{O1}}$  (mono vacancy of oxygen),  $V_{\text{Zn1,O1}}$  (divacancy constituting one Zn and one O),  $V_{\text{Zn2,O1}}$  (trivacancy constituting two Zn and one O) defects are shown in Table 6.2 and these values are in good agreement with the reported literature values

[Brauer et al., 2006 and Chen et al., 2004]. The ZnO super cell used for the calculation and positron density in a plane having Zn vacancy is shown in Figs. 6.5(a) and (b)

**Table 6.2.** Calculated positron lifetime in ZnO wurtzite supercell bulk and having various combinations of vacancies

Defects	Positron life time (ps)
Bulk life time (no defects)	161
$V_{Zn1}$	196
$V_{O1}$	169
$V_{Zn1,O1}$	223
$V_{Zn2,O1}$	254

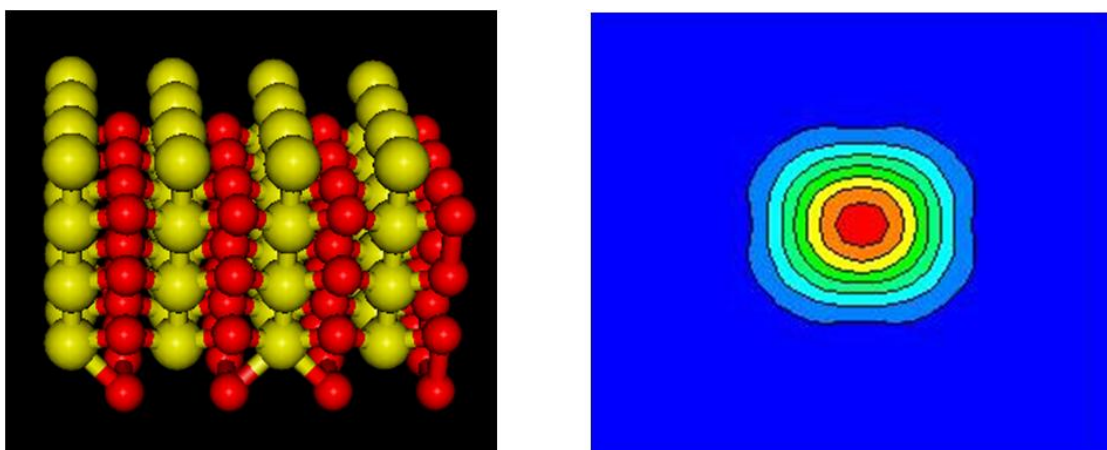


**Figure 6.5(a) and (b):** ZnO supercell and positron density in a plane having Zn vacancy, respectively

A careful look at the computed lifetime (Table 6.2) shows that the change in lifetime from the bulk value is small for oxygen vacancy (8 ps for  $V_{O1}$ ) due to the inability of the positively charged O vacancies to trap positrons. This small increase in lifetime can be due to the reduction in average electron density in the lattice. However, for negatively charged,  $V_{Zn1}$ , and for neutral vacancies,  $V_{Zn1,O1}$ , the changes are large (30-60 ps).

In ZnO supercell having large vacancy cluster defect, the calculated positron lifetimes in the range of 265 -375 have been reported [Chen et al., 2004]. We, therefore,



believe that  $\tau_1$  in the ZnO nanoparticles are associated with multi  $V_{Zn}$  or multi  $V_{Zn,O}$  located either at the grain boundaries or in bulk of the nanoparticles as structural defects. As seen in Table 6.1,  $\tau_1$  for the smallest (4 nm) particles is 261 ps, which increases to 306 ps for 11 nm particle and then decreases monotonically with increase in the average size of the nanoparticles. On annealing the 4 nm particles at 200°C leading to 11 nm particles, agglomeration of  $V_{Zn}$  or  $V_{Zn,O}$  occurs due to the migration of vacancies from the bulk of the particles to the grain boundaries that increases the lifetime to 306 ps. At higher temperatures (400°C to 500°C) the Zn interstitials,  $I_{Zn}$ , might substitute  $V_{Zn}$  at the grain boundaries leading to a reduction in the concentration of  $V_{Zn}$  and concomitant reduction in lifetime is observed [Mishra et al., 2007 and Gupta et al., 1989]. In the case of sample (f) with the largest average particle size 40 nm, the lifetime decreases drastically to 201 ps from 274 ps in 30 nm particles. This is a clear indication of the absence of vacancy clusters in the nanoparticles. Therefore it can be concluded that in sample (f) positrons primarily annihilate in the bulk which has some kind of defects or imperfection left in the sample. Similar observations have also been made by Chen et al. (2004) who reported a lifetime of 189 ps (higher than the bulk lifetime) in ZnO single crystal annealed at 900°C. The observed lifetime of 201 ps is, however, close to the theoretically calculated positron lifetime for  $V_{Zn}$  (196 ps) and it seems very likely that monovacancies are present in the sample (f).

The intensity of shorter component ( $I_1$ ), which is the fraction of positrons annihilating in the nanoparticles behave similar to  $\tau_1$  in all the samples except for sample (f). It was observed that  $I_1$  increases in the sample (f), unlike  $\tau_1$ . The enhancement in  $I_1$  can be due to large particle size. In the case of sample (f), large particle size reduces the concentration of nanovoids present at the intersection of grain boundaries and  $I_2$  decreases significantly.

The  $S$ -parameter, on the other hand, indexes the fraction of positrons annihilating with the valence electrons.  $S$ -parameter is known to increase in the presence of defects (vacancy, vacancy clusters, voids) because in case of trapped positrons, the reduction in positron overlap with core electrons is much more as compared to the valence electrons. When different types of defects are present in the material,  $S$ -parameter has the contribution from different annihilation sites and can be correlated to the average positron life-time,  $\tau_{av} [= (\tau_1 I_1 + \tau_2 I_2) / (I_1 + I_2)]$ . The evaluated  $S$ -parameter and average positron lifetime ( $\tau_{av}$ ) vs. particle size are shown in Figs. 6.6 (a) and 6.6 (b), respectively. It is seen that both the  $S$ -parameter and  $\tau_{av}$  decrease with the increase in the particle size as concentration of both type of defects reduce with the growth of particles size. For 4 nm ZnO nanoparticles the  $S$ -parameter as well as  $\tau_{av}$  are higher than other samples because in this case  $\tau_2$  and  $I_2$  are higher due to small particle size and large number of nanovoids at the intersection of grain boundaries.

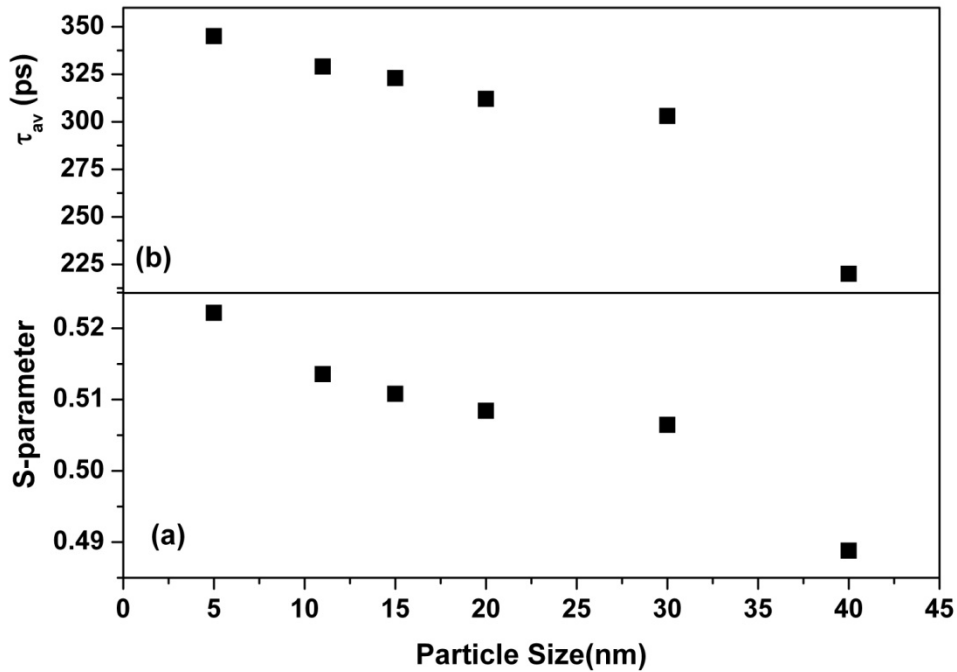


**Figure 6.6 (a) and (b):**  $S$ -parameter and average positron lifetime ( $\tau_{av}$ ) as a function of size of ZnO nanoparticles, respectively

The ratio curves obtained from CDB measurements and theoretical calculations are shown in Figs. 6.7(a) and (b), respectively. A systematic increase in the area under the high momentum region of ratio curve is observed with particle size, the ratio curve for 40 nm particle being highest indicating high overlap with core electrons. The calculated ratio curves for perfect lattice and with oxygen vacancies are indistinguishable (Fig. 6.7b). However, when  $V_{Zn}$  or  $V_{Zn,O}$  are introduced in the supercell, the ratio curves in high momentum region are considerably reduced. Comparing the experimental and simulated ratio curves, it can be inferred that nanoparticles except for 40 nm sample have higher concentration of defects, either  $V_{Zn}$  and/or  $V_{Zn,O}$  that is consistent with the observation from lifetime measurements. It is also evident that the high momentum region has dominant signature of Zn core electrons.

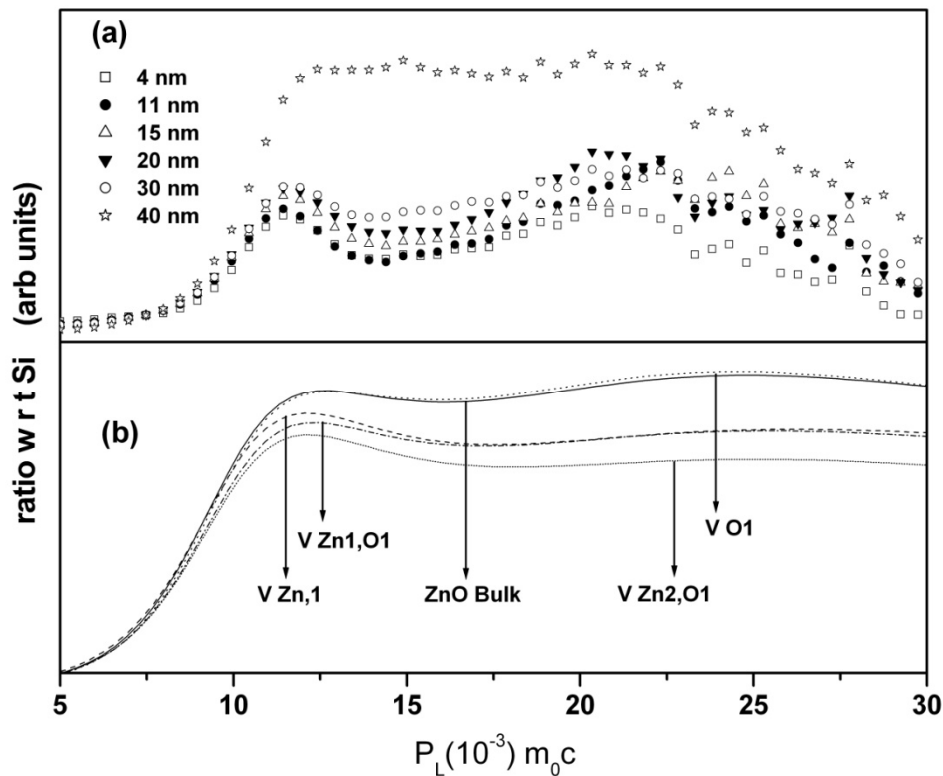


**Figure 6.7(a) and (b):** Ratio curves with respect to Si from CDB measurements on ZnO nanoparticles and calculated ratio curves in ZnO with different vacancies, respectively

The  $S$ - $W$  plot is shown in Fig. 6.8, which is a correlation plot of relative contribution in the valence and core electrons momentum. It is interesting to note that sample (a) shows identical  $W$ -parameter but higher  $S$ -parameter than sample (b). The higher  $S$ -parameter for sample (a) is due to the higher concentration of grain boundaries as described before. Near identical  $W$ -parameter [sample (a) with sample (b)] indicates the extents of overlap with Zn core electrons are identical since Zn has a predominant contribution to the high momentum region. At higher temperature,  $S$ -parameter decreases due to particle growth and reduction in the defects concentration while  $W$ -parameter increases.

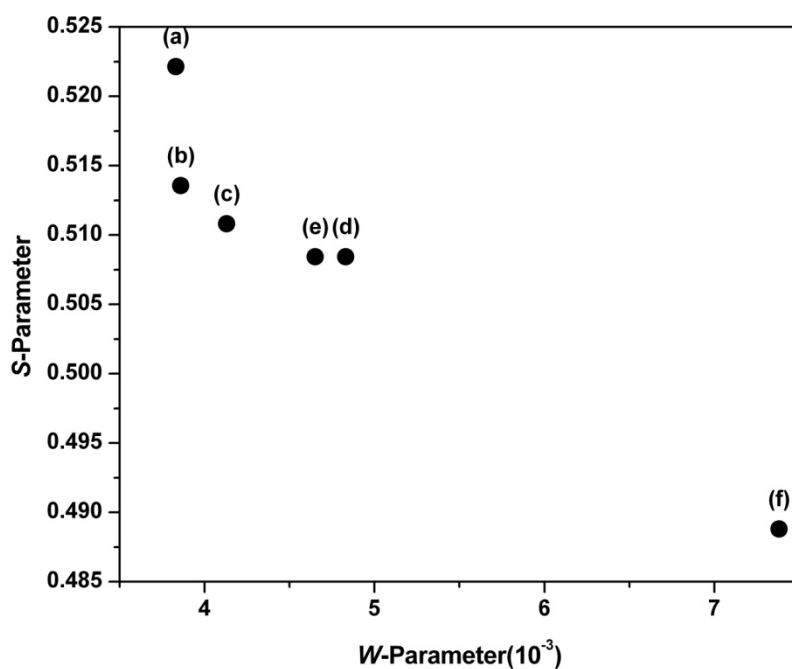


**Figure 6.8:**  $S$ - $W$  plots of ZnO nanoparticles

It has been observed that annealing in the range of 400-500°C, Zn vacancies migrate to the grain boundaries containing excess of interstitial Zn ( $I_{Zn}$ ) that acts like a sink for Zn vacancies [Chen et al., 2004 and Gupta et al., 2009]. Overlap of positrons trapped in the vacancies, therefore, increases with Zn electrons that explain the increase in  $W$ -parameter with the increase of particle size. For sample (f), a large decrease in  $S$ -parameter and a concomitant increase in  $W$ -parameter are seen. Decrease in  $S$ -parameter is due to near

absence of vacancy clusters and larger fractions of positrons annihilating in the bulk due to larger particle size (decrease in  $I_2$  as discussed earlier). Annealing in the range of 800°C leads to escape of oxygen from ZnO [Sanyal et al., 2008 and Selim et al., 2007] that effectively increase the overlap of positrons with Zn electrons. This effective increase of overlap of annihilating positron with Zn core electrons causes higher  $W$ -parameter for sample (f).

### ***(ii) Role of defects in photoluminescence properties***

Photoluminescence measurements showed two peaks corresponding to UV and visible region (green) in all the samples. While the emission in the UV region is ascribed to the direct combination of conduction electron and valence band hole, the origin of the green emission is not fully understood. The latter is often ascribed to the presence of various types of defects. From theoretical studies it has been proposed that  $V_{Zn}$  (acceptor site) as well as  $V_O$  (donor site) have comparable enthalpy of formation and are primary trapping sites for electrons.  $I_{Zn}$  (donor site) can also be a trapping site of excited electron but the enthalpy of formation of  $I_{Zn}$  is higher than  $V_O$  [Kohan et al., 2000]. Tuomisto et al. (2003) have shown that Zn vacancy is a dominant acceptor in the case of single crystal ZnO. However, they have not ruled out the influence of  $I_{Zn}$  and  $V_O$  in the photoluminescence spectrum.

In Fig. 6.9, the ratio  $R = I_{VIS}/I_{UV}$  ( $I_{VIS}$  and  $I_{UV}$  being the intensities of emission peak in visible and UV region respectively) is plotted against the particle size where  $R$  is seen to be higher in sample (b) and sample (f). From positron annihilation study, Zn vacancy cluster was observed in sample (b), which enhances the trapping at Zn vacancy acceptor level increasing the emission in the visible region. In sample (c), (d) and (e) there is a reduction in vacancy concentration (reduction in  $\tau_{av}$  as well as  $S$ -parameter) with

annealing that improves the crystal quality due to grain growth. The ratio,  $R$ , also reduces from sample (c) to (e). Sample (f) where only  $V_{Zn1}$  seems to be present shows an intense peak in UV as well as in visible region as compared to other samples. As mentioned earlier, annealing at temperature  $\sim 800^\circ\text{C}$ , oxygen vacancies are produced due to evaporation of oxygen from the sample and donor levels become available for the excited electrons. Therefore  $V_O$  seems to be responsible for the enhanced visible emission in sample (f). These studies indicate that both  $V_{Zn}$  and  $V_O$  may be responsible for the origin of visible emission in ZnO.

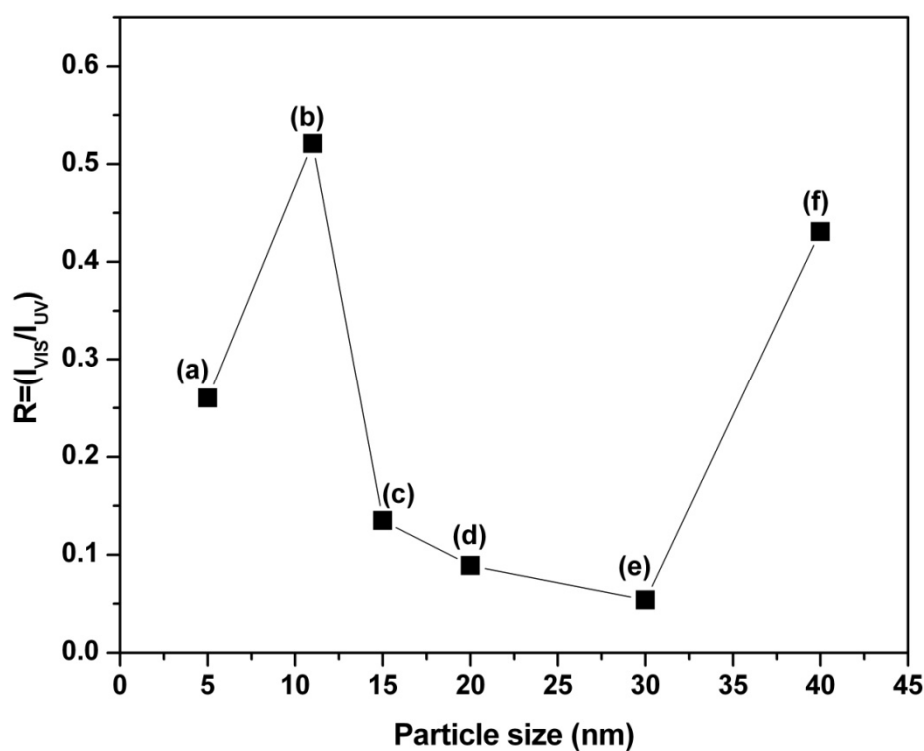


**Figure 6.9:** Ratio of the intensities of visible ( $I_{VIS}$ ) to UV ( $I_{UV}$ ) emission  $R = (I_{VIS}/I_{UV})$  as a function of particle size.

### 6.3.2.2 CdSe nanoparticles

CDB measurements were carried out in the CdSe nanoparticles samples as well as in pure Cd and Se. The ratio curves of the nanoparticles samples with respect to Si single crystal along with the ratio curves of Cd and Se are shown in Fig. 6.10. The ratio curves are very much similar upto  $P_L \sim 5 \times 10^{-3} m_0c$  and under statistical uncertainty beyond  $P_L \sim 23 \times 10^{-3} m_0c$ . The ratio curves of the CdSe nanoparticles in the range of  $P_L \sim 5 \times 10^{-3} m_0c$  to  $\sim 23 \times 10^{-3} m_0c$  show a peak with peak position at  $P_L \sim 11 \times 10^{-3} m_0c$  having the contribution from semi core electrons of the atoms which are annihilating with positrons. In this momentum range, the major contributions come from the semi core states of Cd (4d) and Se (3d) [Eijt et al., 2006]. Positrons at the surface may annihilate with the electrons of constituting elements (C, H and O) of capping ligands but their contribution in high momentum region has been observed to be negligible [Eijt et al., 2006].

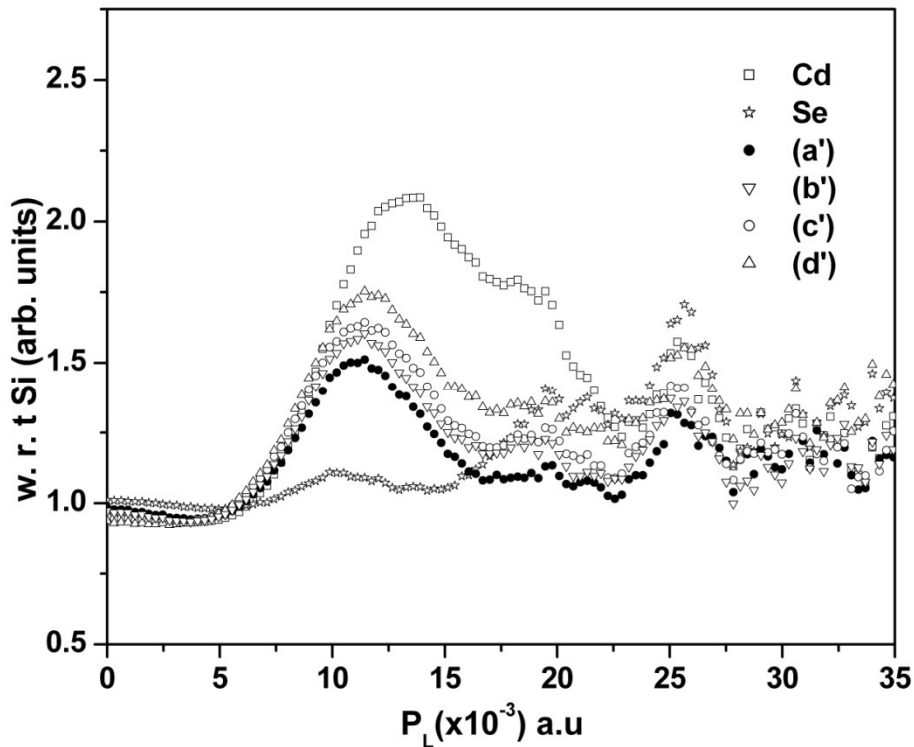


**Figure 6.10:** Ratio curves with respect to Si single crystal from coincidence Doppler broadening measurements on different CdSe nanoparticles, Cd and Se. The representative error bars are shown in the peak and back ground region.

The peak present in ratio curves for the nanoparticles samples, Cd and Se were fitted to Gaussian distribution having base line at ordinate equals to 1. The values of the peak positions and area under the peak are reported in Table 6.3. The peak positions for pure Cd and Se are  $12.58 \times 10^{-3} m_0c$  and  $10.23 \times 10^{-3} m_0c$ , respectively. The peak positions for CdSe nanoparticles samples lie between that of pure Cd and Se peak's positions, indicating the contribution from both Cd and Se semi core electrons. The peak positions from the ratio curves of CdSe nanoparticles are plotted against the size of nanoparticles in Fig. 6.11. The peak position shifts to the higher  $P_L$  values as a function of particle size showing more contribution from Cd semi core electrons. The variation of the peak position with particle size is not linear (Fig. 6.11). The non linear variation of the peak position with particle size indicates variation in contribution of Cd and Se semi core electrons towards positron annihilation as a function of nanoparticles size indicating non-uniform distribution of Cd and Se atoms present at the annihilation site.

**Table 6.3** The peak positions and area under the peak in the experimental ratio curves of CdSe nanoparticles of different sizes, and pure Cd and Se.  $f_{Cd}$  and  $f_{Se}$  are the fraction of positrons annihilating with semi core electrons from Cd and Se in CdSe nanoparticles, respectively.

Sample	Size (nm)	Peak position ( $\times 10^{-3} m_0c$ )	Area under the peak (arb. units)	$f_{Cd}(\%)$	$f_{Se}(\%)$
(a')	7	11.16	3.0937	69.76	30.24
(b')	11.5	11.16	3.1937	72.24	27.75
(c')	15.5	11.24	3.6383	83.51	16.48
(d')	17	11.37	3.8448	88.75	11.25
Cd	bulk	12.58	4.2885	100	0
Se	bulk	10.23	0.3435	0	100



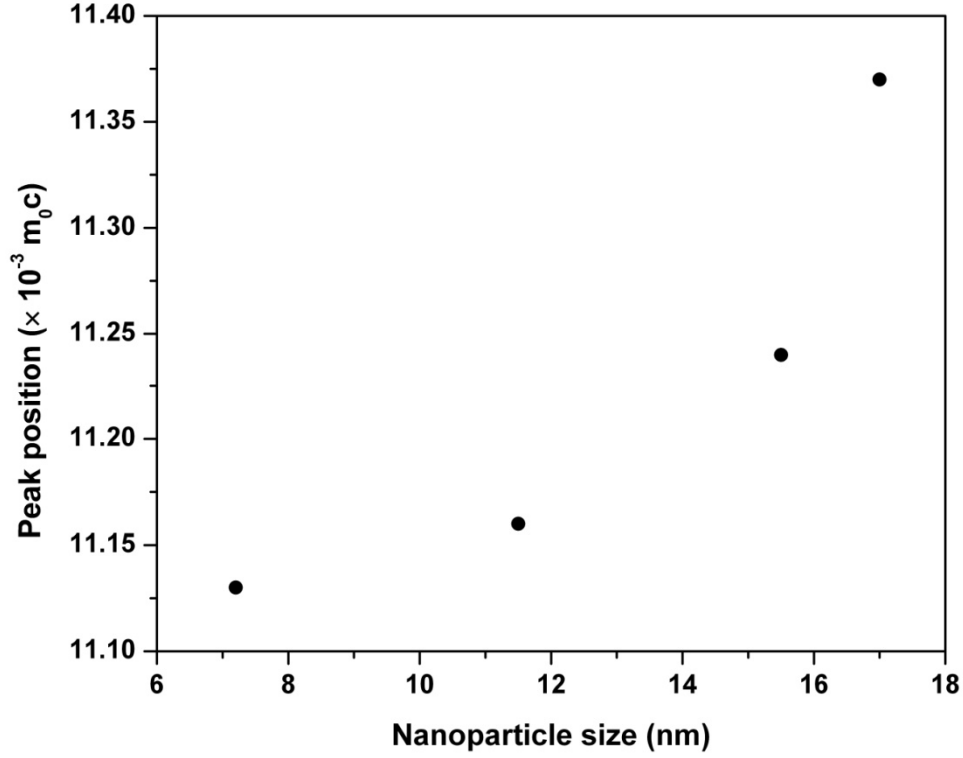


**Figure 6.11:** The plot of peak position obtained from the Gaussian fit to the experimental momentum distribution ratio curves vs. the size of CdSe nanoparticles.

The fractions of positrons annihilating with Cd and Se atoms are calculated from the area under the peak using equations 6.3 and 6.4.

$$A = f_{Cd} \cdot A_1 + f_{Se} \cdot A_2, \quad (6.3)$$

$$f_{Cd} + f_{Se} = 1. \quad (6.4)$$

Where,  $A$ ,  $A_1$  and  $A_2$  are the areas under the peaks of the nanoparticles sample, Cd and Se, respectively and,  $f_{Cd}$  and  $f_{Se}$  represent the fractions of the positrons annihilating with semi core electrons of Cd and Se in CdSe nanoparticles . These fractions calculated using equations 6.3 and 6.4 are given in Table 6.3. These data show that the fraction of positrons annihilating with Se ( $f_{Se}$ ) reduces continuously with the increase in the nanoparticles size. In CdSe nanoparticles, positrons annihilate either in the bulk or at the surface. With the increase in nanoparticles size, a reduction in the Se atoms at the annihilation site either in the bulk or at the surface will result in the reduction of  $f_{Se}$ . In

the bulk, the presence of different vacancy defects e.g. Cd or Se vacancy defects can make the variation in the fraction of positrons annihilating with either Cd or Se. This is because in the presence of defects, the trapped positrons annihilate exclusively with the surrounding atoms which may be different depending on the type of vacancy defect. It is noteworthy to mention that a fraction of positrons diffuse to the surface of nanoparticles and annihilate with the atoms present at the surface. The smaller size nanoparticles, sample (a'), showing the higher Se contribution,  $f_{\text{Se}}$ , indicates Se enrichment of the nanoparticles surface. The fraction of the positrons diffused to the surface decreases as a function of nanoparticles size, and consequently, the contribution from Se ( $f_{\text{Se}}$ ) present at the surface will decrease with the increase in the nanoparticles size. Based on *ab-initio* calculations, it has also been reported in the literature that Se atoms relax outward in the case of CdSe quantum dots and surface becomes Se enriched compare to the bulk [Puzder et al., 2004].

To investigate the effect of vacancy defects on momentum distribution ratio curves in CdSe, annihilating electron momentum distribution calculation in bulk CdSe supercells as well as in vacancy defects of Cd and Se have been performed using 'MIKA/DOPPLER' package. The ratio curves of CdSe, Cd and Se with respect to Si obtained from theoretical calculations are plotted in Fig. 6.12. The theoretical ratio curves for Cd and Se are very much similar to the experimental ratio curves for pure Cd and Se (Figs. 6.10 and 6.12). The ratio curves for bulk CdSe is not discernible from Cd in Fig. 6.12. This shows a very large contribution of Cd electrons as compared to Se electrons for positron annihilation in bulk CdSe. In the bulk CdSe, positron annihilate from the delocalized state having positron density distributed in the interstitial regions of CdSe lattice. The *d*-electron density reaches far into the interstitial region and the electron density from (Cd) 4*d* state will be much higher than that from (Se) 3*d* state [Barbiellini et

al., 1995]. The calculations show that the fraction of the positrons annihilating with Cd ( $4d + 3d$ ) electrons in pure Cd is 80.17 % and with Se ( $3d$ ) electrons is 6.32 % in pure Se. Thus, positron electron overlap for Cd electrons ( $4d$  and  $3d$ ) is much higher than Se electrons ( $3d$ ) and the ratio curves of CdSe having 88.22 % fraction of positrons annihilating with ( $4d$  and  $3d$ ) is indiscernible from pure Cd in this high momentum range.

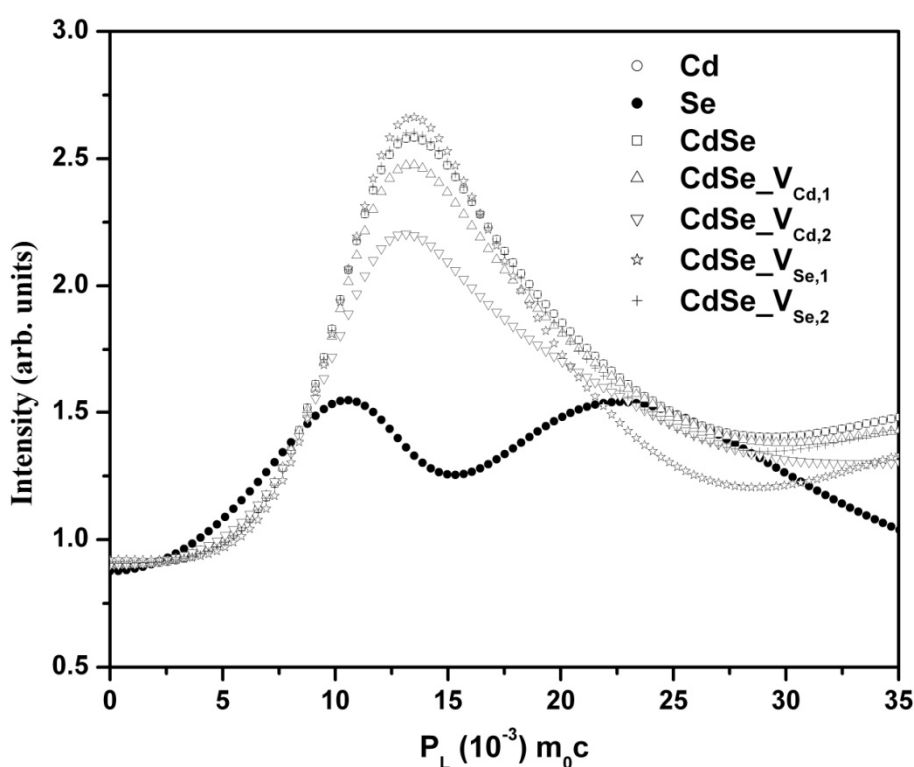


**Figure 6.12:** Theoretically calculated momentum distribution ratio curves for CdSe, Cd and Se with respect to Si.

In CdSe zincblende lattice, Se atom is surrounded by four Cd atoms and vice versa. In the presence of Se vacancies, positrons are trapped at Se vacancy defects and have maximum overlap with Cd electrons from the surrounding Cd atoms. Figure 6.12 shows the ratio curves of CdSe having mono and di vacancy of Se where it is observed that the peak positions of the ratio curves in the presence of Se vacancy are at the same

position as of bulk CdSe. It is because in delocalized state, positrons have maximum overlap with Cd electrons which does not change significantly when the positrons are trapped at Se vacancy defects. When Cd vacancies are present in the CdSe supercell, positrons will be trapped at the Cd vacancy sites and will have maximum overlap with the surrounding Se atoms. This will enhance the contribution from Se electrons ( $3d$ ) and the peak position would shift to lower  $P_L$  values as seen in Fig. 6.12. Due to the same reason, the area under the peak also decreases in the presence of Cd vacancy defects. In the presence of Cd di vacancy, contribution from Se electrons will further increase which shifts the peak position again to a lower value and the area under the peak further decreases. Thus, the presence of Cd vacancy defects in CdSe lattice shifts peak position to lower  $P_L$  values (towards Se peak position) and reduces the area under the peak (more contribution from Se electrons).

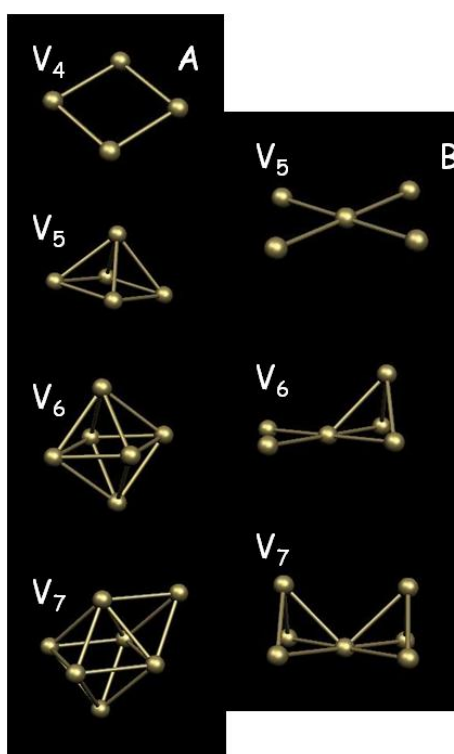
The experimental ratio curves in Fig. 6.10 shows that peak positions for all CdSe nanoparticles samples are at the lower values than the pure Cd indicating that the positrons are not annihilating from their delocalized state in the interstitials of CdSe lattice and, they annihilate from the trapped state in Cd vacancy defects as observed from the calculated ratio curves (Fig. 6.12). The peak positions for sample ( $a'$ ) is  $11.16 \times 10^{-3} m_0c$  which shifts to  $11.37 \times 10^{-3} m_0c$  for sample ( $d'$ ) in a non-linear trend (Fig. 6.11) and area under the peak increases from sample ( $a'$ ) to sample ( $d'$ ) (Table 6.3). This shows that sample ( $a'$ ) has large fraction,  $f_{Se}$ , of positrons annihilating with Se atoms surrounding the Cd vacancy defects that decreases with the increase in particle size *i.e* the concentration of Cd vacancy defects reduces with the increase in particle size.

### 6.3.2.3 Gold nanoparticles

Three positron lifetime components were observed in the gold nanoparticles. Third lifetime component (1.8 ns) with very small intensity corresponds to *o*-positronium *pick-off* annihilation. In metals generally, positronium formation does not occur due to very high electron density. In the case of nanoparticles, a small fraction of positronium formation has been observed and assigned to the surface states and large voids present at the intersections of grain boundaries. The first two components observed in the gold nanoparticles *i.e* ( $\tau_1 = 225$  ps) and ( $\tau_2 = 387$  ps) are ascribed to positron annihilation from gold nanoparticles either in the bulk or at the surface. Both lifetime components  $\tau_1$  and  $\tau_2$  are higher than the calculated bulk positron lifetime  $\tau_B = 131.6$  ps (reported experimental value for annealed gold foils = 121 ps) [Hall et al., 1974] which indicates that these two lifetime components arise from two distinct defect states present in the nanoparticles either in the bulk or at the surface. In earlier studies of nanocrystalline gold prepared by different routes [Ito et al., 2000], first two positron lifetime components ( $\tau_1 = 146$ -180 ps and  $\tau_2 = 280 - 360$  ps) have been attributed to the defects (dislocations and grain boundaries) in the particles and microvoids at the intersection of the grain boundaries, respectively. In that case,  $\tau_1$  was not attributed to monovacancy defects most probably due to its lower value compared to lifetime in monovacancy. From the annealing studies [Ito et al., 2000], it has been argued that vacancy clusters having size of nanovoids corresponding to  $\tau_2$  are present in the nanoparticles which are not annealed out even at very high temperature. In the present study, we have only considered the vacancy types of defects corresponding to positron lifetime components and ignored the role of dislocations and grain boundaries as positron traps. The defects such as vacancy or vacancy clusters are thermodynamically stable as they increase the degrees of freedom for the system to exist in different states. To elucidate the size and shape of the defects

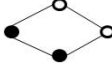
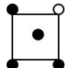
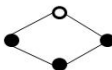
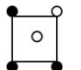
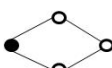
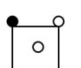
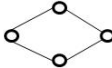
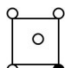
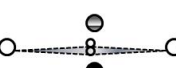
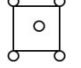
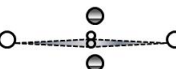
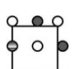
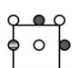
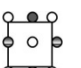
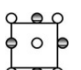
corresponding to these lifetime components, positron lifetimes were calculated in the vacancy defects in gold supercell. Gold has FCC lattice and different configuration are possible for multivacancies ( $V_n$ ,  $n \geq 3$ ). Two different configurations namely *A* and *B* were considered for the calculations as shown in Fig 6.13.

Positron lifetimes calculated in vacancy defects in the two configurations along with the schematic of the vacancy defects are shown in Table 6.4. The solid and open circles (corner and centre) represent atoms and vacancy in a plane ( $z = ma$ ), respectively. The solid and gradient field circles (out of plane and on the edges) represent atom and vacancy in a plane ( $z = 3ma/2$ ), where  $a$  and  $m$  are the lattice constant of gold supercell and an integer.



**Figure 6.13:** Vacancy defects in Gold lattice in two configurations A and B

**Table 6.4** The calculated positron lifetimes in vacancy defects in two different configurations *A* and *B* in gold supercell. Positron lifetime under Unrelaxed and Relaxed columns show the values using unrelaxed and relaxed gold atoms coordinates. (In configuration *A*, the schematic for  $V_n$  where  $n = 7, 8$  and  $9$  are not shown).

Defect ( $V_n$ )	Configuration <i>A</i>	Lifetime (ps)		Configuration <i>B</i>	Lifetime (ps)	
		Unrelaxed	Relaxed		Unrelaxed	Relaxed
$V_1$		232.6	.....		232.6	.....
$V_2$		266.3	.....		266.3	.....
$V_3$		281.8	284.1		275.9	260.9
$V_4$		305.3	311.0		291.6	250.7
$V_5$		378.2	388.2		302.1	264.8
$V_6$		442.5	454.5		342.4	279.8
$V_7$	-----	468.0	473.7		364.1	330.8
$V_8$	-----	489.0	488.2		438.1	391.0
$V_9$	-----	520.9	522.7		500.2	449.0

From Table 6.4, it is observed that positron lifetime values are different in defects having same number of vacancies in two configurations for  $n \geq 3$ . This difference is mainly due to the shape of the defect as the volume of the defects having  $n$  number of vacancy should remain constant. From Table 6.4, it is observed that the calculated lifetime for  $V_1$  is very close to the experimentally observed shorter component which indicates that monovacancy defects are present in the nanoparticles either in the bulk or at

the surface. The reported value for positron lifetime in monovacancy is 211 ps which is lower compared to the present calculations [Hall et al., 1974]. This lower value might be due to presence of dislocations along with monovacancy in the studied sample. The second lifetime component,  $\tau_2$ , is observed to be very close to  $V_5$  in configuration *A* and  $V_7$  in configuration *B* indicating that these defects,  $V_5(A)$  and  $V_7(B)$ , can be present in the nanoparticles either in the bulk or at the surface. The calculated values in  $V_5(A)$  and  $V_7(B)$  differ from  $\tau_2$  by  $\sim 9$  and 23 ps, respectively. In the presence of vacancy defects, the neighbour atoms undergo either inward or outward relaxation to balance the acting forces and consequently the volume of the defect changes. Hence, positron lifetime calculated in unrelaxed lattice in the presence of vacancy defects may differ from the experimental value.

The first nearest neighbours (FNN) of the vacancy defects were relaxed for  $n \geq 3$  in gold supercell using VASP. The positron lifetimes calculated in the defects ( $n \geq 3$ ) using the relaxed coordinates are also given in Table 6.4. For configuration *A*, the positron lifetime has increased after the relaxation of the FNN indicating the outward relaxation of the FNN or decrease in lattice parameter in the surrounding of the defect site. This outward relaxation is caused by the balance of the acting forces on FNN. In the absence of atom at defect sites, FNN atoms of the defect are attracted strongly by its coordinated atoms and undergo outward relaxation resulting in a longer positron lifetime. In the case of configuration *B*, It is observed that positron lifetime has decreased from the unrelaxed lattice indicating inward relaxation of FNN or increase in lattice parameter in the surrounding of defect site. It is observed that in the presence of defects, inward and outward relaxation of FNN atoms depends on their coordination number.

The FNN atoms with 11 coordination number undergo outward relaxation while the FNN with 10 coordination number undergo inward relaxation. In the presence of



defects in configuration  $B$ , the number of FNN with coordination number 10 are more compared to the defect in configuration  $A$ . For example, the number of FNN with coordination 10 in configuration  $A$  and  $B$  in case of  $V_3$  are 7 and 8, and, in case of  $V_4$  are 6 and 10, respectively. Second positron lifetime component  $\tau_2$ , when compared with calculated positron lifetime in relaxed lattice (Table 6.4), is observed to be very close with  $V_5(A)$  and  $V_8(B)$ . This observation is different for configuration  $B$  from the unrelaxed calculation where  $\tau_2$  is found to be close to calculated lifetime for  $V_7(B)$ .

As we have mentioned earlier, defects are thermodynamically stable in the nanoparticles as they increase the entropy of the system but their probability of existence in the system can be correlated to their formation energy. The formation energy of the defects in configuration  $A$  and  $B$  have been calculated using VASP through equation 6.1. The total formation energy increases with the increase in the size of defects or the number of vacancy,  $n$ . The formation energy per vacancy,  $\hat{E}_f(V_n)$ , of the defect in configuration  $A$  and  $B$  is plotted in Fig. 6.14. It is seen from Fig.6.14 that  $\hat{E}_f(V_n)$  has lowest value for  $n = 8$  in both configuration  $A$  and  $B$ . The probability of the formation of a defect decreases with number of vacancies as the total formation energy of defect increases with the number of vacancy. The stability of defect ( $V_n$ ) over two non-interacting defects ( $V_{n-1}$ ,  $V_1$ ) is given by the binding energy  $E_B(V_n)$  as defined by equation 6.2. The binding energy as a function of number of vacancy basis is shown in Fig. 6.15. It is observed from figure 6.15 that  $V_5$  in configuration  $A$  and  $V_8$  in configuration  $B$  have the minima for the binding energy. This indicates that  $V_5(A)$  and  $V_8(B)$  have higher probability of formation compared to two non-interacting defects equivalent to these defects. The total formation energy of  $V_8$  would be always higher than  $V_5$  as the total formation energy increase with the number of vacancy. Hence, the second positron lifetime component is ascribed to the

$V_5(A)$  i.e penta vacancy in square pyramidal configuration which can exist either in the bulk or at the surface of the nanoparticles.

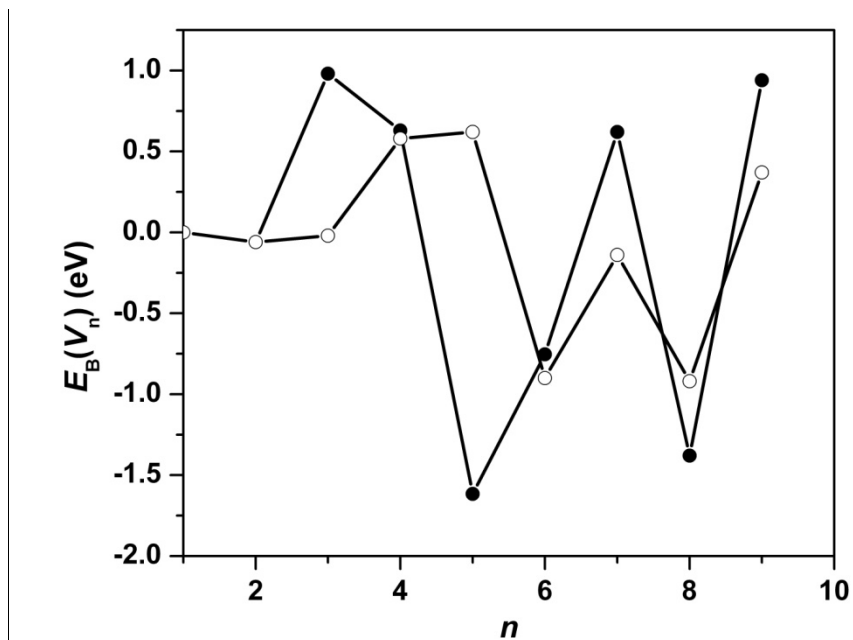


**Figure 6.14:** Formation energy per vacancy as a function of number of vacancy,  $n$ .

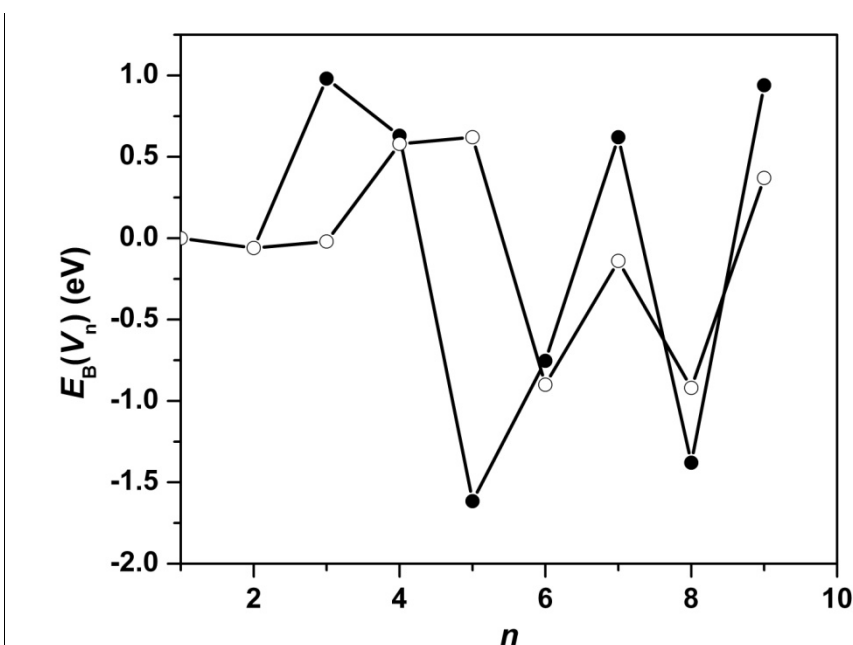


**Figure 6.15:** Binding energy per vacancy as a function of number of vacancy,  $n$ .

## 6.4 Conclusion

Positron annihilation lifetime and coincidence Doppler broadening measurements corroborated with theoretical calculations have been successfully used for the defects characterization in semiconductor (ZnO and CdSe) as well as in metal (Au) nanoparticles in the size range of 4 – 40 nm. These studies strongly suggest the presence of Zn vacancies in ZnO nanoparticles prepared by solid state pyrolytic reaction method similar to observations made on ZnO nanoparticles synthesized by other methods. The Zn vacancies are observed to migrate to the grain boundaries with the increase in the particles size and finally anneal out at higher temperature. Photoluminescence measurements reveal that both Zn and O vacancies may be responsible for the origin of visible emission in ZnO. Momentum distribution calculations in CdSe show that in bulk CdSe, Cd semi core electrons (3d and 4d) have major contribution in the high momentum region. The present study on CdSe nanoparticles suggests that Cd vacancies are predominantly produced in CdSe nanoparticles during synthesis, the concentration of which reduces with the increase in particle size. The present study also provides an evidence of Se enrichment of the surface of CdSe nanoparticles with the decrease in the particle size. In metal (Au) nanoparticles, two types of defects viz. monovacancy and pentavacancy in square pyramidal configuration have been observed as the most probable defects produced during the synthesis using present method.

In the present study, positron annihilation in defects has been considered to explain positron parameters. To elucidate more information about the positron states in the nanoparticles, more specific studies like positron age momentum correlation are required.

## **SUMMARY**

---

Positron annihilation spectroscopy (PAS) consists of different techniques such as positron annihilation lifetime spectroscopy (PALS), Doppler broadening of annihilation radiation (DBAR)/ coincidence Doppler broadening (CDB) measurements and Age momentum Correlation (AMOC). Positron annihilation spectroscopy involves positron and positronium as probes for the investigation of atomic level defects (vacancy) in crystalline materials and molecular level vacant spaces (nanoholes) in polymers, respectively. The measurements of positron/positronium lifetime in a material provide the information of defect (vacancy or nanoholes) size and concentration in the material. Doppler broadening measurements of annihilation radiation provides the complementary information to positron/positronium lifetime. Coincidence Doppler broadening measurements are element sensitive and provide information about the chemical surrounding of annihilation site (vacancy or nanoholes) in the material. Age Momentum Correlation is comparatively new technique and provides the electron momentum distribution in time domain. This technique is very useful to study the positron/positronium states in a complex system. To corroborate the experimental results obtained from PALS and CDB measurements in crystalline materials, density functional theory based calculations are carried out in perfect lattice or in the presence of vacancy defects. These calculations help identify the types of defects and their chemical surrounding in the lattice. In the presence of defects, the atoms in the vicinity of the defect undergo outward/inward relaxation depending on the acting forces on the atoms in the presence of defects. To mimic the real experimental conditions, the relaxed coordinates of the atoms are used for the positron lifetime and electron momentum distribution calculations.

The triplet state (*o*-Ps) has been extensively used as probe to study the nanoholes in synthetic polymers as reported in literature where its lifetime and corresponding

intensity are related to nanoholes size and their density, respectively. The use of *o*-Ps to study the nanostructure of natural polymers like starch is limited in literature. In the case of synthetic polymers, their nanostructure is modified by grafting, ion-irradiation and nanocomposite formation. The use of *o*-Ps as probe to study the nanostructure of these modified polymeric systems is expected to enhance the understating about the role of nanostructure in physical properties of the system. In the present study, nanostructure of starch/sucrose matrix has been studied as a function of temperature and water. It was observed that nanoholes size increases as a function of temperature and their density remains constant up to about 440 K followed by a two step decrease at higher temperature. The observed decrease is attributed to the decomposition of matrix to carbon black at higher temperature. Similar trends have been observed from TGA measurements. In such a case, glass transition temperature of the matrix was determined using a simple model which provides the nanoholes size in the absence of decomposition. Thus measured glass transition temperature is 446 K which is little lower compared to DSC measurements. With inclusion of water in the matrix, free volume size was observed to increase with no change in their density. It was observed that temperature and water have similar effect on the nanostructure of starch/sucrose matrix leading to glass transition process. A new approach has been developed for the measurement of  $T_g$  of hydrated samples using PALS. The present study showed that water molecules do not block the existing nanoholes in the starch/sucrose matrix and they are uniformly distributed in the matrix through hydrogen bonding.

In case of synthetic polymer based systems Acrylic acid grafted and Cl ion-irradiated poly ethylene terephthalate (PET) and phenol formaldehyde resin-carbon nanotubes composites, PAS supplemented with conventional measurements like *FTIR*, DMA and XRD was observed to be useful method to investigate the nanostructure. The

variation in *o*-Ps lifetime and intensity in PET grafted with acrylic acid was observed to follow additive rule up to 6.0 % followed by a complex behavior indicating the phase segregation at higher degree of grafting. These observations were consistent with DMA results. On ion-irradiation of PET at lower fluence ( $9 \times 10^7$  ions/cm<sup>2</sup>), the changes were primarily seen in free volume size and concentration as no change was observed from FTIR and XRD measurements. These changes were predominant at surface and subsurface region. AMOC measurements in phenol-formaldehyde resin-carbon nanotubes composites showed that *o*-Ps annihilation occurs at the interface of polymer matrix and carbon nanotubes. These measurements also showed that large fraction of free positrons annihilate in the carbon nanotubes dispersed in the polymer matrix. These observations were consistent with PALS data.

In recent years, PAS has been used for the investigation of electronic structure of various nanoscale crystalline materials. The observed changes in positron parameters have been correlated to presence of defects, widening of band gap, quantum confinement of electrons etc. However, the positron systematic in nanoparticles is not yet well understood and extensive studies are required to increase the applications of PAS in nanoscale crystalline materials. In the present study, PALS and CDB measurements have been carried out in semiconductor (ZnO and CdSe) and metal (Au) nanoparticles. These studies were corroborated with density function theory based calculations of positron parameters and formation energy of vacancy defects. It was observed that atomic vacancies are produced during synthesis of nanoparticles through various methods. In case of ZnO, it was seen that Zn vacancies start migrating with increase in temperature and at very high temperature (800<sup>0</sup>C) they are annealed out. Photoluminescence measurement in ZnO nanoparticles showed that both Zn and O vacancies present in the nanoparticles are responsible for the visible emission in ZnO. The concentration of Cd

vacancies was observed to reduce with the increase in CdSe particle size. In case of smallest size, 4 nm, CdSe nanoparticles, enrichment of surface by Se is also observed. In case of gold nanoparticles, two types of vacancy defects were observed. The gold atoms in the vicinity of defects undergo outward and inward relaxation depending on their coordination number. The formation energy calculations of defects provide supportive information to the defects studies using positron annihilation spectroscopy. The present studies confirmed two types of vacancy defects, monovacancy and penta vacancy in square pyramidal configuration, as most probable defects in Au nanoparticles synthesized through chemical route.

The studies showed that positron and positronium are excellent probes to study the nanostructure i.e. atomic level vacancy defects in nanoscale crystalline materials and molecular level vacant spaces in polymers. Age momentum correlation measurements in complex systems like polymer nanocomposites help providing information about the positron states in the system unambiguously. In view of this, there is scope for use of positronium and positron as probe for the nanostructure of complex polymers systems and nanoscale crystalline materials prepared through various methods. It is a great hope that AMOC will be useful to investigate the positron/positronium states in these systems leading to the better understanding of positron/positronium systematics.



## **BIBLIOGRAPHY**

---

**A**

1. Alatalo, M.; Barbiellini, B.; Hakala, M.; Kauppinen, H.; Korhonen, T.; Puska, M.J.; Saarinen, K.; Hautojarvi, P., and Nieminen, R.M., **1996**. *Phys. Rev. B.*, 54, 2397.
2. Alivisatos, A.P., **1996**. *Science* 271, 933.
3. Anderson, C.D., **1933**. *Phy. Rev.* 43, 491.
4. Apel, P.Yu.; Blonskaya, I.V.; Dmitriev, S.N.; Orelovitch, O.L., and Sartowska, B., **2006**. *J. Mem. Sci.*, 282, 393.
5. Arponen, J., and Pajanne, E., **1979**. *Ann. Phys. (N. Y.)* 121, 343.
6. Avny, Y.; Rebenfeld, L., and Weighmann, H.D., **1978**. *J. Appl. Polym. Sci.*, 22(1), 125.
7. Awad, S.; Chen, H.; Chen, G.; Gu, X.; Lee, J.L.; Abdel-Hady, E.E., and Jean, Y.C., **2011**. *Macromolecules*, 44, 29.

**B**

8. Bandzuch, P.; Kristiak, J.; Sausa, O., and Zrubcova, J., **2000**. *Phys. Rev. B.*, 61(13), 8784.
9. Banipal, P.K.; Banipal, T.S.; Lark, B.S., and Ahluwalia, J.C., **1997**. *J. Chem. Soc., Faraday Trans.*, 93(1), 81.
10. Bansil, A.; Pankaluoto, R.; Rao, R.S.; Mijnders, P.E.; Długosz, W.; Prasad, R., and Smedskjaer, L.C., **1988**. *Phys. Rev. Lett.*, 61, 2480.
11. Barbiellini, B.; Puska, M.J.; Torsti, T., and Nieminen, R.M., **1995**. *Phys. Rev. B.*, 51 7341.
12. Beiser, A., **2002**. *Concepts of Modern Physics*, McGraw-Hill.
13. Benczedi, D.; Tomka I., and Escher, F., **1998**. *Macromolecules*, 31, 3055.
14. Boronski, E., and Nieminen, R.M., **1986**. *Phys. Rev. B.*, 34, 3820.
15. Botelho, G.; Qeiros, A.; Liberal, S., and Gijnsman, P., **2001**. *Polym. Degrad. Stabl.*, 74, 39.
16. Branca, C.; Frusteri, F.; Magazu, V., and Mangione, A., **2004**. *J. Phys. Chem. B*, 108, 3469.
17. Brandt, W., and Dupasquier, A., *Proceedings of the international school of physics "ENRICO FERMI" Course LXXXIII, positron solid state physics* **1981**.
18. Brandt, W., and Paulin, R., **1977**. *Phys. Rev. B.*, 15, 2511

19. Brauer, G.; Anwand, W.; Skorupa, W.; Kuriplach, J.; Melikhova, O.; Moisson, C.; von Wenckstern, H.; Schmidt, H.; Lorenz, M., and Grundmann, M., **2006**. *Phy. Rev. B.*, 74, 045208.
20. Brust, M., and Kiely, C.J., **2002**. *Colloids surf. A: Physiochem. Eng. ASP.*, 175, 202.
21. Budai, J.D.; White, C.W.; Withrow, S.P.; Chisholm, M.F.; Zhu, J., and Zhur, R.A., **1997**. *Nature (London)*, 390, 384.

## C

22. Campbell, J.L., **1977**. *Appl. Phys.*, 13(4), 365.
23. Chakrabarti, K.; Nambissan, P.M.G.; Mukherjee, C.D.; Bardhan, K.K.; Kim, C., and Yang, K.S., **2006**. *Carbon*, 44, 948.
24. Chan, L.P.; Lynn, K.G., and Harshman, D.R., **1992**. *Int. J. of Mod. Phys. B.*, 6 (11), 617.
25. Chan, W.C.W., and Nie, S., **1998**. *Science*, 281, 2016.
26. Charlesby, A., **1960**. *Atomic radiation and polymers*. Pergamon: New York, p. 348.
27. Chatterjee, A.J., **2010**. *Appl. Polym. Sci.*, 116, 3396.
28. Chen, L.P.; Yee, A.F., and Moskala, E.J., **1999**. *Macromolecules*, 32, 5944.
29. Chen, Z.Q.; Maekawa, M.; Yamamoto, S.; Kawasuso, A.; Yuan, X.L.; Sekiguchi, T.; Suzuki, R., and Ohdaira, T., **2004**. *Phy. Rev. B.*, 69, 035210.
30. Chopra, K.L.; Major, S., and Pandya, D.K., **1983**. *Thin Solid Films*, 102, 1.
31. Chu, L-Q.; Tan, W-J.; Mao, H.Q., and Knoll, W., **2006**. *Macromolecules*, 39, 8742.
32. Ciesielski, K.; Dawidowicz, A.L.; Goworek, T.; Jasinska, B., and Wawryszczuk, J., **1998**. *Chem. Phys. Lett.*, 289, 41.
33. Coleman, P.G., **2003**, in *Principles and Applications of Positron and Positronium Chemistry*, Jean, Y.C.; Mallon, P.E., and Schrader, D.M., (Eds.), World Scientific publishing, Singapore, p. 54.
34. Couchman, P.R., and Karasz, F.E., **1978**. *Macromolecules*, 11, 117.

**D**

35. Dauwe, C.; van Waeyenberge, B., and Balcaen, N., **2003**. *Phys. Rev. B*, 68, 132202.
36. de la Cruz, R.; Pareja, M.R.; Gonzalez, R.; Boatner, L.A., and Chen, Y., **1992**. *Phy. Rev. B*, 45, 6581.
37. de Sitter, K.; Winberg, P.; D’Haen, J.; Dotremont, C.; Leysen, R.; Martens, J.A.; Mullens, S.; Maurer, F.H.J., and Vankelecom, I.F.J., **2006**. *J. Membr. Sci.*, 278, 83.
38. Dekhtyar, I.Ya, **1974**. *Physics Reports*, 9(5), 243.
39. Deng, A.H.; Panda, B.K; Fung, S.; Beling, C.D., and Schrader, D.M., **1998**. *Nucl. Instr. Meth. B*, 140, 439.
40. Dirac, P.A.M., **1930**. *Proc. Camb. Phil. Soc.*, 26, 361.
41. Dirac, P.A.M., **1935**. *The Principles of Quantum Mechanics*, Oxford University Press.
42. Djourellov, N., and Misheva, M., **1996**. *J. Phys: Condens. Matter*, 8, 2081.
43. Dlubek, G.; Bondarenko, V.; Al-Qaradawi, I.Y.; Kilburn D., and Krause-Rehberg, R., **2004**, *Macromol. Chem. Phys.*, 205, 512.
44. Dlubek, G.; Borner, F.; Buchhold, R.; Sahre, K.; Krause-Rehberg R., and Eichhorn, K.-J., **2000**. *J. Polym. Sci. B: Polym. Phys.*, 38, 3062.
45. Dlubek, G.; Buchhold, R.; Hubner, Ch., and Nakladal, A., **1999**. *Macromolecules*, 32(7), 2348.
46. Dlubek, G.; Hassan, E.M.; Krause-Rehberg, R., and Pionteck, J., **2006**. *Phys. Rev. E*, 73, 031803.
47. Dlubek, G.; Redmann, F., and Krause-Rehberg, R., **2002**. *J. Appl. Polym. Sci.*, 84 (2), 244.
48. Dlubek, G.; Stejny, J., and Alam, M.A., **1998**. *Macromolecules*, 31, 4574.
49. Domain,C., **2006**, *J. Nul. Mater.*, 351, 1.
50. Dreizler, R.M., **1990**. *Gross density functional theory*, Springer-Verlag.
51. Dryzek, J., SP version 1.0, Downloaded from  
<http://www.Positronannihilation.net/software.html>
52. Dryzek, J., and Quarles, C.A., **1996**. *Nucl. Instr. Meth. A*, 378, 337.
53. Dryzek, J.; Pamula, E., and Blazewicz, S., **1995**. *Phys. Status Solidi A*, 151(1), 39.

54. Dupasquier, A., and Mills, Jr., A.P., (Eds), **1995**. *Positron Spectroscopy of Solids*, Proc. International School of Physics «Enrico Fermi», Course CXXV, Varenna **1993**, IOS Press, Amsterdam.
55. Duplatre, G., and Billard, I., **2003**, in *Principles and Applications of Positron and Positronium Chemistry*, Jean, Y.C.; Mallon, P.E., and Schrader, D.M., (Eds.) World Scientific, London, p. 253.
56. Dutta, D.; Ganguly, B.N.; Gangopadhyay, D.; Mukherjee, T., and Dutta-Roy, B., **2004**. *J. Phys. Chem.*, 108, 8947.
57. Dutta, D.; Pujari, P.K.; Sudarshan, K., and Sharma, S.K., **2008**. *J. Phys. Chem. C*, 112, 19055.
58. Dutta, D.; Sachdeva, A. and Pujari, P.K., **2006**. *Chem. Phys. Lett.*, 432, 116.
59. Dutta, S.; Chakrabarti, M.; Chattopadhyay, S.; Jana, D.; Sanyal, D., and Sarkar, A., **2005**. *J. Appl. Phys.*, 98, 053513.
60. Dutta, S.; Chattopadhyay, S.; Jana, D.; Banerjee, A.; Manik, S.; Pradhan, S.K.; Sutradhar, M., and Sarkar, A., **2006**. *J. Appl. Phys.*, 100, 114328.

## E

61. Eijt, S.W.H.; van Veen, A(Tom).; Schut, H.; Mijnders, P.E.; Denison, A.B.; Barbiellini, B., and Bansil, A., **2006**. *Nature Mat.*, 5, 23.
62. Eldrup, M.; Lightbody, D., and Sherwood, J.N., **1981**. *Chem. Phys.*, 63, 51.

## F

63. Farhat, I.A.; Mousia, Z., and Mitchell, J.R., **2003**. *Carbohydr. Poly.*, 52(1), 29.
64. Ferain, E., and Legras, R., **1994**. *Nucl. Instrum. Method Phys. Res. Sect. B.*, 84, 331.
65. Ferry, J.D., **1980**. *Viscoelastic Properties of Polymers*, John Wiley and Sons, New York.
66. Firestone, R.B.; Baglin, C.M., and Frank Chu, S.Y., **1999**. *Table of isotopes*, 8<sup>th</sup> Edition, Wiley-Interscience.
67. Fukutomi. T.; Murakami, H., and Sano, M., **2001**. *Mgt. Abstr. Phys. Soc. Japan*, 56, 681.

**G**

68. Gea, L.A.; Budai, J.D., and Boatner, L.A., **1999**. *J. Mater. Res.*, 14, 2602.
69. Gebauer, J.; Krause-Rehberg, R.; Prokesch, M., and Irmischer, K., **2002**. *Phys. Rev. B*, 66, 115206.
70. Ghoshal, T.; Biswas, S.; Kar, S.; Chaudhury, S., and Nambissan, P.M.G., **2008**. *J. Chem. Phys.*, 128, 074702.
71. Gidley, D.W.; Peng, H.G., and Vallery, R.S., **2006**. *Ann. Rev. Mater. Res.*, 36, 49.
72. Gleiter, H., **2000**. *Acta. Mater.* 48, 1.
73. Gomma, E., **2007**. *Physica B: Condensed matter*, 390, 203.
74. Goworek, T.; Ciecieski, K.; Jasinska, B., and Wawryszczuk, J., **1997**. *Chem. Phys. Lett.*, 272, 91.
75. Goworek, T.; Ciesielski. K.; Jasinska, B., and Wawryszczuk, J., **1998**. *Chem. Phys.*, 230, 305
76. Gregory, R.B., **1991a**. *J. Appl. Phys.*, 70 (9), 4665.
77. Gregory, R.B., **1991b**. *Nucl. Instr. Meth. A*, 302, 496.
78. Gregory, R.B., and Zhu, Y., **1990**. *Nucl. Instr. Meth. A* 290, 172.
79. Gupta, B.; Mishra, S., and Saxena, S., **2008**. *Rad. Phys. Chem.*, 77, 553.
80. Gupta, B.; Plummer, C.; Hilborn, J.; Bisson, I., and Frey, P., **2002**. *Biomaterials*, 23, 863.
81. Gupta,T.K.; Straub,W.D.; Ramanachalam, M.S.; Schaffer, J.P., and Rohatgi, A., **1989**. *J. Appl. Phy.*, 66, 6132.

**H**

82. Hall, T.M.; Goland, A.N., and Snead, Jr., C.L., **1974**. *Phys. Rev. B.*, 10 (8), 3062.
83. Harms, S.; Ratzke, K.; Gerald, F.F.; Schneider, J.; Willner, L., and Richter, D., **2010**. *Macromolecules*, 43, 10505.
84. Hautakangas, S.; Oila, J.; Alatalo, M.; Saarinen, K.; Liskay, L.; Seghier, D., and Gislason, H.P., **2003**. *Phys. Rev. Lett.*, 90(13), 137402.
85. He, C., and Gu, Z., **2003**. *Rad. Phys. Chem.*, 68, 873.
86. He, C.-Q.; Dai, Y.-Q.; Wang, B.; Wang, S.-J.; Wang G.-Y., and Hu, C.-P., **2001**. *Chin. Phys. Lett.*, 18, 123.
87. Heiskanen, M., **1999**. *Master Thesis*, Helsinki University of Technology, Espoo.

88. Heiskanen, M.; Torsti, T.; Puska, M.J., and Nieminen, R.M., **2001**. *Phys. Rev. B*, 63, 245106.
89. Helbeish, A.; Shalaby, S.E., and Bayazeed, A.M., **1978**. *J. Appl. Polym. Sci.*, 22 (11), 3335.
90. Hsu, F.H., and Hadely Jr, J.H., **1971**. *Phys. Lett.*, 34A, 317.
91. Hsu, F.H.; Chu, K.C., and Liu, C.T., **1990**. in *Positron and Positronium Chemistry*, Schrader D.M., and Jean, Y.C., (Eds.) World Scientific, Singapore, p. 47.
92. Hu, Y.S.; Mehta, S.; Schiraldi, D. A.; Hiltner, A., and Baer, E., **2005**. *J. Polym. Sci.: Part B: Polym. Phys.*, 43, 1365.
93. Huglin, M.B., and Zlatev, V.B., **1973**. *Eur. Polym. J.*, 9, 761.
94. Hynes, R.C., and Le Page, Y., **1991**. *J. Appl. Cryst.*, 24, 352.

## **I**

95. Inoue, K.; Nagai, Y.; Tang, Z.; Toyama, T.; Hosoda, Y.; Tsuto, A., and Hasegawa M., **2011**. *Phys. Rev B*, 83, 115459.
96. Ishibashi, S., **2002**. *J. Phys.: Condens. Matter*, 14, 9753.
97. Ito, K.; Ujihira, Y.; Yamashita, T., and Horie, K., **1998**. *J. Polymer Sci. B*, 36, 1141.
98. Ito, K.; Ujihira, Y.; Yamashita, T., and Horie, K., **1999a**. *Polymer*, 40, 4315.
99. Ito, K.; Nakanishi, H., and Ujihira, Y., **1999b**. *J. Phys. Chem. B*, 103, 4555.
100. Ito, K.; Ujihira, Y.; Yamashita, T., and Horie, K., **2000**. *J. Polymer Sci. B*, 38, 922.
101. Ito, Y., and Suzuki, T., **1999**. *Phys. Rev. B*, 60, 15636.
102. Ito, Y.; Takamura, S., and Kobiyama, M., **2000**. *Phys. Stat. Solid. (a)*, 179, 297.
103. Itoh, N., and Tanimura, K., (Eds), **1994**. *Nucl. Instrum. Methods Phys. Res. Sect. B*, 91, 1.

## **J**

104. Jean, Y.C.; Mallon, P.E., and Schrader, D.M., (Eds.) **2003**. *Principles and Applications of Positron and Positronium Chemistry*, World Scientific, London.
105. Jean, Y.C.; Sandreczki, T.C., and Ames, D.P., **1986**. *J. Polym. Sci.: Polym. Phys.*, 24, 1247.

106. Jefrey, K., and Pethrick, R.A., **1994**. *Eur. Polym. J.*, 30, 153.

## **K**

107. Kalichevsky, M.T.; Jaroszkiewicz, E.M., and Blanshard, J.M.V., **1992**. *Int. J. Biol. Macromol.*, 14, 257.

108. Kansy, J., **1996**. *Nucl. Instrum. Methods Phys. Res. A*, 374, 235.

109. Karagiannidis, P.G.; Stergiou, A.C., and Karayannidis, G.P., **2008**. *Eur. Polym. J.*, 44, 1475.

110. Karaman, M.; Kooi, S.E., and Gleason, K.K., **2008**. *Chem. Mater.*, 20, 2262.

111. Kilburn, D.; Claude, J.; Mezzenga, R.; Dlubek, G.; Alam, A., and Ubbink, J., **2004**. *J. Phys. Chem. B*, 108, 12436.

112. Kilburn, D.; Dlubek, G.; Pionteck, J., and Alam, M.A., **2006**. *Polymer*, 47, 7774.

113. Kirkegaard, P., and Eldrup, M., **1991**. *Comput. Phys. Commun.*, 17, 401.

114. Kirkegaard, P., and Eldrup, M., **1972**. *Comp. Phys. Comm.* 3, 240.

115. Kirkegaard, P.; Eldrup, M.; Mogensen, O.E., and Pedersen, N.J., **1981**. *Comp. Phys. Comm.* 23, 307

116. Kirkegaard, P.; Pedersen, N.J., and Eldrup, M., **1989**. PATFIT-88: A data-processing system for positron annihilation spectra on mainframe and personal computers, RISO-M-2740, RISO National Laboratory, Denmark.

117. Kobayashi, Y.; Kojima, I.; Hishita, S.; Suzuki, T.; Asari, E., and Kitajima, M., **1995**. *Phy. Rev. B*, 52, 823.

118. Kobayashi, Y.; Zheng, W.; Meyer, E.F.; McGervey, J.D.; Jamieson, A.M., and Simha, R., **1989**. *Macromolecules*, 22, 2302.

119. Kohan, A.F.; Ceder, G.; Morgan, D.; Chris, G., and de Walle, van., **2000**. *Phy. Rev. B.*, 61, 15019.

120. Krause-Rehberg, R., and Leipner, H. S., **1999**. *Positron annihilation in semiconductors: Defect studies*, Springer-Verlag Berlin Heidelberg New York.

121. Kresse, G., and Furthermüller, J., **1996**. *Phys. Rev. B.*, 54(11), 169.

122. Kresse, G., and Joubert, D., **1999**, *Phys. Rev.*, 59, 1758.

123. Kristiak, K.; Kristiakova, K.; Sausa, O.; Banzuch, P., and Bartos, J., **1993**, *J. Phys. IV*, 3, 265.

124. Kuan, H.C.; Chiu, S.L.; Chen, C.H.; Kua, C.F., and Chiang, C.L., **2009**. *J. Appl. Polym. Sci.*, 113, 1959.



**L**

125. Lazea, A.; Kravets, L.I.; Dmitrev, S.N., and Dinescu, G., **2005**. *Rom. Rep. Phys.*, 57, 396.
126. Levine, H., and Slade, L., **1993**. in *The Glassy state in Foods*, Blanshard, J.M.V., and Lillford, P.J., (Eds.) Nottingham University Press, Leicestershire, U. K.
127. Liou, G.S.; Lin, P.H.; Yen, H.J.; Yu, Y.Y., and Chen, W.C., **2010**. *J. Polym. Sci., Part A: Polym. Chem.*, 48, 1433.
128. Liu, J.; Jean, Y.C., and Yang, H., **1995**. *Macromolecules*, 28, 5774.
129. Liu, Y.H.; Chang, M.C.; Liu, P.I.; Chung, L.C.; Shao, H.; Huang, M.S.; Horng, R.Y., and Yang, A.C.M., **2010**. *J. Mater. Sci.*, 45, 6212.
130. Look, D.C.; Hemskey, J.W., and Sizelove, J.R., **1999**. *Phys. Rev. Lett.*, 82, 2552.
131. Look, D.C.; Reynolds, D.C.; Hemskey, J.W.; Jones, R.L., and Sizelove, J.R., **1999**. *Appl. Phys. Lett.*, 75, 811.

**M**

132. Magalhaes, W.F.; Abbé, J.C., and Duplâtre, G., **1989**. *Chem. Phys.*, 136, 141.
133. Mallon, P. E., **2003**, in *Principles and Applications of Positron and Positronium Chemistry*, Jean, Y.C.; Mallon, P.E., and Schrader, D.M., (Eds.) World Scientific, London, p. 253.
134. McGonigle, E.A.; Daly, J.H.I.; Jenkins, S.D.; Liggat, J.J., and Pethrick, R.A., **2000**. *Macromolecules*, 33, 480.
135. Miranda, L.A. de; Mohallem, N.D.S., and Magalhaes W.F. de, **2006**. *Appl. Surf. Sci.*, 252, 3466.
136. Miranda, R.; Ochoa, R., and Huang, W.F., **1993**. *J. Mol. Catal.*, 78, 67.
137. Mishra, A.K.; Chaudhuri, S.K.; Mukherjee, S.; Priyam, A., and Das, D., **2007**. *J. Appl. Phys.*, 102, 103514.
138. Mizuno, A.; Mitsuiki, M., and Masao, M., **1998**. *J. Agric. Food Chem.*, 46, 98.
139. Mogensen, O.E., **1974**. *J. Chem. Phys.* 60, 998.
140. Murray, C.B.; Kagan, C.R., and Bawendi, M.G., **2000**. *Annu. Rev. Mater. Res.*, 30, 545.
141. Myler, U.; Xu, X.L.; Coleman, M.R., and Simpson, P.J., **1998**, *J. Polym. Sci. Part B: Polym. Phys.*, 36, 2413.

**N**

142. Nagai, Y.; Chiba, T.; Tang, Z.; Akahane, T.; Kanai, T.; Hasegawa, M.; Takenaka, M., and Kuramoto, E., **2001**. *Phy. Rev. Lett.*, 87, 176402.
143. Nagai, Y.; Hasegawa, M.; Tang, Z.; Hempel, A.; Yubuta, K.; Shimamura, T.; Kawazoe, Y.; Kawai, A., and Kano, F., **2000**. *Phy. Rev. B*, 61, 6574.
144. Nasef, M.M., **2000**. *J. Appl. Polym. Sci.*, 77, 1003.
145. Nasef, M.M., **2002**. *J. Appl. Polym. Sci.*, 84, 1949.

**O**

146. Ohdaira, T.; Suzuki, R.; Kobayasi, Y.; Akahane, T., and Dai, L., **2002**, *Appl. Surf. Sci.*, 194, 291.
147. Ore, A., and Powell, J.L., **1949**. *Phys. Rev.* 75(11), 1696.
148. Orford, P.D.; Parker, R.; Ring, S.G., and Smith, A.C., **1989**. *Int. J. Biol. Macromol.*, 11, 91.

**P**

149. Pirlot, C.; Willems, I.; Fonseca, A.; Nagy, J.B., and Delhalle J., **2002**. *Adv. Eng. Mater.*, 4(3), 109.
150. Poirier-Brulez, F.; Roudaut, G.; Champion, D.; Tanguy, M., and Simatos, D., **2006**. *Biopolymers*, 81, 63.
151. Provencher, S.W., **1982**. *Comput. Phys. Commun.*, 17, 213 and 229.
152. Pujari, P.K.; Dutta, T.; Tomar, B.S., and Das, S.K., **1992**. *Report: BARC/1992/E/043*.
153. Puska, M., **1997**. *Mat. Sci. Forum*, 171, 255.
154. Puska, M., and Nieminen, R., **1994**. *Rev. Mod. Phys.*, 66(3).
155. Puzder, A.; Williamson, A.J.; Gygi, F., and Galli, G., **2004**. *Phys. Rev. Lett.*, 92, 217401.

**R**

156. Ranki, V., **1999**. *Special Assignment*, Helsinki University of Technology, Espoo
157. Reynolds, D.C.; Look, D.C., and Jogai, B., **1996**. *Sol. Stat. Commun.*, 99, 873.
158. Richards, G.N., and Shafizadeh, F., **1978**. *Aust. J. Chem.*, 31, 1825.

159. Richman, E. K., and Hutchison, J. E., **2009**. *ACS Nano*, 3, 2441.
160. Roudaut, G., and Duplâtre, G., **2009**. *Phys. Chem. Chem. Phys.*, 11, 9556.

## S

161. Saarinen, K., Hautajarvi, P., Corbel, C., *Identification of Defects in Semiconductors*, Ed. M. Stalova, **1977**. Academic press, New York.
162. Saito, F.; Yotoriyama, T.; Fujji, Y.; Nagashima, Y.; Nakao, A.; Iwaki, M.; Nishiyama, I., and Hyodo, T., **2007**. *Rad. Phys. and Chem.*, 76, 200.
163. Sanyal, D.; Roy, K.T.; Chakrabarti, M.; Dechoudhary, S.; Bhowmick, D., and Chakrabati, A., **2008**. *J. Phys.: Condens. Matter*, 20, 045217.
164. Sato, K.; Murakami, H.; Ito, K.; Hirata, K., and Kobayashi, Y., **2009**. *Rad. Phys. Chem.*, 78, 1085.
165. Schaefer, H-E.; Würschum, R.; Birringer, R., and Gleiter, H., **1988**, *Phy. Rev. B*, 38, 9545.
166. Scheer, M.D., **1982**. *Int. J. Chem. Kin.*, 15, 141.
167. Schneider, H.; Seeger, A.; Siegle, A.; Stoll, H.; Castellaz, P., and Major, J., **1997**. *Appl. Surf. Sci.*, 116, 145.
168. Schrader, D.M., and Jean, Y.C., (Eds) **1988**. *Positron and Positronium Chemistry* Elsevier, New York.
169. Schultz, P. J., and Lynn, K.G., **1988**. *Rev. Mod. Phys.* 60 (3), 701.
170. Schwinberg, P.B.; VanDyck, R.S. Jr., and Dehmelt, H.G., **1981**. *Phys. Rev. Lett.*, 47, 1679.
171. Selim, F.A.; Weber, M.H.; Solodovnikov, D., and Lynn, K.G., **2007**. *Phys. Rev. Lett.*, 99, 085502.
172. Sergent-Engelen, T.; Halleux, C.; Ferain, E.; Hanot, H.; Legras R., and Schneider, Y.-J., **1990**. *Biotechnology Techniques*, 4, 89.
173. Shah, C.P.; Kumar, M., and Bajaj, P.N., **2007**. *Nanotechnology*, 18, 385607.
174. Shah, C.P.; Rath, M.; Kumar, M., and Bajaj, P.N., **2010**. *Beilstein J. Nanotechnol.* 1, 119.
175. Shukla, A.; Peter M., and Hoffmann, L., **1993**, *Nucl. Instrum. Methods A*, 335, 310.
176. Singh, R.; Samra, K.S.; Kumar, R., and Singh, L., **2008**. *Rad. Phys. and Chem.*, 77, 575.

177. Singh, S., and Prasher, S., **2006**. *Nucl. Instrum. Method Phys. Res. Sect. B.*, 244, 252.
178. Slotte, J.; Saarinen, K.; Salmi, A.; Simula, S.; Aavikko, R., and Hautajarvi, P., **2003**. *Phys. Rev. B*, 67, 115209.
179. Smedskjaer, L.C.; Liu, J.Z.; Benedek, R.; Legnini, D.G.; Lam, D.J.; Stahulak, M.D.; Claus, H., and Bansil, A., **1998**. *Physica C*, 156(2), 269.
180. Song, Y-W.; Do, H.S.; Joo, H.S.; Lim, D-H.; Kim, S., and Kim, H.J., **2006**. *J. Adhes. Sci. Technol.*, 20, 1357.
181. Sreekumar, T.V.; Liu, T.; Min, B.G.; Guo, H.; Kumar, S., and Hauge, R.H., **2004**. *Adv. Mater.*, 16(1), 58.
182. Srithawatpong, R.; Peng, Z.L.; Olson, B.G.; Jamieson, A.M.; Simha, R.; McGervey, J.D.; Mair, T.R.; Halasa, A.F., and Ishida, H., **1999**. *J. Polym. Sci. Part B: Polym. Phys.*, 37(19), 2754.
183. Stoll H., et al., in *Principles and Applications of Positron and Positronium Chemistry*, World Scientific, London, 2003, Y. C. Jean, P. E. Mallon and D. M. Schrader, (Eds.),.
184. Sudarshan, K.; Dutta, D.; Sharma, S.K.; Goswami, A., and Pujari P.K., **2007**. *J. Phys.: Condens. Matt.*, 19, 386204.
185. Sudarshan, K.; Rath, S.K.; Patri, M.; Sachdeva, A., and Pujari, P.K., **2007**. *Polymer*, 48, 6434.
186. Sun, Y.; Zhu, Z.; Wang, Z.; Jin, Y.; Liu, J.; Hou, M., and Zhang, Q., **2003**. *Nucl. Instrum. Method Phys. Res B*, 209, 188.
187. Suzuki, N.; Hirade, T.; Saito, F., and Hyodo, T., **2003**. *Rad. Phys. Chem.*, 68, 647.
188. Suzuki, T.; Oki, Y.; Numajiri, M.; Miura, T.; Knodo, K., and Ito, Y., **1992**. *J. Polym. Sci. B: Polym. Phys.*, 30, 517..

## I

189. Tahara, H.; Kawabata, T.; Zhang, L.; Yasu, T., and Yoshikawa, T., **1997**. *Nucl. Instrum. Method Phys. Res. Sect. B*, 121, 446.
190. Talamoni, J.; Abbé, J.Ch.; Duplâtre G., and Haessler, A., **1981**. *Chem. Phys.*, 58, 13.
191. Tao S.J., **1972**. *J. Chem. Phys.*, 56, 5499.

192. Torsti, T.; Eirola, T.; Enkovaara, J.; Hakala, T.; Havu, P.; Havu, V.; Hoynalanmaa, T.; Ignatius, J.; Lyly, M.; Makkonen, I.; Rantala, T.T.; Ruokolainen, J.; Ruotsalainen, K.; Rasanen, E.; Saarikoski, H., and Puska, M.J., **2006**. *Phys. Status Solidi B*, 243, 1016.
193. Townrow, S.; Kilburn, D.; Alam, A., and Ubbink, J., **2007**. *J. Phys. Chem. B*, 111, 12643.
194. Trautmann, C., **1995**. *Nucl. Instrum. Methods Phys. Res. Sect. B*, 105, 81.
195. Tuomisto, F.; Ranki, V.; Saarinen, K., and Look, D.C., **2003**. *Phy. Rev. Lett.*, 99, 205502

## U

196. Uchida, E.; Uyama, Y., and Ikada, Y., **2000**. *J. Appl. Polym. Sci.* 41, 3609

## V

197. Valles Pamies, B.; Roudaut, G.; Dacremont, C.; Le Meste, M., and Mitchell, J. R., **2000**. *J. Sci. Food Agr.*, 80, 1679.
198. van Huis, M.A.; van Veen, A.; Schut, H.; Falub, C.V.; Eijt, S.W.H.; Mijnders, P.E., and Kuriplach, J., **2002**. *Phy. Rev. B*, 65, 085416.
199. van Krevelen, D.W., **1990**. *Properties of Polymers*, 3rd, ed.; Elsevier: Amsterdam, The Netherlands, chapter 6.
200. van Resandt, R.W.W.; Vogel, R.H., and Provencher, S.W., **1982**. *Rev. Sci. Instr.*, 53, 1392.
201. van Veen, A.; Schut, H.; Vries, J. De; Hakvroot, R.A., and Ijpma, M.R., **1990**. *AIP conf. Proc.*, 218, 171.
202. Vanderbilt, D., **1990**. *Phys. Rev. B.*, 41, 7892.
203. Venditti, R.A.; Gillham, J.K.; Jean, Y.C., and Lou, J., **1995**. *J. Appl. Polym. Sci.*, 56, 1207.
204. Vilgis, T.A.; Heinrich, G., and Kluppel, M., **2009**. *Reinforcement of Polymer Nano-Composites; Theory, Experiments and Applications*, Cambridge University Press: New York.

**W**

205. Wang, Y.Y.; Nakanishi, H., and Jean, Y.C., **1990**. *J. Polym. Sci., Part B: Polym. Phys.*, 28, 1431.
206. Wawryszczuk, J.; Goworek, J.; Zaleski, R., and Goworek, T., **2003**. *Langmuir*, 19, 2599.
207. Weber, M.H.; Lynn, K.G.; Barbiellini, B., Sterne, P.A., and Denison, A.B., **2002**. *Phy. Rev. B*, 66, 041305.

**X**

208. Xie, L.; DeMaggio, G.B.; Frieze, W.E.; DeVries, J., and Gidley, D.W., **1995**. *Phys. Rev. Lett.*, 74, 4947.
209. Xu, J.; Moxom, J.; Somieski, B.; White, C.W.; Mills Jr., A.P.; Suzuki, R., and Ishibashi, S., **2001**. *Phy. Rev. B*, 64, 113404.
210. Xu, J.; Mills Jr., A.P.; Ueda, A.; Henderson, D.O.; Suzuki, R., and Ishibashi, S., **1999**. *Phy. Rev. Lett.*, 83, 4586.
211. Xu, J., **2003**, in *Principles and Applications of Positron and Positronium Chemistry*, Jean, Y.C.; Mallon, P.E., and Schrader, D.M., (Eds.) World Scientific, London, p. 329.

**Y**

212. Yang, Y.N., and Wang, P., **2006**. *Polymer*, 47, 2683.

**Z**

213. Zaleski, R.; Kierys, A.; Grochowicz, M.; Dziadosz, M., and Goworek, J., **2011**. *J. Coll. Int. Sci.*, 358, 268.
214. Zhang, J.; Chen, H.; Li, Y.; Suzuki, R.; Ohdaira, T., and Jean, Y.C., **2007**, *Rad. Phys. Chem.*, 76, 172.
215. Zhang, J.; Yang, M., and Maurer, F.H. J., **2011**. *Macromolecules*, 44, 5711.
216. Zhang, L.; Yasui, T.; Tahara, H., and Yoshikawa, T., **1997**. *Jap. J. Appl. Phys.*, 36, 5268.
217. Zhou, W.; Wang, B.; Zheng, Y.; Zhu, Y.; Wang, J., and Qi, N., **2008**, *Chem Phys Chem*, 9, 1046.

218. Zhou, W.; Wang, J.; Zhenli, G.; Gong, J.; Qi, N., and Wang, Bo., **2009**, *App. Phys. Lett.*, 94, 021904.